mgr. MF & Matar.
8-5

DOE/ER-0046/12

Damage Analysis and Fundamental Studies

Quarterly Progress Report
October-December 1982

February 1983

U.S. Department of Energy
Assistant Secretary for Energy Technology
Office of Fusion Energy
Washington, DC 20545

NOTICE

This report was prepared as an account of work sponsored by an agency of the United States Government. Neither the United States Government nor any agency thereof, nor any of their employees, nor any of their contractors, subcontractors or their employees, makes any warranty, express or implied, or assumes any legal liability or responsibility for the accuracy, completeness, or any third party's use or the results of such use of any information, apparatus, product, or process disclosed, or represents that its use would not infringe privately owned rights. Reference herein to any specific commercial product, process, or service by trade name, trademark, manufacturer, or otherwise, does not necessarily constitute or imply its endorsement, recommendation, or favoring by the United States Government or any agency thereof or its contractors or subcontractors.

Printed in the United States of America
Available from
National Technical Information Service
U.S. Department of Commerce
5285 Port Royal Road
Springfield, VA 22161

NTIS price codes
Printed copy: A12
Microfiche copy: A01

DOE/ER-0046/12
UC-20,20c

Damage Analysis and Fundamental Studies

Quarterly Progress Report
October-December 1982

February 1983

U.S. Department of Energy
Assistant Secretary for Energy Technology
Office of Fusion Energy
Washington, DC 20545

FOREWORD

This report is the twentieth in a series of Quarterly Technical Progress Reports on ***Damage Analysis and Fundamental Studies*** (DAFS), which is one element of the Fusion Reactor Materials Program, conducted in support of the Magnetic Fusion Energy Program of the U.S. Department of Energy (DOE). The first eight reports in this series were numbered DOE/ET-0065/1 through 8. Other elements *of* the Fusion Materials Program are:

- Alloy Development for Irradiation Performance (ADIP)
- Plasma-Materials Interaction (PMI)
- Special Purpose Materials (SPM).

The GAFS program element is a national effort composed of contributions from a number of National Laboratories and other government laboratories, universities, and industrial laboratories. It was organized by the Materials and Radiation Effects Branch, DOE/Office of Fusion Energy, and a Task Group on ***Damage Analysis ana Fundamental Studies,*** which operates under the auspices of that branch. The purpose of this series of reports is to provide a working technical record of that effort for the use of the program participants, the fusion energy program in general, and the DOE.

This report is organized along topical lines in parallel to a Program Plan of the same title so that activities and accomplishments may be followed readily, relative to that Program Plan. Thus, the work of a given laboratory may appear throughout the report. Note that a new chapter has been adoed on Reouced Activation Materials to accomnodate work on a topic not included in the early program plan. The Contents is annotated for the convenience of the reader.

This report has been compiled and edited under the quidance of the Chairman of the Task Group on ***Damage Analysis and Fundamental Studies,*** D. G. Doran, Hanford Engineering Development Laboratory (HEDL). His efforts, those of the supporting staff of HEDL, and the many persons who made technical contributions are gratefully acknowledged. T. C. Reuther, Materials and Radiation Effects Branch, is the DOE counterpart to the Task Group Chairman and has responsibility for the DAFS program within DOE.

G. M. Haas, Acting Chief
Materials ano Radiation Effects Branch
Office of Fusion Energy

CONTENTS

	Page
Foreword	iii
Figures	xii
Tables	xxi
CHAPTER 1: IRRADIATION TEST FACILITIES	1
1. RTNS-II Irradiations and Operations (LLNL)	3
Irradiations were performed for thirteen different experimenters during this quarter.	
A new modular building was completed; it provides office space for Japanese scientists as well as some RTNS-11 personnel. Dedication will take place in early February.	
The RTNS-11 Steering Committee Meeting will be held February 10 and 11, 1983.	
CHAPTER 2: DOSIMETRY AND DAMAGE PARAMETERS	7
1. Standardized Dosimetry and Damage Data File (ANL)	9
The first version of a standardized dosimetry and damage data computer file (DOSFILE), covering 17 recent irradiations at ORR, HFIR, EBR-11, Omega West, CP5, HFBR, and IPNS, was completed.	
Copies of the data file and retrieval programs will be made available to interested parties for testing.	

CONTENTS (Cont'd)

Page

2. Dosimetry and Damage Analysis for the MFE4A Spectral Tailoring Experiment in ORR (ANL) 14

The maximum fluence inside the capsule after 406 full power days was 1.76 x 10^{22} n/cm^2 producing 4.67 dpa and 63 appm He in stainless steel (13%Ni). The status of all other experiments is summarized.

3. Displacement Code Modifications (HEDL) 24

An improved representation of the spectrum of outgoing charged particles was developed and incorporated into the NJOY Nuclear Data Processing System.

4. Helium Generation Cross Sections for Be(d,n) Neutrons (RIES) 31

Helium analyses were completed for the pure elements Be, Si, Ti, Y, Ag, Sn, Ta, W, and Pt, irradiated in a Be(d,n) neutron field, and average integral cross sections were determined.

5. ^{59}Ni + n Cross Section Evaluation (HEDL) 35

^{59}Ni + n reaction cross sections leading to ^{60}Ni, ^{59}Co and ^{56}Fe were evaluated from 10^{-5} eV to 10 MeV and put into ENDF/B format.

6. ^{59}Ni Isotopic Enrichment as a Means of Simulating the Helium/dpa Ratio of a Fusion Neutron Environment (HEDL) 37

A potential technique is examined for achieving fusion-relevant He/dpa ratios in nickel-bearing alloys, especially during the early stages of irradiation when microstructural features are nucleated. The projected material costs are high.

CONTENTS (Cont'd)

Paqe

7. Transmutation-Induced Deposition Profiles in Halos Surrounding Spherical Precipitates (U. of Missouri-Rolla and HEDL) 49

A general derivation was performed to determine the deposition profile concentrations around a precipitate for any transmutation reaction and precipitate/matrix combination; the $^{10}B(n,\alpha)^{7}Li$ reaction is of primary interest.

8. MUXS: A Code to Generate Multigroup Cross Sections for Sputtering Calculations (Union Carbide Nuclear Div., ORNL, U. of Tennessee) 63

Cross sections generated by MUXS can be used in many multigroup transport codes, with minor modifications to these codes, to calculate sputtering yields, reflection coefficients, penetration distances, etc.

CHAPTER 3. REDUCED ACTIVATION MATERIALS 67

1. Activation of Components of a Fusion Alloy (HEDL) 69

Ten days after a two-year irradiation at the STARFYRE first wall position, Mn, Co, and Ni have the highest unshielded dose rates per unit volume. After 3 x 10^5 days, N (considered as a liquid), Ni, and Mo have the highest decay rates per unit volume.

CONTENTS (Cont'd)

Page

CHAPTER 4. FUNDAMENTAL MECHANICAL BEHAVIOR 75

1. Effect of Temperature on the Crack Propagation Characteristics in RTNS-II Irradiated Type 316 Stainless Steel Microspecimens (U. of Virginia) 77

Microtensile specimens irradiated in RTNS-11 at room temperature to a fluence of 1 x 10^{22} n/m^2 and subsequently tensile tested at room temperature, 400°C, and 600°C exhibited the highest ductility at 600°C and a shallow ductility minimum at 400°C.

2. Correlation of Fracture Toughness with Tensile Properties for Irradiated 20% CW 316 Stainless Steel (HEDL and U. of Wisconsin) 86

Plane strain fracture toughness of irradiated 20% CW 316 SS was predicted successfully from tensile properties, using a model originally developed by Krafft.

3. The Dependence on Displacement Rate of Radiation-Induced Changes in Tensile Properties of AISI 304 (HEDL) 101

The dependence of the tensile strength of 304 SS on displacement rate at around 400°C is shown to arise from the sensitivity of microstructural components to this variable.

CHAPTER 5. CORRELATION METHOOOLOGY 115

1. Extension and Comparison of Various Equations of State for Gaseous and Solid Helium (U. of Wisconsin) 117

A previously developed equation of state (EOS) for gaseous helium is further improved so that it can be applied to densities approaching solid densities of helium. A solid EOS has also been developed.

CONTENTS (Cont'd)

Page

2. **Temperature Independence of the Swelling Rate in Austenitic Stainless Steels (U. of Wisconsin and HEOL)** 141

With the new experimental value of 1.1 eV for the vacancy migration energy, the steady-state swelling rate predicted by rate theory becomes nearly independent of temperature after the microstructural sink strength has reached or exceeded 5×10^{10} cm^{-2}, *in agreement with swelling measurements.*

3. **Void Swelling in the Presence of Small Helium Bubbles (U. of Wisconsin)** 149

It is shown that bubbles treated as neutral sinks have no effect whatsoever on the void swelling rate if the sink strength of all other sinks exceeds the value of about 2×10^{10} cm^{-2}

4. **Growth Mechanisms for Helium Inclusions and Bubbles (U. of Wisconsin)** 155

Three mechanisms are considered for pressure-driven growth of small clusters of helium atoms and vacancies: self-interstitial ejection, dislocation loop punching, and stess-assisted thermal vacancy absorption. Regimes of cavity size and of temperature in which the different mechanisms dominate are identified.

5. **Radiation-Induced Evolution of Fe-Ni-Cr Ternary Alloys (HEDL)** 170

During irradiation of austenitic Fe-Ni-Cr alloys with nickel levels of ~35%, some regions become rich in nickel and reduced in chromium and iron, while other regions become depleted in nickel and enhanced in chromium and iron.

CONTENTS (Cont'd)

Page

6. **The Influence of Reactor Spectra and Irradiation Temperature on the Swelling of AISI 316 Stainless Steel (HEDL)** 178

The results of a reanalysis of the swelling for the DO-heat of 316 SS, including ^{56}Fe recoil-induced displacements and three data points inadvertently omitted previously, confirm the earlier proposal that the additional helium generated in HFIR does not substantially alter the swelling behavior from that observed in EBR-II.

7. **Cavity Formation in Single- and Dual-Ion Irradiated V-15 Cr-5 Ti Alloy (ANL)** 194

The swelling of V-15 Cr-5 Ti alloy on self-ion irradiation was negligible for irradiation temperatures $\lesssim$725°C and damage levels $\leq$30 dpa. Dual-ion irradiation produced negligible swelling for irradiation temperatures <675°C, damage levels $\leq$15 dpa for 10 appm He/dpa, and irradiation temperatures <650°C and damage levels $\leq$60 dpa when the He/dpa ratio was reduced to 3 appm He/dpa.

8. **Helium Bubble Formation in Cu, Ni and Cu-Ni Alloys (U. of Wisconsin and ORNL)** 206

Bubble sizes and concentrations were similar in pure copper and Cu-Ni alloys irradiated with 200 - 400 keV ^{3}He ions at T/T_m = 0.65. Smaller bubbles at higher concentrations were found in pure nickel.

CONTENTS (Cont'd)

9. Suppression of Void Nucleation by Injected Interstitials (U. of Wisconsin) 216

The void nucleation rate is drastically reduced by injected interstitials whenever recombination is an important process, leading to a suppression of void nucleation in ion-bombardment experiments below a characteristic threshold temperature. This also leads to a void free zone at intermediate depth in low temperature ion-bombardment experiments.

CHAPTER 6. INSULATORS

1. Comparison of Low Dose Neutron and Gamma Irradiation Damage in G-10CR (LANL) 235

Samples of the epoxy-matrix laminate G-10Cr were irradiated with high energy neutrons in liquid helium to a dose of 2.5 MGy to simulate the operating environment of a fusion reactor magnet. Mechanical and electrical properties were subsequently measured at room and liquid nitrogen temperatures, and the results compared to effects produced by gammas. Interpretation is complicated by the microscopically inhomogeneous nature of the damage production.

FIGURES

Page

CHAPTER 2

2. Dosimetry and Damage Analysis for the MFE4A Spectral Tailoring Experiment in ORR (ANL)

FIGURE 1. Adjusted Neutron Flux Spectrum for the MFE4A Experiment in ORR Normalized to 30 MW After 406 Full Power Days. 20

3. Displacement Code Modifications (HEDL)

FIGURE 1. (a) Ni-58 (n,p), p Spectrum for 14-MeV n. 27

(b) Ni-58 (n,α), a Spectrum for 14-MeV n. 27

FIGURE 2. (a) Mo-92 (n,p), p Spectrum for 14-MeV n. 28

(b) Mo-92 (n,α), a Spectrum for 14-MeV n. 28

5. ^{59}Ni + n Cross-Section Evaluation (HEDL)

FIGURE 1. Evaluated Neutron Cross Sections for ^{59}Ni. 36

6. ^{59}Ni Isotopic Enrichment as a Means of Simulating the Helium/dpa Ratio of a Fusion Neutron Environment (HEDL)

FIGURE 1. Helium Production in Stainless Steel 316 Irradiated in Fast, Thermal, and Fusion Neutron Environments. 40

FIGURE 2. Concentration of ^{59}Ni as a Function of Exposure in HFIR/PTP Spectrum. 42

FIGURE 3. Helium Concentration Versus dpa for Alloys Containing Various Levels of ^{59}Ni Enrichments. 43

FIGURE 4. Helium Concentration Versus dpa for an Irradiation in FTR/MOTA of Alloys Containing Various levels of ^{59}Ni Enrichment. 45

FIGURE 5. Helium Concentration Versus dpa for an Irradiation in a Row 7 FTR Reflector Location for Alloys Containing Various Levels of ^{59}Ni Enrichment. 46

FIGURES (Cont'd)

Page

7. Transmutation-Induced Deposition Profiles in Halos Surrounding Spherical Precipitates (U. of Missouri-Rolla and HEDL)

FIGURE 1. Representative Micrographs of Halo Micro-Structure Found Around $_{84}C$ Particles in Neutron-Irradiated Iron. 51

FIGURE 2. Effect of Precipitate Size on Normalized Deposition Rate of Reaction Products for $^{10}B(n,a)$ Events Occurring in Spherical M_3B_2 Precipitates Embedded in a Stainless Steel Matrix. 53

FIGURE 3. Limits of the Halo are Determined by the Precipitate Size, the Range of the Energetic Particle in the Matrix, and the Ratio m That Defines the Relative Stopping Powers of the Precipitate and Matrix Phases. 53

FIGURE 4. Schematic Illustration of Internal Precipitate Surface Contributing Particles to Point x,o in the Halo. 54

FIGURE 5. Geometrical Relationships Describing the Maximum Angle Defining the Source Surface for Any Point in the Halo. 54

FIGURE 6. rmalized Deposition Rate Profiles for the ,a) Reaction when m = 0.5. 60

FIGURE 7. Normalized Deposition Rate Profiles for the $^{10}B(n,a)$ Reaction when m = 2.0. 60

CHAPTER 4

1. Effect of Temperature on the Crack Propagation Characteristics in RTNS-II Irradiated Type 316 Stainless Steel Microspecimens (U. of Virginia)

FIGURE 1. Crack Length Versus Elongation for RTNS-II Irradiated Specimens, Which Were a) Tensile Tested at 400°C and b) Tensile Tested at 600°C. 80

FIGURES (Cont'd)

Page

FIGURE 2. Schematic Illustration of a Fractured Specimen: a) Top View, b) Near Edge View of Electropolished Region and the Surrounding Thick Area, c) Before and After Fracture Cross-section View, d) Shoulder Left After Fracture. 82

2. Correlation of Fracture Toughness with Tensile Properties for Irradiated 20% CW 316 Stainless Steel (HEDL and U. of Wisconsin)

FIGURE 1. Effect of the Minimum Irradiated Fracture Toughness Level on First Wall Lifetime for Various Wall Thicknesses. 88

FIGURE 2. Failure Mode Map. 90

FIGURE 3. Comparison of Measurements and Estimates of the Fracture Toughness for Irradiated 20% CW 316 Stainless Steel, Assuming $d^*=30\ \mu m$ and Using Duct Tensile Properties. 95

FIGURE 4. Comparison of Measurements and Estimates of the Fracture Toughness for Irradiated 20% CW 316 Stainless Steel, Assuming $d^*=30\ \mu m$ and Using Tubing Tensile Properties. 98

3. The Dependence on Displacement Rate of Radiation-Induced Changes in Tensile Properties of AISI 304 (HEDL)

FIGURE 1. Yield Strength of 20% CW Type 316 Stainless Steel After E8R-II Irradiation. 103

FIGURE 2. Dependence of Tensile Properties of Annealed AISI 304 on Displacement Rate and Total Damage. 105

FIGURE 3. Void and Frank Loops Observed in AISI 304 Irradiated at $\sim 400°C$ and ~ 3 dpa at 7.9×10^{-7} and 0.8×10^{-7} dpa/sec. 108

FIGURE 4. Comparison of the Yield Strength of SA 316 Irradiated in Phenix and Rapsodie. 110

FIGURES (Cont'd)

		Page
FIGURE 5.	Temperature Shift in Saturation Yield Strength of the Same Heat of SA 316 Arising from Differences in Displacement Rate in Phenix and Rapsodie at 400°C.	110
FIGURE 6.	The Dependence of Yield Strength in Annealed AISI 304 on Displacement Rate After Irradiation in EBR-II at ~400°C.	111
FIGURE 7.	Schematic Illustration of the Dependence of Microstructural Densities in this Experiment on Irradiation Temperature and Displacement Rate.	112

CHAPTER 5

1. Extension and Comparison of Various Equations of State for Gaseous and Solid Helium (U. of Wisconsin)

FIGURE 1.	Ranges of Temperature and Pressure in Which Experimental Data Exist for the Equation of State (EOS) of Helium.	119
FIGURE 2.	Interatomic Potential for Helium According to Beck and Young, McMahon, and Ross.	126
FIGURE 3.	Comparison of the Empirical EOS Developed by McCarthy with the Present EOS Derived with the Beck or Young Potential.	128
FIGURE 4.	Ground-State Pressure for Solid He.	130
FIGURE 5.	Melt-Pressure for Helium.	132
FIGURE 6.	Melt-Volume and Its Reciprocal for Helium.	132
FIGURE 7.	Compressibility Factor at Melting for Helium.	133
FIGURE 8.	EOS for Gaseous Helium Using Beck's Potential.	137
FIGURE 9.	EOS for Gaseous Helium Using Young's Potential.	137

FIGURES (Cont'd)

		Page
FIGURE 10.	Comparison of All EOS Using Beck's Potential.	138
FIGURE 11.	Comparison of All EOS Using Young's Potential.	138
2.	Temperature Independence of the Swelling Rate in Austenitic Stainless Steels (U. of Wisconsin and HEDL)	
FIGURE 1.	N-lot, a Heat of AISI 316 Showing a Relative Insensitivity of Swelling to Temperature in a Given Experiment, but also Exhibiting a Sensitivity of the Transient Regime to Environmental History in Each Experiment.	143
FIGURE 2.	The Function F/P, Which Determines the Temperature Dependence of the Steady-State Swelling Rate, Depends on Total Sink Strength, Temperature, and Vacancy Migration Energy.	146
FIGURE 3.	The Temperature Dependence of the Function F/P is Quite Sensitive to the Vacancy Migration Energies.	147
4.	Growth Mechanisms for Helium Inclusions and Bubbles (U. of Wisconsin)	
FIGURE 1.	Energy Expended per Metal Atom Emitted When Bubble Growth Occurs by Self-Interstitial Emission or Punching of Interstitial Loops.	160
FIGURE 2.	Energy Expended per Thermal Vacancy Absorption at a Bubble for Helium Production by Transmutations.	164
FIGURE 3.	Energy Expended per Thermal Vacancy Absorption at a Bubble for Helium Implantation Typical of Blistering Studies.	164
FIGURE 4.	Hydrostatic Stress Produced in the Matrix of a Solid Containing Bubbles with Volume Fraction S and Net Pressure P_0.	168
5.	Radiation-Induced Evolution of Fe-Ni-Cr Ternary Alloys (HEDL)	
FIGURE 1.	Variation of Alloy E37 Matrix Composition Measured at 200-nm Intervals Along a Traverse Across the Specimen.	172

FIGURES (Cont'd)

		Page
FIGURE 2.	Relationship Between Nickel and Chromium Levels in Specimen E37, as Measured in Small Areas ~30 mm in Size.	174
FIGURE 3.	Segregation of Nickel Near a Void Surface in Specimen E37.	175
FIGURE 4.	Segregation of Nickel Near a Void Surface in Specimen E25.	175
6.	The Influence of Reactor Spectra and Irradiation Temperature on the Swelling of AISI 316 Stainless Steel (HEDL)	
FIGURE 1.	Swelling Observed in 20% CW DO-Heat Irradiated in EBR-II and HFIR.	181
FIGURE 2.	(a) Swelling Rate of Annealed DO-Heat in HFIR and EBR-II is Independent of Temperature and Comparable to the High Fluence Behavior of the Composite HFIR/EBR-II Curve for Cold-Worked Material.	
	(b) The Annealed Swelling Behavior in HFIR is Typical of Annealed Swelling at 600°C in EBR-II.	1a2
FIGURE 3.	Comparison of Composite HFIR/EBR-II Trend Line for DO-Heat with Swelling Behavior Observed for a Single Heat of Steel Irradiated in EBR-II in Two Separate Experiments.	183
FIGURE 4.	The Influence of Displacement Rate and Time-in-Reactor on the Swelling of Annealed AISI 316 Fuel Pin Cladding from the Rapsodie Reactor.	184
FIGURE 5.	The Influence of Displacement Rate and Time-in-Reactor on the Swelling at 562°C of Annealed AISI 316 Fuel Pin Cladding from the Rapsodie Reactor.	184
FIGURE 6.	"Double-Bump" Swelling Rate Profiles Observed in Annealed and Aged M316 After Irradiation in the Dounreay Fast Reactor, as Observed by Gittus, Watkin and Standring.	186

FIGURES (Cont'd)

		Page
FIGURE 7.	Apparent Swelling Rate vs Maximum Swelling in Data Set for M316 and 316 Steels from Table 2, Temperatures Greater than 475°C Only.	189
FIGURE 8.	Apparent Swelling Rate vs Maximum Swelling in Data Set for M316 and 316 Steels from Table 2, Temperatures Less than 425°C Only.	190
FIGURE 9.	Two Regimes of Temperature Insensitivity Observed in N-Lot Heat of AISI 316 Irradiated in E8R-II.	190
7.	Cavity Formation in Single- and Dual-Ion Irradiated V-15 Cr-5 Ti Alloy (ANL)	
FIGURE 1.	Swelling of Neutron- and Ion-Irradiated V and V-15 Cr-5 Ti Alloy.	198
FIGURE 2.	Microstructures of Ion-Irradiated V-15 Cr-5 Ti Alloy.	199
FIGURE 3.	Swelling of V and V Alloys on $^{58}Ni^{+}$- or $^{51}V^{+}$-Ion Irradiation.	202
8.	Helium Bubble Formation in Cu, Ni and Cu-Ni Alloys (U. of Wisconsin and ORNL)	
FIGURE 1.	Summary of Previous Studies of Void Formation in Cu-Ni Alloys.	208
FIGURE 2.	Calculated Implanted Helium Profile for the Cu-Ni Alloys Used in This Study.	209
FIGURE 3.	Helium Bubbles Observed in Pure Copper and Nickel Implanted with 200 appm He at the Homologous Temperature T/T_m = 0.65.	210
FIGURE 4.	Helium Bubbles Observed in Cu-Ni Alloys Implanted with 200 appm He at the Homologous Temperature T/T_m = 0.65.	211
FIGURE 5.	Variation in the Visible Bubble Density and Average Bubble Size with Alloy Composition.	213
FIGURE 6.	Percent of Helium Observed in Bubbles for the Cu-Ni Alloys.	213

FIGURES (Cont'd)

Page

9. Suppression of Void Nucleation by Injected Interstitials (U. of Wisconsin)

FIGURE 1. Void Nucleation Rate for a Displacement Rate of 10^{-3} dpa/s, Vacancy Migration Energy of 1.2 eV, Sink Strength of 5 x 10^{13} m^{-2}. 223

FIGURE 2. Void Nucleation Rate for a Displacement Rate of 10^{-2} dpa/s, All Other Materials Parameters as in Figure 1. 223

FIGURE 3. Void Nucleation Rate for a Displacement Rate of 10^{-3} dpa/s, Vacancy Migration Energy of 1.4 eV, Sink Strength of 5 x 10^{13} cm^{-2}. 225

FIGURE 4. Depth Distribution of the Displacement Rate and Injected Interstitial Fraction for 14-MeV Ni-Ions on Ni According to the BRICE Code. 225

FIGURE 5. Void Nucleation Rate Without Injected Interstitials vs Depth, for 14-MeV Ni Ions, Sink Strength of 10^{14} m^{-2}, Vacancy Migration Energy of 1.1 eV. 226

FIGURE 6. Void Nucleation Rate with Injected Interstitials and Parameters as in Figure 5. 226

FIGURE 7. Void Nucleation Rate vs Depth, Vacancy Migration Energy of 1.2 eV, All Other Parameters as in Figure 6. 228

FIGURE 8. Void Nucleation Rate vs Depth, Vacancy Migration Energy of 1.2 eV, Sink Strength of 5 x 10^{13} m^{-2}. 228

FIGURE 9. Void Density vs Depth for Nickel Irradiated at 400°C with 14-MeV Cu Ions to a Fluence of About 5 x 10^{16} Ions/cm2. 229

CHAPTER 6

1. Comparison of Low Dose Neutron and Gama Irradiation Damage in G-10Cr (ANL)

FIGURE 1. Results of Neutron Irradiation on Flexural and Longitudinal Compression Strength of G-10Cr Measured at Room Temperature. 239

FIGURES (Cont'd)

		Page
FIGURE 2.	Characteristic Appearance of Longitudinal G-10Cr Fractures (Before and After Neutron Irradiation) at Two Test Temperatures.	240
FIGURE 3.	Fracture Surfaces on Control Sample and Neutron-Irradiated Sample.	242

TABLES

Page

CHAPTER 2

1. Standardized Dosimetry and Damage Data File (ANL)

TABLE 1. Irradiations Included in DOSFILE. 11

TABLE 2. Data Key Words for DOSFILE. 12

2. Dosimetry and Damage Analysis for the MFE4A Spectral Tailoring Experiment in ORR (ANL)

TABLE 1. Status of Dosimetry Experiments. 15

TABLE 2. Activation Rates Measured for ORR-MFE4A Dosimeters Removed on April 26, 1982 at 12,176 MWd. 17

TABLE 3. Maximum Activation Rates for ORR-MFE4A. 19

TABLE 4. Maximum Flux and Fluence Values for ORR-MFE4A. 20

TABLE 5. Damage Parameters for ORR-MFE4A. 21

TABLE 6. Damage and Helium Calculations for Nickel. 23

3. Displacement Code Modifications (HEDL)

TABLE 1. Damage Energy Cross Sections (keV-b) for 14-MeV Neutrons on Iron. 29

TABLE 2. Damage Energy Cross Sections (keV-b) for 14-MeV Neutrons on Nickel. 29

4. Helium Generation Cross Sections for Be(d,n) Neutrons (RIES)

TABLE 1. Integral Helium Generation Cross Sections for the ~0-32-MeV Be(d,n) Neutron Spectrum Produced by 30-MeV Deuterons. 33

TABLES (Cont'd)

Page

CHAPTER 3

1. Activation of Components of a Fusion Alloy (HEOL)

TABLE 1. Activation at 10 Days After 2-Year Irradiation at STARFIRE First Wall. 72

TABLE 2. Activation at 3 x 10^5 Days (~820 Years) after 2-Year Irradiation at STARFIRE First Wall. 73

TABLE 3. Isotopic Abundances. 74

CHAPTER 4

1. Effect of Temperature on the Crack Propagation Characteristics in RTNS-II Irradiated Type 316 Stainless Steel Microspecimens (U. of Virginia)

TABLE 1. Data from HVEM Microtensile Specimens. 83

2. Correlation of Fracture Toughness with Tensile Properties for Irradiated 20% CW 316 Stainless Steel (HEDL and U. of Wisconsin)

TABLE 1. Tensile Properties and Computed Values for the Fracture Toughness of 20% CW 316 Duct Material Irradiated to 10 x 10^{22} n/cm^2 (E > 0.1 MeV). 93

TABLE 2. Tensile Properties and Computed Values for the Fracture Toughness of 20% CW 316 Tubing Irradiated to Fluences Between 6.1 and 13.0 x 10^{22} n/cm^2 (E > 0.1 MeV). 96

3. The Dependence on Displacement Rate of Radiation-Induced Changes in Tensile Properties of AISI 304 (HEDL)

TABLE 1. Irradiation Conditions for Annealed AISI 304 Irradiated in EBR-II. 104

TABLE 2. Sumnary of Microstructural Data. 107

TABLES (Cont'd)

Page

CHAPTER 5

Extension and Comparison of Various Equations of State Gaseous and Solid Helium (U. of Wisconsin)

TABLE 1. Debye Temperature and Gruneisen Parameter for Solid ^{4}He. 134

4. Growth Mechanisms for Helium Inclusions and Bubbles (U. of Wisconsin)

TABLE 1. Materials Parameters for Nickel and Austenitic Stainless Steels. 159

6. The Influence of Reactor Spectra and Irradiation Temperature on the Swelling of AISI 316 Stainless Steel (HEDL)

TABLE 1. Swelling of M316, 316 and 316L in the Dounreay Fast Reactor. 187

8. Helium Bubble Formation in Cu, Ni and Cu-Ni Alloys (U. of Wisconsin and ORNL)

TABLE 1. Bubble Parameters for Cu, Ni and Cu-Ni Alloys. 212

9. Suppression of Void Nucleation by Injected Interstitials (U. of Wisconsin)

TABLE 1. Materials Parameters. 222

CHAPTER 6

1. Comparison of Low Dose Neutron and Gama Irradiation Damage in G-10Cr (LANL)

TABLE 1. Dosimetry for G-10Cr. 237

TABLE 2. Dielectric Breakdown Strength of 3 Irradiated and 5 Control Samples at 295 K. 238

TABLE 3. Comparison of Retained Flexure and Longitudinal Compression Strength for G-10Cr After Neutron or Gama Irradiation at Liquid Helium Temperature. 243

C H A P T E R 1

IRRADIATION TEST FACILITIES

RTNS-II IRRADIATIONS AND OPERATIONS

C.M. Logan and D. W. Heikkinen
Lawrence Livermore National Laboratory

1.0 Objective

The objectives of this work are operation of RTNS-II (a 14-MeV neutron source facility), machine development, and support of the experimental program that utilizes this facility. Experimenter services include dosimetry, handling, scheduling, coordination, and reporting. RTNS-II is dedicated to materials research for the fusion power program. Its primary use is to aid in the development of models of high-energy neutron effects. Such models are needed in interpreting and projecting to the fusion environment engineering data obtained in other neutron spectra.

2.0 Summary

Irradiations were performed for thirteen different experimenters during this quarter.

The new modular building has been completed and occupied providing office space for Japanese scientists as well as some RTNS-II personnel. Dedication will take place in early February.

The RTNS-II Steering Committee Meeting will be held February 10 and 11, 1983.

3.0 Program

Title: RTNS-II Operations (WZJ-16)
Principal Investigator: C. M. Logan
Affiliation: Lawrence Livermore National Laboratory

4.0 Relevant DAFs Program Plan Task/Subtask

TASK II.A.2,3,4.
TASK II.B.3,4
TASK II.C.1,2,6,11,18.

5.0 Irradiati - M. Logan, D. W. Heikkinen and M. W. Guinan

The irradiation of the MACOR samples for J. Fowler (LANL) continued during this quarter. The front surface fluence has reached 4.1×10^{18} n/cm^2.

The other primary irradiation of this period was the low temperature ($4^{o}K$) irradiation of Cu magnet stabilizer for Guinan (LLNL). During this experiment, a series of five cycles consisting of irradiation followed by annealing and resistivity measurements were done.

The add-on irradiations for R. Mallon (LLNL) R. Hopper (LLNL), R. Borg (LLNL) and G. Woolhouse (Aracor) were continued during the quarter. The irradiation for Mallon to study the transport of oil shale in a fluidized bed has been completed. In addition, the Si samples of Woolhouse for TEM study were finished. The irradiations of various mineral samples for Borg and the ^{235}U laser glass combination for Hopper are continuing. The Borg experiment involves measurement of the production of inert gases while the Hopper experiment involves laser glass surface treatment using fission fragments.

Additional add-on irradiations were done for T. Iida (Osaka) on transistors, microchannel plates, integrated circuits, liquid scintillators, thermocouples, and optical fibers. Fluences ranged from 10^{13} - 10^{16} n/cm^2. R. Hartmann (Northrop) did a low fluence irradiation (10^{13} n/cm^2) on LSI circuits. R. Lougheed and H. Hicks used samples of Tl and As_2O_3 respectively for tracer production. R. Foland (Ohio State Univ.) irradiated samples of albite ($NaAlSi_3O_8$) for inert gas retention studies.

Low fluence irradiations were also done for Heikkinen and Schumacher (LLNL) for neutron monitoring calibration and adhesive/sealant strength tests, respectively.

5.1 RTNS- Status - M. Loaan and D. W. Heikkinen

Installation was completed on new arc power supplies for both the left and right machines. Beam currents up to 110 mA have been obtained on target for the left machine. For prolonged use, however, beam currents have been limited to 90 mA on the 23-cm diameter targets because of beam-related vacuum problems encountered at the higher currents. These problems are not expected to occur for the 50-targets.

Turbo pumps continue to be a problem. During this period, two horizontal pumps (Sargeant Welch) failed destructively. This was the major cause of the unscheduled outage. Conversion to Balzers turbo pumps is in progress. A rotating target bearing seizure was the only other cause of major outage time. Final design and fabrication of parts for the new accelerator column are continuing.

Except for some minor items (smoke detectors] paging system, and landscaping), the modular building has been completed and occupied. This provides office space for people formerly housed in the set-up lab, as well as visiting Japanese scientists. Dedication will be held preceding the RTNS-II Steering Committee Meeting scheduled for February 10 and 11.

6.0 Future Work

Short irradiations for D. Nethaway (LLNL) on U and Pu and T. Norris (LANL) on *Am* are planned for the next quarter. These are non-fusion experiments. One of the primary irradiations during the next quarter will be the joint Japan/U.S. high temperature irradiation using the HEDL furnace. The principal contacts are N. Yoshida (Kyushu) and E. R. Bradley (PNL). The MACOR irradiation for Fowler (LANL) will be continued. Various add-on experiments are also expected.

6.1 Publications

None

C H A P T E R 2

DOSIMETRY AND DAMAGE PARAMETERS

STANDARDIZED DOSIMETRY AND DAMAGE DATA FILE

L. R. Greenwood (Argonne National Laboratory)

1.0 Objective

To establish standardized dosimetry procedures in order to reduce uncertainties in damage analysis and correlation studies.

2.0 Summary

The first version of our standardized dosimetry and damage data computer file (DOSFILE) has been completed. At present, data is available for 17 recent ir-irradiations at ORR, HFIR, EBR-II, Omega West, CP5, HFBR. and IPNS. Copies of the data file and retrieval programs will be made available to interested parties for testing.

3.0 Program

Title: Dosimetry and Damage Analysis

Principal Investigator: L. R. Greenwood

Affiliation: Argonne National Laboratory

4.0 Relevant DAFS Program Plan Task/Subtask

Task II.A.6	Dosimetry Standardization
Subtask II.A.6.3	Establish a Permanent Standard Dosimetry File

5.0 Accomplishments and Status

Version I of our standarized dosimetry and damage data file, DOSFILE, is now available. Data has been recorded for 17 recent irradiations, as listed in Table 1. Older data is now being reviewed for entry into the file. The data is written in a simple card-image format similar to ENDF. However, alpha-numeric titles and header records have been used extensively to make the files more readable, without the need to reference external manuals.

The types of data stored in the file are listed in Table 2. A short fortran retrieval program is provided to aid users. By typing in the key words for the irradiation and type of data wanted, a user can rapidly obtain a listing. For example, the key words HFR-32 and FSM would instruct the program to list a flux and fluence summary table for the HFIR-CTR32 irradiation. The identification (IDN) file contains a plain-English description of the irradiation history, gradients, and references to more complete publications as well as reference cross section, self-shielding, and uncertainty data files. These latter files are also contained in the DOSFILE package to facilitate cross-referencing.

In establishing the file we have attempted to not only document data and procedures, but also provide all input data required for spectral adjustment. Specifically, the input data is provided for the STAYSL computer code which is used for spectral adjustment. Uncertainties and covariances are thus listed for the activities, cross sections, input, and output flux spectra. Co-variances on the input spectrum and cross sections are assumed to be described

TABLE 1

IRRADIATIONS INCLUDED IN DOSFILE

Irradiation*	Key Word
HFIR-CTR32	HFR32
HFIR-CTR34	HFR34
HFIR-CTR35	HFR35
ORR-ME1	ORMF1
ORR-MFE2	ORMF2
ORR-MFE4A-1	OR4A1
ORR-MFE4A-2	OR4A2
ORR-Spectral Run	ORRLP
ORR-TBC07	ORRT7
om-TRIO-1	TRIO1
Omega West-Spectral Run	OMWSP
Omega West-HEDL-1	OMWH1
IPNS-9-VT2-REF	IPN9C
EBRII-X287	EB287
CP5-Fission Converter	CP5FC
HFBR-VT15-2	HFBR2
HFBR-VT15-3	HFBR3

*

HFIR: High Flux Isotope Reactor (ORNL)
ORR: Oak Ridge Research Reactor (ORNL)
Omega West Reactor (LANL)
IPNS: Intense Pulsed Neutron Source (ANL-E)
EBRII: Experimental Breeder Reactor II (ANL-W)
CP5: Chicago Pile 5 (ANL)
HFBR: High Flux Beam Reactor (BNL)

TABLE 2

DATA KEY WORDS FOR DOSFILE:

Key Word	Description
IDN	Identification, irradiation history, gradients, references
ACT	Activities with uncertainties, covers, and self-shielding
FLI	Input flux data
FUN	Input flux uncertainties
FLO	Output flux data
FCV	Output flux covariance matrix
FSM	Flux, fluence summary
DAM	Damage parameters

by a Gaussian function. However, the output covariances have no such simple functional dependence and hence must be reported as a complete 100 x 100 element matrix, although only half the terms need be listed since the matrix is symmetric. This output matrix must be used to determine errors on derived quantities such as DPA or gas production.

At present copies of WSFILE will be sent to interested parties for testing. Feedback from the user community would be particularly useful at this stage in determining suitability of data and formats as well as future changes and additions to the file. In the near future the file will be placed on the NMFE Computer System at Lawrence Livermore Laboratory for general access by the fusion community. A manual is now being written and this will be published as an Argonne report.

6.0 References

None.

7.0 Future Work

Older dosimetry data will be included in DOSFILE. This data will require some review to update nuclear data and procedures to ensure complete compatibility of all data in the file.

DOSIMETRY AND DAMAGE ANALYSIS FOR THE MFE4A SPECTRAL TAILORING EXPERIMENT IN ORR

L. R. Greenwood (Argonne National Laboratory)

1.0 Objective

To characterize neutron irradiation facilities in terms of neutron flux, spectra, and damage parameters (DPA, He, transmutation) and to measure these exposure parameters during fusion materials irradiations.

2.0 Summary

Measurements and calculations are presented for the ORR-MFE4A spectral-tailoring experiment after an irradiation of 406 full power days (30 MW) between June 12, 1980 and April 26, 1982. The maximum fluence inside the capsule was 1.76 x 10^{22} n/cm^2 producing 4.67 DPA and 63 appm He in stainless steel (13% Ni). Values outside the sample holders were 1.88 x 10^{22} n/cm^2, 4.94 DPA and 73 appm He in stainless steel. Helium calculations include epi-thermal effects and the extra displacements from the energetic ^{56}Fe recoils. The status of all other experiments is summarized in Table 1.

3.0 Program

Title: Dosimetry and Damage Analysis

Principal Investigator: L. R. Greenwood

Affiliation: Argonne National Laboratory

4.0 Relevant DAFS Program Plan Task/Subtask

DAFS Task II.A.l - Fission Reactor Dosimetry

TABLE 1

STATUS OF DOSIMETRY EXPERIMENTS

Facility	Experiment	Status/Change
ORR	MFE 1	Completed 12/79
	MFE 2	Completed 06/81
	MFE 4A1	Completed 12/81
	MFE 4A2	Completed 11/82
	MFE 4 B,C	Irradiation in Progress
	TBC 07	Completed 07/80
	TRIO-Test	Completed 07/82
	TRIO-1	Samples Sent 10/82
HFIR	CTR 32	Completed 04/82
	CTR 31, 34, 35	Samples Received 09/82
	CTR 30	Irradiation in Progress
	T1, T2, T3	Irradiations in Progress
	RBI, RB2, RB3	Irradiations in Progress
	CTR 39-45	Samples Sent 10/82
Omega West	Spectral Analysis	Completed 10/80
	HEDL1	Completed 05/81
EBR-II	X287	Completed 09/81
IPNS	Spectral Analysis	Completed 01/82
	LANL1 (Hurley)	Completed 06/82
	Hurley/Coltman	Samples Received 11/82

5.0 Dosimetry and Analysis for the MFE4A Spectral Tailoring Experiment in ORR

The MFE4A experiment in the Oak Ridge Research Reactor (ORR) was designed to achieve fusion-like helium-to-DPA ratios in stainless steel by altering the neutron spectrum. The irradiation in core position E3 began on June 12, 1980 and was first removed on January 19, 1981 after an exposure of 5481 MWD. Dosimeters were removed at that time and our results were reported previously. [Damage Analysis and Fundamental Studies, Quarterly Progress Report, DOE/ER-0046/6, p. 24, 1981.] The experiment was then further irradiated from March 19, 1981 to September 16, 1981 for 4404 MWD and finally from February 2, 1982 to April 26, 1982 for 2291 MWD. The net exposure was thus 12,176 MWD.

Dosimetry capsules for this entire exposure have been analyzed and the results are reported below. The MFE4A experiment is still being irradiated; hence, these interim results are intended to check the progress of the planned exposure.

Four of our original eight stainless steel dosimetry tubes were removed in the present experiment. The other four were left in for further irradiation along with four new dosimeters to replace those which were removed. Each tube was about 1/16" OD by 2.75" long and contained small quantities of Pe, Co, 80% Mn–Cu, Ti, Nb, Cu, Ni, and helium accumulation monitors. All of the samples were gamma counted by Ge(Li) spectroscopy techniques. The samples were then sent to Rockwell International for helium analyses.

The measured activities are listed in Table 2. All values have been corrected for burnup; however, self–shielding effects are not included since this correction is spectral–dependent and hence must be done concurrently with subsequent spectral adjustment. The values agree quite well with those reported previously, although the previous $^{59}Co(n,\gamma)$ value was altered due to a reanalysis of the Co–V alloy, as reported later. [Damage Analysis and Fundamental Studies, Quarterly Progress Report, DOE/ER-0046/8, p. 21, 1982.] Furthermore, neutron self–shielding corrections are slightly larger in the present run. The final activity ratios of the present measurements divided by the earlier measurements are, as follows:

TABLE 2

ACTIVATION RATES MEASURES FOR ORR-MFE4A DOSIMETERS REMOVED
APRIL 26, 1982 AT 12,176 MWd
(Values normed to 30 MW, accuracy ±1.5%)

Reaction	Height, in.	$\sigma\phi$ (atom/atom-s) Inside	Outside
$^{58}Fe(n,\gamma)^{59}Fe$	-0.62	1.72×10^{-10}	1.85^{-10}
	-2.47	1.68	1.88
	-3.75	1.72	
	-3.94		1.83
	-4.50		1.82
	-5.78		1.68
	-5.84	1.54	
$^{59}Co(n,\gamma)^{60}Co$	-0.84	5.09×10^{-9}	5.65×10^{-9}
	-3.97	5.09×10^{-9}	
	-4.16		5.48×10^{-9}
$^{58}Fe(n,\gamma)^{59}Fe(n,\gamma)^{60}Co$	-0.62	1.59×10^{-11}	1.88×10^{-11}
	-2.47	1.59	1.92
	-3.75	1.61	
	-3.94		1.87
	-5.78		1.52
	-5.84	1.23	
$^{50}Cr(n,\gamma)^{51}Cr$	-1.19		2.44×10^{-9}
$^{54}Fe(n,p)^{54}Mn$	-0.62	1.01×10^{-11}	1.05×10^{-11}
	-2.47	1.03	1.08
	-3.75	1.02	
	-3.94		1.06
	-4.31	1.00	
	-4.50		1.02
	-5.78		1.01
	-5.84	0.96	
$^{46}Ti(n,p)^{46}Sc$	-1.19	1.41×10^{-12}	
	-1.66	1.46	1.56×10^{-12}
	-4.81	1.43	
	-4.97		1.54
	-5.03	1.44	
$^{55}Mn(n,2n)^{54}Mn$	-1.00	3.21×10^{-14}	3.40×10^{-14}
	-4.13	3.23	
	-4.31		3.35
$^{63}Cu(n,\alpha)^{60}Co$	-2.13	7.12×10^{-14}	7.49×10^{-14}
	-5.44		7.07
	-5.50	6.65	
$^{58}Ni(n,p)^{58}Co$+	-2.31	5.68×10^{-12}	5.63×10^{-12}
	-4.56	5.74	
	-4.75		5.55
	-5.63		5.70
	-5.69	5.80	
$^{60}Ni(n,p)^{60}Co$+	-2.31	1.51×10^{-14}	1.74×10^{-14}
	-4.56	1.39	
	-4.75		1.60
	-5.63		1.48
	-5.69	1.20	
$^{58}Ni(n,x)^{57}Co$	-2.31	1.63×10^{-12}	1.73×10^{-12}
	-5.63		1.62
	-5.69	1.52	

+Burnup correactions are not included but are very high (~50%) for ^{58}Co. The ^{60}Co values are correspondingly too high (~50%) due to burnin of ^{59}Co.

Reaction	Ratio (New/Old)
$^{58}Fe(n,\gamma)$	1.00 ± 0.03
$^{59}Co(n,\gamma)$	0.93 ± 0.06
$^{54}Fe(n,p)$	1.01 ± 0.03
$^{46}Ti(n,p)$	1.05 ± 0.03

Hence, we conclude that there has been no significant change in the spectrum between the two irradiations. The small difference in flux may be due to fuel burnup effects.

The activities in Table 2 are grouped by their position in the MFE4A assembly. Two tubes were on the inside and two on the outside of an annulus surrounding the experimental samples. The top tubes (0 to −2.5") were irradiated at 400°C and the bottom (−3.9" to −5.8") were at 300°C. All of the activities for a specific reaction fall on smooth curves for the inner and outer positions. At each position the maximum gradient was only about 8% over the entire length (~6") where samples were irradiated. The gradients can all be described quite well by a simple polynomial of form:

$$A_i(h) = A_i(0)(0.9712 - 0.02497\,h - 0.00540\,h^2) \qquad (1)$$

where A_i is the activity for reaction i and $A_i(0)$ is the maximum value which occurs at −2.3" below midplane. This expression was then used to estimate the maximum activation rates for all reactions and these values are listed in Table 3. The thermal activities are about 8% lower on the inside compared to the outside of the assembly whereas the fast neutron values only decrease by about 5%. Actually, we expect two effects to be operative – a slow flux gradient away from core center and neutron attenuation by the stainless steel sleeve around the inner samples.

TABLE 3

MAXIMUM **ACTIVATION RATES FOR ORR-MFE4A**
(Values at -2.3 in. Below Midplane)

Reaction	$\sigma\phi$ (atom/atom-s) Inside	$\sigma\phi$ (atom/atom-s) Outside	Ratio (In/Out)
$^{58}Fe(n,\gamma)^{59}Fe$[a]	1.75×10^{-10}	1.88×10^{-10}	0.93
$^{59}Co(n,\gamma)^{60}Co$	5.16×10^{-9}	5.65×10^{-9}	0.91
$^{54}Fe(n,p)^{54}Mn$	1.03×10^{-11}	1.08×10^{-11}	0.95
$^{46}Ti(n,p)^{46}Sc$	1.47×10^{-12}	1.58×10^{-12}	0.93
$^{55}Mn(n,2n)^{54}Mn$	3.26×10^{-14}	3.43×10^{-14}	0.95
$^{63}Cu(n,\alpha)^{60}Co$	7.10×10^{-14}	7.48×10^{-14}	0.95

*Neutron self-shielding corrections are about 2% for Fe and 10% for the $Co(n,\gamma)$ reactions.

The maximum activation rates in Table 3 were used to adjust the flux spectrum calculated by R. A. Lillie, et al.[1] The resultant fluxes are listed in Table 4 and the spectrum is shown in Figure 1. The thermal flux was calculated assuming that the neutrons have a Maxwellian distribution centered at 95°C, the temperature of the surrounding moderator. This corresponds to the temperature used in the neutronics calculations at ORNL. In any case, the derived 2200 m/s thermal flux is independent of the assumed distribution and this value is also listed for comparison.

Displacement damage and gas production calculations were performed for both the inner and outer positions and the calculated He and DPA values are listed in Table 5.

The He and DPA values at other heights in the assembly can be calculated using Eq. (1) where $A_i(0)$ is taken from Table 5; however, the N_i values deserve special consideration, as discussed later. The effects of (n,γ) and β-decay

TABLE 4

MAXIMUM FLUX AND FLUENCE VALUES FOR ORR-MFE4A
(Values at -2.3 in. Below Midplane, Normalized to 30 MW,
Fluences Calculated for 12,176 MWd)

Energy, MeV	Error	Flux (x 10^{14} n/cm^2-s) Inner	Outer	Fluence (x 10^{21} n/cm^2) Inner	Cuter
Total	(5%)	5.01	5.37	17.6	18.8
Thermal (<.5 eV)*	(5%)	1.70	1.85	5.96	6.51
(2200 m/s)		1.34	1.46	4.71	5.15
0.5 eV - 0.11	(12%)	1.64	1.75	5.77	6.16
>0.11	(10%)	1.66	1.76	5.83	6.19
0.11 - 1	(15%)	0.75	0.80	2.63	2.79
1 - 5	(9%)	0.84	0.88	2.95	3.10
5 - 10	(8%)	0.071	0.075	0.25	0.26
10 - 20	(12%)	0.0021	0.0022	0.0073	0.0077

* Maxwellian thermal distribution assumed centered at the moderator temperature of 95°C.

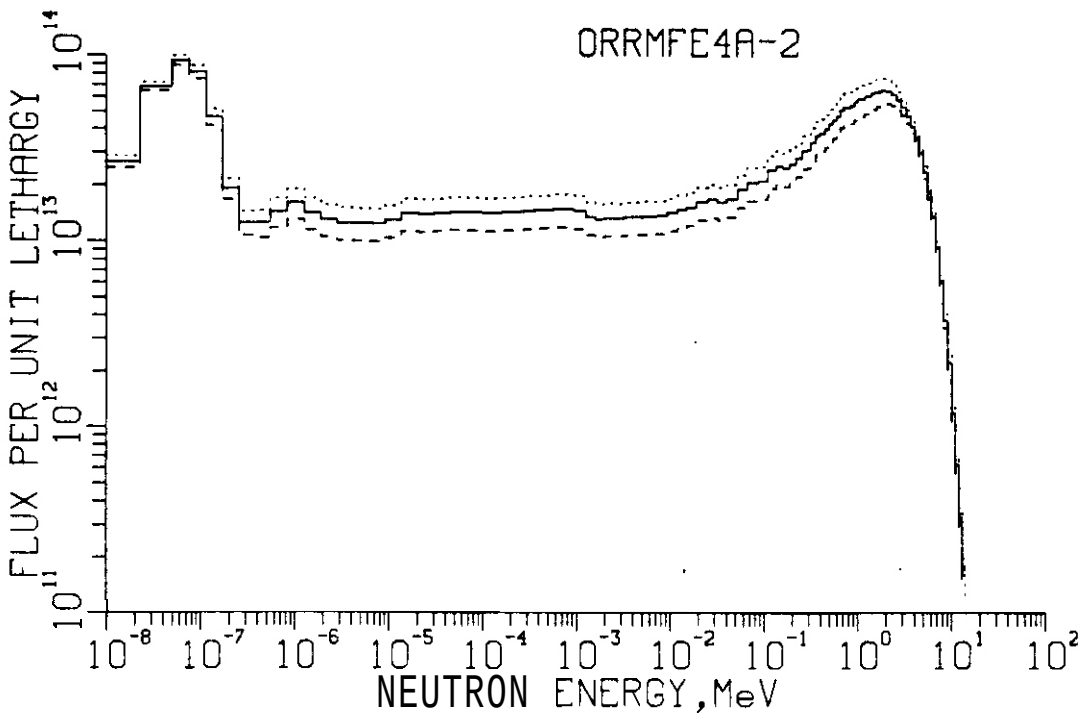

FIGURE 1. Adjusted Neutron Flux Spectrum for the MFE4A Experiment in ORR Normalized to 30 MW After 406 Full Power Days. The dotted and dashed lines represent one standard deviation; however, the flux groups are highly correlated.

TABLE 5

DAMAGE PARAMETERS FOR ORR-MFE4A
(Maximum Exposure at −2.3 in. 'Below Midplane,
Fluences Calculated at 12,176 MWd Were
1.88 x 10^{22} Outer and 1.76 x 10^{22} Inner)

Element	He (appm)		DPA	
	Inner	Outer	Inner	Outer
Al	3.65	3.86	7.87	5.31
Ti	2.75	2.90	5.04	5.31
V	0.12	0.13	5.59	5.89
Cr	0.90	0.96	5.01	5.28
Mn*	0.71	0.75	5.35	5.65
Fe	1.50	1.57	4.45	4.70
co+	0.75	0.79	5.15	5.45
Ni**	478.	552.	5.50	5.89
cu	1.31	1.39	4.30	4.53
Zr	0.14	0.15	4.63	4.89
Nb	0.30	0.31	4.27	4.50
Mo	—	—	3.14	3.31
Ta	—	—	2.15	2.27
316 SS***	63.4	73.1	4.67	4.94

* Self-shielding corrections may be needed for thick samples for the (n,γ) reaction which contributes (5.2%) for Mn and (16.8%) for Co.

** Thermal helium and DPA effects included (see text).

*** Composition assumed: Cr(.18), Mn(.019), Fe(.645), Ni(.13), Mo(0.026).

are included in the table. For nickel-bearing materials, two effects must be taken into account. First, the helium generation is increased by the two-step process $^{58}Ni(n,\gamma)^{59}Ni(n,\alpha)^{56}Fe$. Secondly, this process increases the DPA in nickel by the ratio of He(appm)/DPA = 567 (see Reference 2).

In order to determine the helium generation we need to know the spectral-averaged cross sections for the two successive thermal captures. If we start from the usual equations based on the 2200 m/s values (see References 2 and 3), then we must estimate corrections for the epithermal flux. If we knew the

cross sections versus energy, then we could simply average over our adjusted spectrum. However, these data are not available. If we assume that resonance contributions are not large, then the epithermal corrections for the two nickel capture reactions should be similar to those for our two dosimetry reactions, namely ^{58}Fe and $^{59}Co(n,\gamma)$. Both of these dosimetry reactions have an epithermal contribution to the reaction rate of about 15%. Hence, the equivalent 2200 m/s fluences to be used to calculate helium production are 5.44 (inner) and 5.90 (outer) x 10^{22} n/cm^2. These values happen to be close to the total thermal fluences (<.5 eV) corrected to room temperature. A simpler way to think about this is to say that the nickel capture rates should be roughly proportional to the Fe and Co rates times the ratios of the appropriate 2200 m/s cross sections.

The nickel damage and helium production values are listed in more detail in Table 6. The same procedures were used previously to predict a helium value of about 122 appm in nickel at an interim exposure of 5481 MWD. This value was later found to agree quite well with helium measurements at Rockwell International.4 Of course, helium measurements are now in progress for the present exposure and these values will not only provide the precision needed in the MFE4A experiment, but also can be used to fine tune our calculations if necessary.

6.0 References

1. T. A. Gabriel, R. A. Lillie, T. Thorns, and R. L. Childs, J. Nucl. Mater. 104, p. 1445, 1981.

2. L. R. Greenwood, "A New Calculation of Thermal Neutron Damage and Helium Production in Nickel," J. Nucl. Mater, to be published.

3. F. W. Wiffen, E. J. Allen, H. Farrar, IV, E. E. Bloom, T. A. Gabriel, H. T. Kerr, and F. G. Perey, "The Production Rate of Helium During Irradiation of Nickel in Thermal Spectrum Fission Reactors," J. Nucl. Mater., to be published.

4. J. G. Bradley, D. W. Kneff, and H. Farrar IV, "Helium Production in Orr MFE4A Nickel, Damage Analysis and Fundamental Studies Quarterly Progress Report, DOE/ER-0046/7, p. 24, 1981.

TABLE 6

DAMAGE AND HELIUM CALCULATIONS FOR NICKEL

Reaction	Inner		Outer	
	DPA	He, appm	DPA	He, appm
Fast Neutrons:	4.70	22.5	4.96	23.7
Thermal*	0.80	455.6	0.93	528.6
Total	5.50	478.1	5.89	552.3

*Thermal calculations use equations in References 2 and 3 with effective thermal fluences of 5.44 and 5.90 x 10^{21} n/cm^2 for the inner and outer positions, respectively.

7.0 Future Work

The MFE4A experiment is continuing and further measurements will be needed to check the progress, especially to measure the helium-to-DPA rates in stainless steel. Helium measurements are now in progress at Rockwell International and these values will be integrated with our radiometric data.

8.0 Publications

A paper entitled "A New Calculation of Thermal Neutron Damage and Helium Production in Nickel" was presented by L. R. Greenwood at the TMS-AIME Symposium on Radiation Damage Analysis for Fusion Reactors in St. Louis, MO on October 25-28, 1982.

DISPLACEMENT CODE MODIFICATIONS

F. M. Mann (Hanford Engineering Development Laboratory)

1.0 Objective

The objective of this work is to develop and maintain a computer code system to calculate damage energy (or displacement per atom) cross sections using basic nuclear data.

2.0 Summary

A better representation of the spectrum of outgoing charged particles has been developed and has been incorporated into the NJOY Nuclear Data Processing System. A comparison with the ANL code DISCS is presented.

3.0 Program

Title: Irradiation Effects Analysis (AKJ)
Principal Investigator: D. G. Doran
Affiliation: Hanford Engineering Development Laboratory

4.0 Relevant DAFS Program Plan Task/Subtask

Subtask II.B.l Defect Production Cross Section

5.0 Accomplishments and Status

5.1 Introduction

Damage energy (or displacement per atom) cross sections are calculated using evaluated nuclear data libraries, usually ENDF/B. However, as these libraries are developed primarily for neutron transport applications, some data needed for damage calculations are not present. Instead, assumptions

are built into the processing codes to compensate for missing nuclear data. An important example of such missing data is the spectra of outgoing charged particles.

5.2 Outgoing Charged Particle Spectra

The present NJOY nuclear data processing code[1] assumes that the outgoing charged particle spectrum is a delta function around the Coulomb barrier, E_{cb}. E_{cb} is given by

$$E_{cb} \cong Z_1 \, Z_2 \, / \, (A_1 \, A_2)^{1/3}$$

where Z and A are the charge and mass of the outgoind pair of particles. The DISCS code[2] (as applied by L. R. Greenwood at ANL) follows the method of Kikuchi and Kawaii[3] who postulate an energy-shifted evaporation model

$$\frac{d\sigma}{d\Omega}(E \rightarrow E^1) = \sigma(E) \, C \, [E^1 - K(Z) \, E_{cb}]$$

$$\exp\,[-(E^1 - K(Z) \, E_{cb}) \, / \, \theta(E,Z,A)]$$

where C is a normalization constant, $\sigma(E)$ the angle integrated cross section, K(Z) a function fitted to available data, and θ is another fitted function which takes the place of a nuclear temperature

$$\theta(E,Z,A) = \left[\frac{\mu E + Q - E_{cb}}{a(Z,A)}\right]^{\frac{1}{2}}$$

Here μ is the reduced mass of the system, Q is the Q value for the reaction, and a is the nuclear level denisty. Greenwood has fitted the values of K and e found in Kikuchi and Kawaii.

The Hauser-Feshbach computer code HAUSER*5 was used to calculate the outgoing proton and alpha spectra from n + ^{27}Al, n + ^{56}Fe, n t ^{58}Ni, n t ^{64}Ni, n + ^{92}Mo,

and n t ^{100}Mo. Very good agreement has been obtained with such calculations and the sparse available experimental data. Using the data for aluminum and iron, a new fitting function was found:

$$d\sigma_(E \rightarrow E^1) \quad \sigma(E)\ C\ [E - f(Z)\ E_{cb}\quad E + Q - E^1]^2$$

$$\exp\ [-g(A)\ x\ E^1]$$

where

$$f(Z) = 0.1\ x\ Z \quad \text{protons}$$
$$0.254\ x\ Z \quad \text{alphas}$$

and

$$g(A) = -0.072\ A^{\frac{1}{2}}$$

Figures 1 and 2 show a comparison for n t ^{58}Ni and for n t ^{92}Mo for 14-MeV incident neutrons. For all the cases studied, the new formula gives good agreement with the calculated values. The new formula works better than the formula and parameters of Kikuchi and Kawaii, especially for the cases where E + Q is small.

5.3 Implementation in NJOY and Comparison with DISCS

The new formula was incorporated into NJOY. Tables 1 and 2 present the results from **DISCS** (kindly supplied by Greenwood) and from the new and old versions of NJOY for 14-MeV neutrons. Following the philosophy of NJOY, the quadrature scheme incorporated is 4 point in the angular space and 5 in energy.

The (n,p) results are in good agreement, as would be expected from the good agreement seen in the Ni (n,p) spectra of Figure 1. However, the new

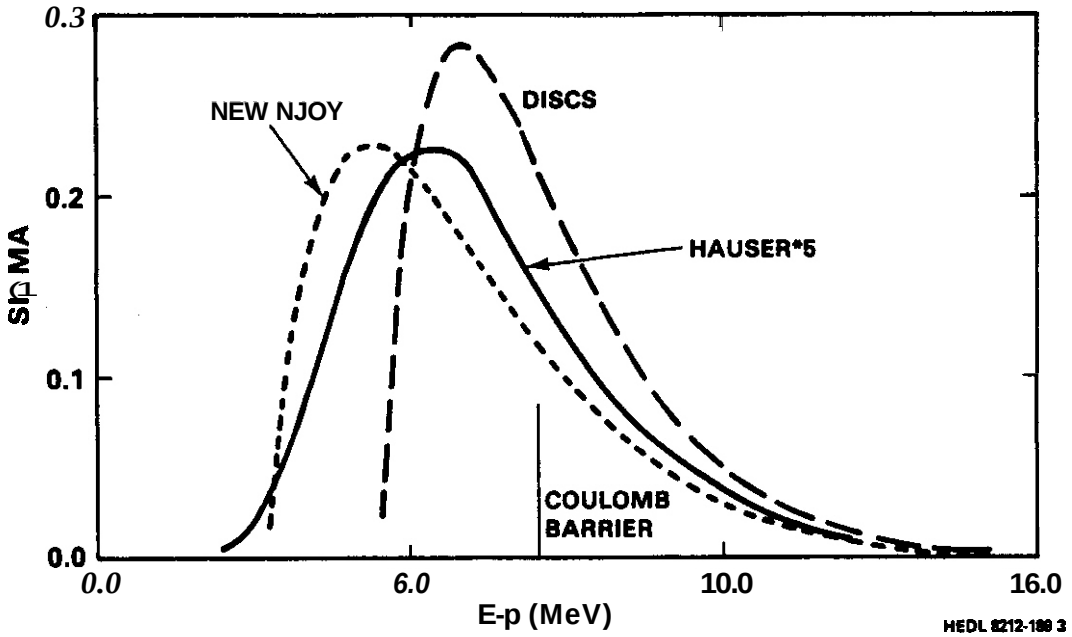

FIGURE 1. (a) Ni-58 (n,p), p Spectrum for 14-MeV n.

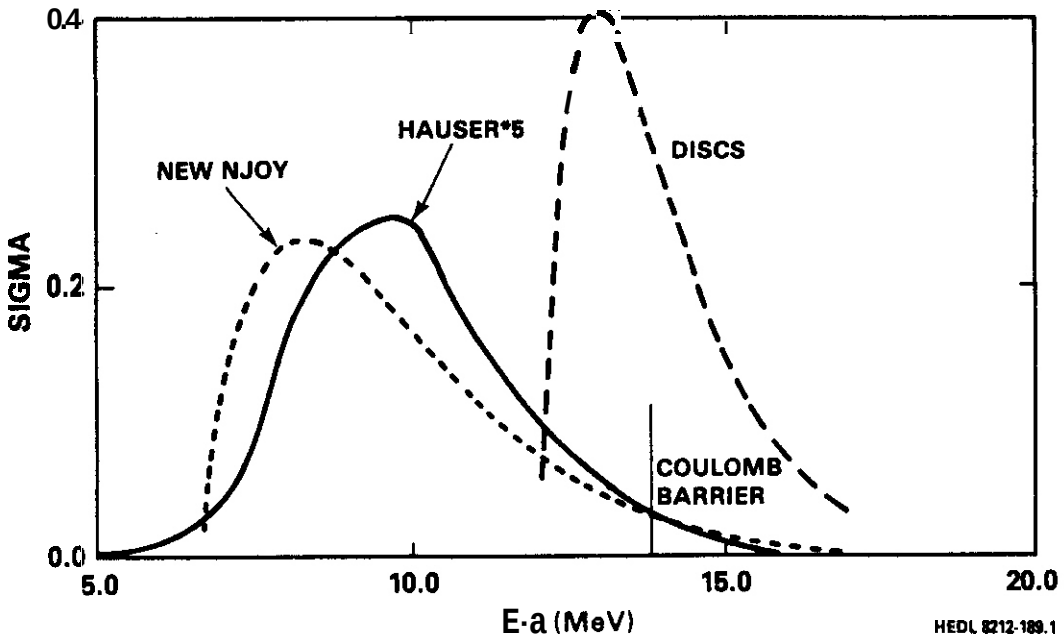

FIGURE 1. (b) Ni-58 (n,α), *a* Spectrum for 14-MeV n.

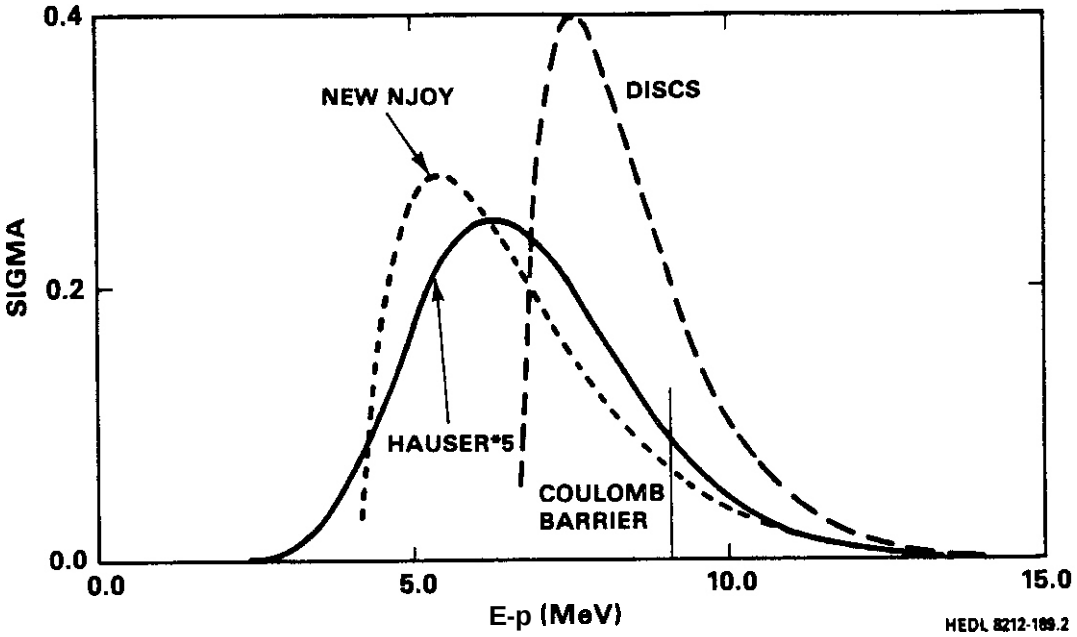

FIGURE 2. (a) Mo-92 (n,p), p Spectrum for 14-MeV n.

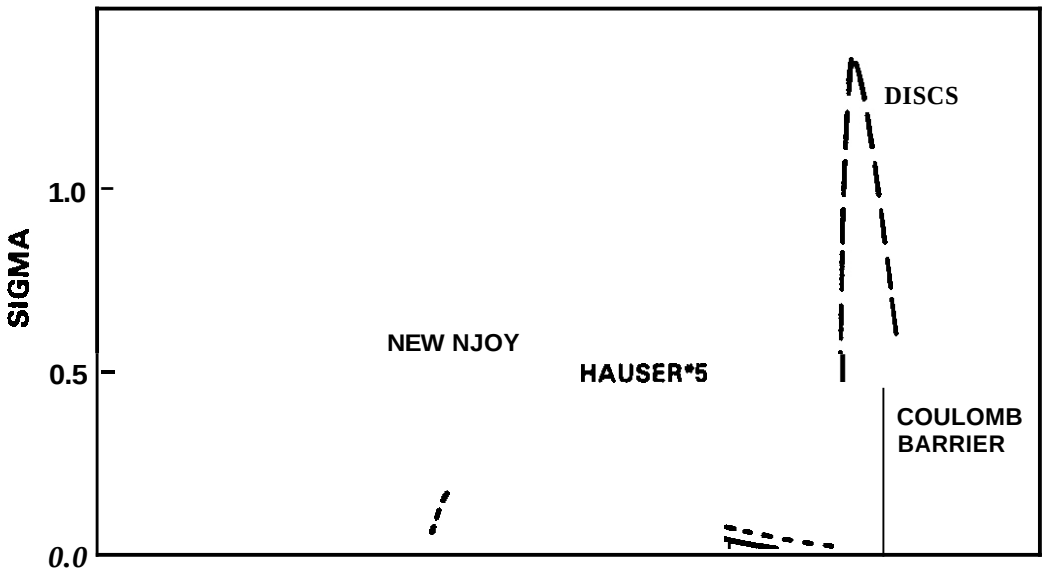

TABLE 1

DAMAGE ENERGY CROSS SECTIONS (keV-b)
FOR 14-MeV NEUTRONS ON IRON

Reaction	Code		
	DISCS	Old NJOY	New NJOY
(n,p)	23.3	19.2	19.4
(n,d)	included in above	4.0	3.8
(n,α)	12.3	7.5	7.1
Absorption	35.6	31.2	30.8
Elastic	62.3	63.4	63.4
3 Body	82.0	85.9	85.9
Inelastic	110.	114.	114.
Total	290	295	294

TABLE 2

DAMAGE ENERGY CROSS SECTIONS (keV-b)
FOR 14-MeV NEUTRONS ON NICKEL

Reaction	Code		
	DISCS	Old NJOY	New NJOY
(n,p)	41.6	48.4	48.5
(n,d)	included in (n,p)	3.6	3.5
(n,α)	47.9	45.2	26.6
Absorption	89.5	100.2	81.5
Elastic	62.3	63.4	63.4
3 Body	83.5	45.4	45.4
Inelastic	64.7	58.0	58.0
Total	300	267	249

and old versions of NJOY differ for Ni(n,α), while the new version of NJOY differs from DISCS for Fe(n,α).

Although the elastic and inelastic results are in good agreement, the 3 body contributions for DISCS and NJOY differ for nickel. In iron where the only significant 3 body reaction is (n,2n), the agreement is very good. Nickel, on the other hand, has a large (n,np) cross section [σ(n,np) = 2 σ(n,2n) at 14-MeV]. The DISCS value seems too high, but a detailed comparison of the calculational models is needed to resolve the discrepancy.

6.0 References

1. R. E. MacFarlane, D. W. Muir, and R. M. Borcourt, The NJOY Nuclear Data Processing System, Volume 11: The NJOY, RECONR, BROADR, HEATR, and THERMR Modules, LA-9303-M, Vol. 11 (ENDF-324), Los Alamos National Laboratory, 1982.

2. G. D. Odette and D. R. Doiron, "Neutron-Energy-Dependent Defect Production Cross Sections for Fission and Fusion Applications,: Nuclear Tehnology 29 (1976) 346; R. K. Smither and L. R. Greenwood, "Displacement Damage Calculations using ENDF/B-V Cross Sections Including Thermal Neutron Capture and Beta Decay Effects," Proc. of the 4th ASTM-Euratom Sym. on Reactor Dosimetry, EUREG/CP-0029, p. 793 (1982).

3. K. Kikuchi and M. Kawaii, Nuclear Matter and Nuclear Reactions, p. 135 (1968).

7.0 Future Work

The treatment of the (n,np) reaction will be investigated.

HELIUM GENERATION CROSS SECTIONS FOR Be(d,n) NEUTRONS

D. W. Kneff, B. M. Oliver, R. P. Skowronski, and H. Farrar IV (Rockwell International, Energy Systems Group)

1.0 Objective

The objectives of this work are to measure helium generation rates of materials for Magnetic Fusion Reactor applications in the Be(d,n) neutron environment, to characterize this neutron environment, and to develop helium accumulation neutron dosimeters for routine neutron fluence and energy spectrum measurements in Be(d,n) and Li(d,n) neutron fields.

2.0 Summary

Helium analyses have been completed for nine additional pure elements irradiated in the Be(d,n) neutron field, and average integral cross sections have been determined.

3.0 Program

Title: Helium Generation in Fusion Reactor Materials
Principal Investigators: D. W. Kneff and H. Farrar IV
Affiliation: Rockwell International, Energy Systems Group

4.0 Relevant OAFS Program Plan Task/Subtask

Subtask II.A.2.1 Flux-Spectral Definition in the Be(d,n) Field
Subtask II.A.4.3 Be(d,n) Helium Gas Production Data

5.0 Accomplishments and Status

Helium analyses have been completed for the pure elements Be, Si, Ti, Y, Ag, Sn, Ta, W, and Pt, irradiated in a Be(d,n) neutron field at the University

of California at Davis Cyclotron, for 30-MeV deuterons. The measured helium concentrations were combined with integral neutron fluence values for the individual sample locations to derive average helium generation cross sections. These cross sections extend the tabulation of measured Be(d,n) cross sections presented in previous Quarterly Reports.[1,2] The measurements are based on a joint Rockwell International-Argonne National Laboratory (ANL)-Lawrence Livermore National Laboratory (LLNL) irradiation experiment that has been described in detail previously.[3] The helium measurements were performed by high-sensitivity gas mass spectrometry. The integral neutron fluence distributions were calculated by L. R. Greenwood at ANL,[3] using the least-squares analysis code STAY'SL.

The new cross section results are presented in Table 1, where they are given in two forms: spectrum-integrated total helium production cross sections evaluated for the total Be(d,n) neutron fluence, and spectrum-integrated cross sections evaluated for the neutron fluence above 5 MeV. The cross sections representing the total neutron yield provide a means of estimating the helium generation in these materials for any similar Be(d,n) or Li(d,n) spectrum if the total neutron fluence is known. The cross sections evaluated using the 5-MeV neutron energy cutoff provide a rough estimate of the average differential total helium generation cross sections for high-energy neutrons.[1] The Table 1 cross section values are based on multiple samples of each element located at different positions within the irradiation volume, in a flux of neutrons having angles ranging between 0° and 42° from the forward direction. The cross section values are thus expected to vary with sample location, because of the spatial dependence of the neutron spectrum shape and the neutron energy sensitivity of the differential cross sections. The data given in Table 1 are average values for the various samples, and, because they represent a range of energy spectra, the uncertainties in the tabulated cross sections for a given Be(d,n) irradiation position are large. They are estimated to be ~±35% for cross sections based on the total fluence, and ~±18% for cross sections based on the fluence above 5 MeV.[1]

TABLE 1

INTEGRAL HELIUM GENERATION CROSS SECTIONS FOR THE -0-32-MeV Be(d,n) NEUTRON SPECTRUM PRODUCED BY 30-MeV DEUTERONS

Material	Average Cross Section (mb)*	
	Total Fluence	Fluence >5 MeV
Be	560	1430
Si	85	194
Ti	13	30
Y	3	8
Ag	3	8
Sn	1.1	2.6
Ta	0.8	1.7
W	0.6	1.5
Pt	0.5	1.3

*The cross-section uncertainty for a given Be(d,n) irradiation position is ~±35% for the total fluence and ~±18% for the fluence above 5 MeV, reflecting the changing neutron spectrum and thus cross section with source angle.

The cross sections determined for fluences >5 MeV are similar to those measured for -14.8-MeV T(d,n) neutrons where comparisons can be made. The measured cross sections for Si, Ti, Sn, and Pt for 14.8-MeV neutrons are 218, 37, 1.5, and 0.71 mb, respectively.[4,5] Similar correlations were also observed for previous Be(d,n) results.[1,2] Helium analyses are now in progress for samples of Be, Y, Ag, Ta, and W irradiated in a T(d,n) neutron environment, which will complete the comparison. Platinum was included in the Be(d,n) irradiation for later use as a sample encapsulating material, and silver was included to extend cross section systematics as a function of atomic mass.

6.0 References

1. D. W. Kneff, B. M. Oliver, M. M. Nakata, and H. Farrar IV, "Helium Generation Cross Sections for Be(d,n) Neutrons," in Damage Analysis and Fundamental Studies, Quarterly Progress Report July-September 1981, DOE/ER-0046/7, U.S. Department of Energy, 34 (1981).

2. D. W. Kneff, B. M. Oliver, M. M. Nakata, and H. Farrar IV, "Helium Generation Cross Sections for Be(d,n) Neutrons," in Damage Analysis and Fundamental Studies, Quarterly Progress Report October-December 1981, DOE/ER-0046/8, Vol. 1, U.S. Department of Energy, 34 (1982).

3. D. W. Kneff, H. Farrar IV, L. R. Greenwood, and M. W. Guinan, "Characterization of the Be(d,n) Neutron Field by Passive Dosimetry Techniques," in Proc. Symp. on Neutron Cross-Sections from 10 to 50 MeV, M. R. Bhat and S. Pearlstein, eds., BNL-NCS-51245, Brookhaven National Laboratory, N.Y. (1980), p. 113.

4. B. M. Oliver, D. W. Kneff, M. M. Nakata, and H. Farrar IV, "Helium Generation Cross Sections for 14.8-MeV Neutrons," DOE/ER-0046/7, 28 (1981).

5. B. M. Oliver, D. W. Kneff, M. M. Nakata, and H. Farrar IV, "Helium Generation Cross Sections for 14.8-MeV Neutrons," DOE/ER-0046/8, Vol. 1, 31 (1982).

7.0 Future Work

The analysis of Be(d,n)-irradiated materials will continue, and correlations will be made between the integral helium generation results and helium production cross section evaluations.

8.0 Publications

None.

^{59}Ni + n CROSS SECTION EVALUATION

F. M. Mann (Hanford Engineering Development Laboratory)

1.0 Objective

To supply evaluated nuclear data needed for damage studies

2.0 Sumnary

^{59}Ni + n reaction cross sections leading to ^{60}Ni, ^{59}Co, and ^{56}Fe have been evaluated from 10^{-5} eV to 10 MeV and put into ENDF/B format.

3.0 Program

Title: Irradiation Effects Analysis (AKJ)
Principal Investigator: D. G. Doran
Affiliation: Hanford Engineering Development Laboratory

4.0 Relevant DAFS Program Plan Task/Subtask

II.A.4.5 Gas Generation Rates.

5.0 Accomplishments and Status

Because of its large alpha production cross section at low neutron energies, ^{59}Ni plays an important role in material experiments which attempt to achieve the same He/dpa as that expected in the first wall of a fusion device. Unfortunately, the evaluated data which exist are 0.025-eV data[1] or restricted to isolated positions in certain test reactors (see, for example, Reference 2).

Using the compiled resonance data from Reference 1, the (n,γ), (n,p), and (n,α) cross sections were generated from 10^{-5} eV to 10-keV. The large

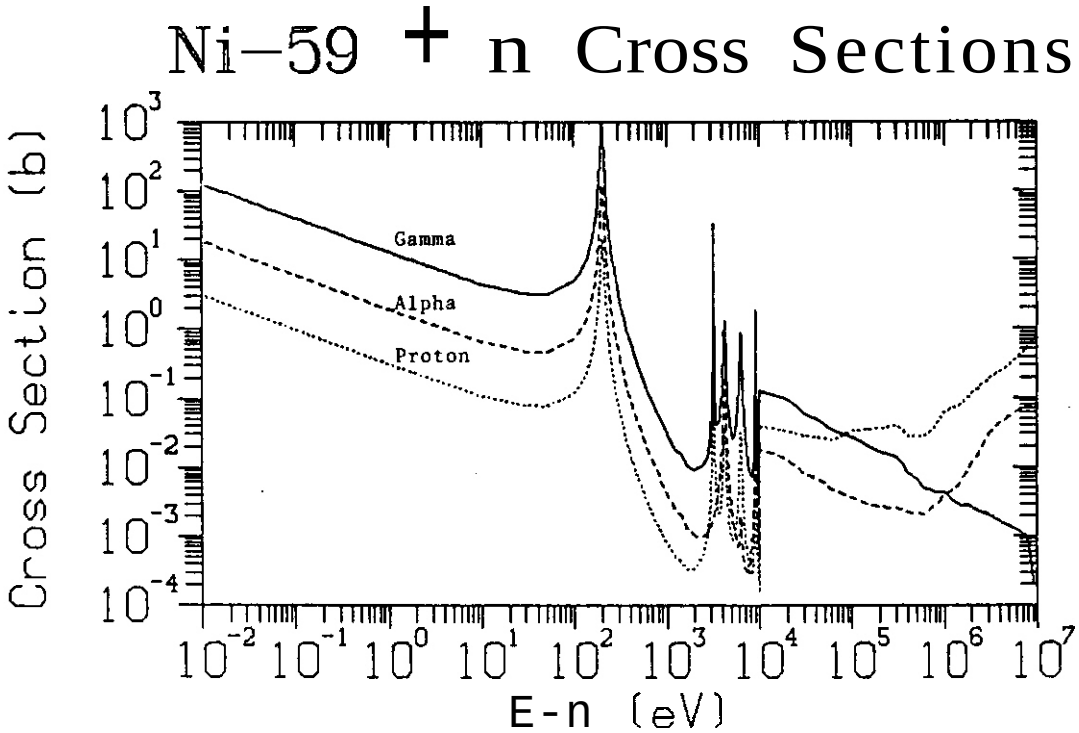

FIGURE 1. Evaluated Neutron Cross Sections for ^{59}Ni.

resonance at 203.4-eV generates the large thermal cross sections through its l/v tail. The evaluation from 10-keV to 10-MeV is taken from Hauser-Feshback calculations. There is excellent agreement with the ^{59}Ni (n_0, α_0) ^{56}Fe cross section inferred through detailed balance from the experimental data of R. W. Kavanagh (California Institute of Technology).

Figure 1 shows the three evaluations from 10^{-2} eV to 10-MeV. The evaluation is available from the author and is at the National Magnetic Fusion Energy Computing Center.

6.0 References

1. S. F. Mughabghab, M. Divadeenam, and N. E. Holden, Neutron Cross Sections, Volume 1 Neutron Resonance Parameters and Thermal Cross Sections, Part A Z = 1-60, Academic Press, 1981.

2. F. W. Wiffen, E. J. Allen, H. Farrar IV, E. E. Bloom, T. A. Gabriel, H. T. Kerr, and F. G. Perey, "The Production Rate of Helium During Irradiation of Nickel in Thermal Spectrum Fission Reactors," accepted for publication in Journal of Nuclear Materials.

^{59}Ni ISOTOPIC ENRICHMENT AS A MEANS OF SIMULATING THE HELIUM/DPA RATIO OF A FUSION NEUTRON ENVIRONMENT

R. L. Simons (Hanford Engineering Development Laboratory)

1.0 Objective

The objective of this effort is to investigate the potential of enriching nickel-bearing alloys, such as the Prime Candidate Alloy (PCA) and HT-9, with the isotope ^{59}Ni to produce the helium-to-dpa ratio of a fusion reactor first wall in a fission reactor irradiation experiment.

2.0 Summary

Fission reactors are not able to produce the correct concentration of helium relative to displacements per atom (dpa) in engineering materials that is characteristic of the first wall of a fusion device. Various methods are in use or have been proposed to enhance or modify helium production in engineering materials irradiated in fission reactors, but they are far from ideal. Another potential technique for achieving the correct helium/dpa ratio is isotopically enriching the nickel constituent with ^{59}Ni. This requires no modification of the alloy composition, and several irradiation facilities could be used. Three of them are: 1) High Flux Isotope Reactor (HFIR), 2) Fast Test Reactor/Materials Open Test Assembly (FTR/MOTA), and 3) FTR Reflector. Each has a unique advantage but all can yield the correct helium/dpa ratio. One of the most attractive features of this method is the exact duplication of the helium/dpa ratio during the first 30 or more dpa where nucleation of bubbles or voids is critical in setting the stage for subsequent swelling of material.

3.0 Program

Title: Irradiation Effects Analysis (AKJ)
Principal Investigator: D. G. Ooran
Affiliation: Hanford Engineering Development Laboratory

4.0 Relevant OAFS Program Plan Task/Subtask

Subtask II.C.2 Effects of Helium on Microstructure.
Subtask II.C.7 Effects of Helium and Displacements on Flow.

5.0 Accomplishments and Status

5.1 Introduction

One objective of the Magnetic Fusion Energy (MFE) research programs is to develop a first wall material that is resistant to swelling and maintains acceptable mechanical properties over all or a large fraction of a reactor's operating life. The high energy neutrons in a fusion reactor are known to cause greater rate of change (per neutron) of the material properties by displacement of atoms and a higher helium production rate than is observed from fission reactor irradiations. The incubation period of swelling can be shifted to lower or higher dpa values depending on the rate of introducing the helium.[1] At the same time, higher helium generation rates can produce a higher density of bubbles or voids and thus a higher density of obstacles to dislocation motion which increases the change in yield strength. In addition, it is known that low concentrations of helium on grain boundaries cause premature intergranular failure of the material for irradiation and test temperatures above about one-half the melting temperature.

Fast fission reactors produce low quantities of helium relative to displacements (<0.5 appm/dpa) compared to that produced in the first wall of a fusion device (~14 appm/dpa). Likewise, thermal reactors produce ≤1 appm/dpa provided that nickel is not present in the material. If it is present, the ratio varies as a function of irradiation time to values as high as ~100 appm/dpa due to the build-up of ^{59}Ni which has a large thermal neutron cross section. In such cases the void distribution is similar to the fast reactor irradiations but there is a high denisty of

small bubbles disbursed through the lattice. The latter is due to the increase in helium production rate later in the irradiation cycle. On the other hand, recent experiments featuring preinjection of helium and subsequent irradiation in the Oak Ridge Research Reactor showed a high density of small bubbles and reduced swelling relative to the normal sample.[1,2] This leads one to believe that the rate of introduction of helium early in the irradiation determines the cavity density and subsequent swelling. The only foreseeable irradiation facility that will give a constant helium/dpa ratio to high exposures is the Fusion Materials Irradiation Test Facility (FMIT). The Rotating Target Neutron Source-I1 (RTNS-II) Facility does not have sufficient flux to study helium effects on swelling.

Figure 1 shows calculated helium concentration versus dpa for HFIR, FTR, and a fusion spectrum. The helium calculations are based on earlier work in this area.[3] The parallel curves for FTR/MOTA and the fusion spectrum indicate constant helium production rate but the rates differ by a factor of 35. In the HFIR Peripheral Target Position (HFIR/PTP) the helium concentration starts out approximately a factor of ten low but ends up about a factor of three to five higher than the fusion curve. This behavior is due to the build-up of ^{59}Ni and subsequent helium production. If 5 ppm wt of boron is present in the steel, the low exposure portion of the curve coincide fairly well with the fusion curve. However, the boron is usually present in clumps or concentrated near grain boundaries. Consequently, the helium distribution in the material may not be typical of that produced in a fusion reactor irradiation.

A potential solution to the discrepancy in helium/dpa production in test reactor neutron environments is to start the irradiation with a steel isotopically enriched in ^{59}Ni. Enhanced helium production would then be obtained from the 203-eV resonance in the ^{59}Ni cross section. The balance of this report will discuss this approach to obtaining the correct helium/dpa ratio in PCA and ferritic alloys being developed in the MFE materials research program.

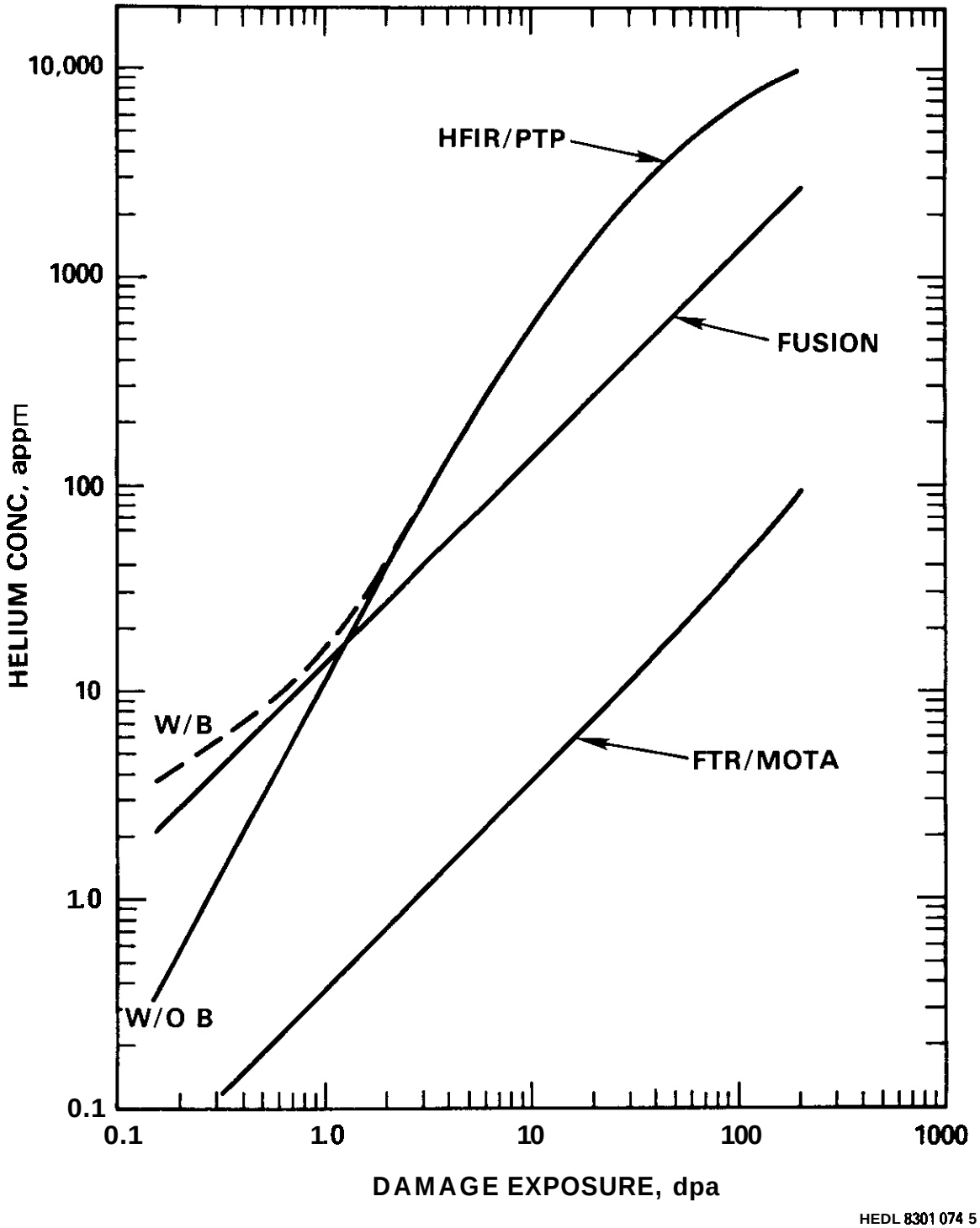

FIGURE 1. Helium Production in Stainless Steel 316 Irradiated in Fast, Thermal and Fusion Neutron Environments.

5.2 Analysis

Figure 2 shows the concentration of ^{59}Ni as a function of dpa during irradiation in HFIR. The concentration peaks at about 16 dpa (~8-10 months). Above 16 dpa the concentration drops due to burn-out of ^{59}Ni by the large (n,γ) cross section ($\sigma(n,\gamma)\approx 80$ barns). Irradiating natural nickel produces a peak ^{59}Ni concentration of 2.5%. However, by preirradiation enriching the ^{58}Ni to ~100%, the peak ^{59}Ni concentration reaches 3.5%. This analysis will assume a minimum ^{59}Ni enrichment of 3.5%.

Figure 3 shows the helium versus dpa for three irradiation conditions in HFIR/PTP compared with that expected in a fusion environment. The upper curve shows unshielded PCA with nickel enriched to 3.5% ^{59}Ni. This irradiation condition produces a factor of nine too much helium per dpa. However, the curve is nearly parallel to that in the fusion first wall (i.e., the effective production rate is a constant). The second condition uses thermal neutron shielding to reduce the helium production rate. In this case there is close agreement with the helium production in the fusion first wall. The down turn at high dpa in these two curves is due to burn-out of the ^{59}Ni. The third condition shows the helium production in PCA using natural nickel in HFIR with thermal neutron shielding. The upturn at high exposures is due to the slow burn-in of ^{59}Ni from the resonance at 203-eV. Data from all three irradiations potentially would enable a good correlation of material properties as a function of helium concentration and dpa.

It is noteworthy that the ferritic steel HT-9 contains ~0.5% nickel. Since the enriched PCA contains 0.49% ^{59}Ni, the helium production behavior of PCA is equivalent to HT-9 with the nickel 100% enriched to ^{59}Ni. Therefore, both PCA and HT-9 can be isotopically tailored to duplicate the helium/dpa ratio found in the first wall of a fusion device.

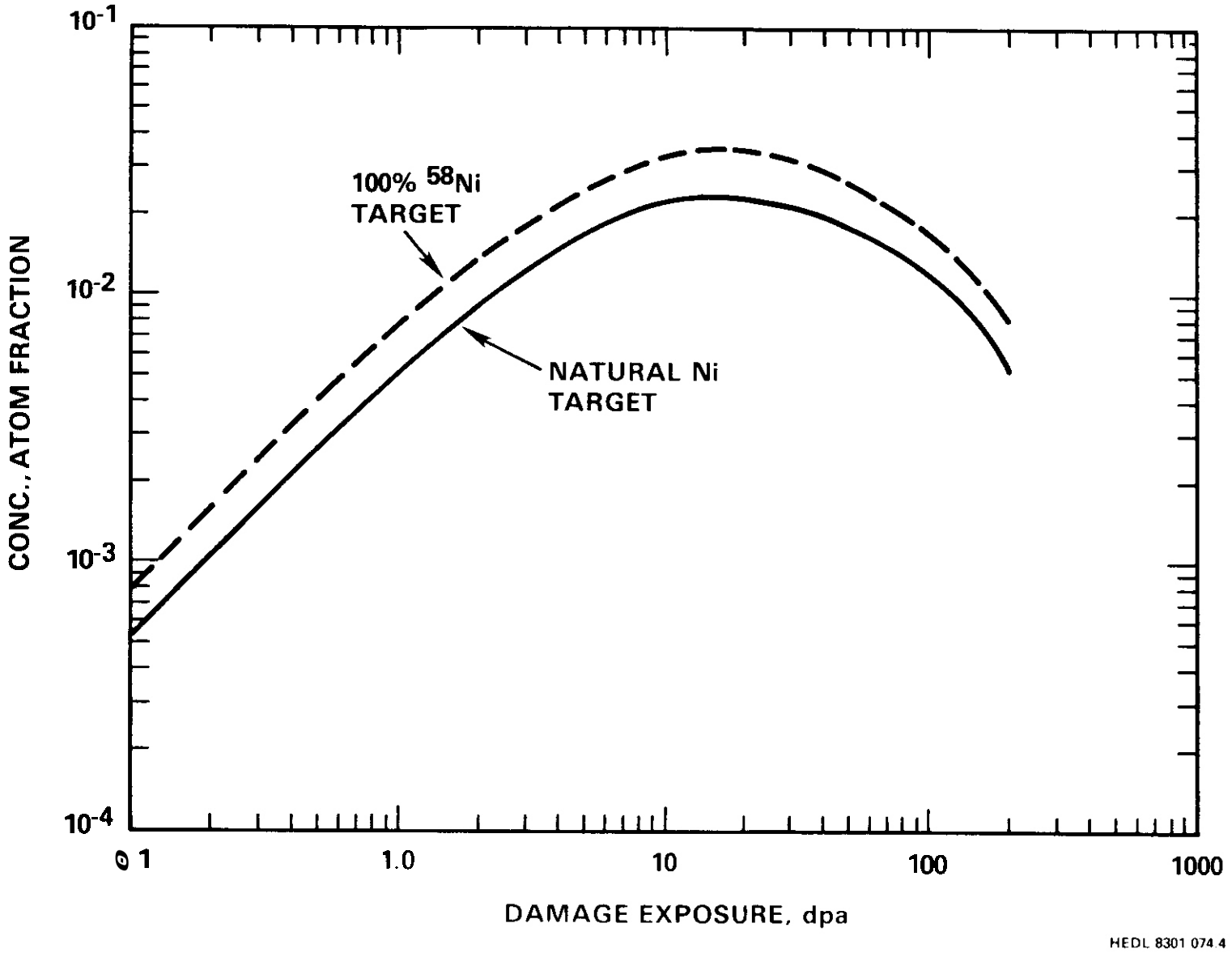

FIGURE 2 Concentration of ^{59}Ni as a Function of Exposure in HFIR/PTP Spectrum

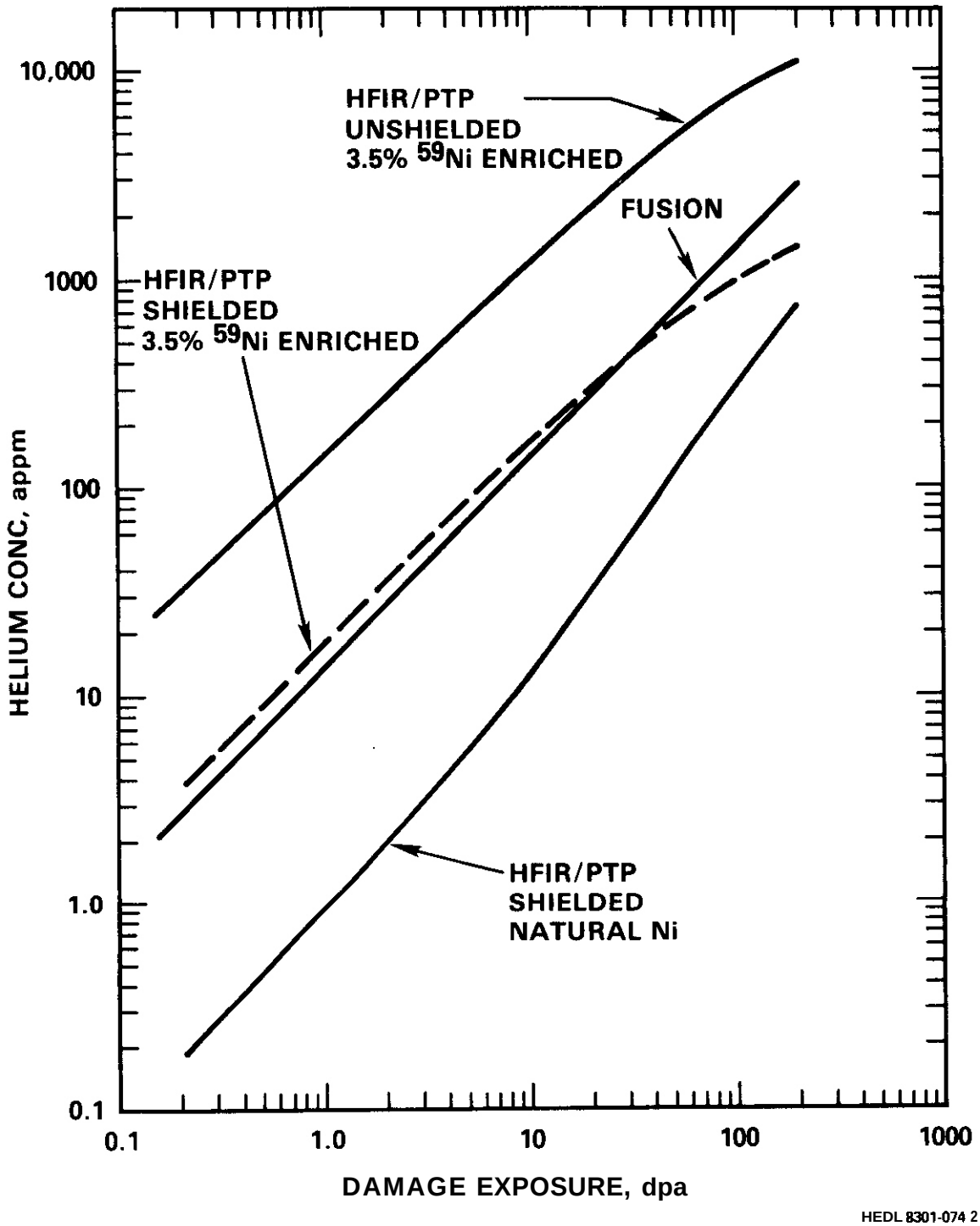

FIGURE 3. Helium Concentration Versus dpa for Alloys Containing Various Levels of ^{59}Ni Enrichments.

The maximum dpa obtainable in the HFIR/PTP location in one year is ∿16 dpa. In order to instrument the experiment for better temperature control, the irradiation would have to be out of core.[4] This drops the exposure rate to ∿7 dpa/year. At that rate it would take more than 25 years to achieve fusion first wall goal fluences (175 dpa).

The exposure rate in the FTR/MOTA is about 32 dpa/year. Figure 4 shows the performance of three levels of ^{59}Ni enrichment in the FTR/MOTA location. If the nickel in PCA is enriched to 40% ^{59}Ni, remarkably good agreement with the helium/dpa production in a fusion first wall is obtained. There is very little burn-out of ^{59}Ni for irradiations to 200 dpa. The 3.5% enrichment (the middle curve) shows a factor of five enhancement in helium production rate over the material with natural nickel (lower curve). The middle curve also illustrates the performance of the HT-9 alloy with 100% enrichment of the nickel. Note that the lower curve shows a small upturn at high dpa due to burn-in of ^{59}Ni.

In the FTR/MOTA the helium/dpa ratio (for 3.5% enrichment) is about a factor of seven lower than the expected in the first wall of a fusion device *(see* Figure 4, middle curve). This can be corrected by irradiating the alloy in a Row 7 FTR/reflector location. This location has a high population of low energy neutrons which can be captured by the 203-eV resonance in ^{59}Ni. Figure 5 shows the performance of PCA with 3.5% enrichment, or equivalently, HT-9 with 100%enrichment (top dashed curves) compared to that expected in the first wall of a fusion device (solid curve). Out to about 30 dpa the helium/dpa ratio is in good agreement with the ratio for a fusion device first wall. At higher exposures burn-out of the ^{59}Ni causes the ratio to fall below the fusion ratio by up to a factor of three at 200 dpa. The flux gradient and spectrum moderation across the Row 7 reflector subassembly is significant. The "inner" designation refers to a location adjacent to the fuel in Row 6 and the "outer" designation refers to a location in the subassembly adjacent to the Row 8 reflector. The "outer" position sees a larger

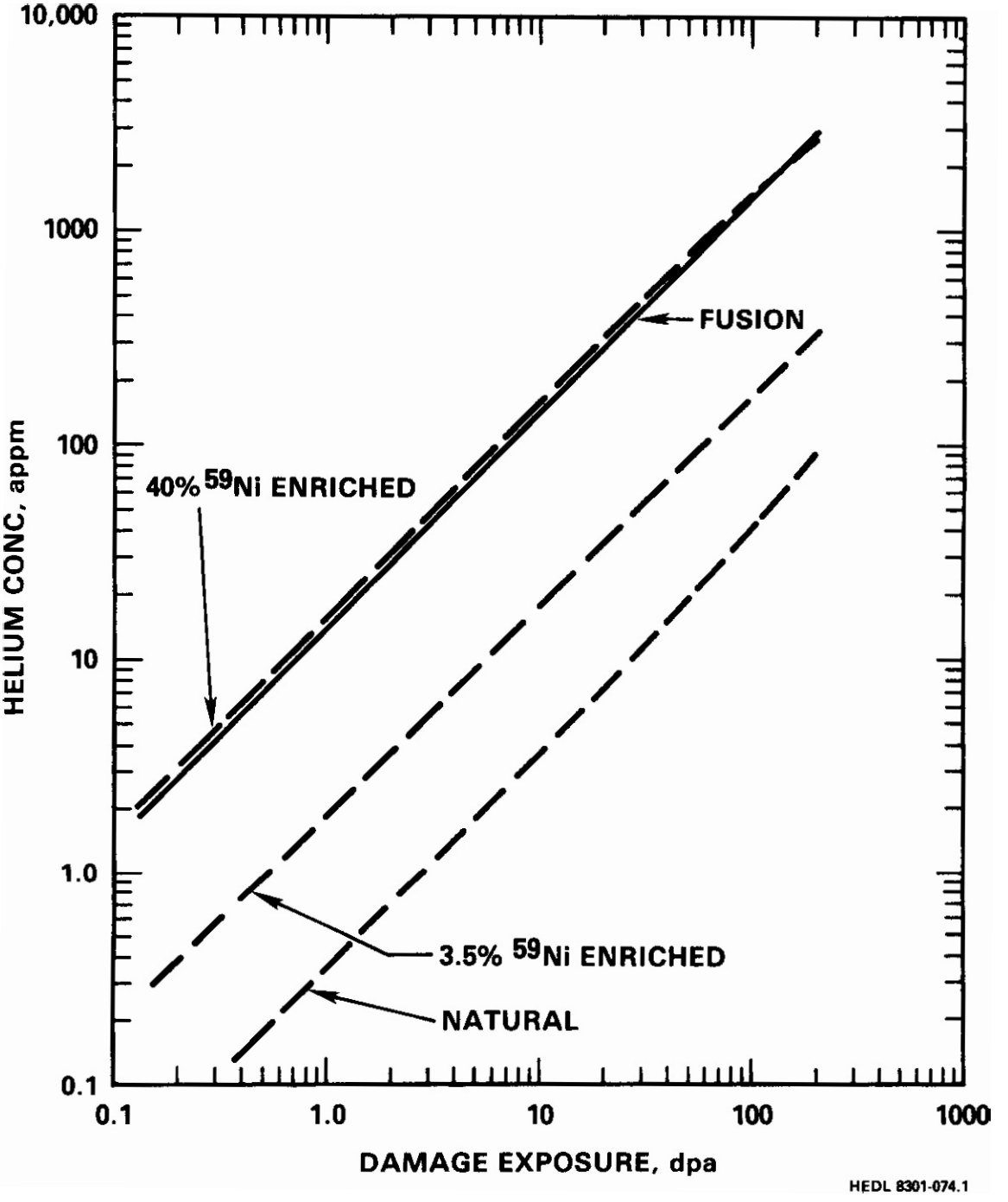

FIGURE 4. Helium Concentration Versus dpa for an Irradiation in FTR/MOTA of Alloys Containing Various Levels of ^{59}Ni Enrichment.

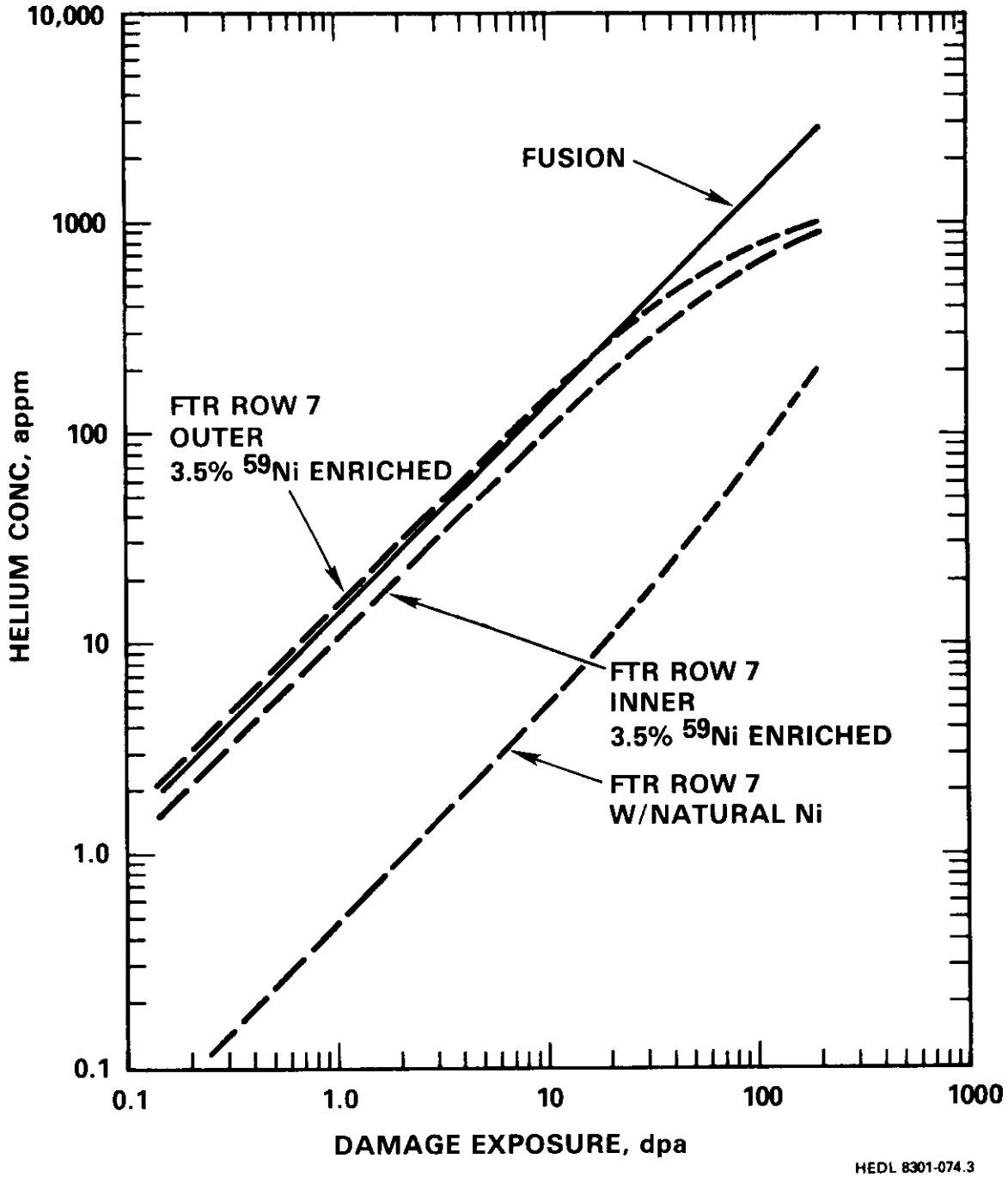

FIGURE 5. Helium Concentration Versus dpa for an Irradiation in a Row 7 FTR Reflector Location for Alloys Containing Various Levels of ^{59}Ni Enrichment.

fraction of low energy neutrons reflected back to the core than the "inner" location, hence experiences increased production of helium due to the 203-eV resonance. The bottom curve shows the performance of the PCA alloy (and approximately the HT-9) using natural nickel. Some burn-in of ^{59}Ni would be seen at high dpa in PCA.

The FTR/reflector at the "outer" location will receive ~12 dpa/year, intermediate between that expected from in-core and out-of-core HFIR irradiations. It may be possible to increase the exposure rate to ~16 dpa/year by placing a mini beryllium reflector on the outer edge of the subassembly to reflect back low energy neutrons to the inner edge which has a higher dpa/year.

The limiting feature of using the concept of enriching the nickel in an alloy with ^{59}Ni may be the cost of producing the isotope. Preliminary and unofficial estimates are currently at $12K/gm for 25-50 gm lots of 2.5% ^{59}Ni in a ^{58}Ni solid solution. The 3.5% enrichment level can be achieved with additional irradiation time (see Figure 1). The preirradiation target would be 100% enriched ^{58}Ni. The cost of producing ^{59}Ni in a purer state (90% enrichment) would be substantially more. At this cost and quantities the material test specimens would be limited to miniature tensile and charpy specimens, and TEM disks. However, this may be adequate for answering questions about the sensitivity of helium effects on mechanical properties and swelling to the schedule of helium production.

5.3 Conclusions

It has been shown that the helium/dpa ratio in a fusion device first wall can be duplicated well by enriching the nickel content of the alloy with the isotope ^{59}Ni. With a 40% enriched alloy, the high dpa rates of FTR/MOTA could be used to reach 150-200 dpa in a reasonable irradiation time. Other test locations in HFIR and FTR can also be used to duplicate the helium/dpa ratio of a fusion neutron environment using 3.5% enrichment in a PCA alloy or 100% enrichment in the ferritic steel HT-9.

6.0 References

1. A. Hishinuma, et al., "Effect of Preinjected Helium on Swelling and Microstructure of Neutron Irradiated Pressurized Tubes of Type 316 Stainless Steel," ASTM STP 782, (1982), pp. 92-107.

2. H. R. Brager, and F. A. Garner, "The Influence of Cold-Work Level, Solute, and Helium Content on the Swelling of Pure AISI 316 (Fe-17Cr-16.7Ni-2.5Mo)," ASTM STP 782, (1982), pp. 152-165.

3. R. L. Simons, "Helium Production on Fast Breeder Reactor Out-of-Core Structural Components," ASTM 683, (1979), pp. 365-379.

4. A. M. Ermi and J. M. Vitek, "HFIR/FFTF Irradiation Experiment-Conceptual Plan," Alloy Development for Irradiation Performance Semi-Annual Proaress Report for Period Ending March 31, 1982, DOE/ER-045/8, Sept. 1982, pp. 17-24.

TRANSMUTATION-INDUCED DEPOSITION PROFILES IN HALOS SURROUNDING SPHERICAL PRECIPITATES

A. Kumar (University of Missouri-Rolla) and F. A. Garner (Westinghouse Hanford Company)

1.0 Objective

The object of this effort is to determine the effect of helium, lithium and other elements on microstructural development of irradiated metals, employing the energetic reaction products produced by transmutation reactions occurring in precipitates.

2.0 Sumnary

The deposition profiles that form around precipitates undergoing energetic transmutation reactions can be used to study the effects of helium, hydrogen and lithium on microstructural development during neutron irradiation. A completely general derivation has been performed to determine the deposition profile concentrations for any transmutation reaction and precipitate/matrix combination.

3.0 Program

Title: Irradiation Effects Analysis (AKJ)
Principal Investigator: D. G. Doran
Affiliation: Westinghouse Hanford Company

4.0 Relevant DAFS Program Plan Task/Subtask

Subtask II.C.2. Effect of Helium on Microstructure
II.C.4. Effect of Solid Transmutants on Microstructure

5.0 Accomplishments and Status

5.1 Introduction

In an earlier report[1] a method was described which allows the determination of some aspects of the role of helium on microstructural evolution in complex alloys. It involves a direct comparison of the materials response to the rate of helium generation, a variable of prime importance in fusion reactor materials studies. This is accomplished by irradiating specimens in either a fast or mixed spectrum reactor and conducting microstructural analyses on matrix regions adjacent to precipitates rich in boron. Such precipitates produce well-defined atmospheres of helium and lithium generated by the $^{10}B(n,\alpha)^{7}Li$ reaction. Microstructural comparisons are made between the regions bearing implanted helium and those just beyond the helium-implanted zone, an excellent example[2] of which is shown in Figure 1. A variety of helium/dpa ratios can be obtained in one specimen by using precipitates of various sizes. This method takes advantage of the virtual absence of variations in alloy composition, preirradiation microstructure and displacement rate over small distances, and can be used to study any material of interest if appropriate and identifiable precipitates can be developed.

Other transmutation reactions can also be employed for this purpose. Examples are the $^{6}Li(n,\alpha)^{3}H$ and $^{58}Ni(n,\gamma)^{59}Ni(n,\alpha)^{56}Fe$ reactions.[3-5] Both of these have the advantage that they do not produce lithium, an element shown to have a large effect on void nucleation and growth.[1] Both ^{6}Li and ^{3}H will be present in a fusion reactor environment, however, and their separate or synergistic effects with helium can be studied using this method. The precipitates can be produced either by addition of appropriate solutes to the alloy melt or by introduction of fine insoluble precipitates into the metal by various techniques. ZrB_2 precipitates have been proposed using the first method[6] and the use of oxides of lithium[3] and B_4C[7] powders are examples of the latter type of technique. Nickel-rich precipitates do not need to be introduced since they tend to form naturally during irradiation of nickel alloys containing silicon, manganese, molybdenum and other minor solutes.[8]

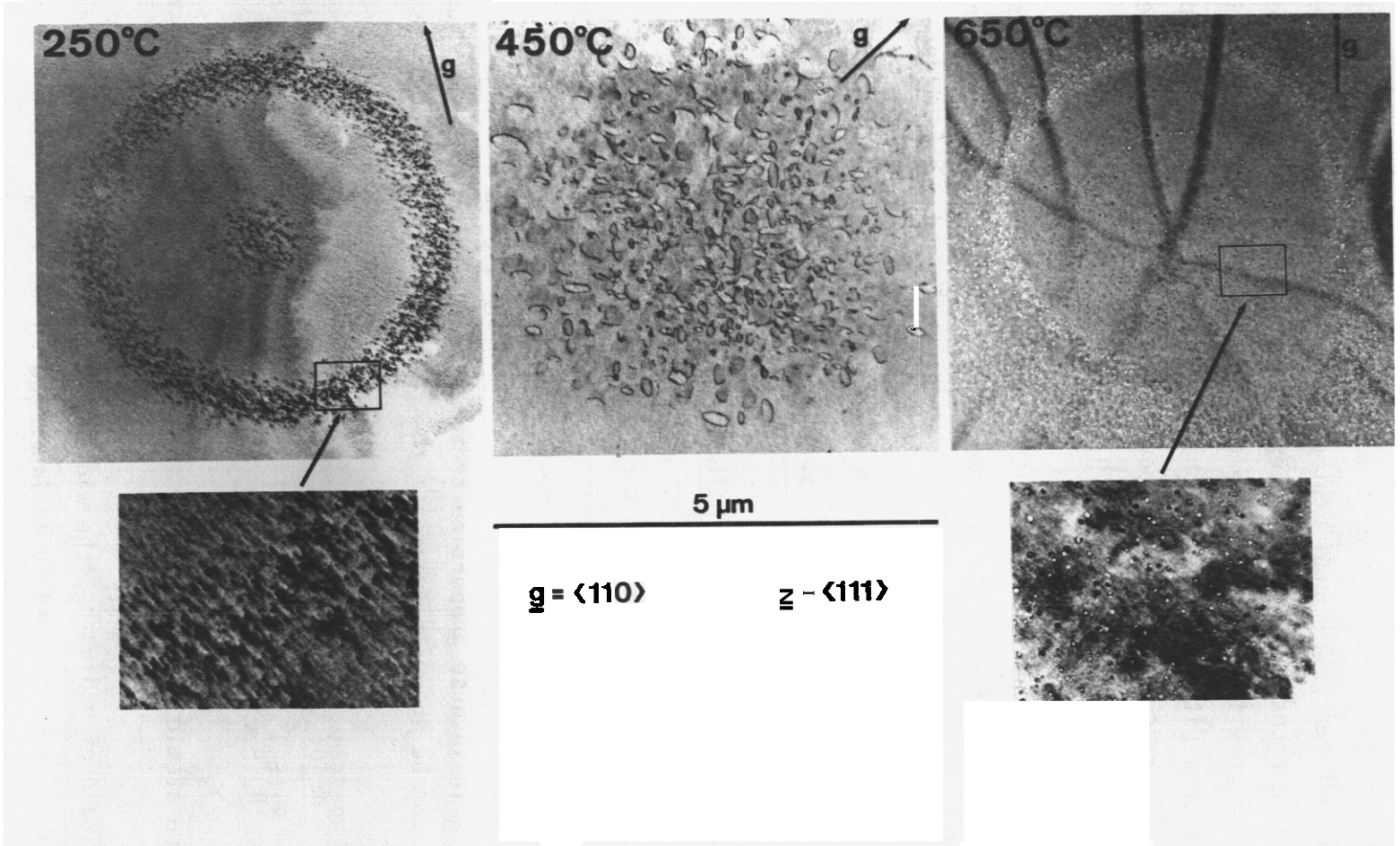

FIGURE 1. Representative Micrographs of Halo Microstructure Found Around B_4C Particles in Neutron-Irradiated Iron, as Published by L. L. Horton and Co-workers of Oak Ridge National Laboratory.(2)

The range of precipitate compositions and introduction methods available allows the use of this technique in almost all materials of fundamental or technological interest. The confident utilization of this technique requires knowledge of the deposition rates occurring throughout the region where the implanted atoms come to rest. For the rare occurrence where the stopping powers of the precipitate and matrix phases are equal, the deposition profiles are easily calculated and have been presented earlier.[1] Figure 2 shows typical injection profiles for this case.

In general, however, the energy deposition characteristics of the transmutation products are different in the two phases. The simple assumptions employed in the earlier analysis are no longer valid and a more general treatment is required.

5.2 Determination of Injection Profile for Spherical Precipitates

5.2.1 Limits of the Deposition Halo Outside the Precipitate

Consider a reaction product emitted isotropically at a fixed energy E_o, traveling in a straight line and coming to rest at a fixed distance from its source. The distance traveled will be $R_m(E_o)$ if the entire travel is in the matrix phase and $R_p(E_o)$ if all travel is in the precipitate phase. The ranges are in inverse proportion to the stopping power of the medium traveled and can be shown to define[9] the ratio

$$m = \frac{R_m(E_o)}{R_p(E_o)} = \frac{\rho_p \sqrt{A_m}}{\rho_m \sqrt{A_p}} , \qquad (1)$$

where A is the atomic weight and p is the density.

For a precipitate of radius r_p, the width of the deposition region outside the precipitate can be defined by an inner and an outer radius. As shown in Figure 3 the outer radius is always

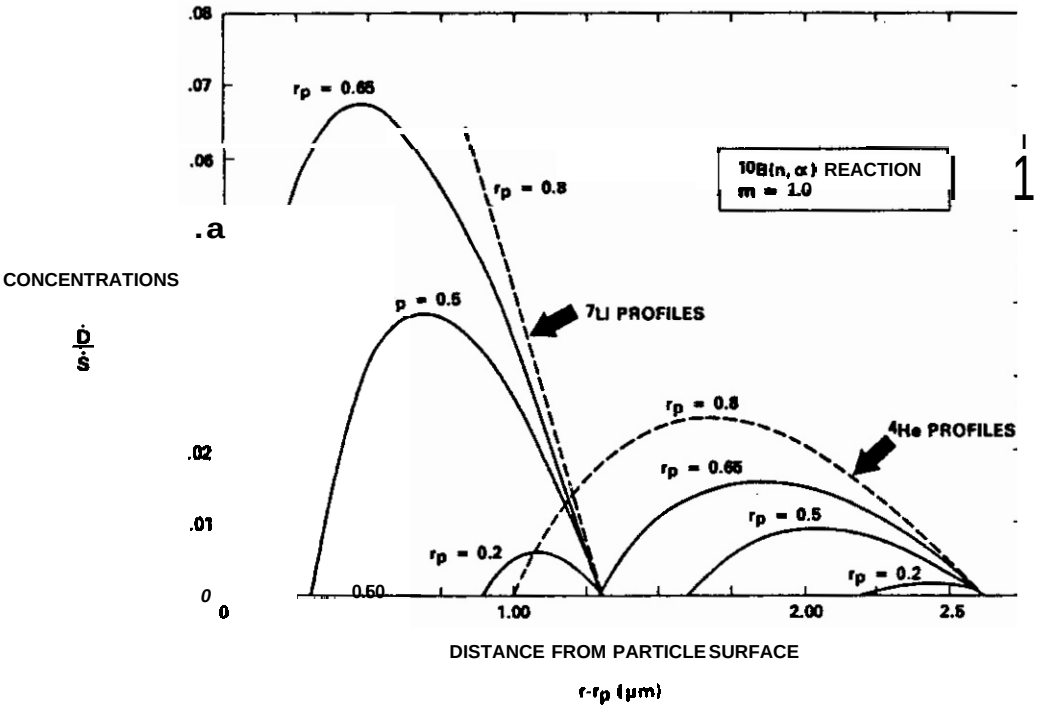

FIGURE 2. Effect of Precipitate Size on Normalized Deposition Rate of Reaction Products for $^{10}B(n,\alpha)$ Events Occurring in Spherical M_3B_2 Precipitates Embedded in a Stainless Steel Matrix. Stopping power ratio m = 1.0 for this case.

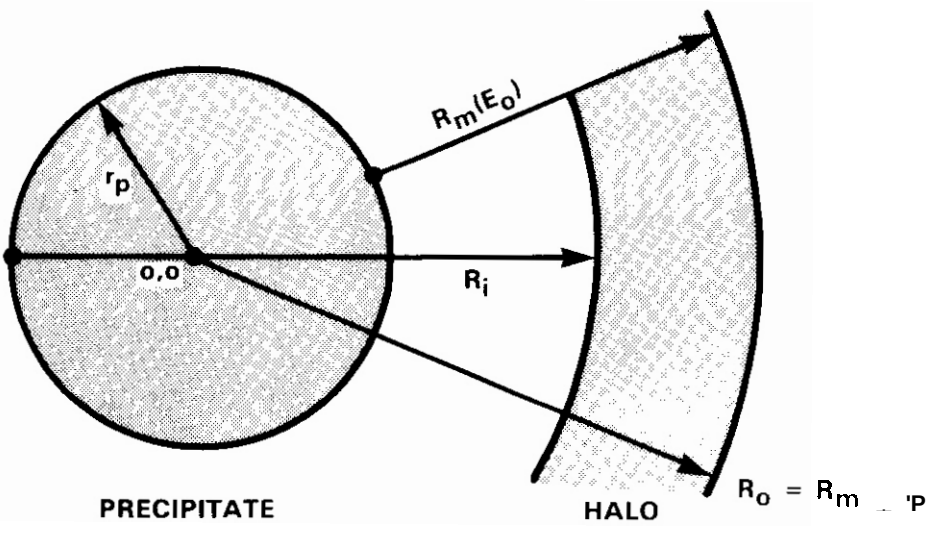

FIGURE 3. Limits of the Halo are Determined by the Precipitate Size, the Range of the Energetic Particle in the Matrix, and the Ratio m That Defines the Relative Stopping Powers of the Precipitate and Matrix Phases.

$$R_o = R_m + r_p \tag{2}$$

The inner radius depends on the precipitate properties such that

$$R_i = \begin{cases} r_p, & \text{if } 2r_p \geq R_p \\ R_m - (2m-1)rp', & \text{if } m \geq E \\ \sqrt{R_m^2 + r_p^2}, & \text{if } m < \end{cases} \tag{3}$$

$$\text{where } \beta = (2r_p)^{-1}\left[(r_p + R_m) - \sqrt{r_p^2 + R_m^2}\right]. \tag{4}$$

The particles arriving at a point(x,o) in the halo were emitted by atoms lying on a surface defined by

$$R(x,\theta) = d_p(x,\theta) + d_m(x,\theta), \tag{5}$$

as shown in Figure 4 and where d is the distance traveled in a particular phase.

5.2.2 The Source Surface Within the Precipitate

The description of $R(x,\theta)$ must now be determined. Geiger[10] stated that the energy loss rate $\frac{dE}{dx}$ of an alpha particle was inversely proportional to the particle velocity. From this statement various forms of the "Geiger Rule" are found in the literature. Some of these are given below.

(a) $\frac{dE}{dx} \sim E^{-1/2}$	instantaneous energy loss rate at any energy E	(6a)
(b) $R(E_o) \sim E_o^{1.5}$	total range in one phase	(6b)
(c) $\frac{E(E_o)}{} = \left[1 - \frac{L}{R(E_o)}\right]^{2/3}$	residual energy at a distance $L \leq R(E_o)$	(6c)

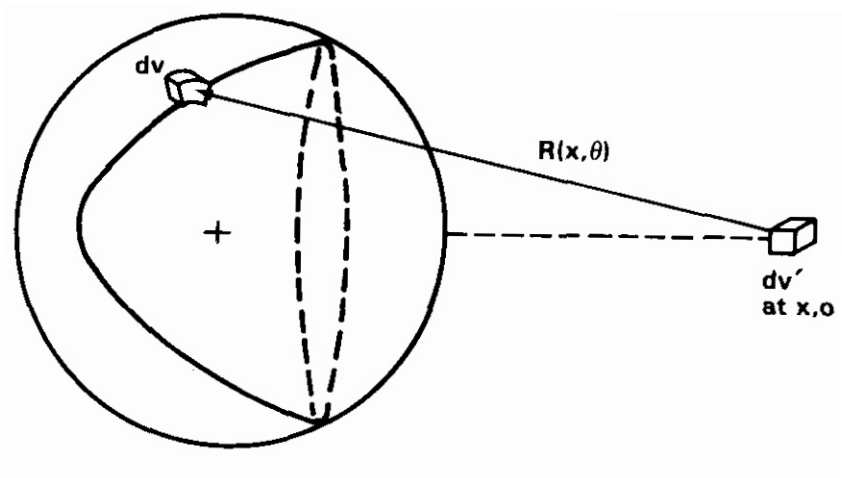

FIGURE 4. Schematic Illustration of Internal Precipitate Surface Contributing Particles to Point x,o in the Halo.

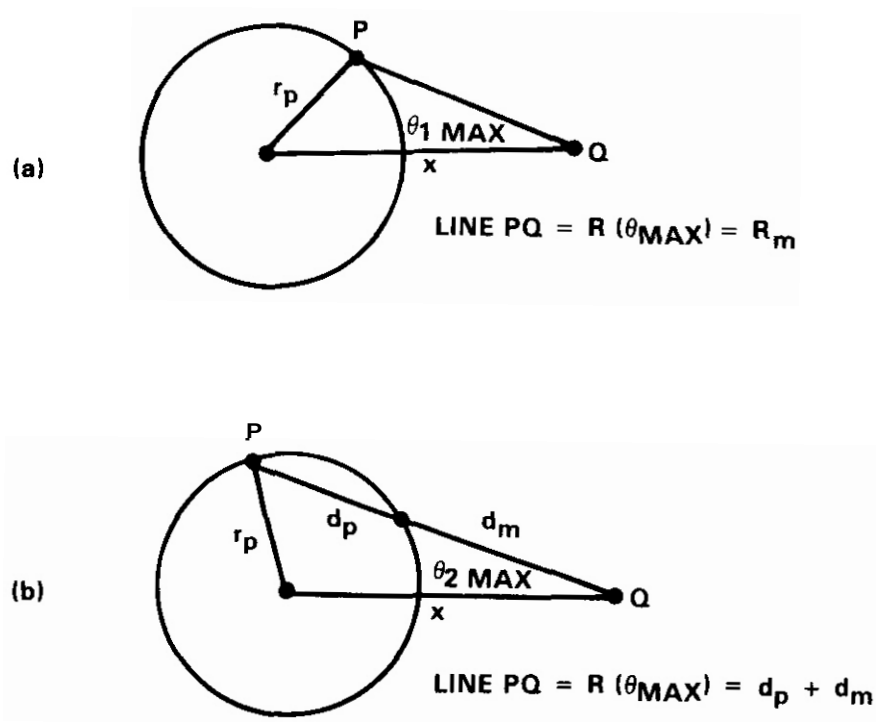

FIGURE 5. Geometrical Relationships Describing the Maximum Angle Defining the Source Surface for Any Point in the Halo. (a) shows the "under the horizon" case and (b) shows the "over the horizon" case. The precipitate horizon is viewed from the point (x,o).

Consider now the obvious corollary of the Geiger Rule when the particle travels a distance d_p in the precipitate phase and then encounters the matrix phase, traveling a distance d_m until its kinetic energy is exhausted. Statements (6b) and (6c) must hold in both phases; therefore

$$\frac{E(d_p)}{E_o} = [1 - \frac{d_p}{R_p(E_o)}]^{2/3} \tag{7a}$$

at the precipitate boundary and

$$\frac{E(d_p)}{E_o} = \left[\frac{d_m}{R_m(E_o)}\right]^{2/3} \tag{7b}$$

describes the remaining range in the matrix relative to the range of the particle at its original energy. Since $E(d_p) = E(d_m)$ at the precipitate boundary, equating these two expressions leads to

$$\frac{d_p}{R_p(E_o)} + \frac{d_m}{R_m(E_o)} = 1. \tag{8}$$

Employing this criterion and the geometry shown in Figure 4 it can be shown that

$$R(x,\theta) = m^{-1}\left\{R_m + (m - 1)\,[x \cos e - \sqrt{r_p^2 - x^2 \sin \theta^2}\,]\right\} \tag{9}$$

Consider a differential volume dV (located in the precipitate on the source surface) that emits the particles deposited in the volume element dV' in the matrix at point (x,o). These elements are separated by the distance $R(x,\theta)$ defined above and hereafter referred to as R. These volume elements can be defined in spherical coordinates as

$$dV = m^{-1} R^2 \sin e \cos e \, dx \, de \, d\phi \tag{10}$$

and

$$dV' = dA' dx \cos e \tag{11}$$

where e is the angle between the direction of R and the x-axis.

5.2.3 The Deposition Rate Within the Halo

The differential deposition rate dD(x) per unit volume at (x,o) is proportional to the source strength per unit volume S, the probability that a particle emitted in the source volume is directed toward (x,o) and the relative source and deposition volumes. Therefore

$$\begin{aligned} dD(x) &= \dot{S} \frac{dA'}{4\pi R^2} \frac{dV}{dV'} \\ &= \frac{S}{4\pi m} \sin\theta \, d\theta \, d\phi . \end{aligned} \tag{12}$$

$$\begin{aligned} D(x) &= \frac{\dot{S}}{4\pi m} \int_{\theta}^{\theta_{max}} \sin\theta \, d\theta \int_{\theta}^{2\pi} d\phi \\ &= \frac{\dot{S}}{2m} (1-\cos\theta_{max}) \end{aligned} \tag{13}$$

where θ_{max} is the maximum value of e defining the surface contributing to deposition at point (x,o).

5.2.4 Determination of θ_{max}

As viewed from the point (x,o) there are two cases, one when the maximum angle describing the source surface defines a boundary which lies in front of the precipitate horizon and another when that boundary lies over the horizon. The transition occurs when $x = \sqrt{R_m^2 + r_p^2}$.

When the boundary defined by θ_{max} falls in front of the precipitate horizon $\sqrt{R_m^2 + r_p^2} < x \leq (R_m + r_p)$ and the line PQ shown in Figure 5a does not go through the precipitate.

$$\theta_1 \max = \cos^{-1}\left[\frac{x^2 + R_m^2 - r_p^2}{2\,xR_m}\right] . \tag{14a}$$

When line PQ goes through the precipitate, the boundary of the source surface lies over the horizon. Using the geometry shown in Figure 5b and Equations 8 and 9,

$$\theta_2 \max = \cos^{-1}\left[\frac{-R_m + \sqrt{R_m^2 + 4m(m-1)\,\{R_m^2 + (2m-1)^2\,(x^2 - r_p^2)\}}}{4xm\,(m-1)}\right] \tag{14b}$$

The total deposition T of any one reaction product outside the precipitate is defined by

$$T = 4\pi \int_{R_i}^{R_o} x^2\,\dot{D}(x)dx \tag{15}$$

Note that the integration must be performed in two parts, integrating from R_i to $\sqrt{R_m^2 + r_p^2}$ and from $\sqrt{R_m^2 + r_p^2}$ to R_o.

With some care it can be shown that this integral equals the total source strength $(4/3\pi r_P^3 \dot{S}$ when $2r_P \leq R_p$. For $2r_P > R_P$ the total deposition in the halo is less than the total source strength since some of the particles come to rest within the precipitate.

5.2.5 Results and Discussion

Equations 13 and 14 define the deposition profiles outside the precipitate and can be applied to any transmutation reaction, precipitate size or matrix/precipitate combination. While the m = 1.0 case is shown in Figure 2 for the $^{10}B(n,\alpha)$ reaction, Figures 6 and 7 show typical profiles for the $^{10}B(n,\alpha)$ case where m = 0.5 and m = 2.0.

When m = 0.5 a discontinuity in the deposition gradients will develop as shown in Figure 6. There is continuity in the deposition rate itself, however. In practice, however, the investigator will probably not see the discontinuity due to range straggling of the energetic particles. The case where m = 0.5 is unique. For all other values of m, both the deposition rate and its derivitive are everywhere continuous.

Several advantages and disadvantages of this technique are clear from a comparison of Figures 6 and 7. When precipitates are employed such that m > 1.0 the width of the halo for a given precipitate size is greater than when m < 1.0, yielding a larger region over which the deposition profile may be considered to be uniform. This is important since the width of the halo limits the size of the microstructural components which can be studied. This enlargement of the halo width also leads to a larger region of overlap of the concentric halos resulting from both transmutation products, which may be an advantage or disadvantage depending on the objectives of the individual experiment. Figures 2, 6 and 7 also demonstrate that one can obtain a variety of helium levels in a single grain if suitably small areas contain more than one size of precipitate.

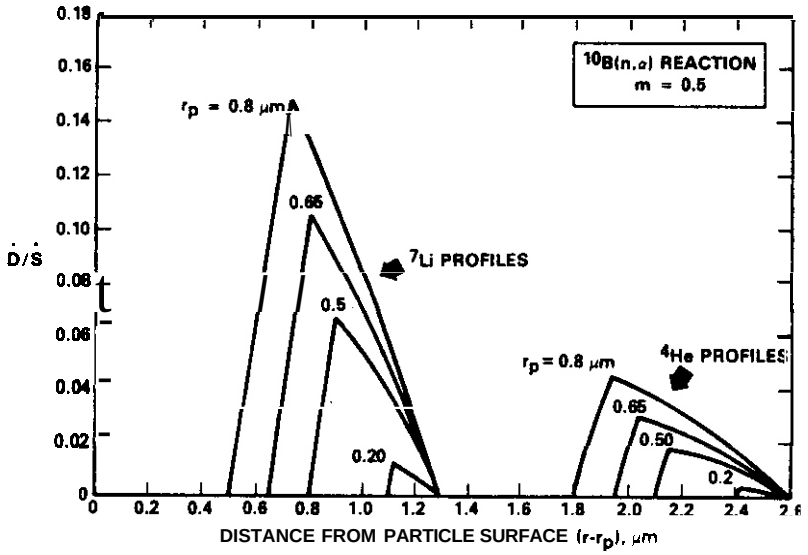

FIGURE 6. Normalized Deposition Rate Profiles for the $^{10}B(n,\alpha)$ Reaction when m = 0.5.

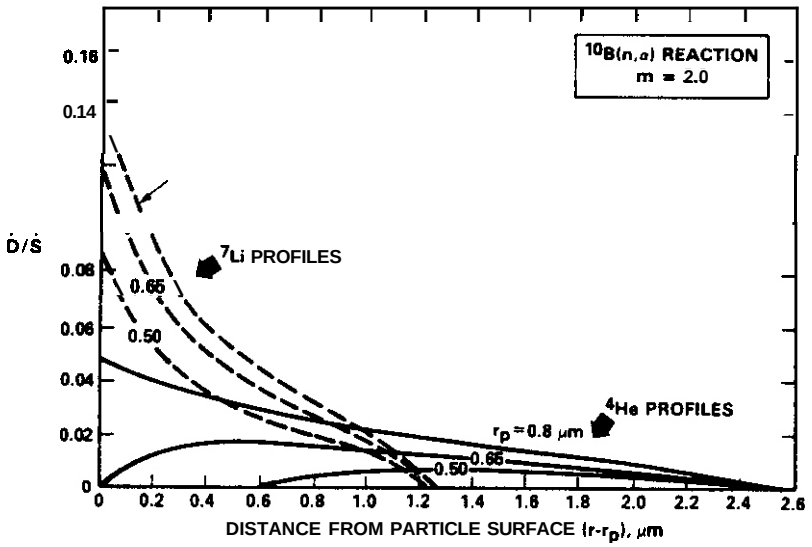

FIGURE 7. Normalized Deposition Rate Profiles for the $^{10}B(n,\alpha)$ Reaction when m = 2.0.

When the masses of the two reaction products are not too dissimilar the two concentric halos can overlap easily. For the $^{58}Ni(n,\gamma)^{59}Ni(n,\alpha)^{56}Fe$ reaction the fragments have quite different energies and ranges. The ^{56}Fe fragment retains only 340 keV of the reaction energy and the alpha particle retains 4.76 MeV.[11] Thus the iron atoms travel less than 100 nm and are retained in or near the precipitate. The helium atoms travel a much larger distance (~15 pm) however. Since most nickel-rich precipitates are only small fractions of a micron in size, the helium in the halo will be far away and very dilute, difficult to recognize above the background helium level and will be very hard to associate with a given precipitate. Therefore, this technique will only be useful for precipitates on the order of 10-15 μm in size. In 300 series stainless steels precipitates of this size occur only at relatively high temperatures (>600°C).

Whereas it has been previously shown that the displacements caused by transmutation products in fission reactors would not be a large fraction of the total damage generated in energetic neutron spectra,[1] Greenwood[11] has shown this not to be true in mixed-spectrum reactors such as HFIR where the "double-nickel" reaction occurs. The 340-keV recoil energy of ^{56}Fe can lead to increases in the displacement rate approaching 100% for pure nickel. Since nickel tends to concentrate in many precipitates during irradiation this will lead to displacement rates in and near the precipitates that are significantly higher than that of the surrounding matrix.

6.0 References

1. D. S. Gelles and F. A. Garner, J. Nucl. Mater. 85 & 86, (1979), 689.

2. L. L. Horton, "A Transmission Electron Microscope Study of Fusion Environment Radiation Damage in Iron and Iron-Chromium Alloys," ORNL/TM-8308, Oak Ridge National Laboratory, July 1982; also L. L. Horton, J. Bentley and K. Farrell, J. Nucl. Mater. 108 & 109, (1982), 222-233.

3. J. Megusar, O. K. Harling and N. J. Grant, "Tritium Doping of 316 Stainless Steel to Simulate Damage in a Fusion Reactor Environment." Damage Analysis and Fundamental Studies Quarterly Report, DOE/ER-0046/10, (1982), 249.

4. J. Weitman, N. Daverhog and S. Farvolden, Trans. Am. Nucl. Soc. 13, (1970), 557.

5. A. A. Bauer and M. Kangilaski, J. Nucl. Mater. 42, (1972), 91.

6. H. Kanani, L. Arnberg and O. K. Harling, J. Nucl. Mater. 103 & 104, (1981), 1115.

7. K. Farrell, private communication concerning research in progress.

8. W. J. S. Yang, H. R. Brager and F. A. Garner, "Radiation-Induced Phase Development in AISI 316," Phase Stability During Irradiation, Conference Proceedings, AIME (J. H. Holland, L. K. Mansur and D. I. Potter, Eds.) (1981), p. 257.

9. F. A. Garner, Radiation Effects 66, Nos. 3 & 4, (1982), 211-216.

10. H. Geiger, Proceedings of Royal Society of London, Series A, 83, (1910), 505-515.

11. L. R. Greenwood, "A New Calculation of Thermal Neutron Damage and Helium Production in Nickel," accepted for publication in J. Nucl. Mater.

7.0 Future Work

No futher work is planned.

8.0 Publications

None.

MUXS: A CODE TO GENERATE MULTIGROUP CROSS SECTIONS FOR SPUTTERING CALCULATIONS

T. J. Hoffman*, M. T. Robinson**, and H. L. Dodds, Jr.***
(Oak Ridge National Laboratory)

1.0 Objective

The purpose of this study is to construct numerical models of the development of collision cascades and to apply them to studies of radiation damage production, sputtering, and plasma particle backscattering, in the context of fusion first wall materials development.

2.0 Summary

The computer code MUXS generates multigroup cross sections for charged particle transport problems. Cross sections generated by MUXS can be used in many multigroup transport codes, with minor modifications to these codes, to calculate sputtering yields, reflection coefficients, penetration distances, and so forth.

3.0 Program

Title: Damage Analysis and Dosimetry
Principal Investigator: M. T. Robinson
Affiliation: Oak Ridge National Laboratory

---

* Computer Sciences Division, Union Carbide Corporation, Nuclear Division

** Solid State Division, Oak Ridge National Laboratory

*** Department of Nuclear Engineering, University of Tennessee, Knoxville

4.0 Relevant DAFS and PMI Program Plan Task/Subtask

Subtask III.B.1.3: Development of Theoretical Model Descriptions of Reflection and Backscattering

Subtask III.C.1.6: Development of Theoretical Models for Physical and Physichemical Sputtering

5.0 Accomplishments and Status

During the past several years, we have presented several papers on the application of neutral-particle multigroup methods to the analysis of charged particle transport problems [l-51. The computer program that was developed in connection with this work has now been documented and prepared for distribution. The documentation is contained in an ORNL report [6], which should be consulted for the details. The report has received the standard fusion materials distribution UC-20c. The code MUXS and the changes required in ANISN to use it for charged-particle transport applications, as well as the ANISN code itself, may be obtained from the Radiation Shielding Information Center, Oak Ridge National Laboratory, P. O. Box X, Oak Ridge, TN 37830. Publication of this report and preparation of the program material for circulation completes work on this topic.

6.0 References

[1] T. J. Hoffman, H. L. Dodds, Jr., M. T. Robinson, and D. K. Holmes, Proc. Intern. Top. Conf. on Advances in Mathematical Methods for the Solution of Nuclear Engineering Problems, (Fachinformationszentrum Energie, Physik, Mathematik Gmbh, Karlsruhe, F. R. G., 1981). Vol. 2, pp. 447-461.

[2] T. J. Hoffman, M. T. Robinson, and H. L. Dodds, Jr., J. Nucl. Mater. 85, 597 (1979).

[3] T. J. Hoffman, H. L. Dodds, Jr., M. T. Robinson, and D. K. Holmes, Nucl. Sci. Eng. 68, 204 (1978).

[4] T. J. Hoffman, M. T. Robinson, H. L. Dodds, Jr., and D. K. Holmes, Trans. Amer. Nucl. Soc. 34, 225 (1980).

[5] T. J. Hoffman, H. L. Dodds, Jr., D. K. Holmes, and M. T. Robinson, Trans. her. Nucl. Soc. 27, 266 (1977).

[6] T. J. Hoffman, M. T. Robinson, and H L. Dodds, Jr., MUXS: A Code to Generate Multigroup Cross Sections for Sputtering Calculations, ORNL/CSD/TM-185 (October 1982).

C H A P T E R 3

REDUCED ACTIVATION MATERIALS

ACTIVATION OF COMPONENTS OF A FUSION ALLOY

F. M. Mann (Hanford Engineering Development Laboratory)

1.0 Objective

The objective of this work is to determine the activation of the constituents of potential fusion alloys so as to guide metallurgists in selecting low activation materials.

2.0 Summary

The activation of various elements at the STARFIRE first wall position for a two (2) year irradiation period was calculated. At ten (10) days, Mn, Co, and Ni have the highest unshielded dose rates per unit volume. After 3×10^5 days, N (considered as a liquid), Ni, and Mo have the highest decay rates per unit volume.

3.0 Program

Title: Irradiation Effects Analysis (AKJ)
Principal Investigator: D. G. Doran
Affiliation: Hanford Engineering Oevelopment Laboratory

4.0 Relevant DAFS Program Plan Task/Subtask

No relevant Task.

5.0 Accomplishments and Status

In order to tailor the composition of an alloy so that the alloy produces a low level of radioactivity, the activation of each of the elements comprising the alloy must be known. Therefore, the activation of various elements (C, N, O, Mg, Al, Si, P, Ti, V, Cr, Mn, Fe, Co, Ni, Mo, W) and at the STARFIRE[1]

first wall position have been calculated for a two (2) year bombardment time and for various cooling times [t_c = 1.0 x 10^y, 3.0 x 10^y days, where y = -2(1)6]. At ten (10) days (a typical delay time for maintenance) Mn, Co, and Ni have the highest unshielded dose rates per unit volumes at 1 meter. After 3 x 10^5 days (~820 years, a time typical of waste studies), N (considered as a liquid), Ni, and Mo have the highest decay rates per unit volume.

Table 1 displays decay and dose rates after ten (10) days for each of the elements calculated. Also shown are the most important reactions and their individual contributions. For short times where maintenance is the prime concern, dose rate is the more relevant quanity, while for long times where waste management is the prime concern, decay rate is more relevant. Table 2 displays similar information for a cooling period of 3 x 10^5 days. Table 3 presents the density and isotopic abundances used in the calculations.

The methods and cross sections used are described in Reference 2. In general the most important cross sections are from ENDF/B-V and should be quite reliable. However, some exotic reactions, such as ^{29}Si (n,2p), come from a consideration of reaction systematics and are somewhat questionable. An effect not considered is gaseous diffusion which probably will be important for tritium. Not only may tritium diffuse out of the alloy, but tritium may also diffuse in from the plasma or from the breeding material.

6.0 References

1. C. C. Baker et al., STARFIRE, A Commercial Tokamak Fusion Power Plant Study, Argonne National Laboratory Report, ANL/FPP-80-1, 1980.

2. F. M. Mann, Transmutation of Alloys in MFE Facilities as Calculated by REAC (A Computer Code System for Activation and Transmutation], HEDL-TME 81-37, August 1982.

3. G. L. Kulcinski, et al., "TASKA, A Fusion Engineering Test Facility for the 1990's," J Nucl Matl 103 & 104 (1981) 67.

7.0 Future Work

Additional work will include additional elements, (Li, Be, B, S, Cu, Zr, Nb, Sn, Hf, Ta, and Pb), a different reactor spectrum or position, and different irradiation times and power histories. Particularly for elements heavier than the iron group, neutron capture is very important. However, the capture rate is very sensitive to the assumed spectrum; e.g., the TASKA[3] first wall flux is harder than the STARFIRE first wall flux, and blanket spectra are softer than first wall spectra. Activation is not linearly related to a reactor-on time, so a range of irradiation periods will be considered. In addition, the sensitivity to power history effects, important for isotopes with half-lives comparable to the time scale of the radiation cycle, will be determined.

8.0 Acknowledgements

The timely assistance of Y. Gohar (STARFIRE) and M. E. Sawan (TASKA) in supplying neutron fluxes is greatly appreciated.

TABLE 1

ACTIVATION AT 10 DAYS AFTER 2-YEAR IRRADIATION AT STARFIRE FIRST WALL

Element	Decay Rate (Curies/cm^3) Value	Major Reaction**		Dose Rate at 1 Meter (Rem /hr-cm^3) Value	Major Reaction**	
C	2.6(-7)*	$^{13}C(n,\alpha)^{10}Be$	(100%)	***	---	
N	8.8(-1)	$^{14}N(n,x)^{3}H$	(98%)	***	---	
O	1.9(-5)	$^{17}O(n,\alpha)^{14}C$	(83%)	***	---	
		$^{18}O(n,n\alpha)^{14}C$	(17%)			
Mg	5.9(-1)	$^{25}Mg(n,\alpha)^{22}Na$	(65%)	6.1(-1)	$^{25}Mg(n,\alpha)^{22}Na$	(82%)
		$^{25}Mg(n,x)^{3}H$	(22%)		$^{24}Mg(n,\tau)^{22}Na$	(15%)
		$^{24}Mg(n,\tau)^{22}Na$	(12%)			
Al	8.2(-3)	$^{27}Al(n,x)^{3}H$	(89%)	1.7(-3)*	$^{27}Al(n,\alpha)^{24}Na$	(97%)
		$^{27}Al(n,\alpha)^{24}Na$	(11%)			
Si	2.6(-1)	$^{29}Si(n,x)^{3}H$	(100%)	3.8(-5)	$^{29}Si(n,2p)^{28}Mg$	(100%)
P	1.2(+1)	$^{31}P(n,x)^{3}H$	(50%)	***	---	
		$^{31}P(n,\gamma)^{32}P$	(50%)			
Ti	2.0(+1)	$^{46}Ti(n,p)^{46}Sc$	(47%)	1.4(+1)	$^{46}Ti(n,p)^{46}Sc$	(68%)
		$^{48}Ti(n,\alpha)^{45}Ca$	(29%)		$^{47}Ti(n,np)^{46}Sc$	(11%)
V	7.7(-1)	$^{51}V(n,\alpha)^{48}Sc$	(57%)	8.6(-1)	$^{51}V(n,\alpha)^{48}Sc$	(97%)
		$^{51}V(n,n\alpha)^{47}Sc$	(43%)			
Cr	1.6(+2)	$^{52}Cr(n,2n)^{51}Cr$	(76%)	4.0(+0)	$^{52}Cr(n,2n)^{51}Cr$	(71%)
		$^{50}Cr(n,\gamma)^{51}Cr$	(19%)		$^{50}Cr(n,\gamma)^{51}Cr$	(18%)
					$^{50}Cr(n,t)^{48}V$	(11%)
Mn	3.4(+2)	$^{55}Mn(n,2n)^{54}Mn$	(100%)	1.7(+2)	$^{55}Mn(n,2n)^{54}Mn$	(100%)
Fe	1.3(+2)	$^{56}Fe(n,2n)^{55}Fe$	(80%)	7.1(+0)	$^{54}Fe(n,p)^{54}Mn$	(95%)
		$^{54}Fe(n,p)^{54}Mn$	(11%)			
Co	2.5(+3)	$^{59}Co(n,\gamma)^{60}Co$	(80%)	3.0(+3)	$^{59}Co(n,\gamma)^{60}Co$	(90%)
		$^{59}Co(n,2n)^{58}Co$	(19%)			
Ni	5.7(+2)	$^{58}Ni(n,np)^{57}Co$	(48%)	1.9(+2)	$^{58}Ni(n,p)^{58}Co$	(80%)
		$^{58}Ni(n,p)^{58}Co$	(44%)		$^{58}Ni(n,np)^{57}Co$	(14%)
Mo	2.6(+1)	$^{98}Mo(n,\gamma)^{99}Mo$	(40%)	9.9(+0)	$^{98}Mo(n,\gamma)^{99}Mo$	(21%)
		$^{100}Mo(n,2n)^{99}Mo$	(19%)		$^{92}Mo(n,n\alpha)^{88}Zr$	(24%)
		$^{92}Mo(n,p)^{92}Nb^{m}$	(11%)		$^{92}Mo(n,p)^{92}Nb^{m}$	(18%)
					$^{100}Mo(n,2n)^{99}Mo$	(10%)
W	6.6(+2)	$^{182}W(n,2n)^{181}W$	(40%)	5.5(+0)	$^{186}W(n,\gamma)^{187}W$	(36%)
		$^{184}W(n,\gamma)^{185}W$	(29%)		$^{182}W(n,2n)^{181}W$	(19%)
		$^{186}W(n,2n)^{185}W$	(24%)		$^{184}W(n,\gamma)^{185}W$	(18%)
					$^{186}W(n,2n)^{185}W$	(15%)

*(x) read as $\times 10^{x}$

**only reactions which contribute at least 10% as listed

***less than 10^{-10}

TABLE 2

ACTIVATION AT 3 x 10^5 DAYS (~820 YEARS) AFTER 2-YEAR IRRADIATION AT STARFIRE FIRST WALL

Element	Decay Rate (Curies/cm^3) Value	Decay Rate Major Reaction**		Dose Rate at 1 Meter (Rem /hr-cm^3) Value	Dose Rate Major Reaction**	
C	2.6(-7)*	$^{13}C(n,\alpha)^{10}Be$	(100%)	***	---	
N	1.6(-2)	$^{14}N(n,p)^{14}C$	(100%)	***	---	
O	1.9(-5)	$^{17}O(n,\alpha)^{14}C$	(83%)	***	---	
		$^{18}O(n,n\alpha)^{14}C$	(17%)			
Mg	***	---		***	---	
Al	4.1(-5)	$^{27}Al(n,2n)^{26}Al$	(100%)	6.0(-5)	$^{27}Al(n,2n)^{26}Al$	(100%)
Si	***	---		***	---	
P	***	---		***	---	
Ti	***	---		***	---	
V	***	---		***	---	
Mn	***	---		***	---	
Fe	1.1(-5)	$^{54}Fe(n,np)^{53}Fe$		***	---	
co	***	---		***	---	
Ni	7.0(-3)	$^{58}Ni(n,\gamma)^{59}Ni$	(63%)	6.7(-8)	$^{61}Ni(n,2p)^{60}Fe$	(83%)
		$^{62}Ni(n,\gamma)^{63}Ni$	(19%)		$^{64}Ni(n,n\alpha)^{60}Fe$	(11%)
		$^{60}Ni(n,2n)^{59}Ni$	(14%)			
Mo	3.8(-2)	$^{92}Mo(n,\gamma)^{93}Mo$	(63%)	2.8(-3)	$^{92}Mo(n,\gamma)^{93}Mo$	(57%)
		$^{94}Mo(n,2n)^{93}Mo$	(136%)		$^{94}Mo(n,2n)^{93}Mo$	(33%)
W	1.5(-8)	$^{186}W(n,n\alpha)^{182}Hf$	(100%)	1.4(-8)	$^{186}W(n,n\alpha)^{182}Hf$	(100%)

*(x) read as $*10^x$

**only reactions which contribute at least 10% are listed

***less than 10^{-10}

TABLE 3

ISOTOPIC ABUNDANCES

Element	Density (g/cm^3)	Isotopic Abundances Mass (% abundances)
C	2.26	12(99.89), 13(1.11)
N	0.81*	14(99.63), 15(0.37)
O	1.14*	16(99.758), 17(0.038), 18(0.204)
Mg	1.74	24(78.909), 25(10.00), 26(11.01)
Al	2.70	27(100.0)
Si	2.33	28(92.33), 29(4.67), 30(3.10)
P	1.82	31(100.0)
Ti	4.51	46(8.25), 47(7.45), 48(73.7), 49(5.4), 50(5.2)
V	6.1	50(0.25), 51(99.75)
Cr	7.19	50(4.35), 52(83.79), 53(9.50), 53(2.3
Mn	7.43	55(100.0)
Fe	7.86	54(5.8), 56(91.8), 57(2.1), 58(0.3)
co	8.9	59(100.0)
Ni	8.9	58(68.3), 60(26.1), 61(1.1), 62(3.6), 64(0.9)
Mo	10.2	92(14.8), 94(9.3), 95(15.9), 96(16.7) 97(9.6), 98(24.1), 100(9.6)
W	19.3	180(0.13), 182(26.3), 183(14.3), 184(30.67), 186(28.6)

* density of liquid

CHAPTER 4

FUNDAMENTAL MECHANICAL BEHAVIOR

EFFECT OF TEMPERATURE ON THE CRACK PROPAGATION CHARACTERISTICS IN RTNS-II IRRADIATED TYPE 316 STAINLESS STEEL MICROSPECIMENS

R. D. Gerke and W. A. Jesser (University of Virginia)

1.0 Objective

The objective of this work is to determine the role of temperature on crack propagation characteristics during tensile tests of neutron irradiated type 316 stainless steel microspecimens.

2.0 Summary

Microtensile specimens irradiated in RTNS-II at room temperature to a fluence of 1 x 10^{22} n/m^2 and subsequently tensile tested at room temperature, 400° and 600" respectively, showed that the effect of tensile test temperature is to enhance those characteristics associated with ductile crack propagation. Ductility as measured by reduction of area was largest at 600°C and least at 400". These results are consistent with those on unirradiated specimens except that the ductility loss at 400°C is more pronounced in that case. All specimens tested showed a relationship of stable crack length per unit elongation, S, to Reduction of Area, ROA, in the thick region of the specimen as $ROA^2 \times S \approx 0.4$.

3.0 Program

Title: Simulating the CTR Environment in the HVEM
Principal Investigators: W. A. Jesser and R. A. Johnson
Affiliation: University of Virginia

4.0 Relevant DAFS Program Plan Task/Subtask

Task 11.C.13 Effects of Helium and Displacements on Crack Initiation and Propagation

5.0 Accomplishments and Status

5.1 Introduction

The embrittling effect of irradiation manifests itself in several ways such as ductility loss and intergranular fracture. The relative embrittlement contributions of the various microstructural and microchemical changes associated with irradiation have not been separated, even though many of the relative contributions to specimen strength have been considered[1]). The role of helium in promoting embrittlement is not well understood. In an effort to determine the irradiation-induced condition of the specimen which is responsible for brittle failure, in-situ HVEM tensile testing of microspecimens has been conducted. Testing a number of specimens exhibiting a variety of microstructural conditions has failed to reveal any critical microstructure responsible for intergranular failure.[2] The data show that intergranular failure of irradiated austenitic stainless steel is largely a temperature-dependent phenomenon rather than being sensitive to microstructure. It is therefore important to understand the role of temperature in controlling embrittlement of irradiated materials.

The development of irradiation induced microstructure and microchemistry is temperature dependent and the plastic deformation processes show a temperature dependence. Both of these temperature dependent processes occur together during a creep experiment and show some interrelated effects; however, the two processes can be separated by investigating the temperature dependence of plastic deformation in several specimens which have a fixed microstructure characteristic of one temperature. In order to accomplish this goal, several austenitic stainless steel specimens were neutron irradiated under the same conditions and then tensile tested at three temperatures up to 600°C. The results of these tests were compared to results from similar tests on unirradiated specimens. The parameters selected for comparison were ones which characterize crack propagation through the thin regions of a specimen with thick edges.

5.1 Specimen Preparation and Test Procedure

Commercial type 316 stainless steel foils were solution annealed in vacuum (pressure < 10^{-4} Pa) for one hour at 1000°C. After annealing the 40-μm thick foils were punched into rectangular microtensile specimens 12.5 mm long by 2.5 mm wide. Next a circular region in the center of the specimen about 2mm in diameter was electropolished to electron transparency for 400 kV electrons in a 90% acetic acid 10% perchloric acid solution at room temperature. Before electropolishing, a number of the specimens were irradiated with 14-MeV neutrons near room temperature in the Lawrence Livermore Rotating Target Neutron Source II (RTNS-II) facility to a total fluence of about 1 x 10^{22} n/m^2.

The irradiated specimens and unirradiated comparison specimens were tensile tested to failure in a quantitative load-elongation tensile stage operating at one of three temperatures: a) room temperature, b) 400°C and c) 600°C. Only one specimen was tested at each temperature because of the limited number of irradiated specimens.

During the tensile test all specimens exhibited microcrack initiation in the thin area at the edge of the perforation which resulted from the electropolishing procedure. HVEM observations of the main propagating crack at low magnification of 10 kX were recorded on video tape while simultaneously recording the load elongation data from the tensile stage, which represents the overall behavior of the whole microspecimen. From this data one can characterize the propagation behavior of the main crack and determine its temperature dependence. A graph of crack length versus specimen elongation has a slope which can be related to specimen ductility. The details of the graph are temperature dependent.

5.2 Experimental Results

Investigation of the crack propagation characteristics of unirradiated type 316 stainless steel has previously been reported for tensile test temperatures of

room temperature and 400°C. [3] In the present report the case of unirradiated stainless steel tested at 600°C has been performed and the tensile testing of the RTNS-II irradiated specimens has been conducted at elevated temperatures.. The two cases of testing at 400°C and at 600°C are shown respectively in the two graphs of total crack length, L, plotted against specimen elongation(Fig.1).

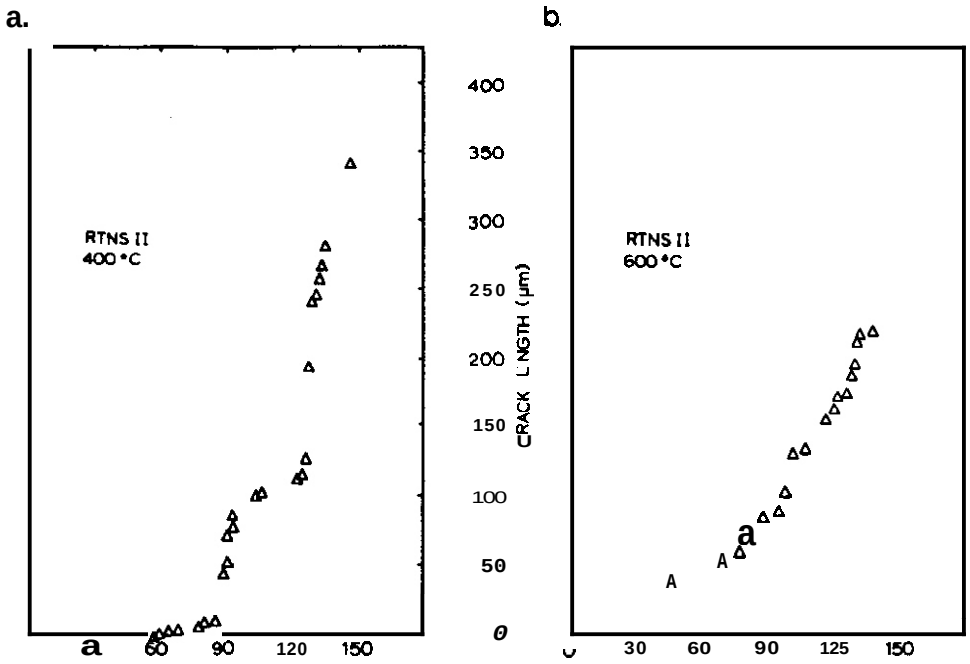

FIGURE 1. Crack Length Versus Elongation for RTNS II Irradiated Specimens, Which Were a) Tensile Tested at 400°C and b) Tensile Tested at 600°C. Notice that the vertical-horizontal steps of the 400°C case are absent from the 600°C case.

A comparison of all of the crack length versus elongation curves, and the crack tip angle, crack angle and crack propagation direction versus elongation data shows a trend which exhibits a temperature dependence. All cracks under all test conditions utilized thus far have the following characteristics in common. Crack propagation through the thin region (electropolished region) of the specimen is stable and exhibits a discontinuous start-stop character. Once the crack reaches the thick sides of the specimen which have not been thinned by

electropolishing, the crack propagation becomes unstable and the crack catastrophically fractures the specimen at a rate too high to observe or record. The crack propagation through the thin region is therefore controlled by the displacement of the thick adjacent regions which are undergoing plastic deformation without cracking.

The effect of neutron irradiation on the crack length versus elongation curves is to introduce a pronounced step shape in the curve. This step is a nearly horizontal section adjacent to a nearly vertical section. The nearly horizontal section, little crack lengthening associated with the elongation, is accompanied by slow changes in crack direction, crack tip angle and crack angle. The nearly vertical section, substantial crack lengthening during the elongation, is accompanied by rapid changes in the above mentioned three parameters for which the amplitude of the parameter oscillations is reduced from that associated with a slowly propagating crack.

The effect of increasing tensile test temperature on the step in the curve is to decrease the magnitude of the vertical-horizontal sections until at 600°C they have disappeared. Another effect of increasing temperature is to decrease the slope of the graphs for the case of the irradiated specimens, except for the 400°C data which shows a slope increase and correspondingly a slight ROA decrease. The graph corresponding to a 600°C test of irradiated stainless steel resembles that for an unirradiated specimen tested at 600°C, but the respective cases for room temperature and for 400°C show strong steps in the irradiated specimens, but steps which are weak or absent in the unirradiated specimens. The effect of increasing test temperature of irradiated microspecimens is to increase the smoothness of the graph of the crack length versus elongation.

Examination of the fracture surface revealed that there are two distinct regions on the separated surfaces. A schematic representation of a fractured microspecimen is shown in Figure 2. The reduction of area, ROA, which occurred in the thick region during stable crack propagation through the thin region is denoted as a shoulder and the remaining region of the fracture surface represents that portion of the sample through which catastrophic crack propaga-

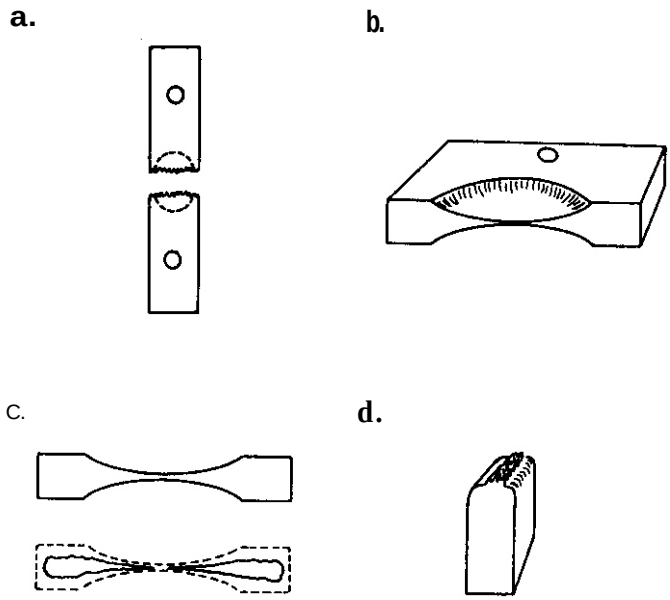

FIGURE 2. Schematic Illustration of a Fractured Specimen: a) Top View, b) Near Edge View of Electropolished Region and the Surrounding Thick Area, c) Before and After Fracture Cross-Section View, d) Shoulder Left After Fracture.

tion took place in the thick region. Measurements of the amount of reduction of area which occurred during stable crack propagation, i.e. that recorded and graphed, can be made by measuring the area of shoulder and subtracting this quantity from the total cross-sectional area. This data is calculated and presented in Table 1 along with the slope, S, of the curve of crack length versus elongation. It is interesting to note that the product of ROA^2 and S is closely constant at 0.4.

TABLE 1

DATA FROM HVEM MICROTENSILE SPECIMENS

	Specimen Tensile Test Condition	Average Slope, S	Original* Cross-sectional Area ($\times 10^{-2}$ mm^2)	ROA*† (%)	(ROA)^2 S
Unirradiated	R.T.	1.7	4.4	49	0.41
	400°C	2.8	4.2	38	0.40
	600°C	1.2	4.3	53	0.34
RTNSII Neutron Irradiated	R.T.	3.6	5.0	34	0.42
	400°C	4.2	4.4	32	0.43
	600°C	2.1	5.9	44	0.41

*estimated from SEM micrographs

'during stable crack growth only

5.3 Discussion

As the tensile test temperature is increased from room temperature to 600°C, the characteristics of crack propagation in the neutron irradiated specimen more closely resemble those of the unirradiated specimens. Even though the crack propagation characteristics of the irradiated and unirradiated specimens are most similar at the test temperature of 600°C, still there is a more brittle crack propagation behavior associated with the irradiated specimen, as is revealed, for example, by the slope S of the crack length versus elongation graph. This graph shows a smooth curve typical of ductile crack propagation in an unirradiated specimen, but the slope of the curve is higher than that of an unirradiated specimen and hence corresponds to less reduction of area i.e., more brittle behavior.

The irradiated specimens all exhibited the same microstructure after irradiation. However, during the tensile test some changes in the microstructure and microchemistry may occur. Small dislocation loops and defect clusters formed during irradiation may anneal at 600°C while transmutational helium produced

by (n,α) reactions are likely immobilized at traps even at 600°C. One might expect, from the above idea, that as test temperature is increased the annealing effect increases specimen ductility until a level is reached which is dominated by the transmutational helium.

In view of the similarity of the geometry of all the specimens tested thus far, the relationship $ROA^2 \times S \simeq 0.4$ may be a result of specimen shape. It has been determined from electron micrographs that the extent of stable crack propagation is about 400 μm and the specimen region which exhibits plastic deformation is about 1000 μm long (gauge length). The ratio of these two geometrical parameters is also 0.4; however, a definite connection between this ratio and the above constant has not yet been established.

5.4 Conclusions

The following conclusions have been reached regarding type 316 stainless steel neutron irradiated to a fluence of 1×10^{22} n/m^2.

i) The length of crack propagation per unit elongation decreases in neutron irradiated specimens as tensile test temperature increases from room temperature to 600°C.

ii) The above crack length per elongation, S, can be related to reduction of area, ROA, for all the specimens tested thus far as $ROA^2 \times S = 0.4$.

iii) Combining results (i) and (ii) shows that over the temperature range 600°C to room temperature, ductility in irradiated specimens is increased by increasing temperature. Notice that this is not true of unirradiated specimens.

iv) The role of temperature in tensile tests is a separate one from its role in establishing an irradiation microstructure.

v) No intergranular, brittle crack propagation was observed in the neutron irradiated specimen tensile tested at 600°C. No visible cavities were present in the specimen.

6.0 References

1. F. A. Garner, M. L. Hamilton, N. F. Panayoutou and G. O. Johnson, Proceedings of the Second Topical Conference on Fusion Reactor Materials, J. Nucl. Mater. 103 and 104, p. 803, 1981.

2. J. I. Bennetch and W. A. Jesser, ibid, p.809.

3. R. O. Gerke and W. A. Jesser, DAFS Quarterly Progress Report, DOE/ER-0046/10, p. 130, August 1982.

CORRELATION OF FRACTURE TOUGHNESS WITH TENSILE PROPERTIES FOR IRRADIATED 20% CW 316 STAINLESS STEEL

F. A. Garner (Westinghouse Hanford Company), W. G. Wolfer (University of Wisconsin), and M. L. Hamilton (Westinghouse Hanford Company)

1.0 Objective

The first-wall lifetime in pulsed Tokamak reactors is expected to be limited by fatigue crack growth. The terminal stage of crack growth depends critically on the fracture toughness after irradiation. The purpose of this study is to establish a valid correlation for irradiated materials between fracture toughness and tensile properties, since the latter can be more easily obtained with miniature specimens.

2.0 Sumnary

Tensile properties measured on irradiated 20% CW 316 stainless steel specimens made from ducts and from cladding are used to predict values for the plane strain fracture toughness according to a model originally developed by Krafft. In contrast to the Hahn-Rosenfield model, this model gives results which agree with recent experimental measurements. It therefore appears that it may be feasible to obtain tensile properties from irradiated miniature tensile samples and use them to predict the toughness for ductile transgranular failure.

3.0 Programs

Title: Effect of Radiation and High Heat Flux on First-Wall Components
Principal Investigator: W. G. Wolfer
Affiliation: University of Wisconsin-Madison

Title: Irradiation Effects Analysis (AKJ)
Principal Investigator: D. G. Doran
Affiliation: Westinghouse Hanford Company

4.0 Relevant DAFS Program Plan Task/Subtask

II.C.1. Effects of Materials Parameters on Microstructure
II.C.8. Effects of Helium and Displacements on Fracture
II.C.14. Model of Flow and Fracture Under Irradiation

5.0 Accomplishments and Status

5.1 Introduction

In order to assess the lifetime of first-wall components exposed to cyclic heat flux and neutron damage in a fusion reactor, it will be necessary to perform a fatique crack growth analysis with realistic correlations for the degradation of mechanical properties as a function of neutron damage. An extensive analysis of this kind has been performed recently by Watson,(1) but rather tenuous correlations were used for the fluence-dependence of the fracture toughness. These correlations were based on theoretical considerations advanced by Odette and Frey(2) and by Wolfer and Jones.(3) In spite of the use of these somewhat hypothetical correlations, the analysis by Watson clearly demonstrated that a reduction in fracture toughness can have a significant impact on the lifetime of the first wall. Figure 1 shows the computed lifetime of a first wall as a function of the saturation* value of fracture toughness. This analysis employs the assumptions that an initial surface flaw exists with a depth of 1 mm and that the wall is exposed to a cyclic heat flux having an amplitude of 50 W/cm^2. It is seen that the lifetime depends strongly on the fracture toughness, particularly for the most desirable wall thicknesses around 5 mm.

The saturation value of the fracture toughness is also of critical importance for safety considerations. Should failure occur, it is most desirable

*Since most mechanical properties of austenitic stainless steels approach a limiting or saturation value during irradiation, it is likewise assumed that fracture toughness will exhibit the same behavior. There is no evidence to support or refute this assumption.

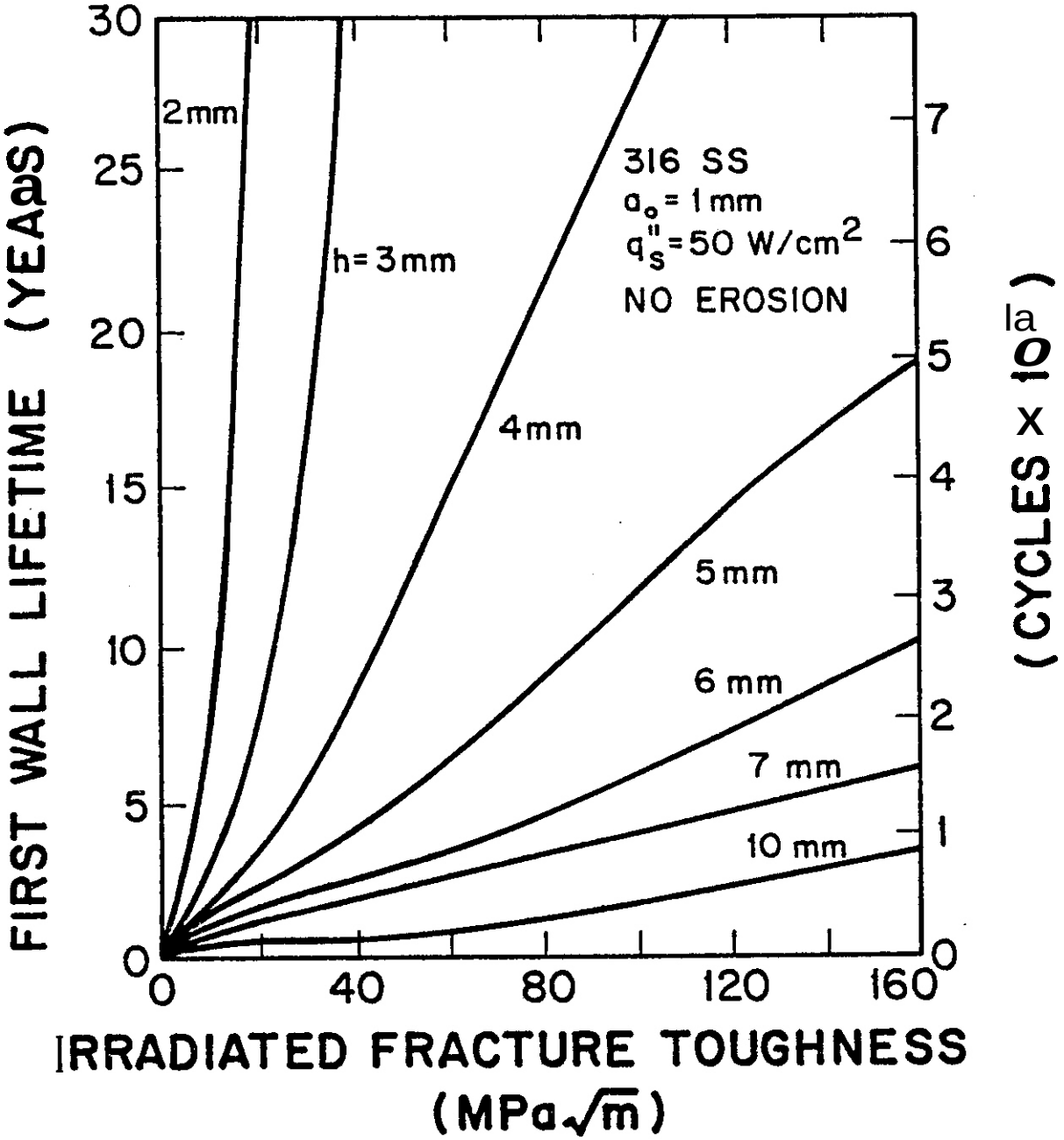

FIGURE 1. Effect of the Minimum Irradiated Fracture Toughness Level on First Wall Lifetime for Various Wall Thicknesses.

that it be a leak rather than a catastrophic propagation of a crack. Which of these failure modes will be encountered depends both on the wall thickness and on the fracture toughness, as shown in Figure 2.

The experimental determination of the fracture toughness for irradiated materials is hampered by several considerations. First, both standard and miniature fracture toughness specimens are rather large with respect to the limited space available in either FMIT or breeder and mixed-spectrum reactors. Second, the minimum size for valid test specimens requires some a priori estimate of the expected fracture toughness. For these reasons it is desirable to explore the possibility that fracture toughness values might be obtained from tensile properties of irradiated samples having a much reduced size. This possibility was discussed at some length by Wolfer and Jones,[3] and it was pointed out that the appropriate correlation between the fracture toughness and tensile properties is fundamentally different for materials exhibiting homogeneous plastic flow and those experiencing localized flow. The latter is expected only for highly irradiated materials with a residual tensile ductility of perhaps less than 1%.

A published data base exists for the tensile behavior of 20% CW 316 stainless steel irradiated in E8R-II.[4,5] In addition, a limited number of fracture toughness measurements have also become available.[6,7] Accordingly, it now is possible to test relationships which attempt to connect fracture and tensile properties. In this report, a comparison of this nature is made and it demonstrates that a model developed by Krafft provides a satisfactory correlation when the appropriate input parameters are used.

5.2 Results

In a previous application[3] of the models by Hahn and Rosenfield[8] and by Krafft[9,10] to HFIR-irradiated 20% CW 316 stainless steel,[11] it was concluded that the Krafft model gives satisfactory results, whereas the Hahn-Rosenfield model predicts values of toughness which are too low by a factor of two. However, this conclusion was based solely on a comparison with the measured fracture toughness for unirradiated material.

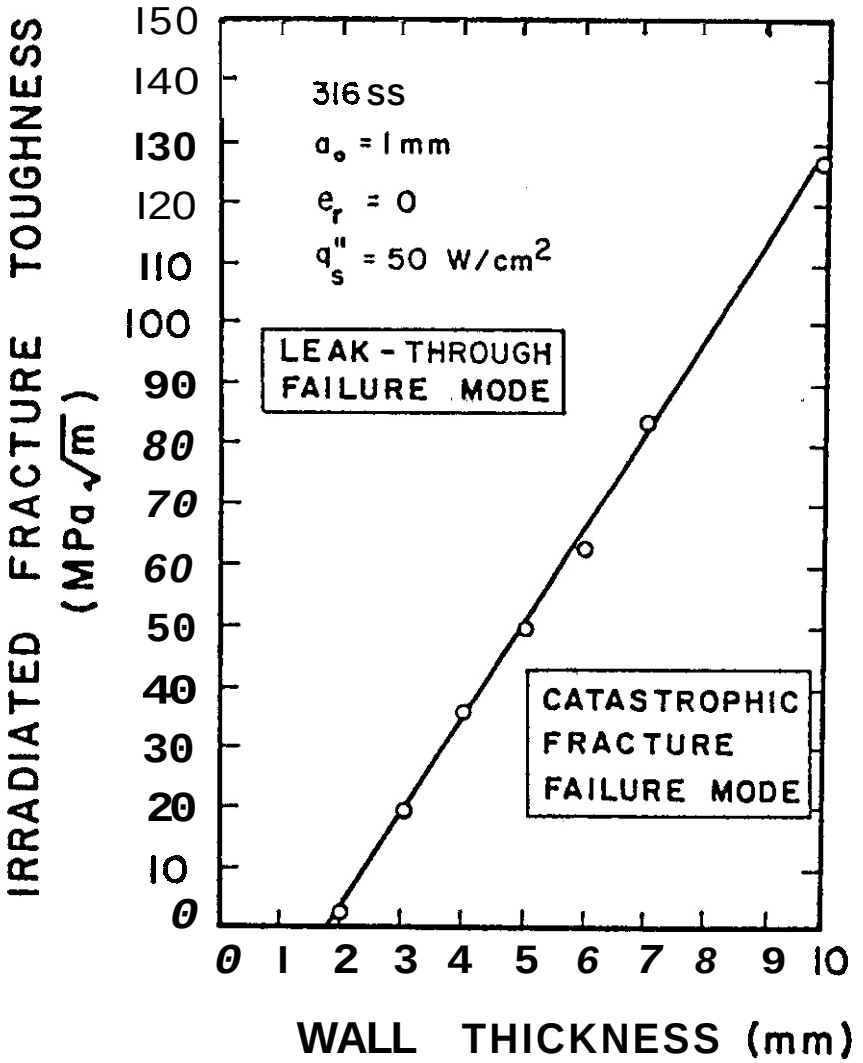

FIGURE 2. Failure Mode Map. The locus of points represents a combination of wall thickness and irradiated fracture toughness such that a leak-through failure mode is as equally probable as a catastrophic fracture failure mode.

In the meantime, several experimental investigations have been made on the fracture toughness of irradiated 20% CW 316 by Huang and coworkers. Huang and Fish[6] performed tensile tests at 593°C on notched and unnotched specimens made from duct material irradiated at 375-415°C in EBR-II to a fluence of 7.8 x 10^{22} n/cm^2 (E > 0.1 MeV). Based on a J-integral analysis of the load-displacement curves from two notched specimens, they obtained fracture toughness values between 57.2 and 67.7 MPa $\sqrt{m}$.

Huang and Wire[7] measured toughness on thin fracture toughness specimens fabricated from EBR-II duct material irradiated to fluences of 11.0 to 11.3 x 10^{22} n/cm^2 (E > 0.1 MeV) and temperatures ranging from 377 to 400°C. The test temperatures were 282, 477, 538 and 649°C. They showed that the Hahn-Rosenfield model could predict toughness of unirradiated material but not for irradiated material.

These two sets of data provide an excellent opportunity to further test the fracture toughness correlation of Krafft[9] as modified by Schwalbe.[10] This correlation is given by

$$K_{Ic} = \frac{\sigma_Y}{(1-2\nu)} \left\{ \pi (1+n) d^* \, (\epsilon_f E / \sigma_Y)^{1+n} \right\}^{1/2} \qquad (1)$$

where:

σ_Y = yield strength
ϵ_f = true fracture strain
E = Young's modulus
ν = Poisson's ratio
n = strain hardening exponent
d* = size of the fracture process zone or dimple diameter

The process zone size d* which determines the dimple size or spacing is not usually measured in tensile tests. For ductile failure by void growth and

coalescence, however, the dimple size is on the order of the average distance between inclusions, particularly between grain boundary precipitates or grain boundary carbides. It is therefore a reasonable assumption to set d^* equal to the grain size. For the present study, a lower limit on d^* of 30 μm and an upper limit of 50 μm was selected based on the measured range of grain sizes in the ducts from which the specimens were made. If the plastic stress-strain law is assumed to be described by the equation

$$\varepsilon/\varepsilon_o = (\sigma/\sigma_o)^{-n} \tag{2}$$

where ε_o and σ_o are two arbitrary reference values of the unaxial strain and stress, respectively, the strain-hardening exponent n can be obtained from the relationship

$$n = \ln(\sigma_u/\sigma_Y) \;/\; \ln(E\,\varepsilon_u/\sigma_Y) \tag{3}$$

where σ_u and ε_u are the ultimate stress and uniform strain.

Although Schwalbe[10] suggests that ε_f in Eq. (1) should be the true fracture strain or the total elongation, it is more in accordance with the spirit of the Krafft model to take for ε_f the uniform elongation as determined from smooth tensile specimens. This is because the model treats the material between deformation-produced voids as miniature tensile specimens and postulates that crack propagation starts when plastic instability is first reached.

Using the tensile data for duct material listed in Table 1 the fracture toughness values were predicted using the above correlations. Note that the two values given for K_{Ic} in the last two columns of Table 1 correspond to the lower and upper values chosen for d^*, respectively. Some entries in Table 1 are designated by a star, and they represent tensile tests carried out at a temperature sufficiently high that failure is expected to be intergranular. For these cases, the correlation in Eq. (1) is not expected to be applicable.

TABLE 1

TENSILE PROPERTIES AND COMPUTED VALUES FOR THE FRACTURE TOUGHNESS OF 20% CW 316 DUCT MATERIAL IRRADIATED TO 10 x 10^{22} n/cm^2 (E > 0.1 MeV)

Specimen	T_t (°C)	σ_y (MPa)	σ_u (MPa)	ε_u (%)	K_{Ic} (MPa $\sqrt{m}$)†	
M1D1	20	793	1121	13.6	147.8	190.8
M1D2	232	859	925	2.7	74.1	95.7
M2D1	379	787	838	1.9	58.2	75.2
M2D2	491	699	747	1.4	57.2	73.8
M3D1	232	894	949	2.2	70.5	91.0
M4D1	538	716	760	0.9	67.2	86.7
M4D2*	649	501	527	1.3	45.8	59.1
M5D1	232	880	957	2.6	75.3	97.2
M5D2	379	782	867	1.1	58.4	75.4
M6D1	538	673	688	0.6	51.1	65.9
M6D2*	649	524	545	0.9	46.5	60.0
M1I1	20	749	870	12.4	121.8	157.3
M1I2	232	707	778	5.6	78.9	101.9
M2I1	452	731	829	4.4	77.6	100.2
M2I2	563	621	659	1.4	48.5	62.6
M3I1	232	834	938	7.7	97.7	126.1
M3I2	427	724	801	6.3	86.0	111.0
M4I1	538	612	652	2.1	51.5	66.4
M4I2*	649	414	448	1.6	42.3	54.6
M5I1	232	832	921	6.8	89.8	116.0
M5I2	452	728	775	2.0	56.1	72.4
M6I1	538	633	681	4.2	67.0	86.5
M6I2*	649	448	525	3.2	59.3	76.5

T_t = test temperature

† The upper and lower limits of K_{Ic} are obtained assuming d* = 30 and 50 μm respectively.

* Possibly intergranular failure.

Figure 3 shows the computed values for K_{Ic} of duct material as a function of the test temperature assuming d^* is 30 μm. It is seen that the predicted fracture toughness decreases with the test temperature. Some of the values at 650°C are suspect for the reason mentioned above. It appears, however, that at least some of the tests carried out at this temperature did result in transgranular or ductile failure as indicated by their relatively high toughness value (> 50 MPa $\sqrt{m}$).

The values of fracture toughness measured by Huang and coworkers are also shown in Figure 3. When compared to the computed values it appears that the lower estimate based on $d^* = 30$ μm compares favorably while the upper estimate with $d^* = 50$ μm seems to be too large.

Huang and Fish also determined in their experiment the tensile properties in addition to the fracture toughness. Accordingly, the correlation can be tested to see whether it reproduces the measured value. The reported yield strength was $\sigma_y = 530.8$ MPa, and the strain hardening exponent was $n = 0.035$. The true strain at failure was estimated from the reduction in area to be $\varepsilon_f = 0.3$. If we assume again that d^* is between 30 μm and 50 μm, Eq. (1) gives values for K_{Ic} ranging from 136 to 176 MPa $\sqrt{m}$. Clearly, these values are too large. The apparent failure of the Krafft model for these input values demonstrates the point made above, namely that ε_f should be set equal to the uniform strain ε_u rather than the total elongation for unnotched soecimens.

The uniform strain of irradiated 20% CW 316 duct material at 593°C was reported by Huang and Fish to be about 0.05. With this value chosen for ε_f, the predicted fracture toughness is between 54 MPa $\sqrt{m}$ and 69 MPa $\sqrt{m}$, which compares very favorably with the measured range of 57.2 to 67.7 MPa $\sqrt{m}$.

Since the data in Table 1 are rather limited, it was decided to attempt a similar correlation using uniaxial tensile data from irradiated tubinq.(5) The tensile data are shown in Table 2 and the predicted values of fracture

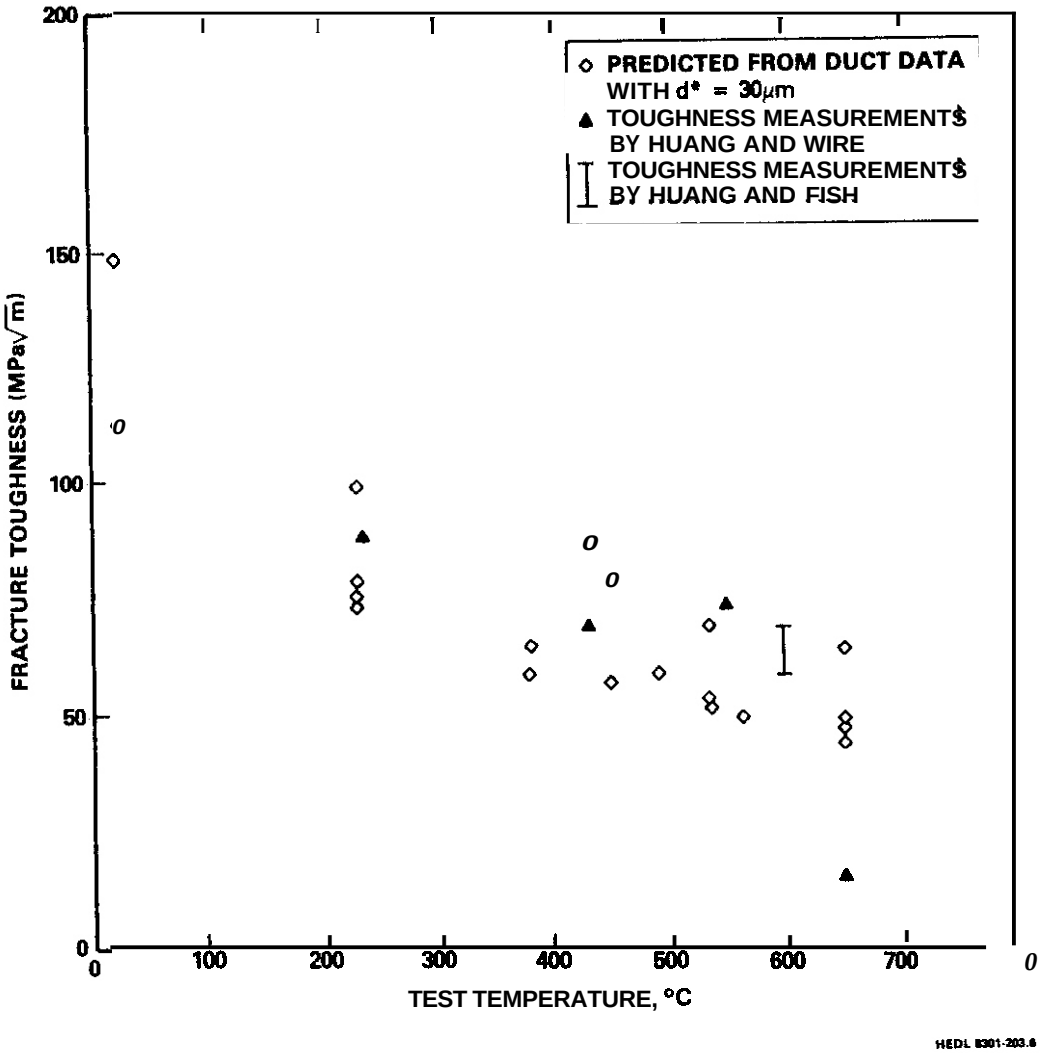

FIGURE 3. Comparison of Measurements and Estimates of the Fracture Toughness for Irradiated 20% CW 316 Stainless Steel, Assuming d*=30 μm and Using Duct Tensile Properties.

TABLE 2

TENSILE PROPERTIES AND COMPUTED VALUES FOR THE FRACTURE TOUGHNESS OF 20% CW 316 TUBING IRRADIATED TO FLUENCES BETWEEN 6.1 AND 13.0 x 10^{22} n/cm^2 (E >0.1 MeV)

Specimen	T_t (°C)	σ_Y (MPa)	σ_u (MPa)	ε_u (%)	K_{Ic} (MPa $\sqrt{m}$)+	
33G2	230	727	925	5.3	93.6	120.9
3363	370	793	887	3.1	63.6	82.1
3366	510	605	721	3.4	68.9	88.9
33H7	370	587	854	3.6	80.6	104.1
34H1	450	587	649	9.7	87.0	112.3
34H2	450	525	621	8.7	85.2	110.0
34H3	20	690	915	13.7	121.5	156.9
35F2*	650	317	348	3.9	39.2	50.6
35H4	230	499	669	16.3	111.8	144.3
3551	540	410	492	13.0	85.9	110.9
3752	577	341	441	13.2	85.1	109.9
3753	595	321	423	11.6	74.2	95.8
41C1	579	480	524	5.0	70.9	91.6
41C3	480	607	690	7.3	81.0	104.6
41C4	480	560	656	6.7	76.1	98.2
4161	20	749	912	17.3	135.9	175.4
4162	230	654	778	9.0	94.9	122.5
4163	468	618	710	7.2	85.9	110.9
45B1*	649	294	416	10.5	85.8	110.8
45B2*	649	276	376	9.5	73.2	94.5
4562	230	385	636	13.7	114.6	148.0
41D2	471	553	652	8.0	84.5	109.0
41D4	582	454	505	6.1	66.9	86.3
45D2*	646	276	314	5.5	45.4	58.6
45D4*	757	174	185	0.7	23.9	30.9

T_t = test temperature

t The upper and lower limits of K_{Ic} are obtained assuming d* = 30 and 50 μm respectively.

* Possibly intergranular failure.

toughness are shown in Figure 4. While there is some overlap in the predictions the tubing-based predictions tend to lie above the duct-based predictions. This may be due to the possibly incorrect assumption that the process zone and grain size of the tubing are identical to that of the ducts. The specimen constraints necessary to grip the tubing specimen also tend to yield different ductilities than observed in duct specimens and this may also impact the results. These possibilites will be investigated further.

There are additional considerations which have not yet been factored into the correlation. These are the possibility of strain rate effects and irradiation temperature effects. Note that the toughness data were derived from material irradiated in the range of 375-415°C. The tensile data in Table 1 span a larger range, 379-452°C and strain rates from 4×10^{-5} to 4×10^{-3} sec^{-1}. There is a sensitivity in the yield strength not only to test temperature but also irradiation temperature.[4,5] The radiation-induced hardening that occurs below 500°C has a temperature sensitivity that arises from the temperature dependence of microstructural components.[12,13] This sensitivity will probably influence the temperature sensitivity of fracture toughness if the correlation addressed in this study is valid.

5.3 Conclusions

It appears that the Krafft correlation in Eq. (1) may provide a satisfactory estimate of the plane strain fracture toughness for irradiated material which fails in the ductile mode. However, when using Eq. (1), the fracture strain ε_f should be set equal to the uniform strain of smooth tensile specimens and not equal to the total strain at failure or the fracture strain estimated from the reduction in area. To confirm this conclusion some experimental determination must be made of the dimple size d^* after tensile testing. This will be more conclusive then relying on an estimate based merely on the grain size.

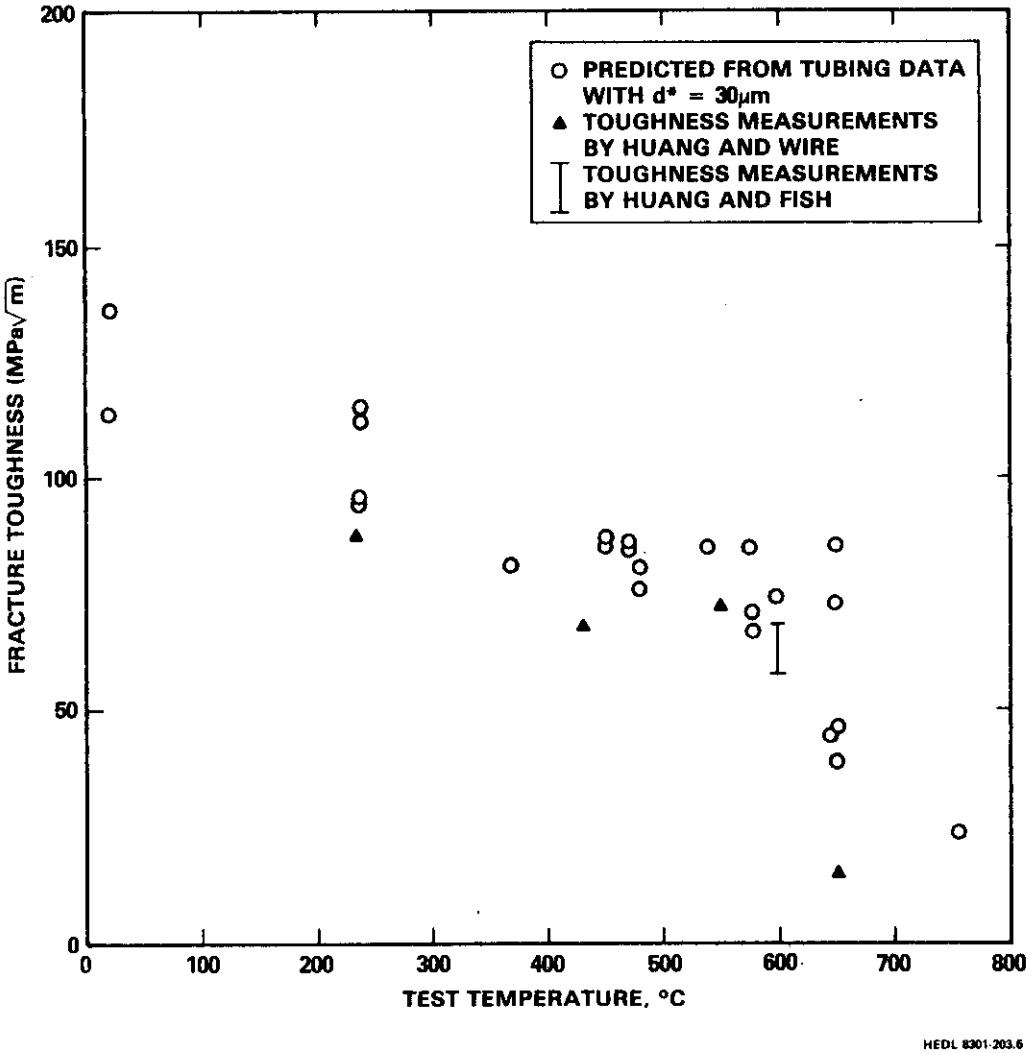

FIGURE 4. Comparison of Measurements and Estimates of the Fracture Toughness for Irradiated 20% CW 316 Stainless Steel, Assuming d*=30 μm and Using Tubing Tensile Properties.

6.0 References

1. R. D. Watson, "The Impact of Inelastic Deformation, Radiation Effects, and Fatique Damage on Fusion Reactor First Wall Lifetime," Doctoral Thesis, December 1981; report UWFDM-460.

2. G. R. Odette and D. Frey, J. Nucl. Mater. 85 & 86, (1979), 817.

3. W. G. Wolfer and R. H. Jones, J. Nucl. Mater. 103 & 104, (1981), 1305.

4. R. L. Fish, N. S. Cannon and G L. Wire, "Tensile Property Correlations for Highly Irradiated 20% Cold Worked Type 316 Stainless Steel, Effects of Radiation on Structural Materials, ASTM STP 683, J. A. Sprague and D. Kramer, Eds., American Society for Testing and Materials, 1979, pp 450-465.

5. M. L. Hamilton, N. S. Cannon and G. D. Johnson, "Mechanical Properties of Highly Irradiated 20% Cold Worked Type 316 Stainless Steel." Effects of Radiation on Materials: Eleventh Conference, ASTM STP 782; H. R. Brager and J. S. Perrin, Eds., American Society for Testing and Materials, 1982, pp 636-647.

6. F. H. Huang and R. L. Fish, "Effect of Fast Neutron Irradiation on the Fracture Behavior of Stainless Steel," ibid, ASTM STP 782, 1982, 701.

7. F. H. Huang and G. L. Wire, "Irradiation Effects on the Fracture Toughness of 20% Cold Worked Type 316 Stainless Steel," HEDL-SA-2669, to be published in Proceedings of International Conference on Dimensional Stability and Mechanical Behavior of Irradiated Metals and Alloys, April 11-13, 1983, Brighton, England.

8. G. T. Hahn and A. R. Rosenfield, "Sources of Fracture Toughness: The Relation Between K_{Ic} and The Ordinary Tensile Properties of Metals," ASTM STP 432 (1968), pp. 5-12.

9. J. M. Krafft, Applied Mater. Research 3, (1964), 88.

10. K. H. Schwalbe and W. Backfisch, "Correlations Between Fracture Toughness, Tensile Properties, Fracture Morphology, and Microstructure of High-Strength Steels," Fracture 1977, Vol. 2, ICF4, Waterloo (Canada), June 1977, pp. 77-78.

11. M. L. Grossbeck and P. J. Maziasz, J. Nucl. Mater. 85 & 86, (1979), 883.

12. G. D. Johnson, F. A. Garner, H. R. Brager and R. L. Fish, "A Microstructural Interpretation of the Fluence and Temperature Dependence of the Mechanical Properties of Irradiated AISI 316," Effects of Radiation on Materials: Tenth Conference, ASTM STP 725, D. Kramer, H. R. Brager and J. S. Perrin, Eds., American Society for Testing and Materials, 1981, pp 393-412.

13. F. A. Garner, M. L. Hamilton, N. F. Panayotou and G. D. Johnson, "The Microstructural Origins of Yield Strength Changes in AISI 316 During Fission or Fusion Irradiation," J. Nucl. Mater. 103-104, (1981) pp. 803-808.

7.0 Future Work

The analysis will continue concentrating on effects of irradiation temperature and strain rate and the experimental determination of d*. An attempt will be made to develop ductility-toughness correlations which are applicable to situations involving flow localization.

THE DEPENDENCE ON DISPLACEMENT RATE OF RADIATION-INDUCED CHANGES IN TENSILE PROPERTIES OF AISI 304

H. R. Brager, L. D. Blackburn and F. A. Garner (HEDL)

1.0 OBJECTIVE

The object of this effort is to provide mechanical property measurements and microstructural evidence to guide the development of fission-fusion correlations that incorporate displacement rate and other important variables.

2.0 SUMMARY

The tensile properties of AISI 304 are sensitive to displacement rate at temperatures around 400°C, at least in the transient regime of property change. Microstructural data obtained in this study as well as from other published data indicate that displacement rate variations can affect the saturation level of yield strength. The dependence of strength on displacement rate is shown to arise from the sensitivity of microstructural components to this variable.

3.0 PROGRAM

Title: Irradiation Effects Analysis
Principal Investigator: D. G. Doran
Affiliation: Westinghouse Hanford Company

4.0 RELEVANT DAFS PROGRAM PLAN TASK/SUBTASK

II.C.14 Models of Flow and Fracture Under Irradiation
II.C.17 Microstructural Characterization

5.0 ACCOMPLISHMENTS AND STATUS

5.1 Introduction

The successful development of fission-fusion correlations for mechanical properties requires that all aspects of the differences between fission and fusion environments be addressed. In addition to differences in neutron spectra, there will also be differences in stress, temperature and displacement rate. In practice, it is usually impossible to study the impact of spectrum without simultaneously spanning differences in temperature and/or displacement rate.

In general, many of the existing fission-derived correlations have not separated the individual influence of each important variable. Displacement rate variations, in particular, are ignored in most breeder correlations and the dependence on this variable is incorporated into the temperature dependence. For instance, the yield strength data shown in Figure 1 span displacement rates differing by roughly a factor of two, but the current correlation describing these data employs only temperature and neutron fluence as variables.[1] In this report, tensile properties are shown to exhibit a dependence on displacement rate.

The data required to confidently assess the consequences of variations in displacement rate should cover the fluence range encompassing both the transient and saturation regimes of property changes and should also span a suitably large range of displacement rates. Since the data available are usually insufficient to meet these criteria, another approach is to seek guidance from the dependence of microstructure on displacement rate and use this guidance to help extrapolate beyond the range of available data.

5.2 Experimental Materials and Procedures

The material chosen for the microscopy portion of this experiment was annealed 304 stainless steel, which had been irradiated in Row 4 of EBR-II as

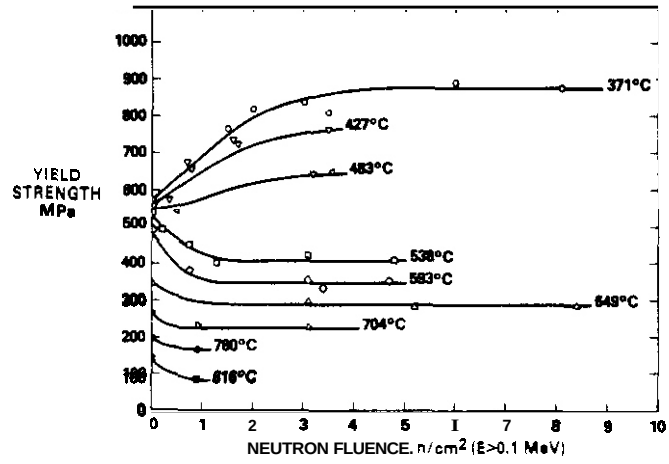

FIGURE 1. Yield Strength of 20% CW Type 316 Stainless Steel After EBR-II Irradiation.(1) The tensile tests were conducted at the irradiation temperature.

part of an earlier breeder reactor experimental program. The temperatures ranged from 371°C to 426°C. Cylindrical tensile specimens were machined from 50.8-mm plate (NE M 5-23T) to have a length of 47.6 mm and shoulder diameter of 6.4 mm. The gauge section was 28.6 mm in length and 3.2 mm in diameter. After machining, the specimens were annealed at 1063°C for 2 hours.

The tensile specimens were irradiated in sodium-filled capsules at six different elevations with respect to the reactor centerline. This provided a range of mean neutron energies from 0.75 MeV to 0.17 MeV and displacement rates varying from 7.9 X 10^{-7} to 0.6 x 10^{-7} dpa/sec. Table 1 lists the irradiation conditions for this experiment.

Tensile tests were conducted at a strain rate of 3.5 x 10^{-5} sec^{-1} with the specimens maintained at 385 ± 1°C. For the present study, the grip portion of two of the specimens was chosen for microscopy examination to minimize the effects of post-irradiation strain during tensile testing. Standard electron microscopy procedures were employed in the examination. Immersion density measurements were also made on these specimens. The selection criteria for the microscopy specimens were minimum difference in temperature, maximum difference in yield strength change, maximum difference in displacement rate but comparable total displacement level.

TABLE 1

IRRADIATION CONDITIONS FOR ANNEALED AISI 304 IRRADIATED IN EBR-II*

Z-Coord cm	$\bar{E}$ MeV	Temp °C	Total Fluence, 10^{26} n/m^2				Fast Fluence (E>0.1 MeV) 10^{26} n/m^2				Total Displacements, dpa			
			B-257	B-258	B-259	B-260	B-257	B-258	B-259	B-260	B-257	B-258	B-259	B-260
-6.5	0.75	392	0.79	1.9	3.4	-	0.63	1.5	2.7	-	3.1+	7.5	13.5	-
-23.0	0.53	376	0.51	1.2	2.2	-	0.32	0.8	1.4	-	1.5	3.7	6.6	-
-35.8	0.29	373	0.34	0.81	1.5	-	0.18	0.43	0.78	-	0.69	1.7	3.0	-
-50.4	0.19	371	0.20	0.49	0.84	1.7	0.09	0.21	0.39	0.74	0.31	0.75	1.4	2.6**
-55.0	0.17	371	-		-	1.4	-	-	-	0.55	-	-	-	2.0
+37.8	0.29	426	-	-	1.3	-	-	-	0.66	-	-	-	2.5	-
Irradiation Time (10^6 s)			3.94	9.21	17.0	33.8	3.94	9.21	17.0	33.8	3.94	9.21	17.0	33.8

*The various irradiation capsules are designated by B-257, B-258, etc.
**These two specimens were chosen for microscopy.

5.3 Results

Figure 2 shows the tensile measurements obtained for these specimens. If one assumes that the use of displacements per atom as an exposure parameter adequately correlates spectral differences, there is clearly an effect of the displacement rate on the duration of the transient regime of the yield and ultimate strengths, as well as in the uniform and total elongations. The saturation level of these properties has not been reached at all displacement rates and no conclusion can be drawn at this point concerning the sensitivity of the saturation levels to displacement rate.

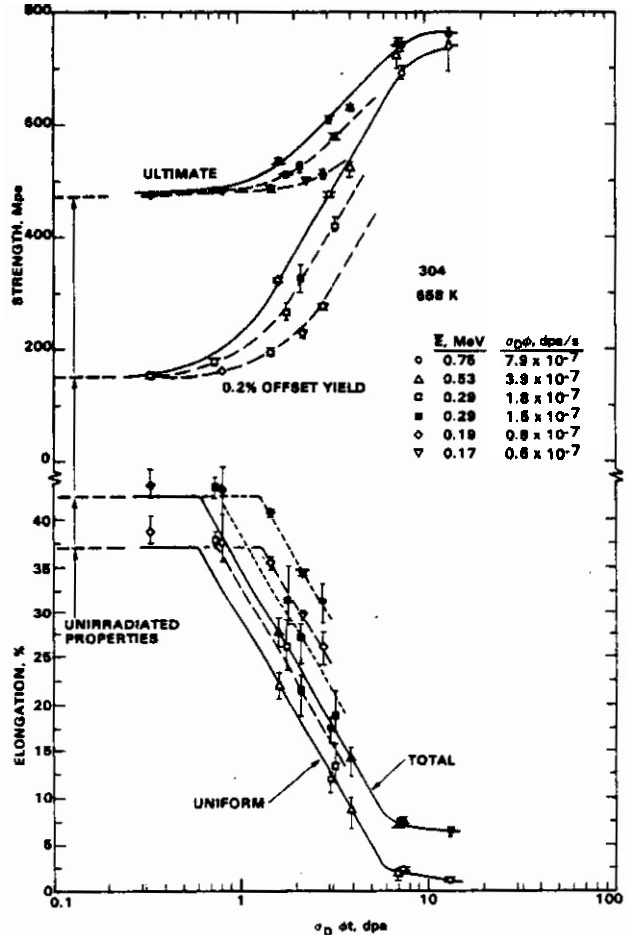

FIGURE 2. Dependence of Tensile Properties of Annealed AISI 304 on Displacement Rate and Total Damage. There are also some small differences in irradiation temperature (see Table 1). Filled in symbols denote the ultimate strength and total elongation; open symbols correspond to 0.2% yield strength and uniform elongation, respectively.

Of the two specimens chosen for microscopy, one was irradiated at 392°C to 3.1 dpa at 7.9 x 10^{-7} dpa/sec, and the other irradiated at 371°C to 2.6 dpa at 0.8 x 10^{-7} dpa/sec. Immersion density measurements of these specimens indicated density changes of -0.17% and -0.39%, respectively. These values are just on the edge of the accuracy of the immersion density technique and are not thought to contain any significant information.

Differences in microstructure were observed in the specimens irradiated at high and low displacement rates, as shown in Table 2 and Figure 3. At the higher displacement rate, the densities of voids, Frank loops and dislocations were higher. Careful examination showed that there was no resolvable precipitation in either specimen.

5.4 Discussion

Before attempting to extrapolate the available tensile data beyond the existing data range, it is important to show that the observed changes can be correlated to the microstructural components causing the changes. This has been successfully accomplished previously using 20% cold-worked AISI 316, but without investigating the influence of displacement rate.[2] Such an effort can only be directed toward the yield strength change, as only this property is directly sensitive to the radiation-induced microstructure. The other tensile properties shown in Figure 2 involve both radiation and deformation-produced microstructure, with substantial deformation-induced alteration of the former.

The correlation of tensile properties with microstructure is simpler in several respects in the case of AISI 304 at low fluence compared to the previous study on AISI 316. First, the specimens in this study were annealed prior to irradiation and therefore possessed little microstructure to cause hardening. In effect, the experimental signal-to-noise ratio was maximized compared to that obtainable in cold-worked material. Second, all hardening contributions are positive since there are few preexisting dislocations which can be reduced in density by recombination.[2] Third,

TABLE 2

SUMMARY OF MICROSTRUCTURAL DATA

	High-Rate Specimen	Low-Rate Specimen
Total Displacements (dpa)	31	2.6
Displacement Rate (dpa/sec)	7.9×10^{-7}	0.8×10^{-7}
Irradiation Temperature (°C)	392	371
Test Temperature (°C)	385 ± 15	385 ± 15
Mean Void Diameter (nm)	5.5	5.0
Void Density (cm^{-3})	4×10^{15}	7×10^{14}
Void Volume (%)	0.03	0.005
Frank Loop Mean Diameter (nm)	17.5	16.0
Frank Loop Density (cm^{-3})	1.45×10^{16}	7.0×10^{15}
Network Dislocation Density (cm^{-2})	8×10^{9}	7×10^{8}

the lack of precipitation simplifies the evaluation since precipitates serve not only as hardening agents but also soften the alloy matrix by removing solute-strengthening elements.

As shown in Reference 2, the yield strength changes from microstructural components can be predicted using the following equation, assuming that the Frank loops are large enough to be treated only as additional dislocation line length instead of as short-range obstacles.

$$\Delta\sigma = \sqrt{3}\, G\, b\, [\alpha \sqrt{\rho_d + \rho_{FL}} + \sqrt{\rho_V d_V} / \beta_V]$$

where $\Delta\sigma$ is the yield strength change, G is the shear modulus, b is the Burgers vector, and ρ_d and ρ_{FL} are the dislocation line lengths per unit volume for the network and Frank loop components, respectively. The voids have density ρ_V and mean diameter d_V. The coefficients α and β_V have values

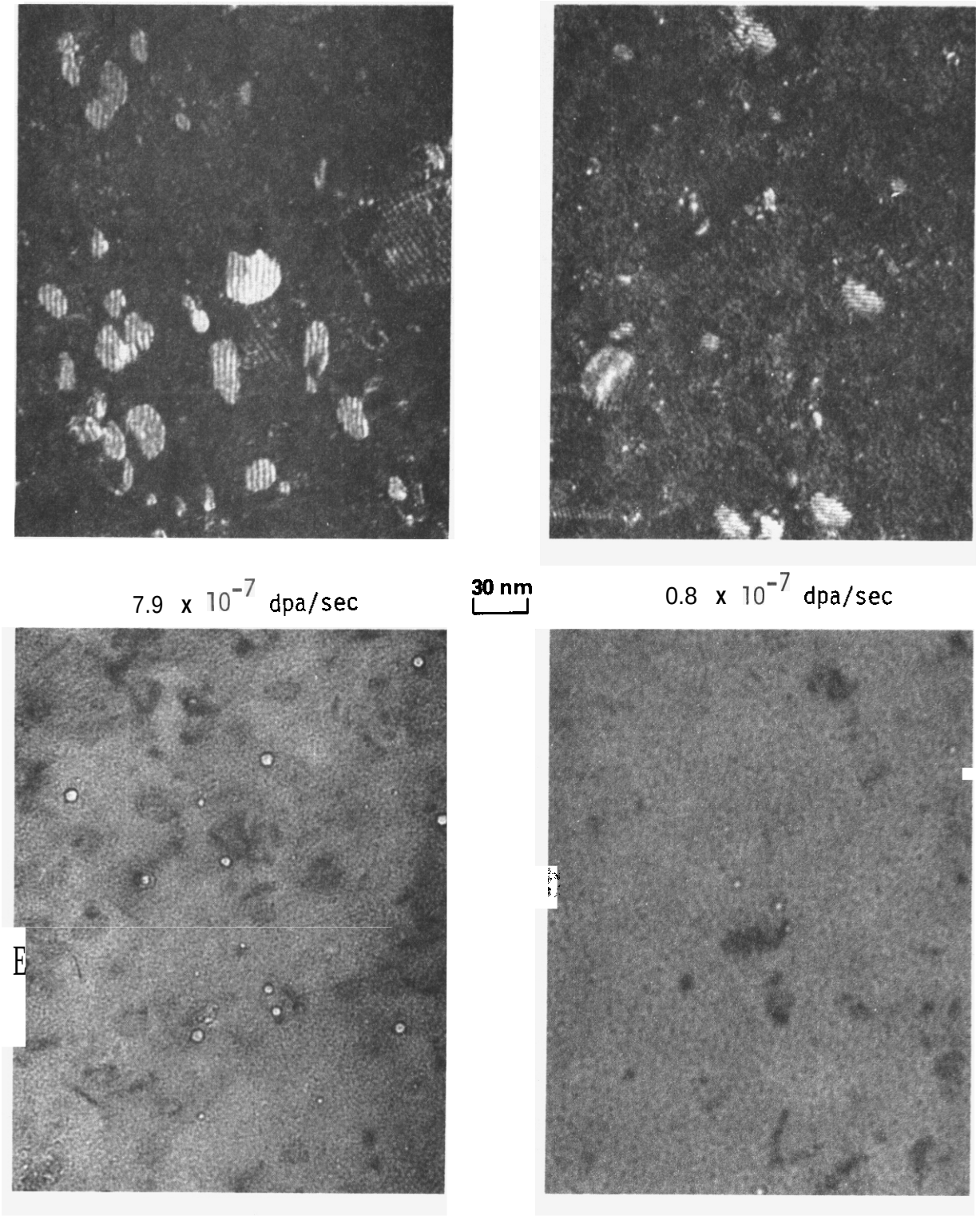

FIGURE 3. Void and Frank Loops Observed in AISI 304 Irradiated at ~400°C and ~3 dpa at 7.9 x 10^{-7} and 0.8 x 10^{-7} dpa/sec.

established previously at 0.2 and 1.0 respectively.[2] The shear modulus at 375°C is 6.7 x 10^{10} Pa[3] and the [110] Burgers vector for austenitic stainless steel is 2.5 x 10^{-8} cm.

Assuming that the areas measured were representative of the specimen as a whole, the predicted yield strength change was 308 MPa compared to the measured value of 330 MPa for the high rate specimen, and 165 MPa compared to the measured 130 MPa for the low rate specimen. This level of agreement is a confirmation of the relationship between microstructure and yield strength.

Since the temperature dependence of the saturation yield strength has previously been shown to arise from the temperature dependence of microstructure,[2] one would anticipate the saturation level to be likewise sensitive to the dependence of microstructure on displacement rate. Temperature and displacement rate are known to be coupled variables in that a drop in temperature has the same effect on point defect concentrations and nucleation rates as an increase in displacement rate. Therefore, one would expect to see a dependence on displacement rate in both the transient and saturation regimes, even though only the former has been demonstrated in this experiment. A sensitivity of both transient and saturation stages of yield strength has been demonstrated in the Phenix and Rapsodie fast reactors[4,5] as shown in Figures 4 and 5. Phenix has a displacement rate that is about a factor of two higher than that of Rapsodie.

Figure 2 shows, however, that a factor of two in displacement rate does not always lead to a change in the yield strength. Note that no change in strength is observed between irradiations conducted at 7.9 x 10^{-7} (392°C) and 3.9 x 10^{-7} dpa/sec (371°C). This may partially reflect the 21°C temperature difference between the two capsules but it may also reflect the relative temperature independence of microstructure at low temperatures. Ignoring differences in temperature for the moment, the data of Figure 2 are replotted in Figure 6 as a function of displacement rate and total exposure.

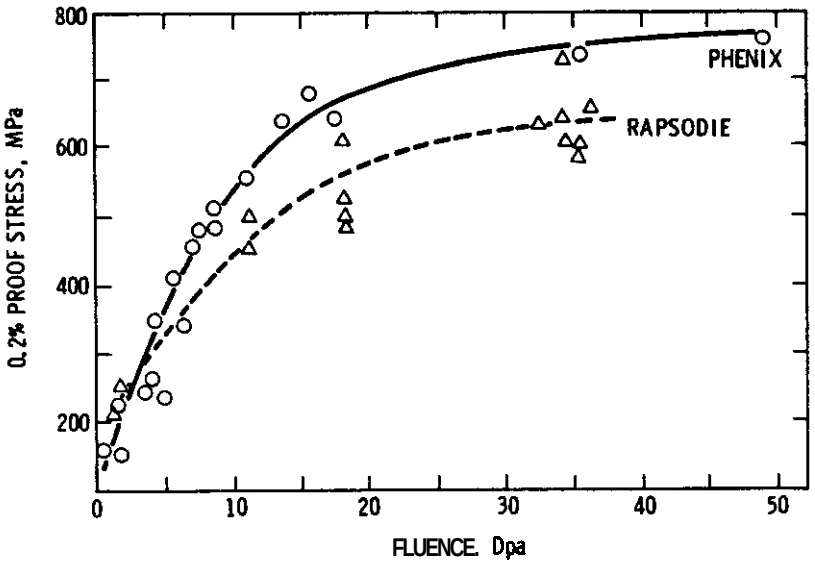

FIGURE 4. Comparison of the Yield Strength of SA 316 Irradiated in Phenix and Rapsodie.(4,5)

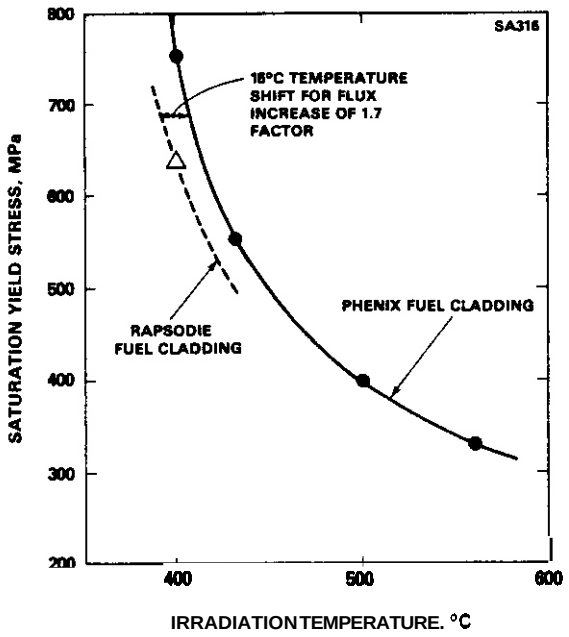

FIGURE 5. Temperature Shift in Saturation Yield Strength of the Same Heat of SA 316 Arising from Differences in Displacement Rate in Phenix and Rapsodie at ∿400°C.(4,5)

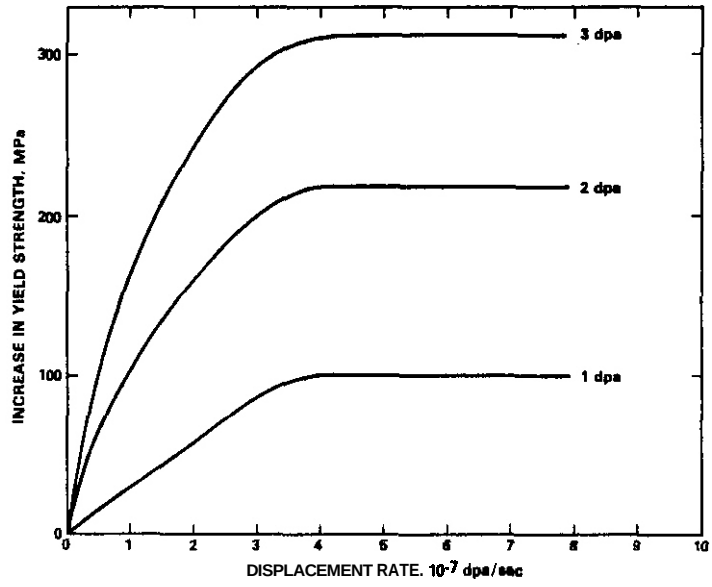

FIGURE 6. The Dependence of Yield Strength in Annealed AISI 304 on Displacement Rate After Irradiation in E8R-II at ~400°C.

The shoulders in these curves divide regions of temperature dependence and temperature independence as shown schematically in Figure 7. A similar shoulder is known to exist in the temperature dependence of the various microstructural components,[6] particularly voids and Frank loops. Differences in displacement rate are expected to cause the microstructural density curves to shift in temperature.[6] Depending on the irradiation conditions, a shift in displacement rate may or may not lead to a change in microstructural densities.

Since the voids are an important part of the total hardening microstructure (~45% in the experiments presented in this report), one might expect a sensitivity of the transient regime to alloy composition since swelling is known to be sensitive to composition.[7] Therefore, one can predict that AISI 316 with its higher nickel content [which inhibits void nucleation[7,8]] will have a longer transient regime than AISI 304.[9] One would also expect variations in tensile strength in different heats of AISI 304. These predictions will be tested in the next reporting period.

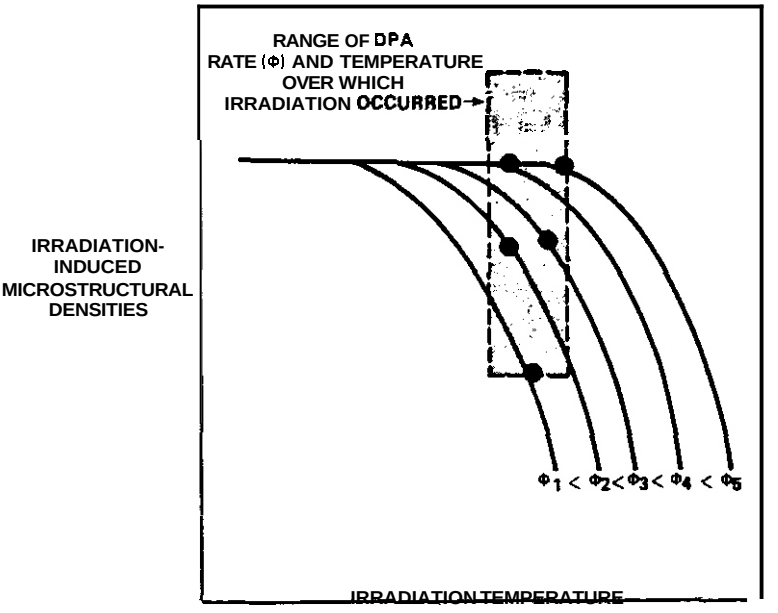

FIGURE 7. Schematic Illustration of the Dependence of Microstructural Densities in This Experiment on Irradiation Temperature and Displacement Rate. The displacement rates increase from left to right.

Additional data and analyses must be collected and analyzed before a quantitative description of a dependence on displacement rate can be introduced into tensile property correlations.

5.5 Conclusions

The tensile properties of AISI 304 are sensitive to displacement rate at temperatures around 400°C, at least in the transient regime of property change. Microstructural data obtained in this study as well as from other published data indicate that displacement rate variations can affect the saturation level of yield strength. The dependence of strength on displacement rate is shown to arise from the sensitivity of microstructural components to this variable.

6.0 REFERENCES

1. R. L. Fish, N. S. Cannon and G. L. Wire, Effects of Radiation on Structural Materials, ASTM STP 693, J. A. Sprague and D. Kramer, Eds., American Society for Testing and Materials, pp. 450-465, 1979.

2. F. A. Garner, M. L. Hamilton, N. F. Panayotou and G. D. Johnson, J. Nucl. Mater. 103 and 104, pp. 803-808, 1981.

3. Proceedings of Symposium on Determination of Elastic Constants, ASTM-STP 29, 1952.

4. G. D. Johnson, F. A. Garner, H. R. Brager and R. L. Fish, Effects of Radiation on Materials: Tenth Conference, ASTM STP 725, D. Kramer, H. R. Brager and J. S. Perrin, Eds., American Society for Testing and Materials, pp. 393-417, 1981.

5. J. M. Dupouy, J. Erler and R. Huillery, Proceedings of the International Conference on Radiation Effects in Breeder Reactor Structural Materials, American Institute of Mining, Metallurgical and Petroleum Engineers, pp. 83-93. 1977.

6. F. A. Garner and J. J. Laidler, "Review of Neutron and Charged Particle Intercorrelation Programs," Proceedings of Workshop on Correlation of Neutron and Charged Particle Damage, CONF-760673, Oak Ridge National Laboratory, Oak Ridge, TN, pp. 177-240, June 8-10, 1976.

7. F. A. Garner, "The Microchemical Evolution of Irradiated Stainless Steels," Proceedings of AIME Symposium on Phase Stability During Irradiation, J. R. Holland, L. K. Mansur and D. I. Potter, Eds., Pittsburg, PA, pp. 165-189, October 5-9, 1980.

8. W. G. Wolfer, F. A. Garner and L. E. Thomas, "On Radiation-Induced Segregation and the Compositional Dependence of Swelling in Fe-Ni-Cr Alloys," Effects of Radiation on Materials: Eleventh Conference, ASTM STP 782, H. R. Brager and J. S. Perrin, Eds., American Society for Testing and Materials, pp. 1023-1041, 1982.

9. F. A. Garner and D. L. Porter, "Factors Influencing the Swelling of 300 Series Stainless Steels," Damage Analysis and Fundamental Studies Quarterly Progress Report, DOE/ER-0046/9, pp. 170-185, 1982.

7.0 FUTURE WORK

Additional microscopy and tensile data on AISI 316 and 304 will be collected from experiments spanning regimes that are both dependent and independent of neutron fluence.

C H A P T E R 5

CORRELATION METHODOLOGY

EXTENSION AND COMPARISON OF VARIOUS EQUATIONS OF STATE FOR GASEOUS AND SOLID HELIUM

B. B. Glasgow and W. G. Wolfer (University of Wisconsin)

1.0 Objective

The intent of this research is to provide an equation of state for helium at all densities encountered in helium-vacancy clusters and helium bubbles. Such an equation is required for the microstructural analysis of materials irradiated in HFIR or in dual-ion facilities.

2.0 Summary

A previously developed equation of state for gaseous helium is further improved so that it can be applied to densities approaching solid densities of helium. Furthermore, quantum corrections and a contribution arising from the attractive part of the interatomic potential are added. The comparison with recently obtained data gives excellent agreement. However, when extrapolated beyond the data range to higher densities and temperatures the results depend strongly on the form of the interatomic potential for small separation distances. A recently proposed potential by Young, McMahon, and Ross gives improved results.

In addition to the improvement of the gaseous EOS for helium, a solid EOS has also been developed. This EOS is based on published results on the ground-state pressure-volume relationship for solid helium at OK and on a quasi-harmonic treatment of solid helium at finite temperatures. Our results are compared with a similar development carried out at Julich, Germany.

3.0 Program

Title: Effects of Radiation and High Heat Flux on the Performance of First Wall Components

Principal Investigator: W. G. Wolfer
Affiliation: University of Wisconsin-Madison

4.0 Relevant DAFS Program Plan Task/Subtask

Task II.C.2 Effects of Helium on Microstructure
Subtask C Correlation Methodology

5.0 Accomplishment and Status

5.1 Introduction

Helium produced by (n,α) reactions or injected in metals is essentially insoluble. Therefore, it has the natural tendency to precipitate and to form bubbles. The pressure in small bubbles can be extremely large, and a realistic equation of state (EOS) is required to evaluate it. Unfortunately, the experimentally determined EOS for helium does not completely cover the range of temperatures and pressures of interest. This is illustrated in Fig. 1 where the various regions are shown in which experimental data have been obtained. It is seen that only the recent measurements by Mills et al.[2] cover the range of pressures equal to $2\gamma/r$, where γ is the surface energy and r the radius of the bubble. A typical value for γ is $2J/m^2$. However, measurement at elevated temperatures are still lacking. Therefore, it is of interest to develop a theoretical EOS and adjust it if required to match the data. This theoretical correlation will then enable us to extrapolate the EOS beyond the data range with greater confidence.

It has recently become feasible to directly measure the density of helium in small bubbles. In fact, two techniques have been employed for this task: electron energy loss spectroscopy (EELS) and vacuum ultra-violet (VUV) absorption. In both cases, helium is detected by the excitation of the $1\,^1S_0$-$2\,^1P_1$ transition. The energy levels involved in this transition are shifted (by different amounts) with increasing helium density. The shift in the absorption energy can be calibrated with the density, and the pressure can then be computed with a valid EOS.

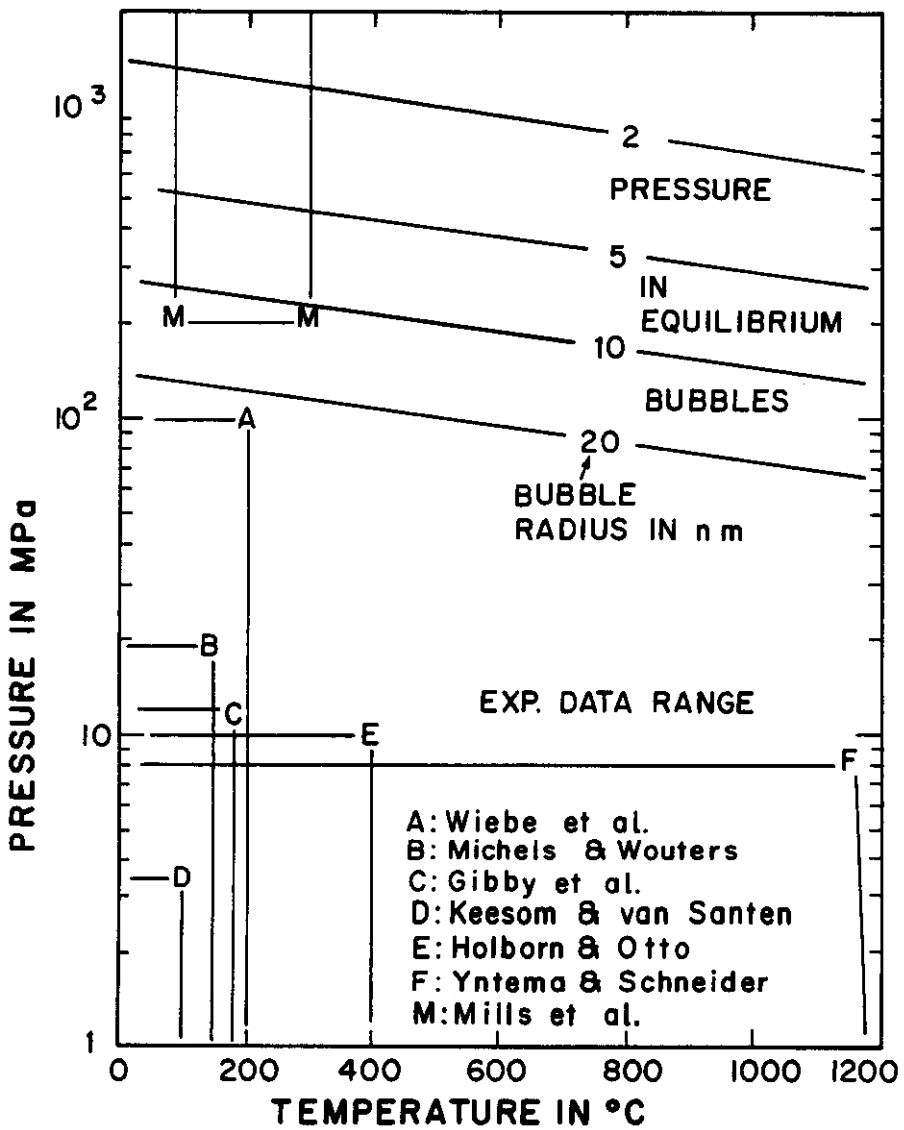

FIGURE 1. Ranges of Temperature and Pressure in Which Experimental Data Exist for the Equation of State (EOS) of Helium (Ref. 1).

Jager et al.[3] have carried out experiments on nickel and aluminum implanted at room temperature with helium to concentrations somewhat below the critical value to produce blistering. The analysis of the measured shift in the absorption peak revealed that the pressure in the helium bubbles was on the order of 50 GPa in the case of nickel, and about 13 GPa in the case of aluminum. Note, that the ratio of the pressure in the bubble to the shear modulus of the host metal is 0.64 and 0.52, respectively.

The ultra-violet absorption measurement of Rife et al.[4] in Al films bombarded at room temperature with 5-keV helium ions yielded a density of 7-14 x 10^{22} cm^{-3} or a helium to vacancy ratio of 1 to 2 in bubbles of about 5 nm in diameter. The measurement by Jager et al.[3] gave a helium density of 14 x 10^{22} cm^{-3}. It is most likely that at these densities helium is in the solid form at room temperature. In fact, there exists at least one singular data point which confirms this. Besson and Pinceaux[5] have solidifed helium at room temperature in a diamond anvil cell, and observed the actual melting process as well as grain boundaries in the solid phase. The pressure at melting and room temperature (297 K) was determined to be 11.5 ± 0.2 GPa, and the density at melting was estimated to be about 15 x 10^{22} cm^{-3}.

In the electron microscopy analysis of helium-implanted molybdenum Evans et al.[6] have identified helium platelets. The formation of non-spherical precipitates is again an indication that these platelets consist of solid helium.

In the following sections we extend a previously developed EOS for gaseous helium using two different interatomic potentials. Furthermore, two terms are added, one due to quantum corrections and the other one due to the attractive part of the interatomic potential. Although both terms are small, their inclusion improves the agreement between the theoretical EOS and the empirical one. Next, we present an equation of state for solid helium and compare it with a similar development due to Trinkaus.[7]

5.2 The Gaseous EOS According to Perturbation Theory

One of the most successful approaches to model a liquid or a dense gas is by the so-called perturbation theory.[8,9] Here, the fluid is modeled as a system of rigid spheres whose diameter is chosen appropriately. The choice is made such that corrections which arise from the finite steepness of the repulsive part of the interatomic potential are minimal, i.e. of second order.

As a result of this choice, the effective diameter d of the atoms in the fluid depends both on the temperature as well as on the density. Once this diameter has been determined, the EOS is determined, apart from minor corrections, by the hard-sphere EOS of Carnahan and Starling[10]

$$z_{HS} = (1 + y + y^2 - y^3)/(1 - y)^3 \tag{1}$$

where $z = pV/NkT$ is the compressibility factor and

$$y = \frac{\pi}{6} d^3 N/V \tag{2}$$

is the "soft-sphere" packing fraction of N atoms in a volume V.

According to Verlet and Weiss[11] the effective diameter is determined by the implicit equation

$$d = d_B(T)[1 + \delta(T)\cdot\psi(y)] \tag{3}$$

where $\psi(y)$ is determined by

$$\begin{aligned} 2\psi\{(2 + 7y)\sigma_0 - (1 - y)\sigma_1 - \tfrac{3}{2} y/(1 - y)^2\} \\ = (1 + 11\, y)\sigma_1 - (1 - y)\sigma_2 + 3yf/(1 - y)^3 \end{aligned} \tag{4}$$

with

$$f = -7.5 + y - 17.3595\, y^2 - 6.04\, y^3 \tag{5}$$

$$\sigma_0 = (1 - y/2)/(1 - y)^3 \tag{6}$$

$$\sigma_1 = (2 - 7.5y + 0.5y^2 - 5.7865\ y^3 - 1.51\ y^4)/(1 - y)^4 \tag{7}$$

$$\sigma_2 = (2 - 20\ y + 30\ y^2 + 0.17\ y^3 - 26.796\ y^4 + 11.2241\ y^5)/(1 - y)^5 \tag{8}$$

The temperature dependent functions d_B and δ are given by

$$d_B/\sigma = \int_0^{x_m} \{1 - \exp[-(V + \varepsilon)/kT]\}\ dx \tag{9}$$

and

$$(1 + \delta)\ d_B^2/\sigma^2 = 2 \int_0^{x_m} \{1 - \exp[-(V + \varepsilon)/kT]\}\ x\ dx \tag{10}$$

where $V(x)$ is the interatomic potential expressed in terms of a dimensionless distance $x = r/\sigma$, and σ denotes the interatomic distance r for which V is equal to zero. ε represents the depth of the potential well situated at $r = x_m\sigma$.

Verlet and Weiss[11] have added a correction term to z_{HS} which is proportional to $\delta(T)$. This term remains negligibly small for "hard sphere" packing fractions

$$y_0 = \frac{\pi}{6}\ \sigma^3 N/V \tag{11}$$

of less than about 0.7, the precise value is actually a function of temperature. In fact the minor contribution it makes to the compressibility factor is insignificant to other corrections discussed below. However as y_0 approaches one, or as the "soft sphere" packing fraction exceeds about 0.5, this correction term increases dramatically and the total compressibility factor decreases again after its initial increase. This is certainly incorrect, indicating a breakdown of the theoretical approach by Verlet and Weiss. This breakdown coincides with two important changes of physical significance. First, the molecular dynamics studies of Adler and Wainwright[12] show that a fluid-solid transition occurs in the hard-sphere system at a packing fraction

of about 0.47. Still, the compressibility factor z_{HS} agrees quite well with the molecular dynamics results at even high packing fractions up to about 2/3.[10] Second, at high packing fractions, the interatomic potential obtained from beam-scattering data is certainly no longer a good representation of the effective interatomic potential which accounts for many-body correlations.

For these reasons we believe that the additional correction term of the Verlet-Weiss theory should simply be omitted; at low densities it is insignificant, and at high densities either more important corrections need to be made to adequately reflect the physical situation, or an EOS for the solid must be used.

The Equation (3) for the effective diameter was solved previously[13] in an iterative manner starting with the assumption $d \simeq d_B$. This approach converges only for small and moderate packing fractions. Therefore, in the present work, the nonlinear Equation (3) was solved numerically. The integrals in Eqs. (9) and (10) are also evaluated numerically.

5.3 The Quantum Correction

For a fluid comprised of light atoms, quantum corrections are important. If A_{Cl} represents the free energy of the fluid treated with classical statistical mechanics, the inclusion of quantum corrections gives the following expression for the total free energy[8,14,15]

$$A = A_{Cl} + \frac{h^2 N^2}{24\,\pi m k T V} \int g(r) \nabla^2 V(r) r^2 \, dr \tag{12}$$

where h is Planck's constant, m the atomic mass, and $g(r)$ is the radial distribution function. This function, in the case of a hard sphere fluid, depends on the dimensionless distance

$$\rho = r/d \tag{13}$$

as well as on the packing fraction y, and an exact solution exists for it in the Percus-Yevick approximation.[16-19] However, the analytical form or the numerical tabulation for $g(r)$ are cumbersome to use, and we shall instead employ a recent approximate expression derived by Shinomoto:[20]

$$g(\rho,y) = \begin{cases} 0 & \text{for } \rho < 1 \\ \exp[y\psi(\rho)] & \text{for } \rho > 1 \end{cases} \tag{14}$$

where

$$\psi(\rho) = \begin{cases} 1/2\ (\rho - 2)^2(\rho + 4) & \text{for } 1 < \rho < 2 \\ 0 & \text{for } \rho > 2 \end{cases} \tag{15}$$

As Shinomoto has shown, the hard sphere EOS derived with this radial distribution function agrees surprisingly well with the molecular dynamics results or with the Carnahan-Starling equation.

The form of this simple radial distribution function in Eq. (14) has the advantage that the derivative $(\partial A/\partial V)$ can be obtained prior to the evaluation of the integral in Eq. (12). Since we are interested in the compressibility factor we write

$$z = pV/NkT = -(V/NkT)(\partial A/\partial V) = y\ \partial(A/NkT)/\partial y = z_{Cl} + z_Q \tag{16}$$

where

$$z_Q = \frac{h^2}{m(kT)^2\sigma^2}\, y\, \frac{\sigma}{d}\, \frac{\partial}{\partial y}\, (yB(y)) \tag{17}$$

Here

$$B(y) = g(1,y)\left(-\frac{dV}{dx}\right)_{x=d/\sigma} + \int_1^2 \left(-\frac{dV}{dx}\right) \frac{\partial g}{\partial \rho}\, \rho^2\, d\rho \tag{18}$$

where $x = r/\sigma$ has been used as a characteristic interatomic distance parameter for the potential $V(x)$. With the above expressions for $g(\rho,y)$ and $\psi(y)$ we find

$$z_Q = \frac{h^2}{m(\sigma kT)^2} \frac{\sigma}{d} y\{(1 + \frac{5}{2} y) \exp(\frac{5}{2} y)(- \frac{dV}{dx})_{x=d/\sigma}$$

$$+ \frac{3}{2} y \int_1^2 (- \frac{dV}{dx})[2 + y\psi(\rho)]g(\rho,y)(\rho^2 - 2)\rho^2 \, d\rho\} \ . \tag{19}$$

For a given interatomic potential $V(x)$, the integral in Eq. (19) can be evaluated numerically.

5.4 The Contribution of the Attractive Part of the Interatomic Potential

So far we have treated gaseous helium as a system of hard spheres, i.e. as a fluid system whose particles possess only a repulsive interaction. For low densities and temperatures, however, the attractive forces between helium atoms play a significant role, and give rise to the actual liquid phase. Since the depth of the potential well, ε, is small for helium, we may approximate it by a square well of the same depth ε and of width $(d_w - d)$. We have chosen for d_w the value of 0.35 nm to approximate the actual shape of the well of the potentials by Beck[21] or Young et al.[22]

For a square-well potential, Reijnhart[23] has derived the following EOS

$$z_{Cl} = z_{HS} + z_A \tag{20}$$

where

$$z_A = -4y(d_w/d)^3 \, g(d_w/d,y)\{1 - \exp(-\varepsilon/kT)\} \ . \tag{21}$$

For the present purpose, we have again selected the radial distribution function of Shinomoto as given in Eq. (14).

5.5 Comparison of Theoretical and Emperical Equations of State for Gaseous Helium

The theoretical EOS derived above is given by

$$z = \frac{pV}{NkT} = z_{HS} + z_Q + z_A \ . \tag{22}$$

The various terms have been evaluated with both the Beck potential and the more recent potential by Young et al. As Fig. 2 shows, the two potentials differ only significantly for small interatomic distances. As pointed out by Young et al., the reduction of the interatomic potential reflects the many-body interactions at high densities and temperatures, an effect not accounted for in the Beck potential.

In comparing the theoretical results with the experimental data, we recall Fig. 1. We find that the data fall into two groups, the earlier experiments at low and moderate pressures, and the recent experiments at ultra-high pressures by Mills et al.[2] The first group of data has been thoroughly analyzed

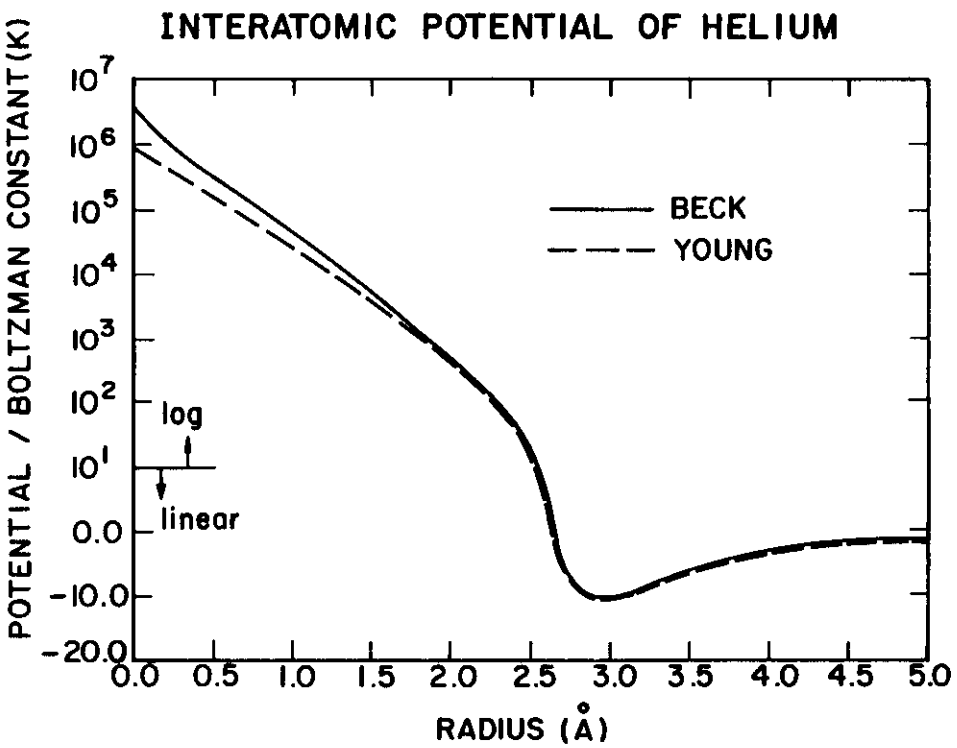

FIGURE 2. Interatomic Potential for Helium According to Beck[21] and Young, McMahon, and Ross.[22]

and fitted to an empirical EOS by McCarthy.[24] It contains 36 numerical constants and about an equal number of terms. This empirical equation for the temperature range between 15 K to 1500 K is applicable to pressures up to 100 MPa, and therefore restricted to rather low densities. In the valid density range, however, it represents perhaps the most accurate EOS for gaseous helium and an important benchmark for any theoretical EOS. In the region of high temperatures (400 K to 1500 K) and high pressures (10 MPa to 100 MPa), the estimated uncertainty for the density computed with this empirical equation is at the most about 2%.

A comparison of our gaseous EOS with the empirical correlation by McCarthy is shown in Fig. 3. It is seen that the theoretical EOS derived with the Beck potential agrees extremely well at 200 K, but deviates somewhat at higher temperatures from the empirical correlation. The results derived with the Young potential give a somewhat better agreement at the higher temperatures but a lesser agreement for 200 K.

5.6 The Solid Equation of State

The interatomic potential (see Fig. 2) of helium has a very shallow potential well with a depth of about 10 K. At the same time, it is a very light element. As a result of these two facts, the zero-point vibrations are large, and helium does not solidify at atmospheric pressures. In fact, the solid phase exists only for pressures greater than about 2.5 MPa (~ 25 atmospheres).

In the quasi-harmonic approximation, the free energy of a solid can be written as the sum of two terms[25]

$$A_S = U_0(V) + A_{vib}(V,T) \tag{23}$$

where U_0 is the internal energy of the solid at 0 K, and A_{vib} is the vibrational contribution to the free energy. Using a Oebyemodel for the vibrational frequency spectrum and a volume-dependent Debyetemperature $\theta(V)$, one

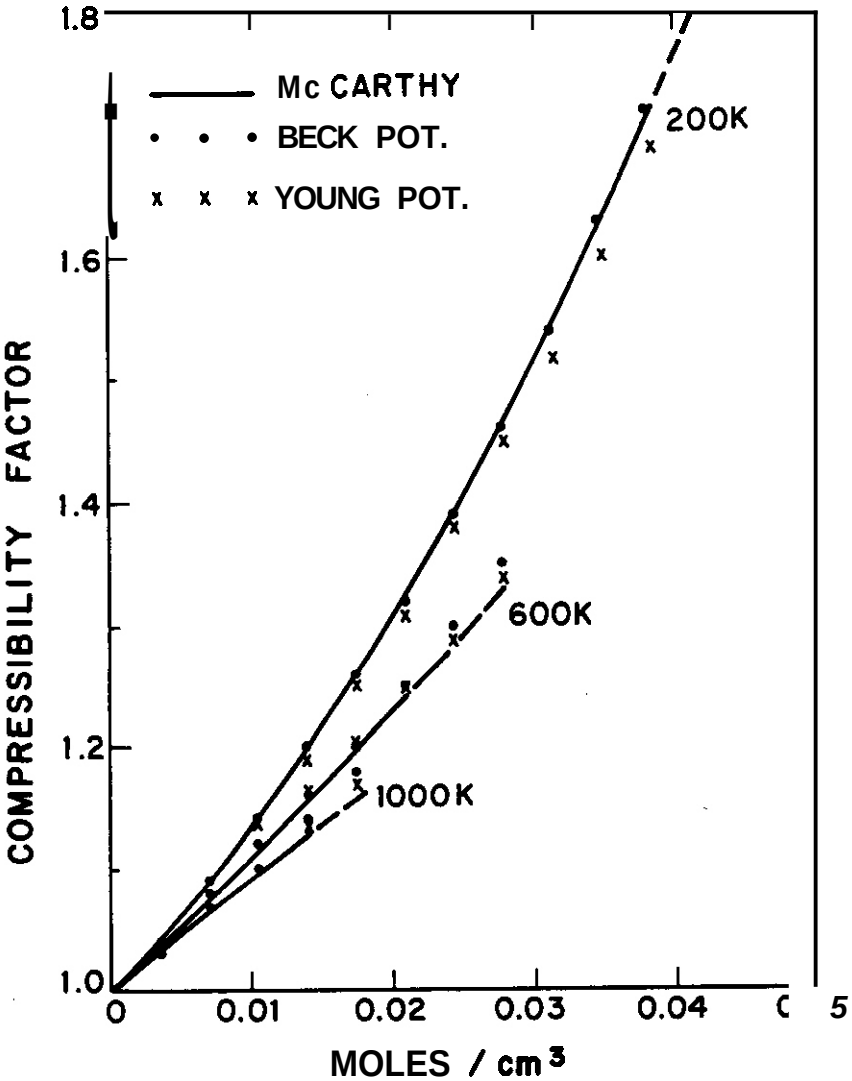

FIGURE 3. Comparison of the Empirical EOS Developed by McCarthy[24] with the Present EOS Derived with the Beck or Young Potential.

obtains the well-known Mie-Grüneisen EOS[25]

$$p_S = p_o + \gamma U_{vib}/V = p_o + p_D \tag{24}$$

where $p_o = -(dU_o/dV)$

is the ground-state pressure

$$U_{vib} = 9\ NkT\ \left(\frac{T}{\theta_D}\right)^3 \int \quad dx\ x^3/(e^x - 1) \tag{25}$$

is the internal energy associated with vibrations, and

$$\gamma = -d \ln \theta_D / d \ln V \tag{26}$$

is the Grüneisen parameter.

It should be noted that the Debyetheory yields the contribution (9/8) $Nk\theta_D$ as the vibrational energy of the ground state. This contribution is not included in U_{vib} of Eq. (25), but assumed to be part of $U_0(V)$. Indeed, any computation of U_0 requires quantum-mechanical wave functions for the helium atoms. Due to the large zero-point vibrations mentioned above, the helium lattice at 0 K cannot be considered as a collection of particles which obey (even approximately) the laws of classical mechanics.[26] Most of the theoretical work on the ground-state properties of solid helium have been for the low density range.[26] However, the recent work by Young et al.[22] have dealt with the solid state of helium at extremely high densities anticipated in the interior of stars. The results of their calculations for the ground-state pressure p_0 are shown in Fig. 4 as a function of the packing fraction $y_0 = \frac{1}{6}\pi\sigma^3 N/V$, where σ = 0.2641 nm. In order to cover the entire range of densities we use the theoretical results of Hansen and Pollock[27] for solid He^4 based on the Beck potential. Again, their results are shown in Fig. 4. It is seen that a gap exists not covered by any theoretical calculations so far. Nevertheless, both sets of theoretical results can be fitted by a smooth functional correlation of the form

$$p_0(\mathrm{MPa}) = (\alpha + \beta)^6 \tag{27}$$

where

$$\alpha = \left[\frac{1}{2}\sqrt{B} + \sqrt{Q}\right]^{1/3}, \tag{28}$$

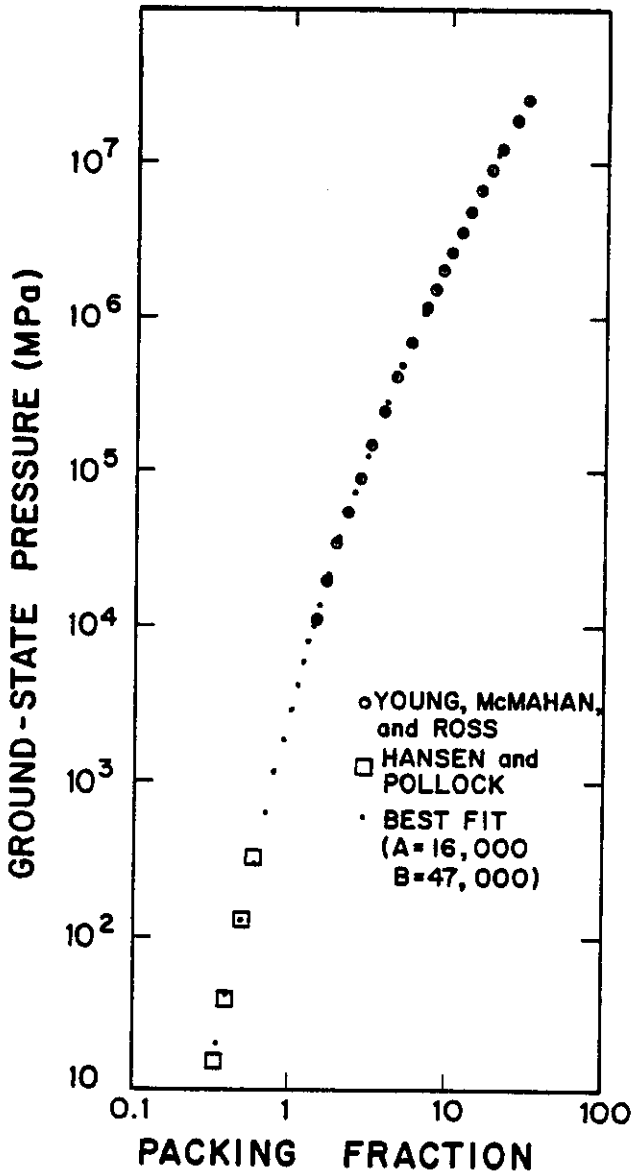

FIGURE 4. Ground-State Pressure for Solid He.

$$\beta = [\frac{1}{2}\sqrt{B} - \sqrt{Q}]^{1/3} , \tag{29}$$

$$Q = \frac{1}{27}\sqrt{B^3/A} + \frac{1}{4} By_o^2 . \tag{30}$$

A and B are two constants used to fit Eq. (27) to the above mentioned results. The best fit, also shown in Fig. 4, is obtained with A = 16,000 and B = 47,700.

Young et al.[22] have also computed the pressure and volume at melting as a function of temperature. These results are shown in Figs. 5 and 6, respectively. It is seen that these results can be represented very accurately by the following mathematical relationships.

For the melt pressure we obtain

$$p_m(\mathrm{Pa}) = 9.423 \times 10^5 \, T_m^{1.634} + 52.535 \, T_m^{3.02} \tag{31}$$

and for the reciprocal melt volume of the solid

$$(1/V_m)(\mathrm{moles/cm^3}) = 0.0269 \, T_m^{0.359} + 1.953 \times 10^{-7} \, T_m^{1.903} \tag{32}$$

From both correlations we can compute the compressibility factor at melting, $p_m V_m / N k T_m$, as a function of the melting temperature. The results are shown in Fig. 7. Although the correlations for both the melt pressure p_m and the melt volume V_m appear to be rather smooth, the compressibility factor at melting exhibits a sudden change in its slope at about 400 K. It is not clear at the present time whether this sudden change in slope is real or indicative of a failure of the theory to deal correctly with the phase change. It appears that the theoretical approaches used by Young et al. for the phase change are different and not entirely consistent with each other for the low and high temperature regions.

The Lindemann melting equation

$$\theta_{Dm}(T_m) = C V_m^{-1/3} \, (T_m/M)^{1/2} \tag{33}$$

relates now the Oebyetemperature of the solid to its melting temperature and melt volume, where M is the molar weight and C is nearly a constant. This Equation (33) has been shown[28] to be remarkably valid for rare gas solids as

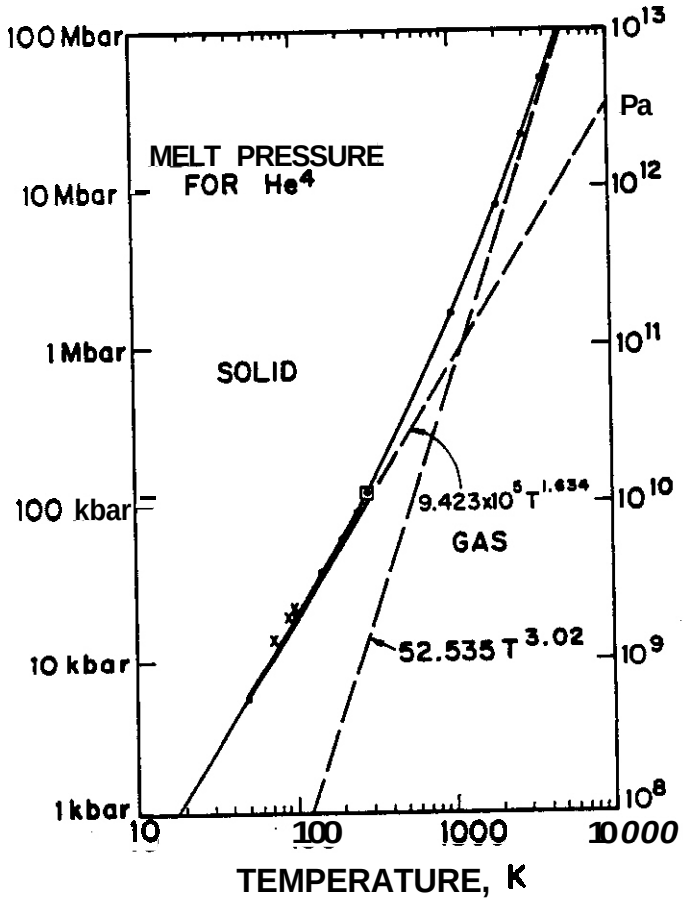

FIGURE 5. Melt-Pressure for Helium.

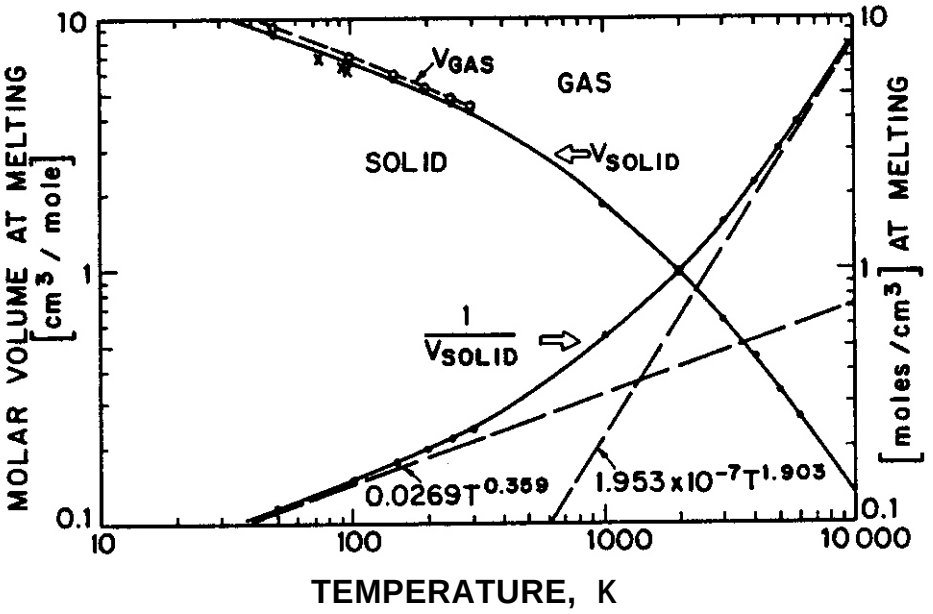

FIGURE 6. Melt-Volume and Its Reciprocal for Helium.

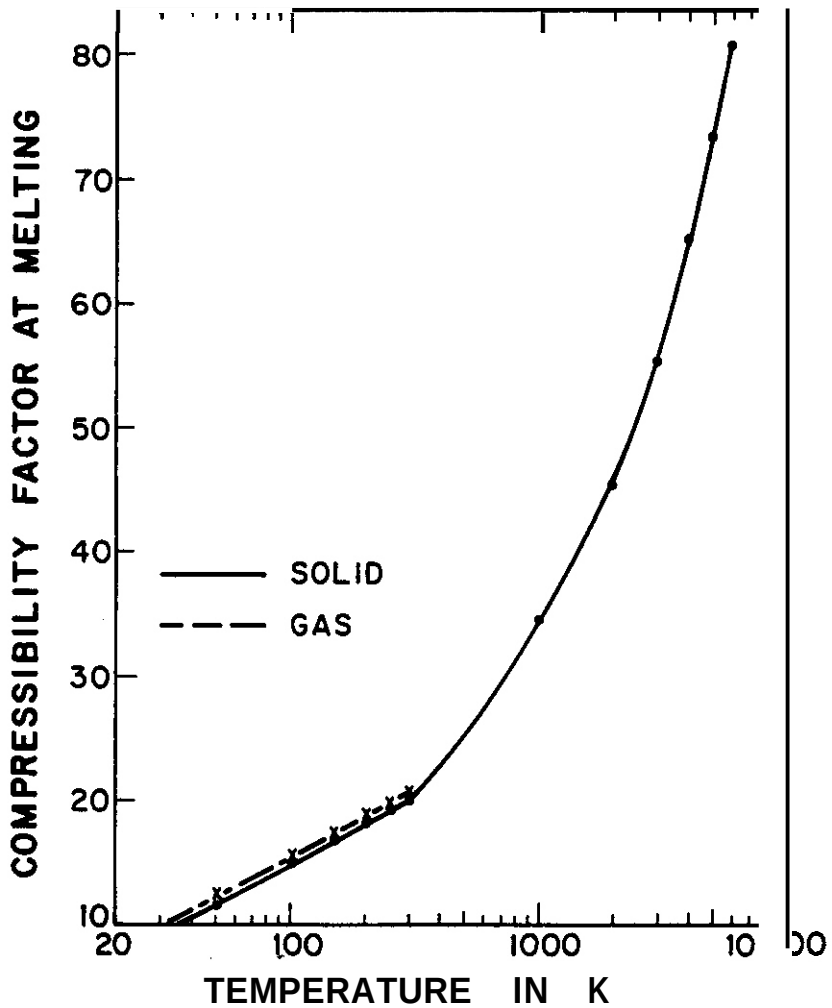

FIGURE 7. Compressibility Factor at Melting for Helium.

well as other substances. For all rare gas solids with the exception of ^{3}He, the constant is between 100 and 140 (cm $g^{1/2}$ $mol^{-5/4}$ $K^{1/2}$). We select the value of 116 (cm $g^{1/2}$ $mol^{-5/4}$ $K^{1/2}$) as recommended by Mills et al.,[2] and obtain

$$\theta_{Dm} = 16.15931\ T_m^{1/2} y_o^{1/3} \tag{34}$$

and

$$\gamma = \frac{1}{3} + \frac{0.269\ T^{-0.641} + 1.953 \times 10^{-7}\ T^{0.903}}{0.0965\ T^{-0.641} + 3.7165 \times 10^{-7}\ T^{0.903}} \tag{35}$$

As the results in Table 1 show, the Grüneisen parameter varies little with temperature, which gives us some confidence that the Mie-Gruneisen EOS provides a reasonable description for solid helium.

TABLE 1

DEBYE TEMPERATURE AND GRUNEISEN PARAMETER FOR SOLID ^4He

Temp. (K)	10	100	200	400	800	1200
θ_D (K)	36.2	151.2	233.6	364.6	584.4	788.8
γ	3.119	3.108	3.088	3.032	2.882	2.714

In evaluating then the term p_D in Eq. (24) we use the relationships in Eqs. (25), (34), and (35) together with

$$\theta_D(V,T) = \theta_{Dm}(T)*(V_m/V)^{\gamma} \tag{36}$$

for the Debye temperature at a given temperature T and for a solid volume $V \leq V_m(T)$. The integral in Eq. (25) is evaluated numerically.

5.7 Comparison of Equations of State for Gaseous and Solid Helium

The empirical EOS developed by Mills et al.[2] gives the volume as a function of the temperature and pressure, i.e. $V(T,P)$. In order to solve this equation for $P(T,V)$, the following cubic equation in $z^{1/3}$ must be evaluated:

$$z = A_2(RT)^{-1/3}V^{-2/3}z^{2/3} + A_1(RT)^{-2/3}V^{-1/3}z^{1/3} + A_o(RT)^{-1} \tag{37}$$

where z is the compressibility factor, R = 0,083146 (kbar cm^3 mol^{-1} K^{-1}) is the gas constant, V (cm^3/mol) the molar volume and

$$A_2 = 22.575 + 0.0064655\ T - 7.2645\ T^{-1/2} \tag{38}$$

$$A_1 = -12.483 - 0.024549\ T \tag{39}$$

$$A_o = 1.0596 + 0.10604\ T - 19.641\ T^{-1/2} + 189.84\ T^{-1} \tag{40}$$

This equation is reported to be valid for the temperature range $75 < T < 300$ K and the pressure range $200 < p < 2000$ MPa. Since it is empirical it should apply to the gaseous and solid state within the specified ranges of temperature and pressure.

Trinkaus[7] has recently developed an EOS by combining the virial EOS for gaseous helium with theoretical results for the solid state. This equation has the form

$$z = (1 - \rho)(1 + \rho - 2\rho^2) + (1 - \rho)^2 \rho b/V_m + (3 - 2\rho)\rho^2 Z_m - 50(1 - \rho)\rho^2 \tag{41}$$

where

$$\rho = V_m/V \tag{42}$$

$$V_m = 56\ T^{-1/4} \exp(-0.145\ T^{1/4}) \tag{43}$$

$$Z_m = 0.1225\ V_m T^{0.555} \tag{44}$$

and

$$b = 170\ T^{-1/3} - 1750\ T^{-1}\ . \tag{45}$$

Again, this equation incorporates both the equations of state for gas and solid. In the following comparison between the two EOS above and our theoretical EOS, it was assumed that the phase transition occurs whenever the compressibility factors for gas and solid become equal. In other words, the phase with the lowest compressibility factor is the one which exists for a given temperature and volume. It must be noted that this is only approximately correct as the phase change at constant pressure is accompanied by a small volume change typically on the order of about 4%.

Let us now compare the various EOS, starting with the one for gaseous helium. Figures 8 and 9 show the present theoretical results for the compressibility factor as a function of the gas density. In the density range from about 0.05 to 0.14 moles/cm^3 and for T = 200 K, we can compare our results with the experimental ones of Mills et al.[2] We find that the Beck potential results in a theoretical EOS which agrees well with the experimental one at low densities (Fig. 8). However, at high densities, the Young potential (Fig. 9) provides better agreement with the experimental EOS. Furthermore, comparing the theoretical results obtained with the two potentials, we find that the Young potential results in lower compressibility factors, and hence pressures, at high helium densities. This is due to the fact that the Young potential is softer for very small interatomic separations due to many-body effects not accounted for in the Beck potential. It appears then, that a hybrid potential, consisting of the Beck form at large interatomic separations and of the Young form at small separations would yield the optimal results.

If we now extend the comparison to include also the solid EOS, we obtain the results shown in Figs. 10 and 11. For this comparison we used the empirical EOS by Mills et al.[2] and simply extrapolated it to densities much higher than the experimental data range. The curves denoted by solid EOS and gas EOS represent our theoretical results. The EOS of state by Trinkaus is obtained by a linear interpolation of his solid EOS and his gaseous EOS. Hence, no discontinuity in slope occurs at the phase transition point. We find that the largest differences among the various EOS occur for solid densities where little or no experimental information exists. Our solid EOS gives the lowest pressures at high solid densities, and this appears to be due to the low ground-state pressures as computed by Hansen and Pollock[27] and by Young et al.[22]

6.0 References

1. N. V. Tsederberg, V. N. Popov, and N. A. Morozova, "Thermodynamic and Thermophysical Properties of Helium," Atomizdat, Moscow 1968; Israel Program for Scientific Translations, Jerusalem 1971.

2. R. L. Mills, D. H. Liebenberg, and J. C. Bronson, Phys. Rev. B 21 (1980) 5137.

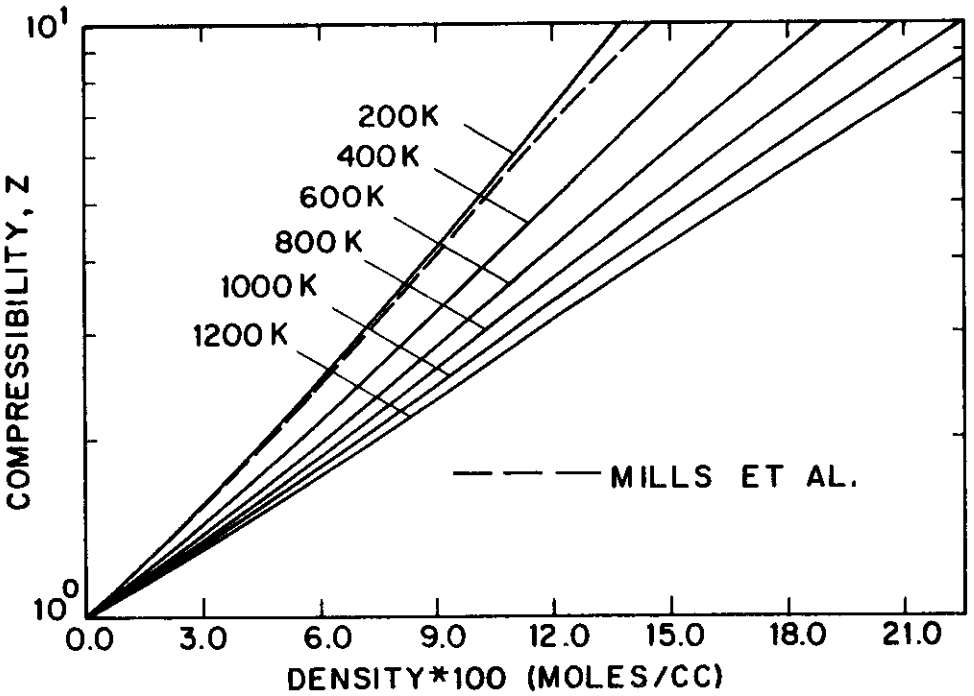

FIGURE 8. EOS for Gaseous Helium Using Beck's Potential.

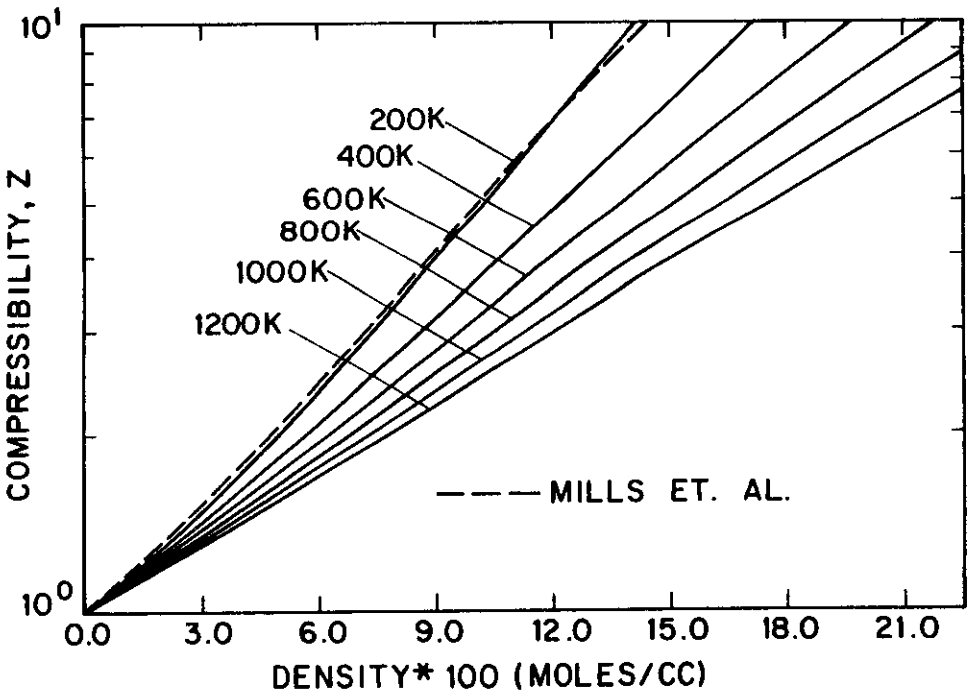

FIGURE 9. EOS for Gaseous Helium Using Young's Potential.

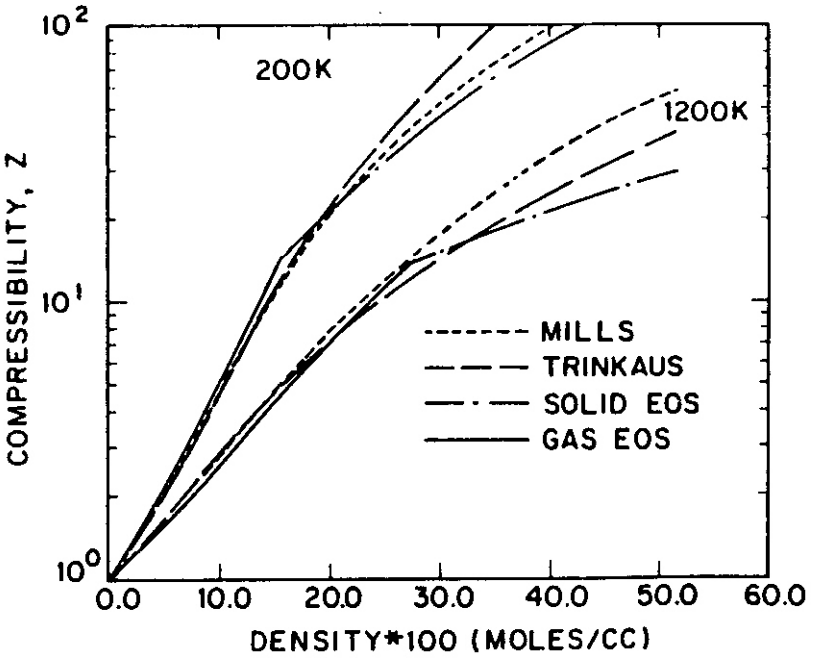

FIGURE 10. Comparison of All EOS Using Beck's Potential.

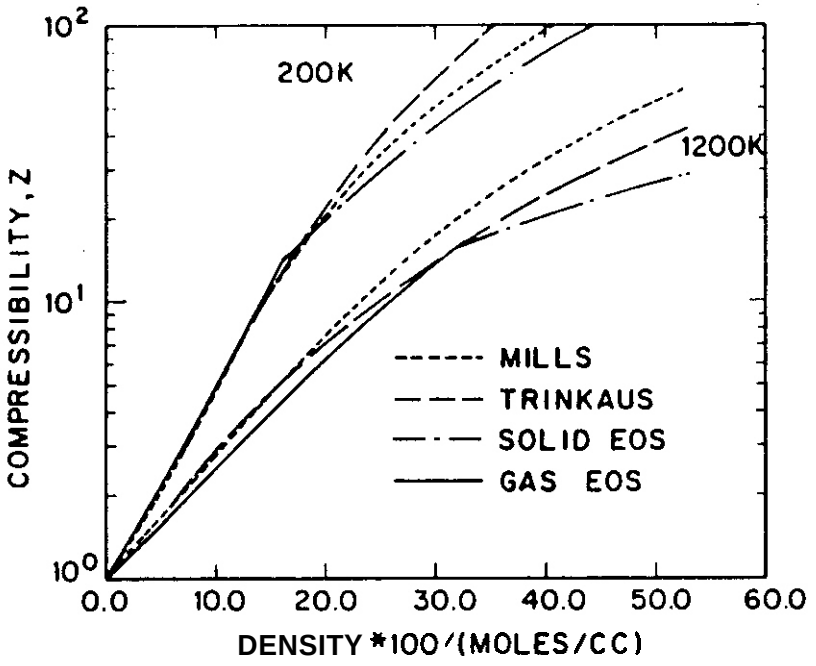

FIGURE 11. Comparison of All EOS Using Young's Potential.

3. W. Jager, R. Manzke, H. Trinkaus, G. Crecelius, R. Zeller, J. Fink, and H. L. Bay, J. Nucl. Matls. 111 & 112 (1982) 674.

4. J. C. Rife, S. E. Donnelly, A. A. Lucas, J. M. Gilles, and J. J. Ritsko, Phys. Rev. Letters 46 (1981) 1220.

5. J. M. Besson and J. P. Pinceaux, Science 260 (1979) 1073.

6. J. H. Evans, A. van Veen, and L. M. Caspers, Scripta Met. 15 (1981) 323.

7. H. Trinkhaus, private communication.

8. J. A. Barker and D. Henderson, Rev. Mod. Phys. 48 (1976) 587.

9. H. C. Anderson, D. Chandler and J. D. Weeks, Adv. Chem. Phys. 34 (1976) 105.

10. N. F. Carnahan and K. E. Starling, J. Chem. Phys. 51 (1969) 635.

11. L. Verlet and J. J. Weiss, Phys. Rev. A5 (1972) 432; and Mol. Phys. 24 (1972) 1013.

12. B. J. Adler and T. E. Wainwright, J. Chem. Phys. 33 (1960) 1439.

13. W. G. Wolfer, in "Effects of Radiation on Materials," Eds. H. R. Brager and J. S. Perrin, ASTM STP 725 (1981) 201.

14. H. S. Green, J. Chem Phys. 19 (1951) 955.

15. S. Kim, D. Henderson, and J. A. Barker, Can. J. Phys. 47 (1979) 99.

16. M. S. Wertheim, Phys. Rev. Letters 10 (1963) 321.

17. G. J. Throop and R. J. Bearmann, J. Chem. Phys. 42 (1965) 2408.

18. W. R. Smith and D. Henderson, Mol. Phys. 19 (1970) 411.

19. J. W. Perram, Mol. Phys. 30 (1975) 1505.

20. S. Shinomoto, Phys. Letters 89A (1982) 19.

21. D. E. Beck, Mol. Phys. 14 (1968) 311.

22. D. A. Young, A. K. McMahon, and M. Ross, Phys. Rev. B24 (1981) 5119.

23. R. Reijnhart, Physica 83A (1976) 533.

24. R. D. McCarthy, J. Phys. Chem. Reference Data 2 (1973) 923.

25. M. Born and K. Huang, "Dynamical Theory of Crystal Lattices," Oxford Univ. Press, 1954, pp. 48-50.

26. H. R. Glyde, "Solid Helium," Chapter 7 of Rare Gas Solids, Vol. I, Eds. M. L. Klein and J.A. Venables, Acad. Press, London, 1976.

27. J. P. Hansen and E. L. Pollock, Phys. Rev. A5 (1972) 2651.

28. R. K. Crawford. "Melting, Vaporization and Sublimation." Chaoter 11 of Rare Gas Solids, Vol. II, Eds. M. L. Klein and J. A. Venables, Acad. Press, London, 1976.

7.0 Future Work

A more refined model will be developed for the solid EOS of helium and for the phase transition from gas to solid. Furthermore, a simple analytical expression will be developed that is more convenient to use than the present EOS for gaseous helium.

TEMPERATURE INDEPENDENCE OF THE SWELLING RATE IN AUSTENITIC STAINLESS STEELS

W. G. Wolfer (University of Wisconsin) and F. A. Garner (Hanford Engineering Development Laboratory)

1.0 Objective

The object of this effort is to determine the physical basis for the temperature independence of the steady-state swelling rate observed in some austenitic alloys.

2.0 Summary

Recent analyses of swelling data for a variety of austenitic stainless steels have revealed that the steady-state swelling rate is nearly independent of temperature and is also independent of composition. This is in apparent contradiction with most earlier analyses showing a large dependence of swelling rate on temperature. It is shown that rate theory does indeed agree with this recent finding if appropriate material parameters are chosen. Among the most critical parameters is the vacancy migration energy, a parameter which has recently been revised significantly based on experiments conducted on nickel. With the new value of 1.1 eV, the steady-state swelling rate becomes nearly independent of temperature after the microstructural sink strength has reached or exceeded 5×10^{10} cm^{-2}

3.0 Programs

Title: Effect of Radiation and High Heat Flux on the Performance of First Wall Components
Principal Investigator: W.G. Wolfer
Affiliation: University of Wisconsin-Madison

Title: Irradiation Effects Analysis (AKJ)
Principal Investigator: D.G. Doran
Affiliation: Hanford Engineering Development Laboratory

The eventual swelling rate also does not appear to be very sensitive to composition or to other environmental variables such as displacement rate. This implies that the sensitivities of microstructural development to temperature and other variables are not as instrumental in determining the swelling rate as previously envisioned. A rationale for this insensitivity can be demonstrated using rate theory.

5.2 Results

According to the rate theory of void growth[7] the swelling rate is given by

$$\frac{d}{dt}\left(\frac{\Delta v}{v}\right) = S_o Z_v^o D_v \left\{\left[\frac{\bar{Z}_i}{\bar{Z}_v} - \frac{Z_i^o}{Z_v^o}\right]\Gamma - \left[C_v^o - \overline{C_v^{eq}}\right]\right\} \tag{1}$$

where

$$S_o = 4\pi N_o r_o \tag{2}$$

is the sink strength of voids with average radius r_o and concentration N_o, D_v is the vacancy diffusion coefficient, $\overline{C_v^{eq}}$ is the vacancy concentration in thermal equilibrium with the sinks, and C_v^o is the same quantity in equilibrium with the voids. At temperatures $T \lesssim 0.6\ T_m$, the void annealing term, being proportional to $D_v[C_v^o - \overline{C_v^{eq}}]$, can be neglected. If the voids contain a gas pressure close to the equilibrium value $2\gamma/r_o$ (γ is the surface energy), or if the void radius is sufficiently large so that $2\gamma/r_o \ll kT/\Omega$ (Ω is the atomic volume), then the annealing term can be neglected even at higher temperatures.

For these conditions, the swelling rate is given by the bias-driven term only and is proportional to

$$\Gamma = \frac{S}{2\lambda D_v}\left\{\sqrt{\alpha^2 + \beta} - \alpha\right\} \tag{3}$$

where

$$\lambda = 32\ \pi/a_o^2 = 4\pi R_c/\Omega$$

with $R_c = 2a_o$ (a_o is the lattice parameter) being the recombination radius,[2]

$$\alpha = 1 + \lambda\overline{C_v^{eq}}/(S\bar{Z}_i) \tag{4}$$

4.0 Relevant DAFS Program Task/Subtask

Task II.C.1 Effects of Material Parameters on Microstructure
Task II.C.2.5 Modeling
Subtask C: Correlation Methodology

5.0 Accomplishment and Status

5.1 Introduction

It has been shown that the eventual swelling rate of several 300 series stainless steels is ~1%/dpa over a wide range of temperature [1-5]. While the transient regime may be sensitive to temperature for some heats of steel, others are relatively insensitive to temperature as shown in Figure 1. At temperatures outside the temperature-insensitive range the transients are longer but eventually the same swelling rate is reached. Ternary alloys without significant solutes such as carbon or silicon also exhibit an independence of steady-state swelling rate on temperature.[6] Once again the steady-state swelling rate is ~1%/dpa but it is reached after a short and rather abrupt transient regime.

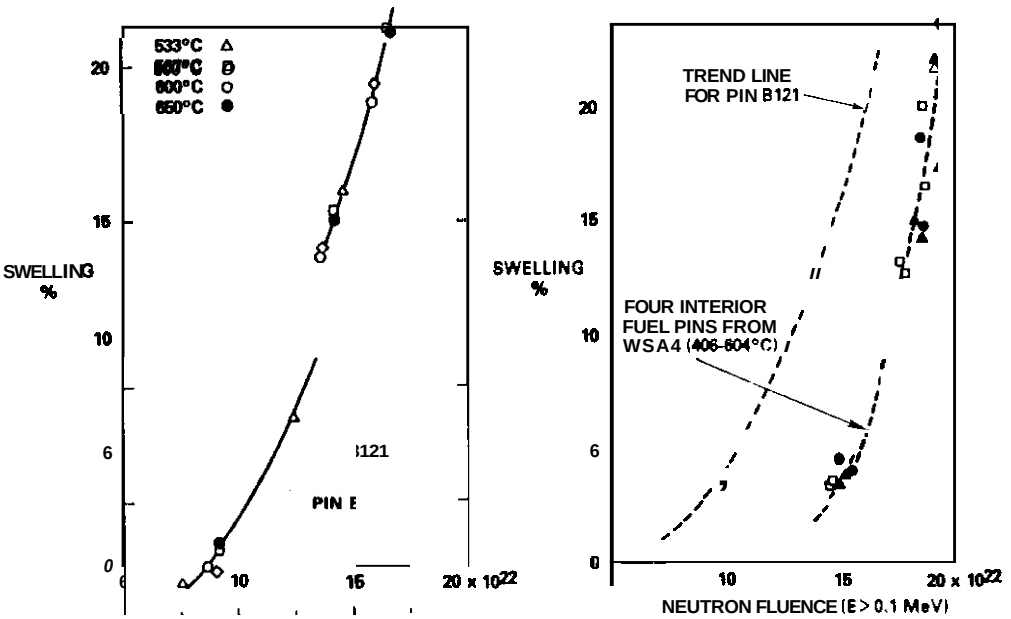

FIGURE 1. N-lot, a Heat of AISI 316 Showing a Relative Insensitivity of Swelling to Temperature in a Given Experiment, but Also Exhibiting a Sensitivity of the Transient Regime to Environmental History in Each Experiment.[2,3,5]

$$6 = 4\lambda D_v P/(S2\, Z_i Z_v) \quad , \tag{5}$$

and S is the total sink strength. Here, P is the production rate of freely migrating point defects, and Z_i and Z_v are the average bias factors for interstitial and vacancy absorption, respectively. These factors are on the order of one. Therefore, in the expression for Γ we may set these factors equal to one without loss of accuracy.

Let us divide the sink structure into two components, voids with sink strength S_o, and the remainder with sink strength S_d. The subscript "d" is to indicate that a significant fraction or perhaps all of the latter sinks are composed of dislocations and loops. We assign these sinks the bias factors Z_i^d and Z_v^d.

Using the definition

$$Z_{i,v} = (Z_{i,v}^d S_d + Z_{i,v}^o S_o)/(S_d + S_o) \tag{6}$$

we can write the swelling rate also in the form

$$\frac{d}{dt}\left(\frac{\Delta v}{v}\right) = \frac{S_o S_d}{(S_o + S_d)^2} \cdot \frac{(Z_i^d Z_v^o - Z_v^d Z_i^o)}{Z_v} \cdot F(P,T) \tag{7}$$

where

$$F(P,T) = S\Gamma D_v \tag{8}$$

is a function which contains a major part of the temperature dependence of the swelling rate. The second factor is the net bias if we set $Z_v \cong 1$, and it depends only weakly on temperature. The first factor may depend rather strongly on the temperature for a sink structure dominated by only one sink type. However, radiation-induced microstructures obtained after void nucleation has ceased are often characterized by a balance of the sink strength, i.e. by $S_o \cong S_d$. In this case, the first factor becomes equal to (1/4), regardless of the irradiation temperature. Even if $S_o \neq S_d$, the two sink strengths usually have a similar temperature dependence. Again, the first factor is then independent of temperature. If we divide Eq. (7) by the

defect production rate P, we obtain the swelling rate in fractions per dpa. Accordingly, the ratio (F/P) was evaluated with the following parameters. The vacancy diffusion coefficient was assumed to be equal to that for nickel, and it is given by

$$D_v = 0.0153 \exp[-E_v^m/kT] \tag{9}$$

whereas the equilibrium concentration was assumed to be

$$C_v^{eq} = \exp(1.5 - E_v^f/kT) \ . \tag{10}$$

The activation energy for self-diffusion in nickel is

$$E_v^f + E_v^m = 2.8 \text{ eV} \tag{11}$$

a fairly well established") value, whereas the migration (and hence formation) energy has been significantly revised recently based on measurements by Khanna and Sonnenberg[9] and Smedskjaer et al.[10] Whereas the widely accepted migration energy was previously $E_v^m = 1.4$ eV, it is now clear that the value is actually $E_v^m = 1.1 \pm 0.1$ eV. We shall see shortly that this new and presumably more reliable value of E_v^m has a significant impact on swelling.

For the production rate of point defect we have selected a displacement rate of 10^{-6} dpa/s and a cascade survival fraction of 0.3; hence $P = 3 \times 10^{-7}$ (point defect pairs/s).

Figure 2 shows the function F/P versus temperature for different values of the total sink strength. For a low sink strength the function F/P and hence the swelling rate exhibits a marked temperature dependence. However, as the sink density increases with irradiation time the function F/P approaches a constant value of 1/2. Previous analysis of the evolution of the dislocation network in austenitic stainless steels showed[11] that a temperature independent value of $\sim 6 \times 10^{10}$ cm^{-2} is reached before the onset of steady-state swelling.

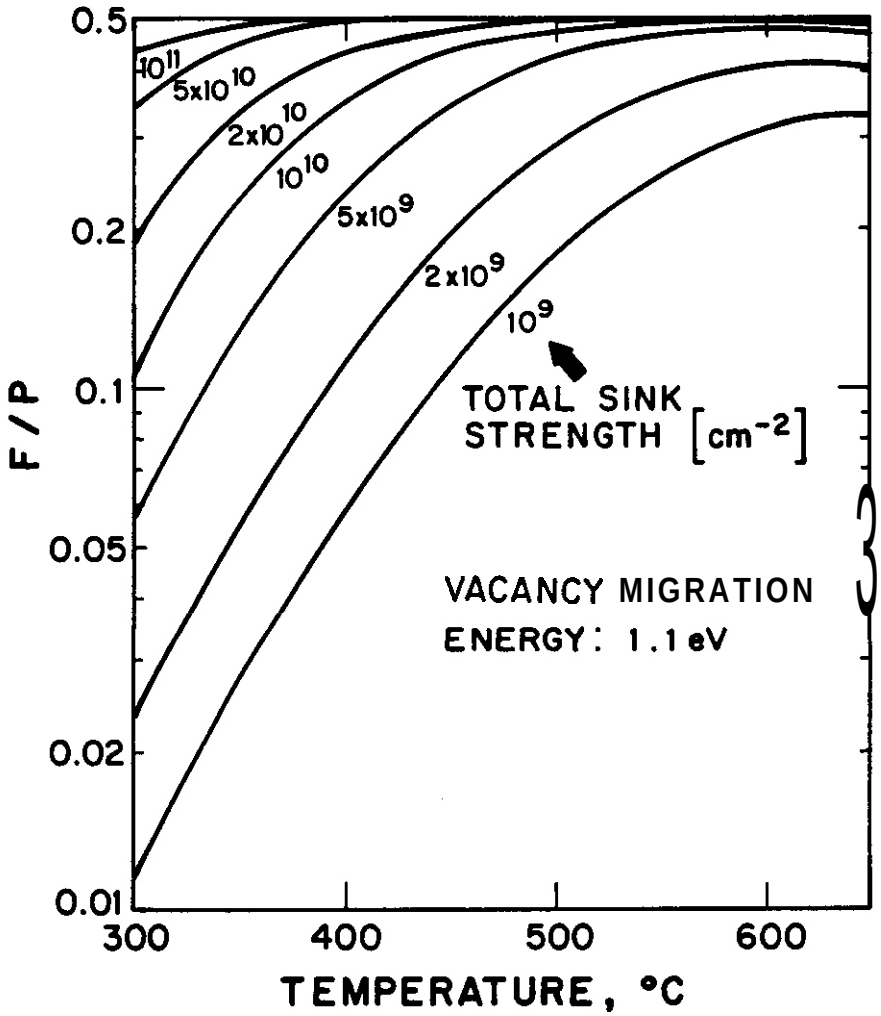

FIGURE 2. The Function F/P, Which Determines the Temperature Dependence of the Steady-State Swelling Rate, Depends on Total Sink Strength, Temperature, and Vacancy Migration Energy.

Adding to this value the sink strength of voids and dislocation loops we find that (F/P) and the swelling rate should indeed become independent of temperature.

Figure 3 shows the function (F/P) for a total sink density of 5 x 10^{10} cm^{-2} but for different migration energies of the vacancy. This figure demonstrates

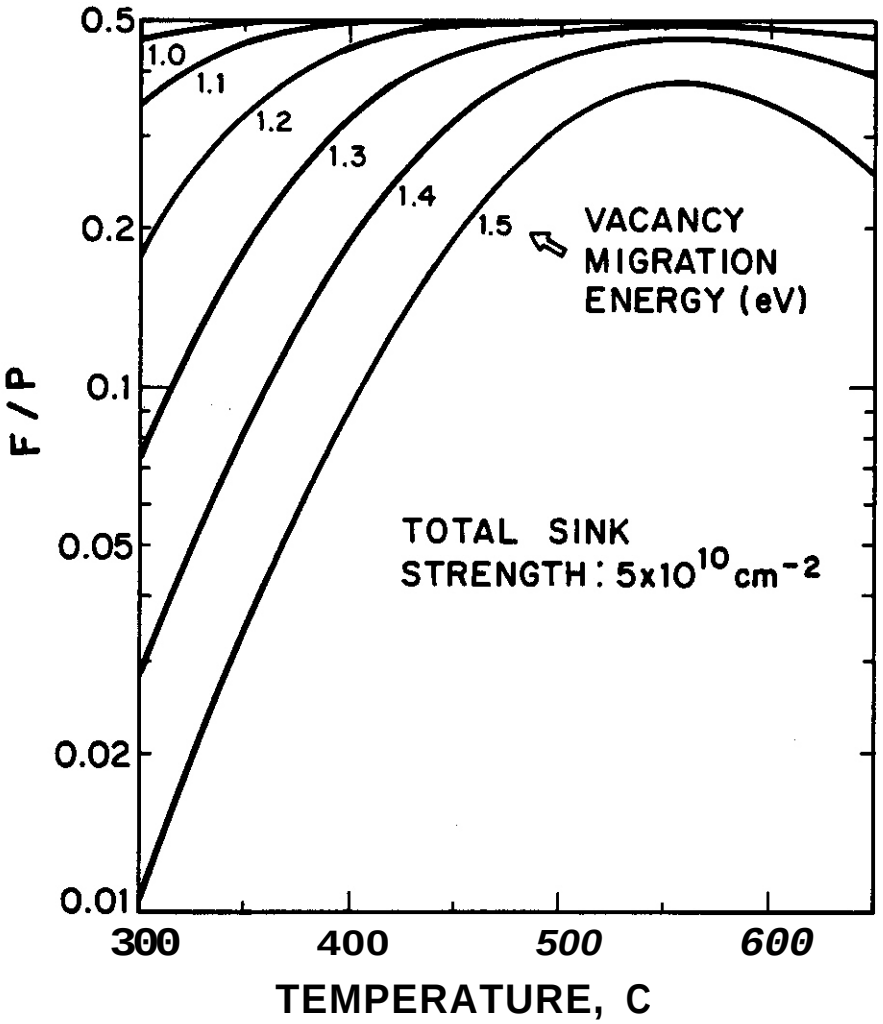

FIGURE 3. The Temperature Dependence of the Function F/P is Quite Sensitive to the Vacancy Migration Energies.

that the previously accepted value of E_v^m = 1.4 eV gave a swelling rate which depended strongly on the irradiation temperature. The present analysis, however, supports the experimental findings that the swelling rate becomes independent of temperature.

6.0 References

1. F. A. Garner and D. L. Porter, "Factors Influencing the Swelling of 300 Series Stainless Steels," DAFS Quarterly Progress Report, DOE/ER-00046/9, 170-185.

2. W. S. J. Yang and F. A. Garner, "Relationship Between Phase Development and Swelling of AISI 316 During Temperature Changes," Effects of Radiation on Materials: Eleventh Conf., ASTM STP 782, H. R. Brager and J. S. Perrin, Eds., American Society for Testing and Materials, 1982.

3. F. A. Garner and W. G. Wolfer, "Recent Experimental and Theoretical Insights on the Swelling of Austenitic Alloys," Proceedings *of* International Conference on Dimensional Stability and Mechanical Behavior of Irradiated Metals and Alloys, April 11, 1983, Brighton, England (in press).

4. H. R. Brager and F. A. Garner, "Microstructural and Microchemical Comparison of AISI 316 Irradiated in HFIR and EBR-II," Proceedings of Symposium on Radiation Damage Analysis for Fusion Reactors, Oct. 24-28, 1982, St. Louis MO., J. Nucl. Mater., in press.

5. A. Boltax, J. P. Foster and U. P. Nayak, "High Dose Stainless Steel Swelling Data on Interior and Peripheral Oxide Fuel Pins," in ref. 3.

6. F. A. Garner, "Impact *of* the Injected Interstitial on the Correlation of Charged Particle and Neutron-Induced Radiation Damage," in ref. 4.

7. W. G. Wolfer and A. Si-Ahmed, J. Nucl. Mater. 99 (1981) 117.

8. J. Askill, Tracer Diffusion Data for Metals, Alloys, and Simple Oxides, Plenum Press, New York, 1970.

9. S. K. Khanna and K. Sonnenberg, Rad. Effects 59 (1981) 91.

10. L. C. Smedskjaer, M. J. Fluss, D. G. Legnini, M. K. Chason, and R. W. Siegel, J. Phys. F: Metal Physics 11 (1981) 2221.

11. F. A. Garner and W. G. Wolfer, "A Model for the Evolution of Network Dislocation Density in Irradiated Metals, in ref. 2, 1073-1087.

7.0 Future Work

The temperature dependence *of* both the void sink strength and the total dislocation sink strength will be analyzed in more detail, and the impact of these on the steady-state swelling rate will be reassessed.

8.0 Publications

None

VOID SWELLING IN THE PRESENCE OF SMALL HELIUM BUBBLES

W. G. Wolfer (University of Wisconsin)

1.0 Objective

The purpose of this study is to explore the microstructural conditions for which small helium bubbles do or do not influence the swelling behavior of austenitic stainless steels.

2.0 Summary

It is shown that bubbles treated as neutral sinks (i.e., acquiring no excess vacancies) have no effect whatsoever on the void swelling rate if the sink strength of all other sinks exceeds the value of about 2×10^{10} cm^{-2}. Swelling proceeds then as if no bubbles were there.

3.0 Program

Title: Effect of Radiation and High Heat Flux on the Performance of First Wall Components

Principal Investigator: W. G. Wolfer

Affiliation: University of Wisconsin-Madison

4.0 Relevant DAFS Program Task/Subtask

Task II.C.1 Effects of Material Parameters on Microstructure

Task II.C.2 Effects of Helium on Microstructure

Subtask C Correlation Methodology

5.0 Accomplishments and Status

5.1 Introduction

Irradiation of materials in HFIR or with dual-ion beams produces often a cavity population consisting of voids and small helium bubbles. The presence of a high density of small bubbles has been discovered also in type 316 stainless steel irradiated recently in HFIR, and it has been considered as a potential suppressant of the high swelling rate observed in breeder reactor irradiations. This expectation is based on rate theory arguments where bubbles and voids are treated as sinks of the same kind. The bimodal size distribution of the cavity population observed is explained then in terms of a different nucleation time: the voids were nucleated earlier when little or no helium was present, whereas the bubbles formed later in response to the increasing helium concentration. This explanation is at odds with several observations. First, the ion-bombardment results of Loomis et al.[1] show that the original bubble density produced under irradiations with a high He/dpa ratio can diminish upon further irradiation. Second, the steady-state swelling rate may be independent of the He/dpa ratio. Third, it has been shown by Brager and Garner[2] that the swelling behavior of 20% CW 316 (DO-Heat) in both HFIR and EBR-II can be interpreted as being identical, inspite of the difference in the helium bubble population.

In the present paper, we explore with rate theory the implication of considering voids and bubbles as different sinks, i.e. with different relative biases. Specifically, we ask how void swelling proceeds in the presence of helium bubbles which do not grow. The latter assumption is considered an approximation to the perhaps more realistic case that voids grow fast in comparison to bubbles.

5.2 Results

Based on rate theory, the void swelling rate is given by

$$\frac{d}{dt}\left(\frac{\theta^{Av}}{V}\right)_o = S_o Z_v^o D_v \left\{\left[\frac{Z_i}{Z_v} - \frac{Z_i^o}{Z_v^o}\right]\Gamma - \left[C_v^o - \overline{C_v^{eq}}\right]\right\} \tag{1}$$

where

$$\Gamma = \frac{S}{2\lambda}\left\{\sqrt{\alpha^2 + \beta} - \alpha\right\} \tag{2}$$

$$\lambda = 4\pi R_o/\Omega = 32\ \pi/a_o^2 \tag{3}$$

$$\alpha = 1 + \lambda\overline{C_v^{eq}}/(SZ_i) \tag{4}$$

$$\beta = 4\lambda D_v P/(S^2\ Z_i Z_v) \tag{5}$$

$$S_o = 4\pi r_o N_o \tag{6}$$

$$C_v^o = C_v^{eq}\ \exp\left[\left(\frac{2\gamma}{r_o} - p_o\right)\frac{\Omega}{kT}\right] \tag{7}$$

Here, $R_c = 2a_o$ is the recombination radius, a_o the lattice parameter, Ω the atomic volume, D_v the vacancy migration coefficient, r_o the average void radius, N_o the void density, γ the surface energy, and p_o the gas pressure inside the void.

The total sink strength is composed of various contributions,

$$S = S_o + S_b + S_d \tag{8}$$

where

$$S_b = 4nr_b N_b \tag{9}$$

denotes the sink strength of bubbles and S_d that of the remaining sinks other than voids and bubbles. Each sink type possesses its bias factors Z_v^s and Z_i^s as well as a vacancy concentration C_v^s in thermodynamic equilibrium with the sink type "s".

The sink-averaged bias factors are then defined as

$$\bar{Z}_{i,v} = (Z^o_{i,v}S_o + Z^b_{i,v}S_b + Z^d_{i,v}S_d)/S \tag{10}$$

and the average thermal vacancy concentration as

$$\overline{C^{eq}_v} = (C^o_v Z^o_v S_o + C^b_v Z^b_v S_b + C^d_v Z^d_v S_d)/(\bar{Z}_v S) \ . \tag{11}$$

The swelling rate due to bubble growth is given by the equation

$$\frac{d}{dt}\left(\frac{\Delta v}{v}\right)_b = S_b Z^b_v D_v \left\{\left[\frac{\bar{Z}_i}{\bar{Z}_v} - \frac{Z^b_i}{Z^b_v}\right]\Gamma - \left[C^b_v - \overline{C^{eq}_v}\right]\right\} \ . \tag{12}$$

The total swelling rate is then the sum of the two expressions in Eqs. (1) and (12).

In the absence of radiation-induced segregation and chemisorption of surface-active impurities, the bias factors of voids and bubbles are nearly identical. In fact, the major contribution to Z^b and Z^o originates from the image interaction which is independent of the gas pressure, and it leads to a very significant interstitial bias particularly for small voids or bubbles. In order for voids to nucleate, some segregation is required to eliminate this cavity bias, as has been shown recently.(3)

Based on this important role of segregation on the cavity bias, it appears then that voids are not only distinct from bubbles with regard to the internal gas pressure, but also with regard to their bias factors. Obviously, the void bias factor $Z^o_i < Z^b_i$ or else the bubbles would have evolved into voids.

Accordingly, we may assume that

$$\frac{d}{dt}\left(\frac{\Delta v}{v}\right)_o >> \frac{d}{dt}\left(\frac{\Delta v}{v}\right)_b \cong 0$$

By setting Eq. (12) equal to zero, we can solve for Z^b_i/Z^b_v and eliminate this

bias factor ratio from the average bias factor ratio $\bar{Z}_i/\bar{Z}_v$ as defined by Eq. (10). We note that even though Z_i^b/Z_v^b depends on C_v^b, the final result for the void swelling rate becomes independent of both Z_i^b/Z_v^b and C_v^b. This result is easily obtained after elementary but length algebraic manipulation which we will not repeat here. As an intermediate result we find

$$\frac{d}{dt}\left(\frac{\Delta V}{V}\right)_o = D_v\left\{\frac{S_o Z_v^o S_d Z_i^d - S_o Z_i^o S_d Z_v^d}{S_o Z_v^o + S_d Z_v^d}\,\Gamma \cdot \frac{S_o Z_v^o S_d Z_v^d}{S_o Z_v^o + S_d Z_v^d}\,(C_v^o - C_v^d)\right\} \tag{13}$$

Let us now define bias factors averaged over all sinks but excluding bubbles as

$$\tilde{Z}_{i,v} = (S_o Z_{i,v}^o + S_d Z_{i,v}^d)/\tilde{S} \tag{14}$$

where $\tilde{S} = S_o + S_d$. Similarly, we may define a sink-averaged thermal vacancy concentration for all sinks except bubbles as

$$\tilde{C}_v^{eq} = (C_v^o Z_v^o S_o + C_v^d Z_v^d S_d)/(\tilde{Z}_v \tilde{S}) \ . \tag{15}$$

Then, it is easy to show again by elementary (but lengthy) algebra that

$$\frac{d}{dt}\left(\frac{\Delta V}{V}\right)_o = S_o Z_v^o D_v\left\{\left[\frac{\tilde{Z}_i}{\tilde{Z}_v} - \frac{Z_i^o}{Z_v^o}\right]\Gamma - [C_v^o - \tilde{C}_v^{eq}]\right\} \tag{16}$$

This equation has a form identical to Eq. (1) but contains no bubble parameters except in the function Γ. The latter function becomes however independent of the total sink strength when $S \gtrsim 5 \times 10^{10}$ cm^{-2} for the temperature range of ~ 350°C to ~ 650°C.[4] As a result, the bias-driven void swelling rate becomes altogether independent of the bubble sink strength.

We can therefore draw the important conclusion that the presence of small gas bubbles which grow at a much lower rate than voids has no effect whatsoever on the void swelling rate, once the total sink strength reaches the value of ~ 5×10^{10} cm^{-2}. This is the case for austenitic steels irradiated to fluences where swelling commences. The present conclusion is of course valid

only as long as gas-driven bubble swelling is negligible, i.e. for temperatures $ 600°C and displacement rates of ~ 10^{-6} dpa/s. In fact, the conclusion only applies to the bias-driven swelling. Therefore, when gas-driven swelling becomes significant, the total swelling rate is simply the void swelling rate evaluated as if the bubbles were not there plus the gas-driven bubble swelling rate evaluated as if the voids were not there. In short, void and bubble swelling can be treated independently, and they are simply additive.

6.0 References

1. B. A. Loomis, G. Ayrault, S. Gerber, and Z. Wang, "Cavity Formation and Solute Segregation in Dual-Ion Irradiated Fe-20Ni-15Cr Alloys," DAFS Quarterly Progress Report, DOE/ER-0046/10, August 1982.

2. H. R. Brager and F. A. Garner, "The Radiation-Induced Evolution of AISI 316 (DO-Heat) in HFIR and EBR-II," DAFS Quarterly Progress Report, DOE/ER-0046/7, November 1981.

3. A. Si-Ahmed and W. G. Wolfer, "Effect of Radiation-Induced Segregation on Void Nucleation," Effects of Radiation on Materials, Eleventh Internat. Symp., ASTM STP 782, H. R. Brager and J.S. Perrin. Eds., American Soc. for Testing and Materiais, 1982, p. 1008.

4. W. G. Wolfer and F. A. Garner, "Temperature Dependence of the Swelling Rate in Austenitic Stainless Steels," this progress report.

7.0 Future Work

Mechanisms other than bias-driven growth will be evaluated for helium bubble growth, and the implications on void swelling will be further investigated.

GROWTH MECHANISMS FOR HELIUM INCLUSIONS AND BUBBLES

W. G. Wolfer and B. B. Glasgow (University of Wisconsin)

1.0 Objective

The distribution of helium in the form of clusters and bubbles has an important effect on the microstructure and on the mechanical properties of irradiated materials. The purpose of this study is to investigate the mechanisms by which helium inclusion and bubbles can grow as a function of the helium concentration and temperature.

2.0 Summary

Small clusters of helium atoms and vacancies have a significant interaction with self-interstitials. As a result, their growth is not bias-driven, but pressure-driven. Three mechanisms are considered for this type of growth: self-interstitial ejection, dislocation loop punching, and stress-assisted thermal vacancy absorption. Under the assumption that the overpressure in the helium cluster is the driving force for all three mechanisms, it is shown that the interstitial ejection is the dominant mechanism for the growth of bubbles with radii less than about 5 to 10 Burgers vectors, while loop punching becomes dominant for larger radii. Finally, thermal vacancy absorption becomes important at still larger radii and temperatures $\lesssim$ 700 K. Above 800 K, and for helium production rates of 10^{-4} appm/s, however, the thermal vacancy absorption is the dominant growth mechanism at all bubble radii.

3.0 Program

Title: Effect of Radiation and High Heat Flux on the Performance of First Wall Components

Principal Investigator: W. G. Wolfer

Affiliation: University of Wisconsin-Madison

4.0 Relevant DAFS Program Plan Task/Subtask

Task II.C.2 Effects of Helium on Microstructure

5.0 Accomplishment and Status

5.1 Introduction

The energy of solution of helium atoms in metals has been shown to be highly negative,[1] indicating insolubility no matter how small the concentration. As a result, it will be energetically favorable for the helium atom to become substitutional, and for more helium atoms to precipitate out in the form of inclusions or overpressurized bubbles. The helium precipitates need not always assume a three-dimensional configuration. Evans et al.[2] have found helium platelets in Mo implanted with helium ions at low temperatures. Upon annealing, the platelets transformed between 600 and 800°C into sheets of small bubbles.

Since the activation energy for interstitial helium migration is on the order of 0.5 eV in fcc metals,[3] any helium atoms either implanted or produced by transmutations will migrate at elevated temperatures and become trapped in vacancies and already existing helium-vacancy clusters. The formation of such clusters has been studied with computer simulation by Wilson and co-workers[4,5] on an atomistic basis. It was shown that up to 5 helium atoms can be trapped in one vacancy. Trapping of additional helium atoms leads then to the creation of self-interstitials which remain however attracted to the helium-vacancy cluster. This athermal growth of helium clusters into bubbles was further investigated with a rate-theory model by Baskes et al.[6] They concluded that the athermal emission of self-interstitials by bubbles which trap more helium atoms can indeed provide an explanation for the formation of the high density of bubbles which preceeds blistering at low temperatures. In all these theoretical studies, effects due to lattice vibrations were not considered; in essence, the results are strictly valid for 0 K only. In ad-

dition, rather small helium-vacancy clusters were modeled containing only a few helium atoms and vacancies. The transition to larger bubbles requires therefore further investigation.

Evans[7] has proposed that the overpressure in helium bubbles is relieved by punching of interstitial-type loops. Again, this is an athermal mechanism of bubble growth.

Finally, it is well known that at elevated temperatures above ~ 0.5 T_m, helium bubbles may grow by the absorption of thermal vacancies. In the present paper, we investigate further the above mentioned mechanisms for helium cluster growth, i.e. interstitial emission, loop punching, and thermal vacancy absorption. The purpose of the investigation is threefold. First, we like to include the effect of temperature for all three mechanisms. Second, we want to find which of these mechanisms is the predominant one for a given temperature, a given helium concentration, and for a given microstructure to be defined below. Third, we wish to extend previous investigations restricted to small helium clusters to larger clusters and bubbles as seen in electron-microscopy studies.

Our present approach is restricted to rather simple considerations aimed at obtaining order of magnitude answers. Refinements will be made in future investigations. The central assumption made here is that the actual bubble growth mechanism is the one which requires the least amount of work to be performed by the helium pressure.

5.2 Bubble Growth by Self-Interstitial Emission

Suppose that the rate of helium generation or implantation is $\dot{P}_{He}$ (per metal atom and per second), and that there are already N_B helium bubbles per unit volume of average radius R. Let us further assume that a stationary condition has been reached such that each new helium atom generated or implanted will after some time be trapped at one of the already existing bubbles. In ad-

dition, the ratio of helium atoms to vacancies in the bubble, η, shall remain constant, and any newly acquired helium atom in a bubble induces the emission of a self-interstitial. The build-up of a significant interstitial concentration around the growing bubble is prevented by their migration to distant sinks. It is then obvious that the following relationship is valid:

$$P_{He} = \eta 4\pi R N_B D_I C_I^o \quad . \tag{1}$$

Here, D_I is the diffusion coefficient for interstitials and

$$C_I^o = C_I^{eq} \exp[(p - \frac{2\gamma}{R}) \frac{\Omega}{kT}] \tag{2}$$

is the interstitial concentration in local thermodynamic equilibrium with the bubble having an internal gas pressure of p. The surface tension is denoted by γ and the volume per metal atom by n. The thermal interstitial concentration, C_I^{eq}, is defined as

$$C_I^{eq} = \exp(-E_I^f/kT) \tag{3}$$

where E_I^f is the formation energy for a self-interstitial. Although this energy is so large that $C_I^{eq} \cong 0$, a sufficiently high pressure p can render the exponent $(-E_I^f + p\Omega)/kT$ sufficiently large so that $C_I^o >> C_I^{eq}$. Using the relation

$$D_I = D_I^o \exp(-E_I^m/kT) \tag{4}$$

where D_I^o is a constant, we obtain for the work done by the gas pressure per self-interstitial emission

$$p\Omega = 2\gamma\Omega/R + E_I^f + E_I^m + kT \ln [\dot{P}_{He}/\eta 4\pi R N_B D_I^o] \quad . \tag{5}$$

In evaluating Eq. (5), the materials parameters listed in Table 1 were employed. It is found that the overwhelming contribution to the work $p\Omega$ comes

TABLE I

MATERIALS PARAMETERS FOR NICKEL AND AUSTENITIC STAINLESS STEELS

Parameter	Symbol	Value	Unit
Lattice parameter	a_o	0.364	nm
Burgers vector	b	$a_o/\sqrt{2}$	nm
Atomic volume	Ω	$a_o^3/4$	
Surface energy	γ	2	J/m^2
Stacking fault energy	γ_f	0.3	J/m^2
Shear modulus	μ	10^{12}	Pa
Poisson's ratio	ν	0.3	
Vacancy formation entropy	S_v^f	1.5 k	
Vacancy formation energy	E_v^f	1.8	eV
Vacancy migration energy	E_v^m	1.1	eV
Interstitial formation energy	E_I^f	3-5	eV
Interstitial migration energy	E_I^m	0.2	eV
Pre-exponential factors			
for vacancy diffusion	D_v^o	0.0153	cm^2/s
for interstitial diffusion	D_I^o	0.001	cm^2/s
Bubble density	N_B	10^{17}-10^{19}	cm^{-3}

from the interstitial formation energy E_I^f. In contrast, the parameters N_B, $\dot{P}_{He}$, π, and T can be varied over large ranges without much change in the work required to emit an interstitial. This is seen from the results shown in Fig. 1. Here, the shaded band covers the values for $p\Omega$ when the helium generation rate is varied between 100 and 1000 appm/s, the bubble density between 10^{17} and 10^{19} cm^{-3}, and the temperature between 300 K and 900 K. Furthermore, the work is only weakly dependent on the bubble radius R.

5.3 Loop Punching

Instead of the emission of one interstitial at a time, it is possible that an entire interstitial platelet may be emitted. Assuming that its radius R is

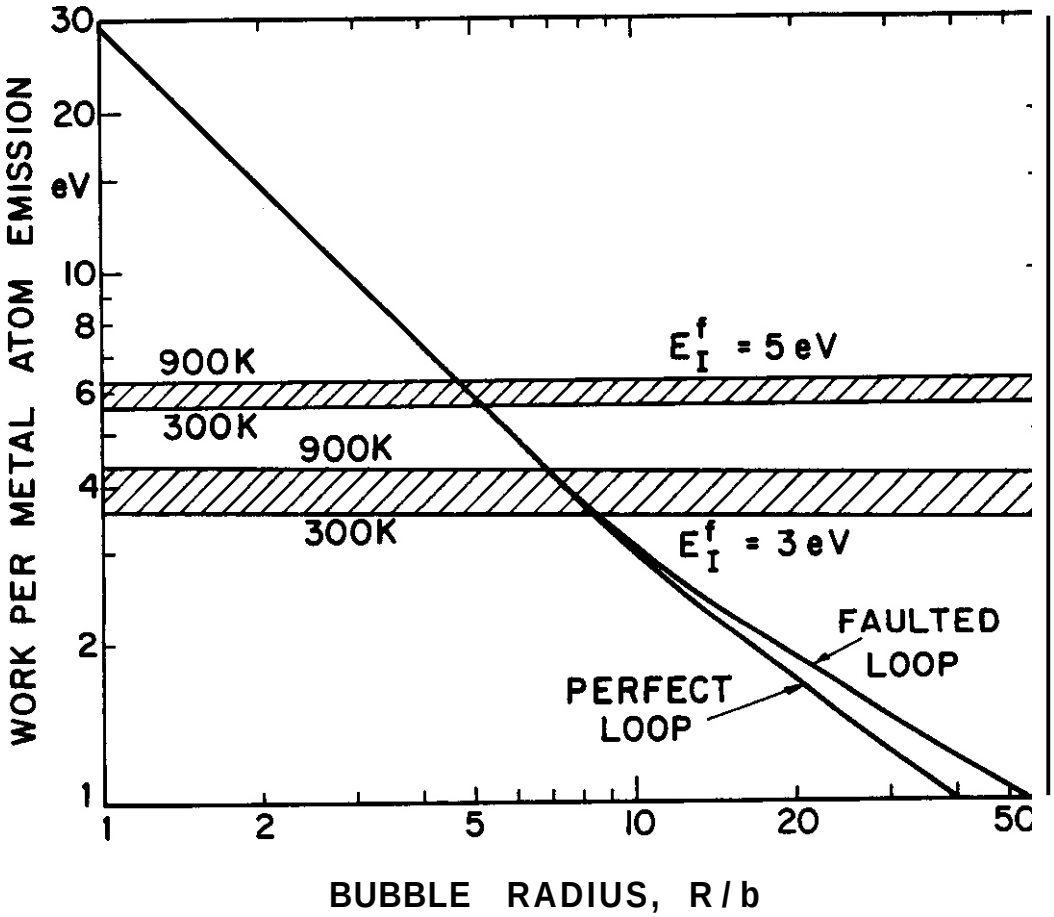

FIGURE 1. Energy Expended per Metal Atom Emitted When Bubble Growth Occurs by Self-Interstitial Emission or Punching of Interstitial Loops.

equal to the bubble radius, the energy expended in this process is the dislocation loop energy. For sufficiently large loop radii, this energy is given by

$$E_{FL} = \frac{\mu b}{2(1-\nu)} R\left[\ln \frac{R}{r_o} + 2 \ln 2 - 1\right] + \pi R^2 \gamma_f \qquad (6)$$

for a faulted loop and by

$$E_{PL} = \frac{\mu b}{\sqrt{6}\,(1-\nu)} R\left[\left(1-\frac{\nu}{6}\right)\left(\ln\frac{R}{r_0} + 2\ln 2\right) - \frac{4}{3}\left(1-\frac{\nu}{4}\right)\right] \tag{7}$$

for a perfect loop.[8] Here, r_0 is the dislocation core radius.

For small loops, the above expressions become invalid. Based on computer simulation results of small interstitial clusters, Trinkaus[9] proposes the following approximation for the energy of a small interstitial loop

$$E_{IC} = 8\pi\mu R/a_0. \tag{8}$$

In order to obtain a continuous dependence of the loop energy on its radius R, we have chosen the core radius r_0 such that $E_{IC} \cong E_{PL}$ or $E_{IC} \cong E_{FL}$ at R = 10 b. This particular matching is accomplished with $r_0 \cong 0.1$ b.

The work performed per metal atom emission is now given by

$$p\Omega = 2\gamma\Omega/R + E_L\Omega/(\pi R^2 b) \tag{9}$$

where E_L is either equal to E_{IC} when $R < 1.0$ b, or equal to E_{FL} or E_{PL} for larger loop radii. We note, that for $R < 10$ b, Eq. (9) gives the simple relationship

$$p\Omega = (2\gamma + \mu b)\Omega/R\ . \tag{10}$$

Figure 1 shows the work expended per metal atom emission according to Eq. (9). It is seen that the loop punching mechanism requires less work per atom for bubble radii greater than 5 to 10 Burgers vectors when compared to the interstitial emission process.

It is important to note, however, that the actual energy expended in the loop punching process is equal to the loop energy plus the additional surface energy. If n is the number of interstitials contained in the loop, then the

actual work done is equal to $np\Omega$. Therefore, the process of loop punching may in fact require a large activation energy. The above comparison based on the energy expended per atom emission represents therefore only a necessary condition but not a sufficient one for the loop punching process to occur.

5.4 Thermal Vacancy Absorption

The vacancy concentration in local thermodynamic equilibrium with a bubble is given by

$$C_v^o = C_v^{eq} \exp(+p_o\Omega/kT) \tag{11}$$

where

$$-p_o = P - 2\gamma/R \tag{12}$$

and

$$C_v^{eq} = \exp[S_v^f/k - E_v^f/kT] \ . \tag{13}$$

If σ_H represents the hydrostatic stress in the matrix of the solid which contains the bubbles, then the vacancy concentration in local thermodynamic equilibrium with dislocations and grain boundaries is given by

$$C_v^u = C_v^{eq} \exp(\sigma_H\Omega/kT) \ . \tag{14}$$

An overpressure in the bubbles ($p_o < 0$) will cause a hydrostatic tension in the matrix. As shown in the Appendix, this hydrostatic stress is approximately given by

$$\sigma_H \cong -p_o S^2 \tag{15}$$

where S is the volume fraction of the bubbles. Due to the overpressure in bubbles, $C_v^d > C_v^{eq} > C_v^o$, and a thermal vacancy flux will be induced from dislocations and grain boundaries to the bubbles. Under stationary conditions, the rate of helium generation becomes then equal to the rate of helium capture at bubbles. In turn, this rate is then also equal to the rate of vacancy ab-

sorption at bubbles. Hence

$$P_{He} = \eta 4\pi R N_B D_v C_v^{eq} \{\exp(-p_o S^2 \Omega/kT) - \exp(+p_o \Omega/kT)\} \quad . \tag{16}$$

This equation can be solved only numerically for $p\Omega$. However, when $|p_o|\Omega/kT << 1$, we may expand the exponentials to first order and obtain

$$p\Omega \cong 2\gamma\Omega/R + kT\dot{P}_{He}/[(1 + S^2)\eta 4\pi R N_B D_{SD}] \tag{17}$$

where $D_{SD} = D_v C_v^{eq}$ is the self-diffusion coefficient. On the other hand, when $(-p_o\Omega/kT) >> 1$, we may neglect the second term in the brackets of Eq. (16), and we obtain the approximation

$$p\Omega \cong 2\gamma\Omega/R + (kT/S^2)\ \ln[\dot{P}_{He}/(\eta 4\pi R N_B D_{SD})] \quad . \tag{18}$$

Equation (16) was solved numerically for $p\Omega$ as a function of the bubble radius R. The results are shown in Figs. 2 and 3. For a helium production rate typical of (n,α) transmutations in HFIR or future fusion reactors, the results in Fig. 2 show that thermal vacancy absorption is the predominant mechanism of bubble growth for irradiation temperature > 800 K. As the swelling due to bubble growth increases, however, the hydrostatic stress σ_H increases in the matrix; and vacancy emission at dislocations can occur at somewhat lower temperatures. Consider, for example, irradiation at 700 K. Initially, small helium clusters grow by interstitial emission until their diameter reaches about ~ 2 nm; then, further growth occurs most likely by loop punching until the bubble swelling reaches about 10%. From then on, bubble growth takes place by thermal vacancy emission at dislocations and absorption at the bubbles.

If the helium concentration increases at a rate of 1000 appm/s as in helium implantation studies for blistering, the transition from one growth mechanism to another occurs at higher temperatures, as shown in Fig. 3.

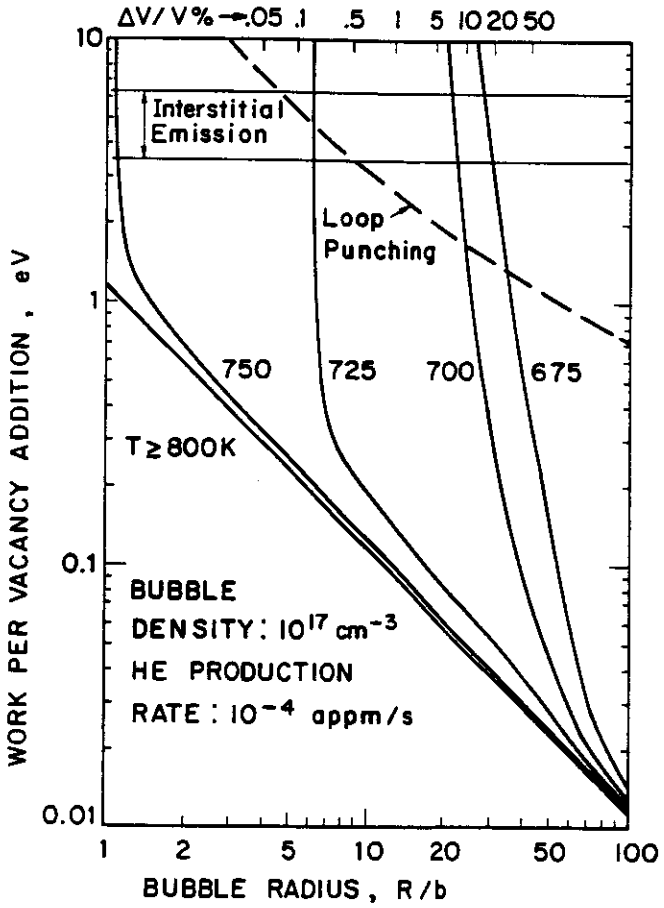

FIGURE 2. Energy Expended per Thermal Vacancy Absorption at a Bubble for Helium Production by Transmutations.

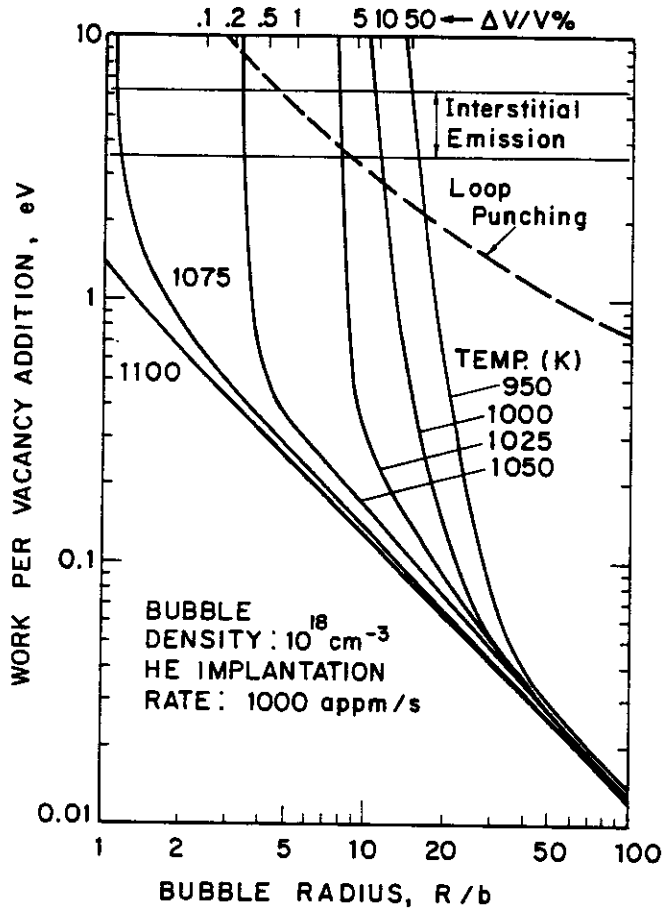

FIGURE 3. Energy Expended per Thermal Vacancy Absorption at a Bubble for Helium Implantation Typical of Blistering Studies.

5.5 Appendix: Hydrostatic Stress Produced By Bubbles

In order to evaluate the stress distribution around pressurized bubbles, we employ the following effective-medium approach. We divide the region around any one bubble into a cellular region $R < r < R_c$, where R is bubble radius and R_c is the cell radius defined such that the volume fraction of bubbles is given by

$$S = \Delta V/V = R^3/R_c^3 \ . \tag{A1}$$

Within this cellular region, the elastic modulii are those of the actual crystal lattice, and denoted by μ and κ for the shear and bulk modulus, respectively. The region $R > R_c$ is treated as an effective medium with average elastic modulii $\bar{\mu}$ and $\bar{\kappa}$.

The radial displacement field, assumed to be spherically symmetric, is given by

$$u(r) = c_1 r/3 + c_2/r^2 \tag{A2}$$

from which we can derive the stress field

$$\sigma_r(r) = \kappa c_1 - 4\mu c_2/r^3 \tag{A3}$$

$$\sigma_\psi(r) = \kappa c_1 + 2\mu c_2/r^3 = \sigma_\theta(r) \ . \tag{A4}$$

Identical expressions hold for the effective medium but with different constants $\bar{c}_1$ and $\bar{c}_2$ and different elastic modulii $\bar{\mu}$ and $\bar{\kappa}$. We denote the corresponding stresses by $\bar{\sigma}_r$, etc.

The four constants c_1, c_2, $\bar{c}_1$, and $\bar{c}_2$ are now determined by the following boundary conditions. On the cavity surface

$$\sigma_r(R) = -p_o = +p - 2\gamma/R \ , \tag{A5}$$

whereas at the cell boundary $r = R_c$

$$u(R_c) = \bar{u}(R_c) \tag{A6}$$

$$\sigma_r(R_c) = \bar{\sigma}_r(R_c) \ . \tag{A7}$$

Finally, on the external surface $r \to \infty$ of the solid

$$\bar{\sigma}_r(r \to \infty) = 0 \ . \tag{A8}$$

As a result of the last condition and Eq. (A3), we find $\bar{c}_1 = 0$ and

$$\sigma_H = \frac{1}{3}(\bar{\sigma}_r + a_\psi + \sigma_\theta) = 0 \ . \tag{A9}$$

However, in the cell region

$$\sigma_H = \frac{1}{3}(\sigma_r + \sigma_\psi + \sigma_\theta) = \kappa c_1 \ , \tag{A10}$$

Equations (A5) to (A7) lead to the relationships

$$\kappa c_1 - 4\mu c_2/R^3 = -p_o \tag{A11}$$

$$\kappa c_1 - 4\mu c_2/R_c^3 = -4\bar{\mu}\,\bar{c}_2/R_c^3 \tag{A12}$$

$$c_1 R_c^3/3 + c_2 = \bar{c}_2 \ . \tag{A13}$$

Solving these equations for c_1 we finally obtain the result

$$\sigma_H = -p_o\left(\frac{\mu}{\bar{\mu}} - 1\right)S/\left[1 + \frac{4\bar{\mu}}{3\kappa} + \left(\frac{\bar{\mu}}{\mu} - 1\right)S\right] \ . \tag{A14}$$

Various derivations have been reported in the literature for the effective

modulii of solids containing spherical cavities or inclusion of different materials.

Hashin[10] has derived the following upper and lower bounds for the shear mudulus:

$$\bar{\mu}(\text{upper})/\mu = 1 - 15(1 - \nu)S/[(7 - 5\nu) + 2(4 - 5\nu)S] \tag{A15}$$

$$\bar{\mu}(\text{lower})/\mu = 1 - 15(1 - \nu)S/[(7 - 5\nu) + F(S)S] \tag{A16}$$

where
$$F(S) = 2(4 - 5\nu) - \frac{126(1 - S^{2/3})^2}{(7 + 5\nu)(1 - S^{7/3})} \tag{A17}$$

With these effective shear moduli, the ratio $(-\sigma_H/p_0)$ is as shown by the curves labelled "H" in Fig. 4.

Christensen[11] reported the following for an upper bound of $\bar{\mu}$,

$$\bar{\mu}/\mu = 1 - 15(1-\nu)S[(7+5\nu)S^{7/3} + 4(7-10\nu)]/[(7-5\nu) - 2(4-5\nu)S]Q \tag{A18}$$

where
$$Q = 4(7-10\nu) + (7+5\nu)^{7/3} + 126S(1 - S^{2/3})^2 \ , \tag{A19}$$

and he claims it to be better than Hashin's. As the curve labelled "C" in Fig. 4 shows, his upper bound gives only a marginal improvement for $S \leq 0.2$, but worse results for $S > 0.2$.

Chen and Acrivos[13] have derived an expression for the effective shear modulus by considering also the stress-induced interaction between two cavities embedded into an effective medium. Their result is given by

$$\bar{\mu}/\mu = 1 - \frac{15(1 - \nu)}{7 - 5\nu} S + \frac{30(1 - \nu)(4 - 5\nu)}{(7 - 5\nu)^2} S^2 H_2(\nu) \tag{A20}$$

where $H_2(\nu) \leq 0.75$ is a function of the Poisson's ratio; for $\nu = 0.3$, $H_2 = 0.67$, whereas for $\nu = 0.4$, $H_2 = 0.6$. Hence, $H_2(\nu)$ is not very sensitive to small variations in ν. With Eq. (A20), we obtain the result shown by the

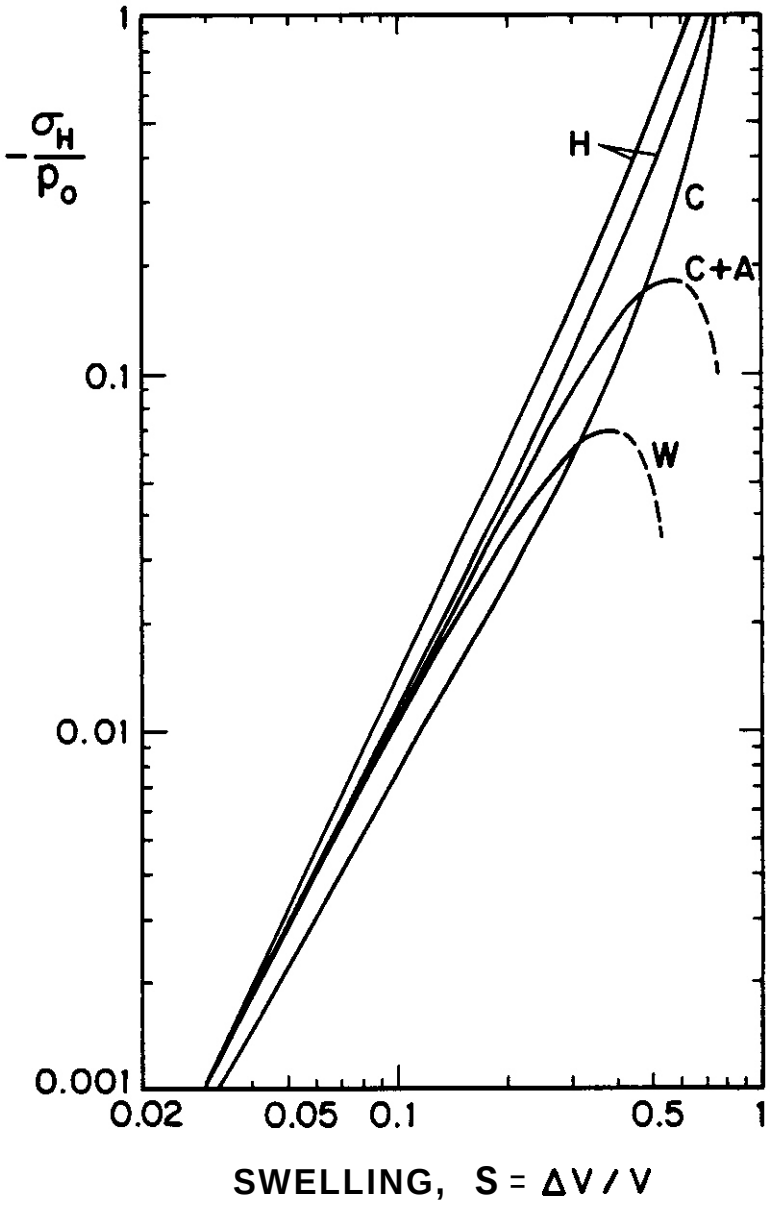

FIGURE 4. Hydrostatic Stress Produced in the Matrix of a Solid Containing Bubbles with Volume Fraction S and Net Pressure P_o.

curve labelled "C + A". Since Eq. (A20) represents a perturbation expansion in powers of S, additional terms would be required for $S \gtrsim 0.3$.

Walpole[12] has carried out a similar perturbation expansion but neglected the pair-interactions between cavities. In his case, $H_2 \equiv 1$, and we obtain the curve labelled "W" in Fig. 4. The various expressions for $\bar{\mu}$ give similar results for small values of S. In fact, we can approximate the curves shown in Fig. 4 by the simple expression

$$-\sigma_H/p_0 \cong S^2 \ . \tag{A21}$$

6.0 References

1. J. E. Inglesfield and J. B. Pendry, Phil. Mag. 34 (1976) 205.
2. J. H. Evans, A. van Veen, and L. M. Caspers, Nature 291 (1981) 310.
3. W. D. Wilson and C. L. Bisson, Phys. Rev. B3 (1971) 3984.
4. W. D. Wilson, M. I. Baskes, and C. L. Bisson, Phys. Rev. B13 (1976) 2470.
5. W. O. Wilson, C. L. Bosson, and M. I. Baskes, Phys. Rev. B24 (1981) 5616.
6. M. I. Baskes, R. H. J. Fastenau, P. Penning, L. M. Caspers, and A. van Veen, J. Nucl. Matls. 102 (1981) 235.
7. J. H. Evans, J. Nucl. Mater. 68 (1977) 129; also J. Nucl. Matls. 76 & 77 (1978) 228.
8. K.A. Jackson, Phil. Mag. 7 (1962) 1117.
9. Trinkaus, private communication.
10. Z. Hashin, J. Appl. Mech. 29E (1962) 143.
11. R. M. Christensen, J. Mech. Phys. Solids 17 (1969) 23.
12. L. J. Walpole, Q. J. Mech. Appl. Math. 25 (1972) 153.
13. H-S. Chen and A. Acrivos, Int. J. Solids Structures 14 (1978) 349.

7.0 Future Work

A more detailed investigation of the loop punching process will be carried out in order to find the activation barrier for this mechanism of bubble growth.

RADIATION-INDUCED EVOLUTION OF Fe-Ni-Cr TERNARY ALLOYS

H. R. Brager and F. A. Garner (Hanford Engineering Development Laboratory)

1.0 Objective

The object of this effort is to identify the microstructural and micro-chemical origins of the compositional dependence of radiation-induced swelling, creep and changes in mechanical properties.

2.0 Summary

Austenitic Fe-Ni-Cr alloys with nickel levels of ~35% tend to change their composition during irradiation. Some regions become enriched in nickel and depleted in chromium and iron, while other regions become depleted in nickel and enhanced in chromium and iron. This segregation should make it easier for voids to nucleate in the nickel-poor regions and also causes the alloy to densify substantially. Once the first voids nucleate, however, their surfaces become the major sink for nickel segregation which leads to a reduced matrix nickel level and subsequent easier nucleation of other voids.

3.0 Program

Title: Irradiation Effects Analysis (AKJ)
Principal Investigator: D. G. Doran
Affiliation: Hanford Engineering Development Laboratory

4.0 Relevant DAFS Program Plan Task/Subtask

Subtask II.C.l. Effect of Material Parameters on Microstructure

5.0 Accomplishments and Status

5.1 Introduction

In a previous report it was shown that the swelling of Fe-Ni-Cr alloys was sensitive to their chromium and nickel levels, and that reproducible immersion density measurements of swelling were obtained in two separate irradiation experiments.[1] Microscopy results on two specimens from the AA-VII experiment were also presented in that report. The first specimen was derived from alloy E25 (Fe-35.1Ni-21.7Cr) irradiated to 7.2 X 10^{22} n/cm2 (E > 0.1 MeV) at 538°C and the second was derived from alloy E37 (Fe-35.5 Ni-7.5Cr) irradiated to 7.6 X 10^{22} n/cm^2 (E > 0.1 MeV) at 593°C. The first specimen had developed 7.7% void-swelling and the second had densified 0.9%. This densification was accompanied by a small amount of swelling, mostly arising from small (≤5nm) cavities that are probably helium bubbles. Examination of these two specimens has continued, concentrating primarily on the microchemical aspects of their evolution.

5.2 Results

Since the E37 alloy was earlier shown to be near a minimum in density it was proposed that segregation of the alloy into regions that were enriched in nickel at the expense of other regions would lead to a net densification of the alloy.[1] The densification that occured in the E37 specimen could not be correlated with the formation of any visible precipitate phases. It was decided, therefore, to measure the compositional variation of the E37 matrix at fixed intervals along a traverse across the specimen.

Figure 1 shows one of four traverses that were made within a single grain using 200 nm EDX sampling intervals and a beam width of 20-40 nm. Fairly large changes in composition were found in such traverses and the figure demonstrates the reproducibility of such measurements. Note that whenever the nickel level was above that of the bulk average concentration, the chromium level tended to be below its bulk-averaged concentration.

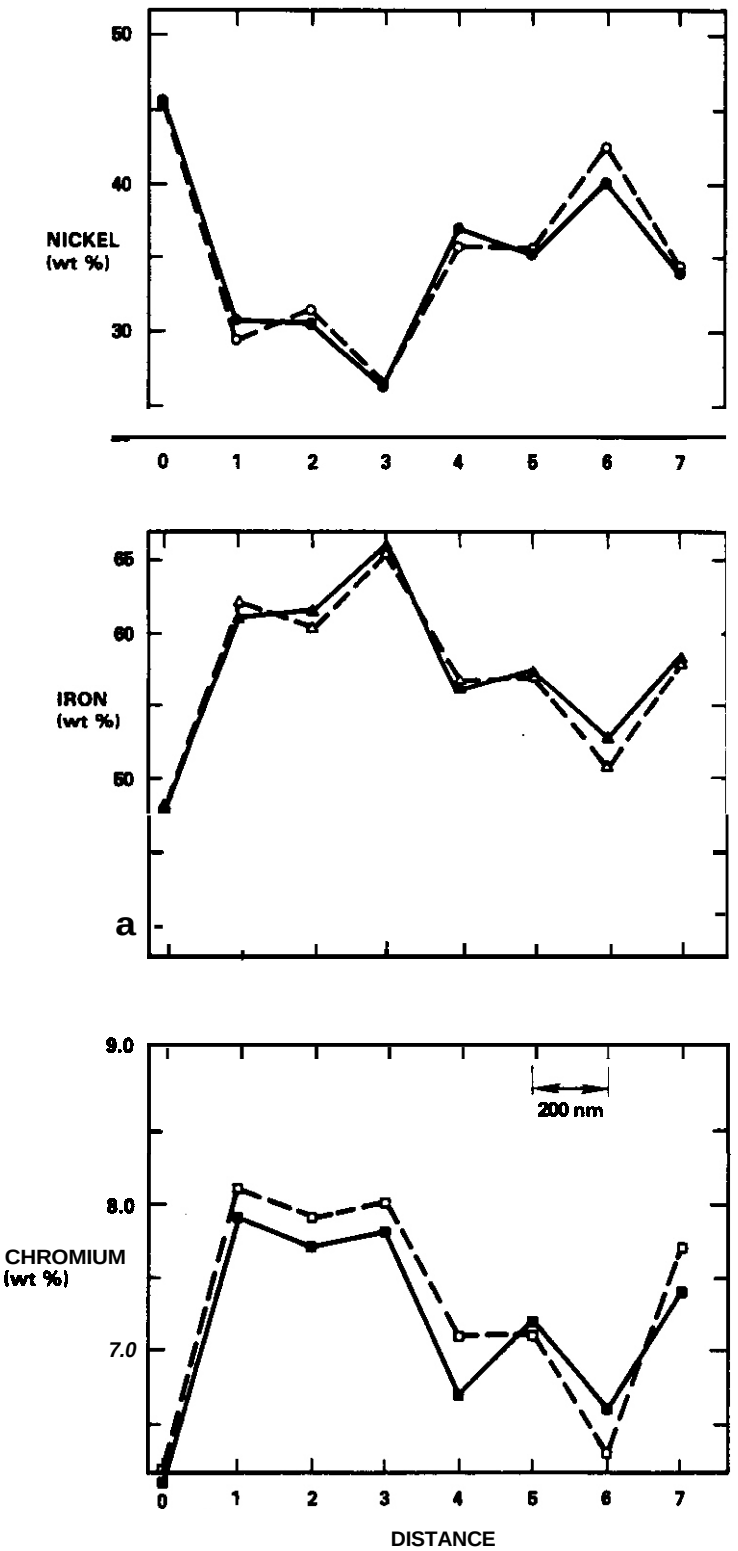

FIGURE 1. Variation of Alloy E37 Matrix Composition Measured at 200-nm Intervals Along a Traverse Across the Specimen. The two lines in each graph represent measurements on separate days, each starting from an identifiable microstructural feature. In this case a void (∿30-nm diameter) is located at point 0.

Correspondingly, when the nickel level was lower than the bulk-average level the chromium level was higher. Iron behaved in a manner similar to that of chromium. Since the alloy densified during irradiation, it is assumed that the compositional variations did not occur prior to irradiation, although this latter possibility is now being investigated.

This trend is better illustrated in Figure 2, in which ~100 compositional measurements of small areas in four separate grains (using ~30 nm diameter electron beam) show a persistent tendency of the alloy to exhibit enhanced nickel at the expense of chromium in some areas and to do the opposite in other areas. The iron concentration follows the same trend as that of the chromium. Variations in the nickel level between 25 and 55% were found which could easily lead to the observed densification of 0.9%.[1] There were very few voids ($\sim 10^{12}$ cm^{-3}) observed in the E37 specimen and they tended to segregate nickel at their surfaces and to reject iron and chromium, as shown in Figure 3. The voidage in this specimen is not sufficiently large to lead to a net compositional change in the matrix, however.

The E25 alloy also exhibited an absence of precipitation but contained a moderate density ($\sim 10^{15}$ cm^{-3}) of voids. Figure 4 shows significant segregation of nickel to the void surfaces in alloy €25, reaching line-of-sight average concentrations approaching 55%. Preliminary results of unfolding analyses indicate that the actual concentration of nickel at the void surface is on the order of 80%. This level of segregation has significantly changed the matrix composition. Note that away from the void surface shown in Figure 4 the nickel level has dropped below the bulk-averaged 35% level. A series of seventeen spot measurements between voids showed that the alloy matrix had developed a mean nickel concentration of 30.5%. The matrix chromium level had increased from 21.7 to 23.6% and the iron had increased from 43.2 to 45.9%.

5.3 Discussion

The tendency of nickel to segregate into precipitates and deplete the matrix of 300 series stainless steels is well-known.[2] In the Fe-Ni-Cr austenitic

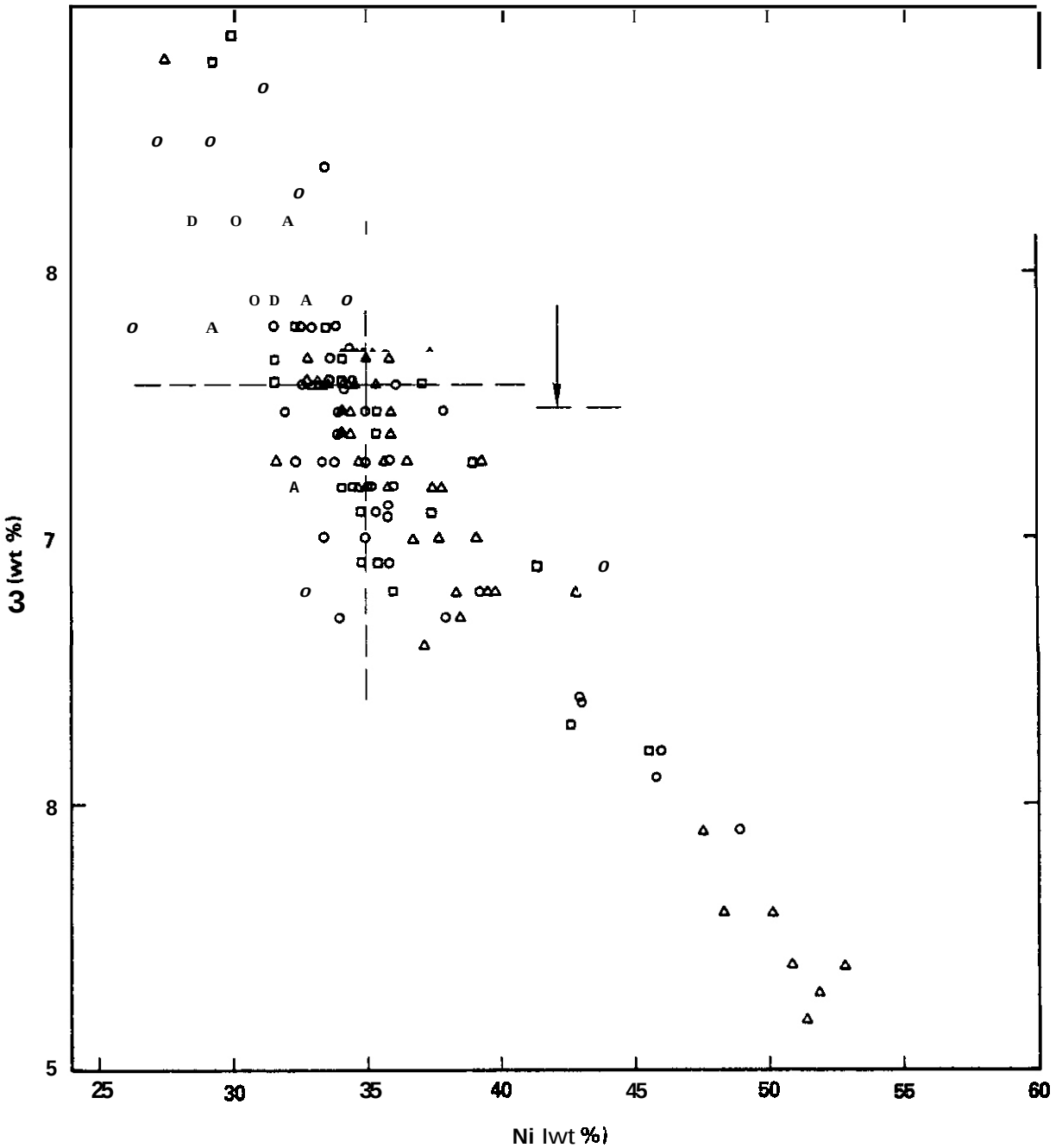

FIGURE 2. Relationship Between Nickel and Chromium Levels in Specimen E37, as Measured in Small Areas ∿30 nm in Size. The three symbols shown on this figure denote measurements on three different days.

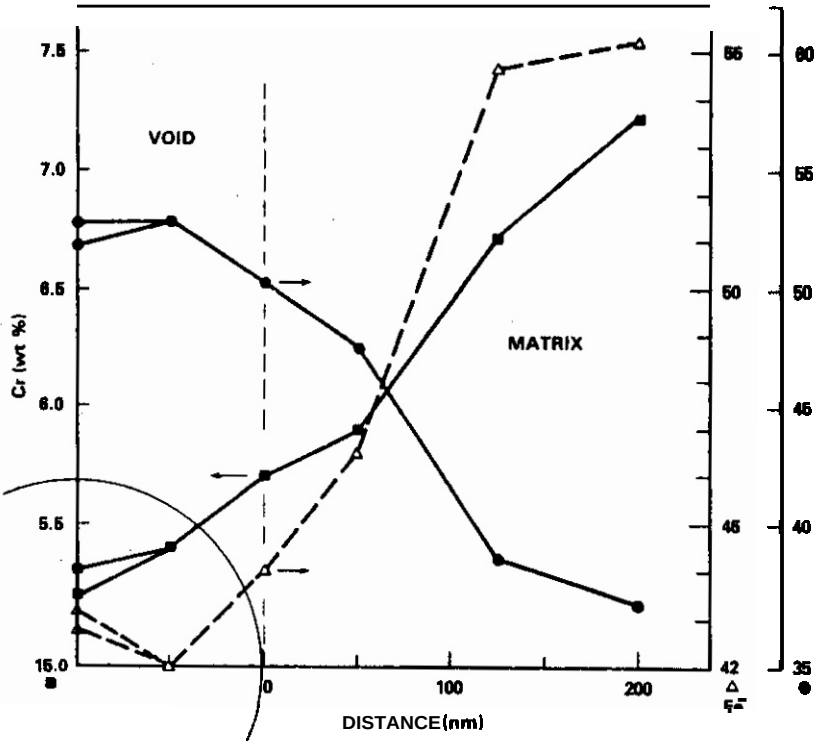

FIGURE 3. Segregation of Nickel Near **a** Void Surface in Specimen E37.

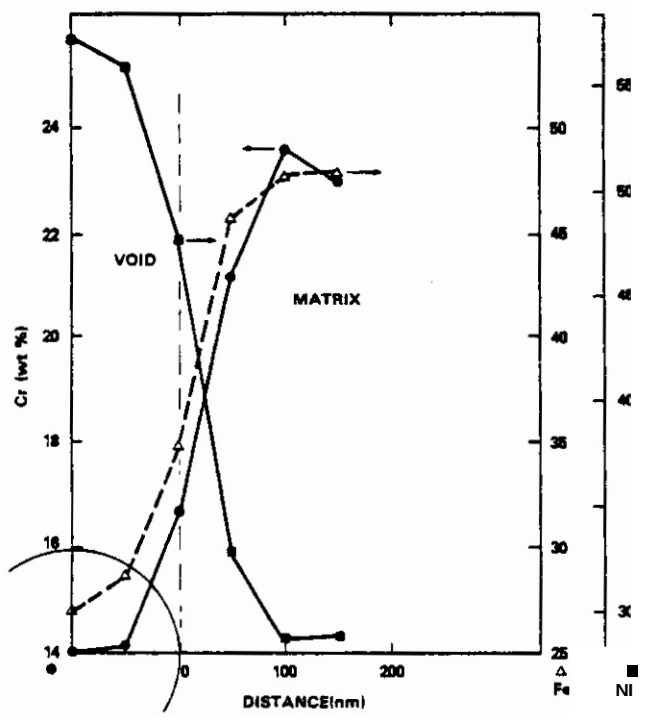

FIGURE 4. Segregation of Nickel Near a Void Surface in Specimen E25. The large reduction of nickel in the matrix **is** a consequence.

ternary system being investigated, however, no precipitates form when solutes such as silicon and carbon are absent. It appears, however, that the voids can become a major sink for nickel once they form, reducing the matrix nickel level substantially. It has also been shown, however, that high nickel levels[2] and low chromium levels[3] tend to discourage void nucleation. The lower chromium level of E37 is thus thought to be the major reason why swelling has not yet started in E37 while it has in E25, which contains 21.7% chromium.

It also appears, however, that the E37 alloy tends during irradiation to develop compositional zones, some of which are depleted in nickel and enriched in chromium. These zones would then be the most likely sites for void nucleation. Once nucleated, however, it is anticipated that the voids will become sinks for nickel and will begin to draw down the matrix level of nickel. In effect, the growth of each void would make it easier for the next one to nucleate.

The origin of the pre-void segregation of nickel may arise from segregation at microstructural sinks such as Frank loops or by a process of spinodal decomposition. Frank loops were not found at significant densities in either of these specimens,[1] so if they were the source of the segregation, there must be a tendency for the segregation to persist after the loops have unfaulted. This also suggests a tendency toward spinodal behavior. This possibility is now being investigated.

5.4 Conclusion

Austenitic Fe-Ni-Cr alloys with nickel levels of ~35% tend to change their composition during irradiation. Some regions become enriched in nickel and depleted in chromium and iron, while other regions become depleted in nickel and enhanced in chromium and iron. This segregation should make it easier for voids to nucleate in the nickel-poor regions and also causes the alloy to densify substantially. Once the first voids nucleate, however, their surfaces become the major sink for nickel segregation which reduces the matrix nickel level, and makes it easier for other voids to nucleate.

6.0 References

1. H. R. Brager and F. A. Garner, "Dependence of Swelling of Fe-Ni-Cr Alloys on Chromium and Nickel Content," Damage Analysis and Fundamental Studies, Quarterly Progress Report, DOE/ER-0046/11, pp. 221-231, November 1982.

2. F. A. Garner, "The Microchemical Evolution of Irradiated Stainless Steels," in Phase Stability During Irradiation, J. R. Holland, L. K. Mansur and D. I. Potter, Eds., AIME, pp. 165-184, 1981.

3. W. G. Johnston, T. Lauritzen, J. H. Rosolowski and A. M. Turkalo, "The Effect of Metallurgical Variables On Void Swelling," Radiation Damage in Metals, ASM, Cleveland, OH, p. 227, 1976.

7.0 Future Work

This effort will continue, with emphasis being placed on microscopy examination of additional specimens, measurement of shear modulii of unirradiated Fe-Ni-Cr alloys and development of theories to explain the compositional dependence of swelling.

8.0 Publications

None.

THE INFLUENCE OF REACTOR SPECTRA AND IRRADIATION TEMPERATURE ON THE SWELLING OF AISI 316 STAINLESS STEEL

F. A. Garner (Hanford Engineering Development Laboratory)

1.0 Objective

The object of this effort is to determine the effect on swelling of differences in helium/dpa ratio as well as in differences in other variables arising from comparative irradiations in HFIR and EBR-II.

2.0 Summary

The swelling data base for the DO-heat of AISI 316 has been reanalyzed to include the impact of additional displacements produced by the ^{56}Fe recoil resulting from the $^{59}Ni(n,\alpha)$ reaction. Also included for the first time are three additional data on the swelling of annealed DO-heat that were inadvertently excluded from the previous analysis. Comparisons are made with swelling data from other heats of steel irradiated in various fast reactors. The results of this study confirm the proposal that the additional helium generated in HFIR does not substantially alter the swelling behavior of AISI 316 from that observed in EBR-II.

3.0 Program

Title: Irradiation Effects Analysis
Principal Investigator: D. G. Doran
Affiliation: Westinghouse Hanford Co.

4.0 Relevant Program Plan Task/Subtask

Subtask IIC.2 Effect of He on Microstructure
IIC.4 Effect of Solid Transmutants on Microstructure

5.0 Accomplishments and Status

5.1 Introduction

In a previous report it was shown that two separate interpretations have arisen concerning the limited amount of swelling data for 20% cold-worked 00-heat AISI 316 irradiated in HFIR and EBR-II.[1] A reanalysis of this data has been performed since the HFIR portion of these data are now known to require increases in their assigned displacement levels. These increases arise from the previously unsuspected displacements resulting from the recoil of the ^{56}Fe atom produced in the $^{59}Ni(n,\alpha)$ reaction.[2,3] The displacement assignments for the earliest data on DO-heat irradiated in EBR-II[4,5] also require adjustment since the reported dpa levels are inconsistent with the reported neutron fluences. Averaged over the positions in which the DO-heat data were irradiated in EBR-II, the conversion factor is ~5.0 dpa per 1×10^{22} n/cm^2 (E > 0.1 MeV). A value of 5.6 dpa per 10^{22} n/cm2 was previously employed.[4]

In addition there were two data on annealed DO-heat from EBR-II[3] and another from HFIR[4,5] that were not included in the earlier analysis[1]. The temperatures shown in this report are the originally reported nominal temperatures. Most of these are lower estimates of the actual irradiation temperatures. The most complete list of HFIR data on cold-worked DO-heat steel is contained in Reference 6.

5.2 Reanalysis of Swelling Data

One of the major influences of the neutron spectra is in the atomic displacement efficiency per neutron. When the neutron fluence is reported for energies above 0.1 MeV, the HFIR spectrum is ~40% more effective per neutron in creating displacements when compared to the EBR-II spectrum. It is assumed in this study that displacements per atom is an adequate exposure parameter.

As discussed earlier there is substantial incentive for treating the DO-heat cold-worked swelling data in aggregate, ignoring differences in displacement rate and particularly in irradiation temperature.[1] Figure la shows that the limited DO-heat cold-worked swelling data can be interpreted in aggregate to exhibit a relative insensitivity to both temperature and helium content. The readers attention is directed toward the 680°C (nominal) datum.

This specimen was actually irradiated somewhere above 700°C and is the only cold-worked datum suggesting that HFIR irradiation can produce swelling rates comparable to those seen in E8R-II. Figure lb shows another interpretation of the potential high fluence swelling behavior that discounts the relevance of this datum.

There is another approach that can be employed to study the impact of helium on swelling. It has been shown that the eventual steady-state swelling rate of AISI 316 in E8R-II is independent of cold work level, and that increasing the cold work level results only in extending the transient regime of swelling.[7] Figure 2a shows that within the data range the swelling of annealed DO-heat data indeed exhibits an independence of irradiation temperature and reactor spectra. As shown in Figure 2b, the swelling rate of annealed DO-heat in HFIR is quite comparable to that of three different heats of AISI 316 irradiated at 600°C in E8R-II. Figure 2a also shows that the swelling rate of annealed steel in HFIR is comparable to the high fluence behavior projected for cold-worked 00-heat in HFIR.

Figure 3 shows that the composite E8R-II/HFIR curve for cold-worked DO-heat is also quite comparable to the temperature-insensitive swelling of another heat of cold-worked steel irradiated in two separate E8R-II experiments.[8,9] Note that the environmental sensitivity of the transient regime of the N-lot heat in E8R-II is greater than the differences seen in Figure 2b between DO-heat in HFIR or E8R-II at any temperature.

Figure 3 also demonstrates the relative insensitivity of swelling to irradiation temperature, a phenomenon observed in several 300 series stainless

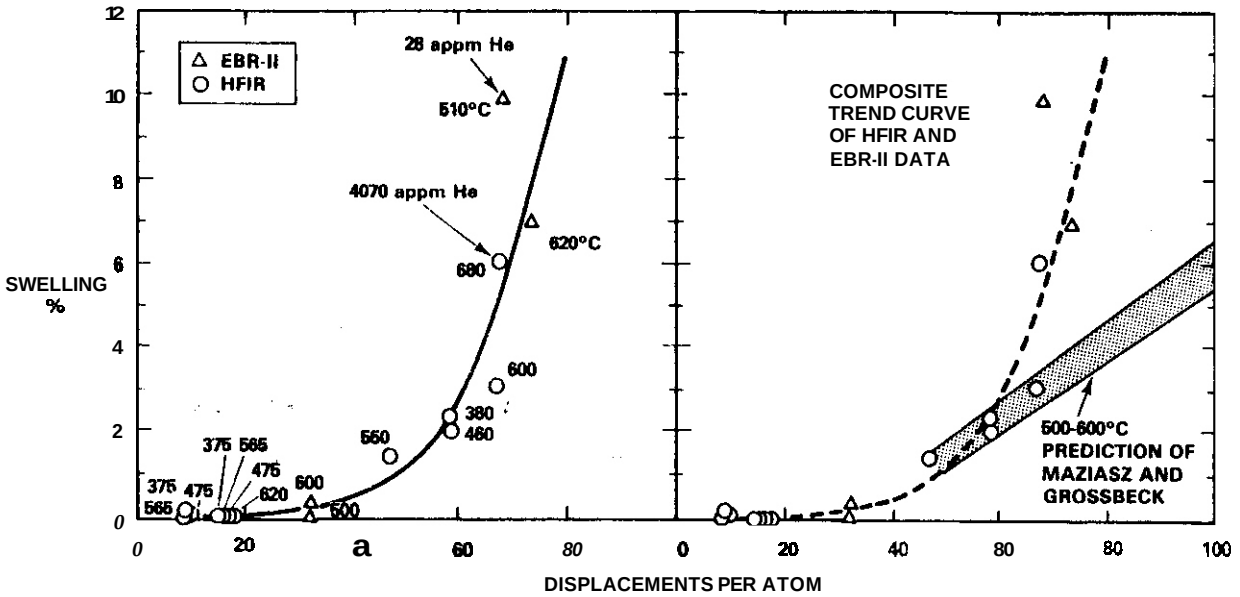

FIGURE 1. Swelling Observed in 20% CW DO-Heat Irradiated in EBR-II and HFIR. (Only originally reported nominal temperatures used.) Corrections have been included for the displacements produced in HFIR by the ^{56}Fe recoil that accompanies the ^{59}Ni (n,) reaction. The composite HFIR/EBR-II trend curve drawn is typical of swelling curves for AISI 316 in EBR-II. An alternate interpretation of these data is shown in the right-hand figure. Reference 6.

steels and also in ternary alloys.[1,8,10-12] Some steels exhibit a larger sensitivity to temperature but this sensitivity manifests itself in the duration of the transient regime and not in the swelling rate at high fluence. A similar sensitivity of the transient regime to displacement rate[13] has also been observed and will be shown later.

Since annealed swelling data are being used to demonstrate the independence of swelling rate on temperature as well as on helium/dpa ratio and solid transmutants, it should also be shown that a similar independence of temperature exists in the swelling rate of annealed steel in EBR-II. Unfortunately, the U. S. Breeder Program has generated very little data on annealed steels, concentrating instead on the 20% cold-worked condition prototypic of current and planned U. S. fast reactors. In particular there is very little annealed data, comparable to that shown in Figure 2b, which can be used to assess the temperature dependence of the steady-state swelling rate.

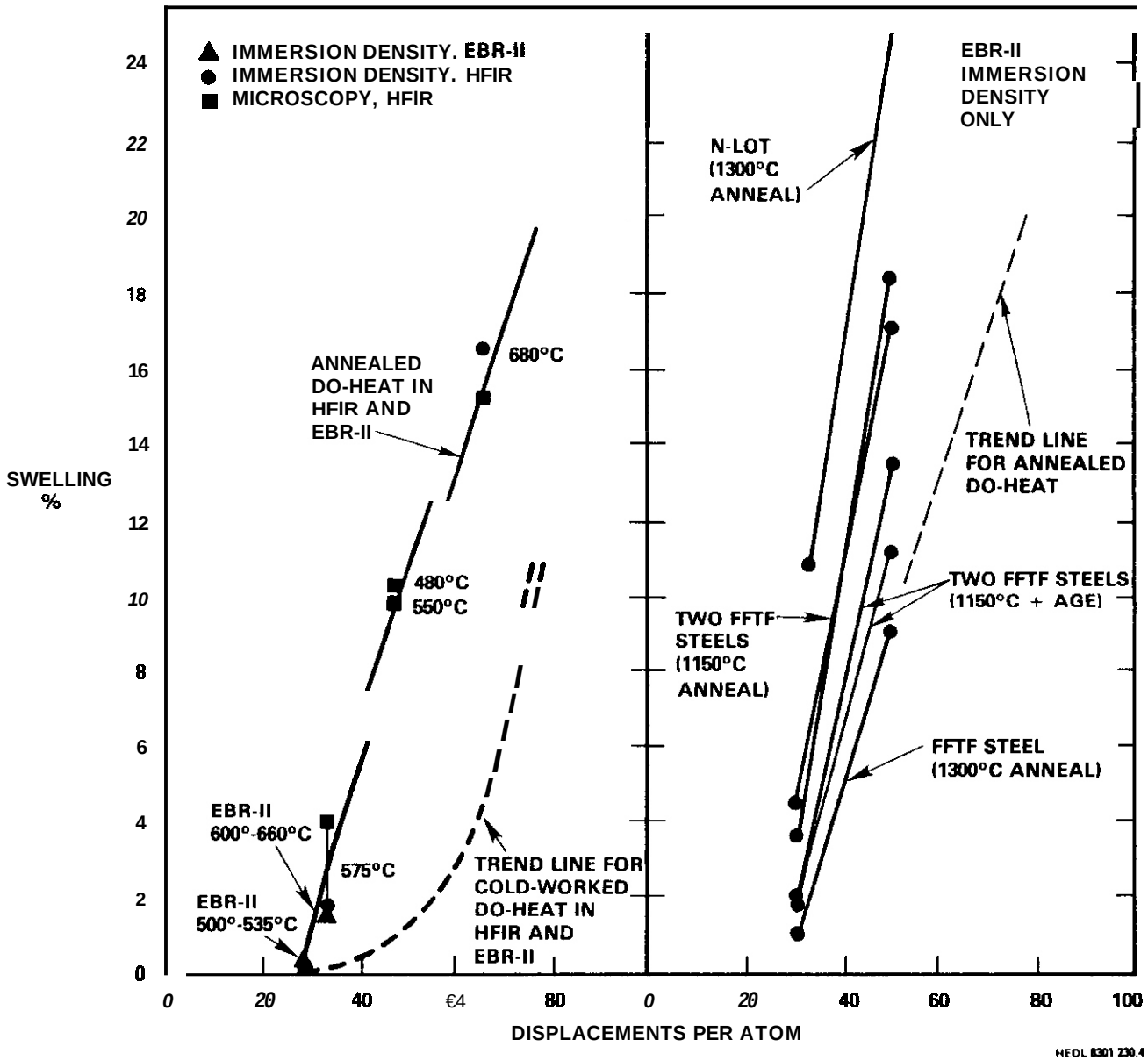

FIGURE 2. (a) Swelling Rate of Annealed DO-Heat in HFIR and EBR-II is Independent of Temperature and Comparable to the High Fluence Behavior of the Composite HFIR/EBR-II Curve for Cold-Worked Material.

(b) The Annealed Swelling Behavior in HFIR is Typical of Annealed Swelling at 600°C in EBR-II. (Previously unpublished data.) Each of the EBR-II lines represent two measurements on the same specimen at different exposures. The straight lines drawn through each set of data appear to increase in slope as swelling increases because the continuing curvature of swelling has been ignored.

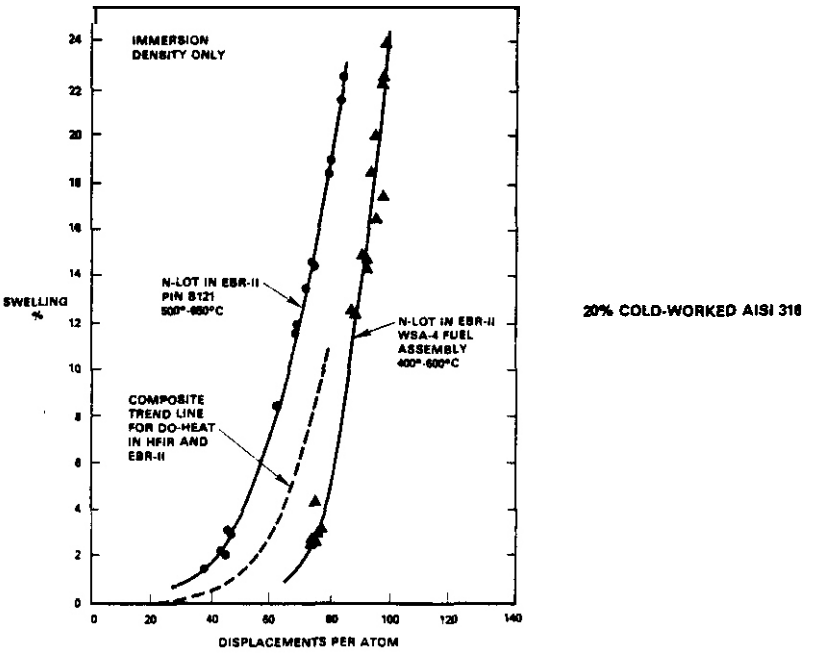

FIGURE 3. Comparison of Composite HFIR/EBR-II Trend Line for DO-Heat With Swelling Behavior Observed for a Single Heat of Steel Irradiated in EBR-II in Two Separate Experiments. All three sets of data display a relative insensitivity to temperature.[8,9]

5.3 Comparison With Other Data

There are data on annealed 316 available from other national programs. As shown in Figures 4 and 5, the high fluence swelling rates of French annealed 316 stainless steel are relatively insensitive to temperature. Note that the duration of the transient regime is somewhat temperature-sensitive but it is even more sensitive to displacement rate, particularly at higher temperatures.

It is obvious from these figures, however, that transient curvature can persist to rather high displacement levels, particularly at low temperatures. This persistence is one reason why the steady-state swelling rate is frequently thought to be temperature-dependent. In actuality the steady-state swelling rate has often not been reached in many data sets at all irradiation temperatures.

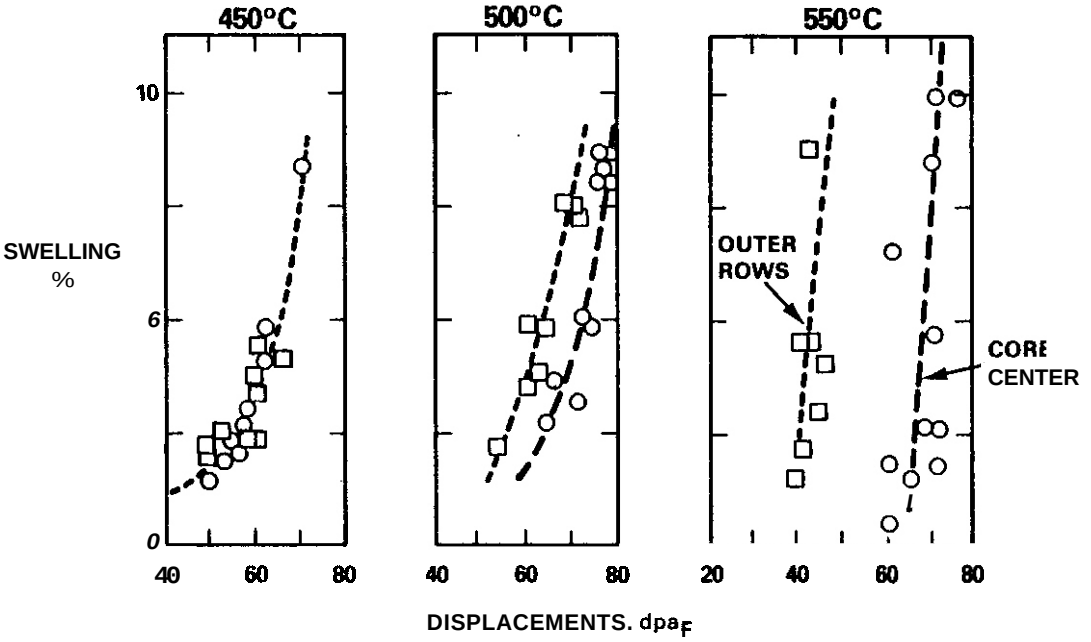

FIGURE 4. The Influence of Displacement Rate and Time-in-Reactor on the Swelling of Annealed AISI 316 Fuel Pin Cladding from the Rapsodie Reactor.(93)

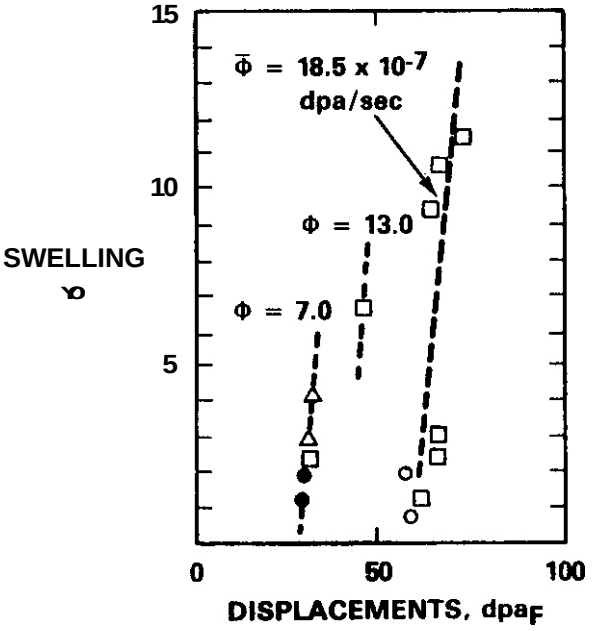

FIGURE 5. The Influence of Displacement Rate on the Swelling at 562°C of Annealed AISI 316 Fuel Pin Cladding from the Rapsodie Reactor.(13)

There is another set of data which can be used to demonstrate that persistence of curvature tends to camouflage the temperature-independence of steady-state swelling. Permission has been granted by J. H. Gittus, J. S. Watkin and J. Standring to cite these data in advance of publication.

A series of annealed (and sometimes aged) M316 and 316 steels were irradiated in the Dounreay Fast Reactor at temperatures ranging from 350 to 600°C. The swelling observed at the maximum dose studied is tabulated in Table 1. Gittus and coworkers assumed a linear-after-incubation swelling relationship of the form

$$\frac{\Delta V}{V_o}(\%) = A\ (D-D_o)\ ,$$

where D is the displacement dose (in Half-Nelson dpa) and A is a constant with units of %/dpa. The values of A and D_o (the incubation dose) are also shown in Table 1. A and D_o were considered to be material constants, varying for each material and with temperature.

It has earlier been shown that linear-after-incubation descriptions of swelling in 300 series stainless steels yield underestimates of the swelling rate compared to curvilinear descriptions.[14] The error arising from the underestimate becomes smaller with accumulated swelling.

Five of the eight irradiated steels were derived from a single heat of M316 stainless steel (Fe-17.2Cr-13.7Ni-2.4Mo-1.85Mn-0.63Si-0.035C) and were irradiated in either the annealed condition (1050°C, 1/2 hr) or the annealed and aged condition, using four annealing temperatures and one aging condition. These temperatures are shown beside Figure 6. The four swelling rate curves shown in Figure 6 exhibit the double-bump behavior usually observed in the swelling of annealed AISI 316.[15] The values of swelling rate plotted in Figure 6 are the values of the materials constant A taken from Table 1. The other steels listed in Table 1 exhibit the same double-bump behavior.

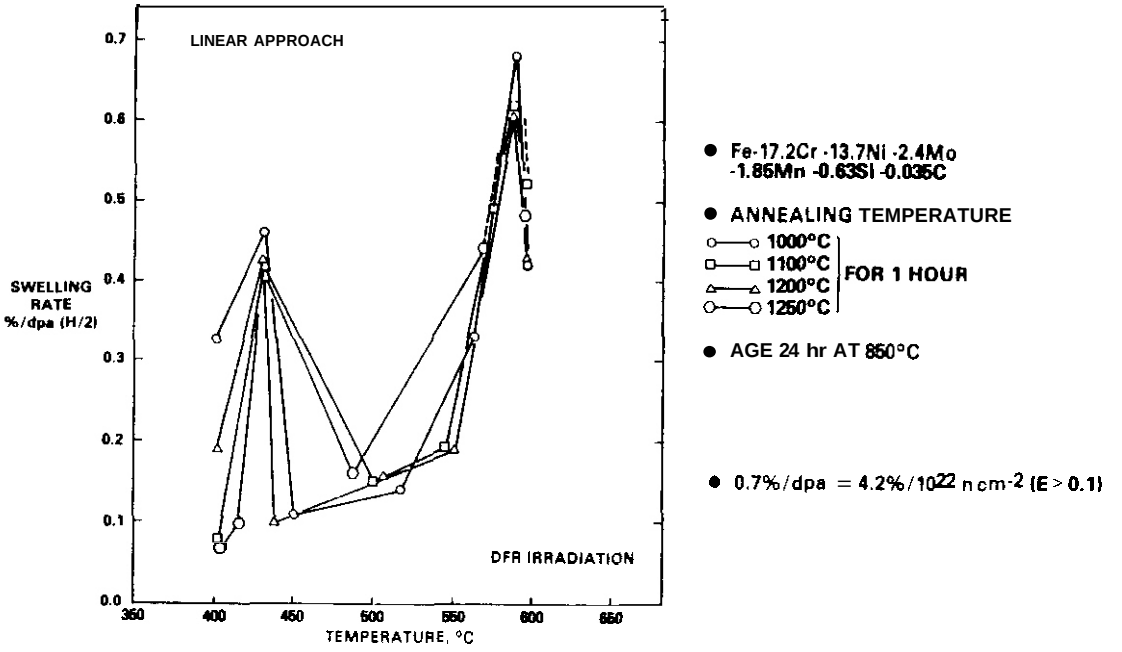

FIGURE 6. "Double-Bump'' Swelling Rate Profiles Observed in Annealed and Aged M316 After Irradiation in the Dounreay Fast Reactor, as Observed by Gittus, Watkin and Standring. The swelling rates shown above are actually underestimates (of varying degree) arising from the premature assumption of swelling being proportional to dose.

The minimums observed in these curves at 475-525°C is thought to represent the longest incubation period for annealed steel and to be related to the temperature dependence of phase evolution.[14] There was a peaked neutron flux profile over the pin in which this experiment was conducted, however. This tends to pull the apparent swelling rate down at the extremities of the temperature range in which this experiment was conducted. The resultant fluence gradients can be normalized out of the data if either the swelling or swelling rate data are plotted against fluence. As seen in Table 1, however, only the maximum swelling values are available.

A more instructive way to view the data for our purpose is to plot the swelling rate observed vs the maximum swelling level in the data set from which the rate was derived. This allows us to test the hypothesis that the swelling rate increases with total swelling and that temperature is not an important variable. Note in Figure 7 that the swelling rate of all eight steels can be described by one curve for all temperatures above 475°C. It

TABLE 1

SWELLING OF M316, 316 AND 316L IN THE DOUNREAY FAST REACTOR[t]

Material Condition	Irradiation Temperature °C	A % per dpa*	Do dpa*	No. of data Points	Standard Deviation $\frac{\Delta V}{V_o}$ %	Swelling at Max Dose Studied $\frac{\Delta V}{V_o}$ %	D
M316, 1050°C, 1/2 h	595	0.4	21.6	6	1.0	10.06	45.7
	565	0.13	20.1	2	-	3.50	47.6
	535	0.19	24.3	2	-	3.70	43.8
	476	0.11	37.2	2	-	2.75	37.2
	430	0.26	20.5	3	0.02	3.47	34.0
	403	-	-	-	-	0	34.4
	380	-	-	-	-	0	23.0
M316, 1000°C, 1 h + 850°C, 24 h	595	0.48	21.5	6	2.5	15.40	47.2
	568	0.44	19.3	2	-	12.76	48.1
	538	-	-	-	-	0.9	11.9
	488	0.16	14.4	2	-	3.84	38.7
	430	0.41	20.4	3	0.01	5.56	33.8
	415	0.098	10.5	2	-	1.66	29.0
	403	0.075	26.3	3	0.03	0.6	34.8
	400	-	-	-	-	0	22.2
	360	-	-	-	-	0	21.8
M316, 1100°C, 1 h + 850°C, 24 h	595	0.52	23.0	4	3.0	13.30	44.2
	588	0.62	18.9	2	-	18.0	47.6
	576	0.49	20.9	2	-	13.45	48.5
	545	0.19	22.3	2	-	4.39	45.2
	499	0.15	14.8	2	-	3.82	40.0
	430	0.41	21.0	3	0.02	5.12	33.4
	422	0.091	12.4	2	-	1.64	30.4
	403	0.081	23.8	4	0.3	0.91	35.0
	350	-	-	-	-	0	20.6
M316, 1200°C, 1 h + 850°C, 24 h	595	0.43	21.4	4	0.8	10.7	44.9
	588	0.61	20.1	2	-	17.2	48.1
	580	0.49	20.2	2	-	14.2	48.8
	553	0.19	23.7	2	-	4.35	46.0
	507	0.16	18.2	2	-	3.88	41.1
	438	0.10	14.1	2	-	1.87	32.0
	430	0.43	21.8	3	0.31	4.61	33.0
	403	0.19	28.7	3	0.59	1.18	35.0
	350	-	-	-	-	0.1	19.2

TABLE 1 (Cont'd)

Material Condition	Irradiation Temperature °C	A % per dpa*	Do dpa*	No. of data Points	Standard Deviation $\frac{\Delta V}{V_o}$ %	Swelling at Max Dose Studied $\frac{\Delta V}{V_o}$ %	D
M316, 1250°C, 1 h + 850°C, 24 h	595	0.42	22.2	4	0.4	9.90	45.6
	588	0.68	23.4	2	-	17.1	48.4
	557	0.33	25.1	2	-	7.07	46.6
	518	0.14	17.9	2	-	3.45	42.1
	449	0.11	13.2	2	-	2.30	33.9
	430	0.46	22.6	3	0.2	4.51	32.8
	403	0.33	30.4	3	0.7	1.92	34.8
316, 1070°C. air cool	595	0.48	20.9	4	1.8	12.95	44.9
	588	0.59	19.7	2	-	16.93	48.1
	568	0.33	19.0	2	-	9.78	48.1
	538	0.23	22.5	2	-	5.15	44.5
	488	0.09	13.2	2	-	2.3	38.7
	430	0.09	18.1	3	0.4	1.23	33.8
	415	0.06	15.4	2	-	0.79	29.0
	403	-	-	-	-	0	34.8
	350	-	-	-	-	0	18.2
316L*, *1050°C, 1/2 h	595	0.25	11.5	6	0.96	6.86	32.8
	584	0.32	17.0	2	-	5.87	35.2
	557	0.19	6.9	2	-	5.12	33.7
	518	0.20	8.3	2	-	4.47	30.4
	430	0.20	8.5	5	0.05	4.65	31.8
	422	0.1	6.9	2	-	1.52	22.1
	403	0.26	11.4	3	0.02	1.33	16.6
	380	0.14	10.2	2	-	1.86	23.0

† Supplied in advance of publication by J. H. Gittus, J. S. Watkin and J. Standring.
*Dose given in Half-Nelson (N/2) displacements; 1 dpa (NRT, Austenitic) = 1.15 dpa (N/2 for Fe), see Ref. 16 for source.

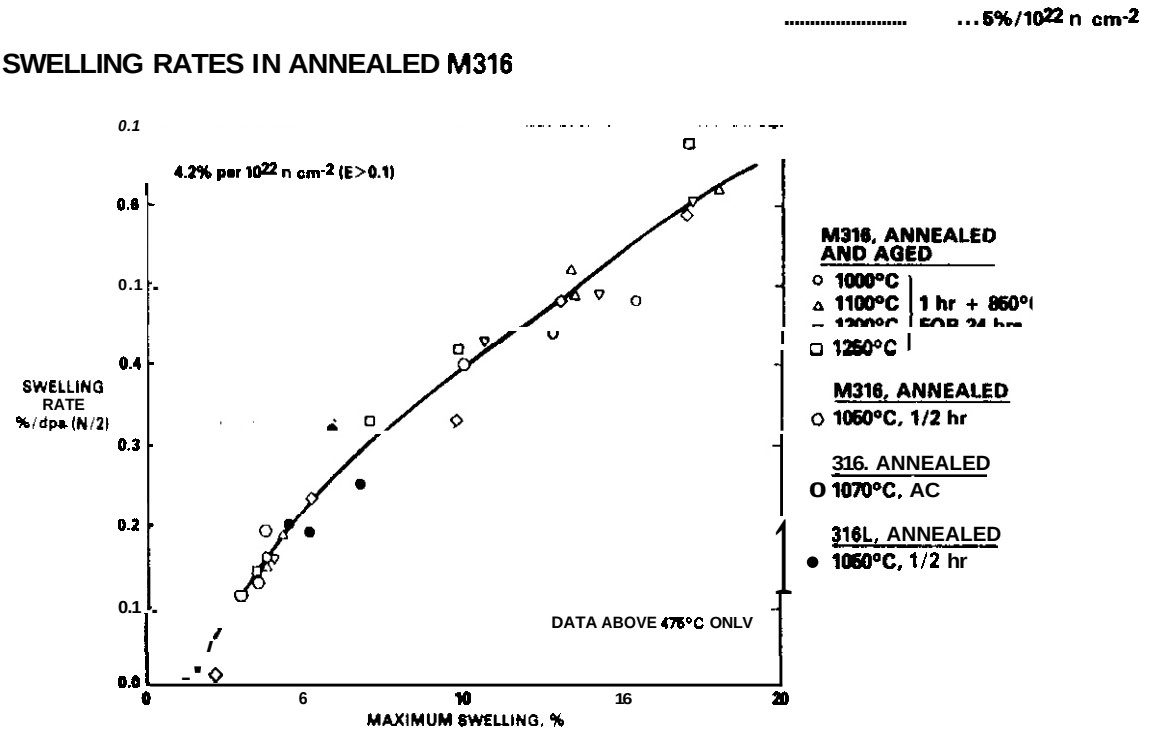

FIGURE 7. Apparent Swelling Rate vs Maximum Swelling in Data Set for M316 and 316 Steels from Table 2, Temperatures Greater than 475°C Only.

also increases with swelling level and is approaching a value of $\sim 5\%/10^{22}$ n/cm^2 (E > 0.1 MeV). This is approximately 1%/dpa when converted from Half-Nelson dpa to the recommended international system for calculating displacements.

A similar trend is observed for data below 475°C as shown in Figure 8. Even though the transients in swelling are longer, the post-transient rate of approach to steady state swelling is faster than that observed above 475°C. In effect, this analysis has demonstrated the relative temperature independence of swelling of annealed AISI 316, but leads to the conclusion that there are two separate incubation regimes. A similar behavior has been observed in the N-lot heat of 20% cold-worked AISI 316, as shown in Figure 9.

5.4 Discussion

It is obvious that the variation observed in the materials constant A (%/dpa) of Table 1 reflects more a consequence of prematurely assuming the linear behavior of swelling with dpa than any real dependence on either composition,

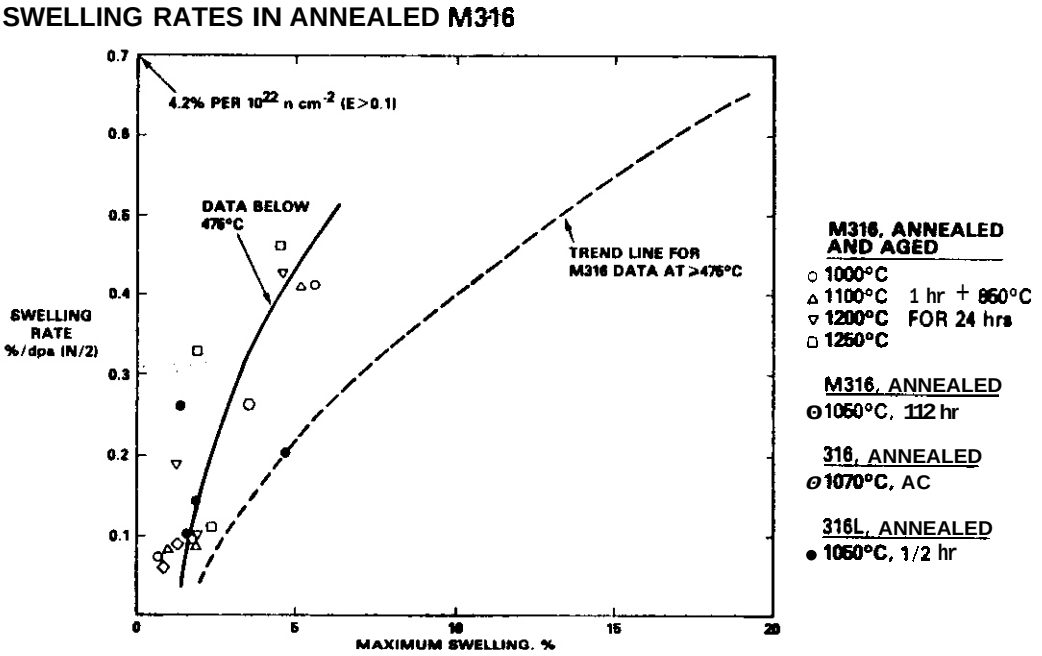

FIGURE 8. Apparent Swelling Rate vs Maximum Swelling in Data Sef for M316 and 316 Steels from Table 2, Temperatures Less than 425°C Only.

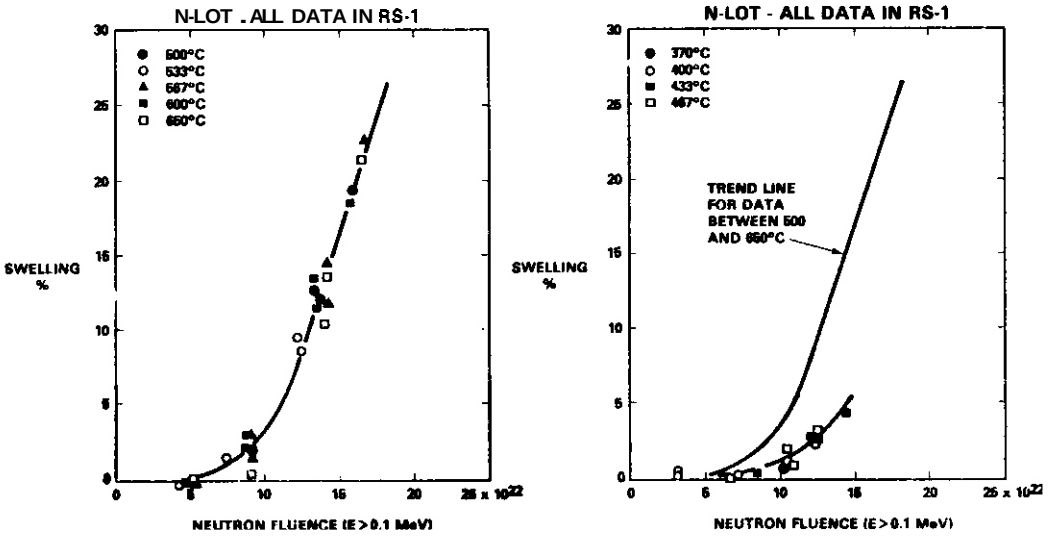

FIGURE 9. Two Regimes of Temperature Insensitivity Observed in N-Lot Heat of AISI 316 Irradiated in EBR-II.(8)

thermal treatment or irradiation temperature. The finding that there are two regimes of temperature insensitivity for AISI 316 does not affect the analysis of the DO-heat data, however, since all of these DO-heat data were derived from the high temperature regime.

Watkin noted in transmitting the data to the author that some caution should be exercised in interpreting the data from the Dounreay reactor. Some of the specimens, particularly those irradiated at higher temperatures, were subjected to changes in temperature due to rig malfunctions. He felt that this may have caused some of the higher swelling levels observed. He also noted that all specimens were in the same rig so that the relative temperature levels were maintained. Based on recent studies, however, it is now known that changes in temperature impact only the duration of the transient regime of swelling and exert no influence thereafter.[8] Since Figures 7 and 8 have been plotted in such a manner as to remove the influence of transient differences, there is no reason to ignore any data.

It is also shown from this analysis that one cannot ignore the continuing curvature of swelling with fluence in AISI 316, whether it be either in cold-worked or annealed steels. The lack of curvature and the low swelling rate proposed by Maziasz and Grossbeck[6] (shown in Figure lb) are inconsistent with the observed behavior not of only of annealed and cold-worked steels in fast reactors but also the annealed DO-heat in HFIR. .

5.5 Conclusions

Analysis of swelling data for the DO-heat of steel irradiated in HFIR and EBR-II indicates that the swelling behavior is not altered substantially by differences arising from the different neutron spectra. The analysis has been facilitated by the relative temperature independence of the swelling rate not only for cold-worked steels but also for annealed steels irradiated in both reactors.

6.0 References

1. H. R. Brager and F. A. Garner, "Microstructural and Microchemical Comparisons of AISI 316 Irradiated in HFIR and EBR-II, DAFS Quarterly Progress Report, DOE/ER-0046/11, p. 115.

2. L. R. Greenwood and R. K. Smither. "Neutron Dosimetry Measurements for the HFIR-CTR3 Irradiation," Damage Analysis and Fundamental Studies Quarterly Progress Report, DOE/ER-0046/9, May 1982, p. 32.

3. F. A. Garner and F. M. Mann, "The Impact of the $^{59}Ni(n,\alpha)^{56}Fe$ Reaction on Damage Calculations for HFIR," in Ref. 2, p. 41.

4. P. J. Maziasz, F. W. Wiffen and E. E. Bloom, Proc. Conf. Radiation Effects and Tritium Technology for Fusion Reactors, CONF-750989, Vol. I, 1976, p. 259.

5. F. A. Garner, P. J. Maziasz and W. G. Wolfer, "Development of a Swelling Correlation for 20% CW 316 in a Fusion Device," DAFS Quarterly Progress Report, DOE/ER-0046/3, p. 159.

6. P. J. Maziasz and M. L. Grossbeck, "Equations to Describe the Swelling of 20% Cold-Worked Type 316 Stainless Steel Irradiated in HFIR," Alloy Development for Irradiation Performance Semiannual Progress Report, DOE/ER-0045/7, March 1982, p. 98.

7. W. K. Appleby, E. E. Bloom, J. E. Flinn and F. A. Garner, "Swelling in Neutron-Irradiated 300 Series Stainless Steels," Radiation Effects in Breeder Reactor Structural Materials, M. L. Bleiberg and J. W. Bennett, Eds; The Metallurgical Society of AIME, 1977, p. 509.

8. W. J. S. Yang and F. A. Garner, "Relationship Between Phase Development and Swelling of AISI 316 During Temperature Changes," Effects of Radiation on Materials: Eleventh Conference, ASTM STP 782, H. R. Brager and J. S. Perrin, Eds., American Society for Testing and Materials, 1982, pp. 186-206.

9. A. Boltax, J. P. Foster and U. P. Nayak, "High Dose Stainless Steel Swelling Data on Interior and Peripheral Oxide Fuel Pins." Proceedings of Conference on Dimensional Stability and Mechanical Behavior of Irradiated Metals and Alloys, Brighton, England, April 11-13, 1983, in press.

10. F. A. Garner and W. G. Wolfer, "Recent Experimental and Theoretical Insights on the Swelling of Austentic Alloys," in Proceedings of Ref. 9.

11. F. A. Garner and D. L. Porter, "Reassessment of the Swelling Behavior of AISI 304 Stainless Steel," in Proceedings, Ref. 10.

12. F. A. Garner, "Impact of the Injected Interstitial on the Correlation of Charged Particie and Neutron-Induced Radiation Damage," Proceedings of Symposium on Radiation Damage Analysis for Fusion Reactors, St. Louis, MO, Oct. 24-28, 1982, J. Nucl. Mater. (in press); also in Ref. 1, p. 167.

13. J.L. Seran and J. M. Dupouy, "The Swelling of Solution Annealed 316 Cladding in Rapsodie and Phenix," in Ref. 8, p. 5-16.

14. F. A. Garner and D. L. Porter, "Factors Influencing The Swelling of 300 Series Stainless Steels," in Ref. 2, p. 170.

15. F. A. Garner, "The Microchemical Evolution of Irradiated Stainless Steels," Proc. of Symposium on Phase Stability During Irradiation, J. R. Holland, L. K. Mansur and D. I. Potter Eds., The Metallurgical Society of AIME, 1981, p. 165.

16. J. I. Bramman et al., "Void Swelling and Microstructural Changes in Fuel Pin Cladding and Unstressed Specimens Irradiated in DFR," in Ref. 7, p. 479.

7.0 Future Work

Modeling of the effects of helium on void growth, irradiation creep and mechanical properties will continue.

8.0 Publications

Portions of this work were earlier published in Ref. 1, which was also presented at the Symposium described in Ref. 12, the proceedings of which will be published in J. Nucl. Mater.

CAVITY FORMATION IN SINGLE- AND DUAL-ION IRRADIATED V-15 Cr-5 Ti ALLOY

B. A. Loomis and G. Ayrault (Argonne National Laboratory)

1.0 Objective

The objective of this work is to determine the evolution of the microstructure in first-wall materials during irradiation with special emphasis on the effects of helium production, displacement damage rates and temperature.

2.0 Sumnary

The propensity for cavity formation in the V-15 Cr-5 Ti alloy during single ($^{51}V^+$)- and dual ($^{51}V^+$ + $^3He^+$)-ion irradiation was determined for alloy temperatures that ranged from 400 to 725°C and irradiation-damage levels that ranged from 15 to 60 dpa. The swelling of the alloy on self-ion irradiation was negligible for irradiation temperatures of $\lesssim$ 725°C and damage levels of < 30 dpa. The dimensional change of the V-15 Cr-5 Ti alloy on dual-ion irradiation was also negligible for irradiation temperatures of < 675°C and damage levels of < 15 dpa if the He-injection rate was 10 appm He/dpa. The swelling of the alloy on dual-ion irradiation was negligible for damage levels of < 60 dpa if the irradiation temperature was < 650°C and the He-injection rate was 3 appm He/dpa. The experimental results obtained on single-ion irradiation corroborated the low swelling of the V-15 Cr-5 Ti alloy obtained on fast neutron irradiation.

3.0 Program

Title: Effects of Irradiation on Fusion Reactor Materials
Principal Investigator: B. A. Loomis
Affiliation: Argonne National Laboratory

4.0 Relevant DAFS Program Plan Task/Subtask

Subtask: II.C.2.1 Mobility, Distribution and Bubble Nucleation

5.0 Accomplishments and Status

5.1 Introduction

Vanadium-base alloys are potentially useful for structural applications in fusion energy devices (FED) for several reasons. These alloys have a resistance to thermal stress at elevated temperatures (> 500°C) that is superior to either the austenitic steels, ferritic/martensitic steels or titanium alloys [1,2]. The compatibility/corrosion resistance of vanadium-base alloys with liquid lithium is clearly superior to either the austenitic or ferritic steels for temperatures above ~500°C [3,4]. The induced-radioactivity and afterheat of some vanadium-base alloys, e.g., V-20 Ti, are the lowest of all the prime-candidate structural metals that are being considered for a FED [5]. On the basis of limited data, the vanadium-base alloys appear to be highly resistant to irradiation damage [6,7].

The fast and mixed fission-spectrum test reactors can be used to simulate the displacement damage in vanadium-base alloys that are candidates for use in a FED. However, the helium produced by (n,α) reactions in these alloys during irradiation in a fission reactor is accumulated at a rate that is totally inadequate to simulate the fusion value, viz., *0.02* appm He/dpa (EBR-II) and 5.4 appm He/dpa (FED, 1 MW•Yr/m^2) [8]. In the absence of a FED or an alternative device with an intense fusion-neutron spectrum, the synergistic effects of high displacement damage (50-300 dpa) and helium production (1-50 appm He/dpa) on the physical and mechanical properties of vanadium-base alloys (as well as other materials) can be determined by simultaneous irradiations with energetic dual-ions, e.g. 3.0-MeV $^{51}V^+$ and 0.87-MeV $^3He^+$ ions. In this report, we present the results of an investigation on the swelling of a "reference" V-15 Cr-5 Ti alloy that arises from the production of displacement damage during $^{51}V^+$-ion irradiation or from simultaneous displacement damage production and helium implantation during $^{51}V^+$- and $^3He^+$-ion irradiation. The single-ion irradiations were intended for the corroboration of the low swelling (< 0.1%) for this alloy that arises from displacement damage production during fast neutron irradiation (Fig. 1, Ref. 6.7). The dual-ion

irradiations were intended to determine the possible synergistic effects on swelling of simultaneous displacement damage and helium production.

5.2 Materials and Procedures

A vanadium alloy containing 15 w/o Cr and 5 w/o Ti was prepared for this study by arc-melting the constituent metals in a purified Ar atmosphere. Sheet specimens of the alloy (0.13 mm thick) were annealed at 1250°C for 1 hour to give a fully recrystallized microstructure with a dislocation density of ~5 x 10^{12} m^{-2}. Alloy specimens, each with a diameter of 3.05 mm, were mounted in a four-by-four array in a W holder for irradiation with 3.0-MeV $^{51}V^{+}$ ions or for simultaneous irradiation with 3.0-MeV $^{51}V^{+}$ and degraded 0.87-MeV $^{3}He^{+}$ ions. The irradiations were carried out in the Dynamitron irradiation facility at Argonne National Laboratory. The specimens were irradiated with 3.0-MeV $^{51}V^{+}$ ions at a typical current density of 3 $mA \cdot m^{-2}$ with a nominal atomic displacement rate of 3 x 10^{-3} $dpa \cdot s^{-1}$. In the case of the simultaneous irradiations of the specimens with $^{51}V^{+}$ and $^{3}He^{+}$ ions, the energy of the $^{3}He^{+}$ ions was degraded to give a He deposition-depth distribution that was similar to the damage-depth distribution produced by the $^{51}V^{+}$ ions. The He deposition rates utilized in this study were 3, 10 and 50 appm He/dpa.

The irradiated specimens were prepared for transmission electron microscopy (TEM) observation by electrochemical removal of an 850 to 950-nm thick layer from the bombarded surface in an 80% CH_3OH-20% H_2SO_4 solution at ~5°C. For 3.0-MeV $^{51}V^{+}$ ion irradiation, the depth of maximum damage in V was ~900 nm with a corresponding peak damage rate of 3 x 10^{-3} $dpa \cdot s^{-1}$. The microstructure of the irradiated specimens were observed in a JEM 100 CX electron microscope.

5.3 Experimental Results

5.3.1 Single-Ion Irradiation

The microstructures in the V-15 Cr-5 Ti alloy specimens following irradiations at 400 to 725°C with 3.0-meV $^{51}V^{+}$ ions to damage levels of ~30 dpa showed a striking absence of clearly distinguishable voids. Thus on the basis of these

observations, the dimensional change ($\Delta V/V$) of the V-15 Cr-5 Ti alloy, that was due to voids produced by self-ion irradiation, was negligible for irradiation temperatures less than 725°C and damage levels of < 30 dpa (Figure 1). The microstructure of the alloy following irradiation at 675°C to 30 dpa is shown in Figure 2a. The single-ion irradiation of the alloy for irradiation temperatures above 675°C and damage levels of ~30 dpa resulted generally in an increase of the dislocation density from ~5 x 10^{12} m^{-2} to ~5 x 10^{15} m^{-2}. Examination of these microstructures with dark-field imaging techniques did not reveal the presence of precipitates in the matrix or on the dislocation network. For irradiations of the alloy with $^{51}V^{+}$ ions at temperatures below 675°C, a high density (~10^{22} m^{-3}) of precipitates were observed in the matrix with an {012} habit (similar to Figure 2c) or on dislocations (similar to Figure 2b). The composition of the precipitates was not determined in this study. However, from previous investigations of V alloys by Santhanam, et al. [9] and Agarwal, et al. [10], the composition of the precipitates may be TiO or V_2C.

5.3.2 Dual-Ion Irradiation

The microstructure of the V-15 Cr-5 Ti alloy specimens following simultaneous irradiation with $^{51}V^{+}$-and $^{3}He^{+}$-ions were also examined in this study. The irradiation parameters for these specimens were

(1) 30 dpa + 10 appm He/dpa at 425, 540 and 625°C,

(2) 30 dpa + 50 appm He/dpa at 625 and 635°C,

(3) 60 dpa + 3 appm He/dpa at 625 and 640°C, and

(4) 15 dpa + 10 appm He/dpa at 650 and 675°C.

Cavities (microstructural features that may contain He) were only observed in the specimens that were irradiated at 650 and 675°C. The cavities with a maximum diameter of 3.5 nm were inhomogeneously distributed in the matrix.

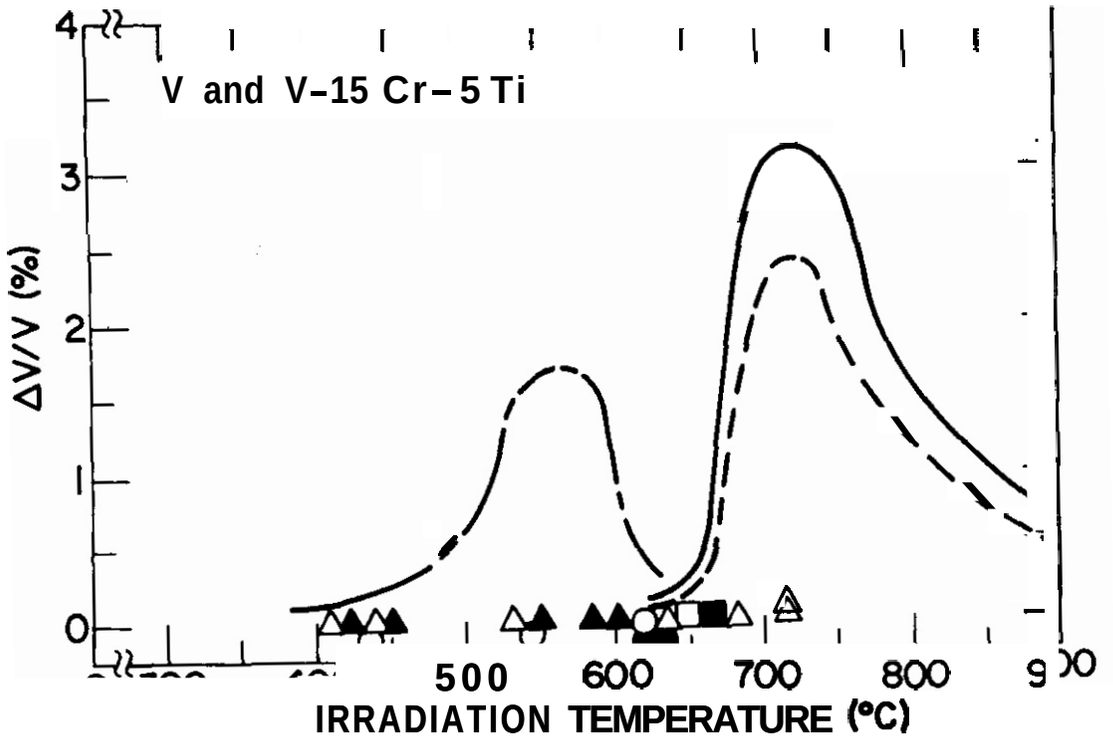

LEGEND:

- V ($^{58}Ni^+$, 60 dpa, Ref. [11]
- V ($^{51}V^+$, 20 dpa, Ref. [10]
- V (Neutron, 7-15 dpa, Refs. [12,13]
- ▲ V-15 Cr-5 Ti (Neutron, 7-15 dpa, Refs. [6,7]
- a V-15 Cr-5 Ti ($^{51}V^+$)
- ○ V-15 Cr-5 Ti ($^{51}V^+$ + $^{3}He^+$, 30 dpa + 10 appm He/dpa)
- ● V-15 Cr-5 Ti ($^{51}V^+$ + $^{3}He^+$, 30 dpa + 50 appm He/dpa)
- □ V-15 Cr-5 Ti ($^{51}V^+$ + $^{3}He^+$, 60 dpa + 3 appm He/dpa)
- ■ V-15 Cr-5 Ti ($^{51}V^+$ + $^{3}He^+$, 15 dpa + 10 appm He/dpa)

FIGURE 1. Swelling of Neutron- and Ion-Irradiated V and V-15 Cr-5 Ti Alloy.

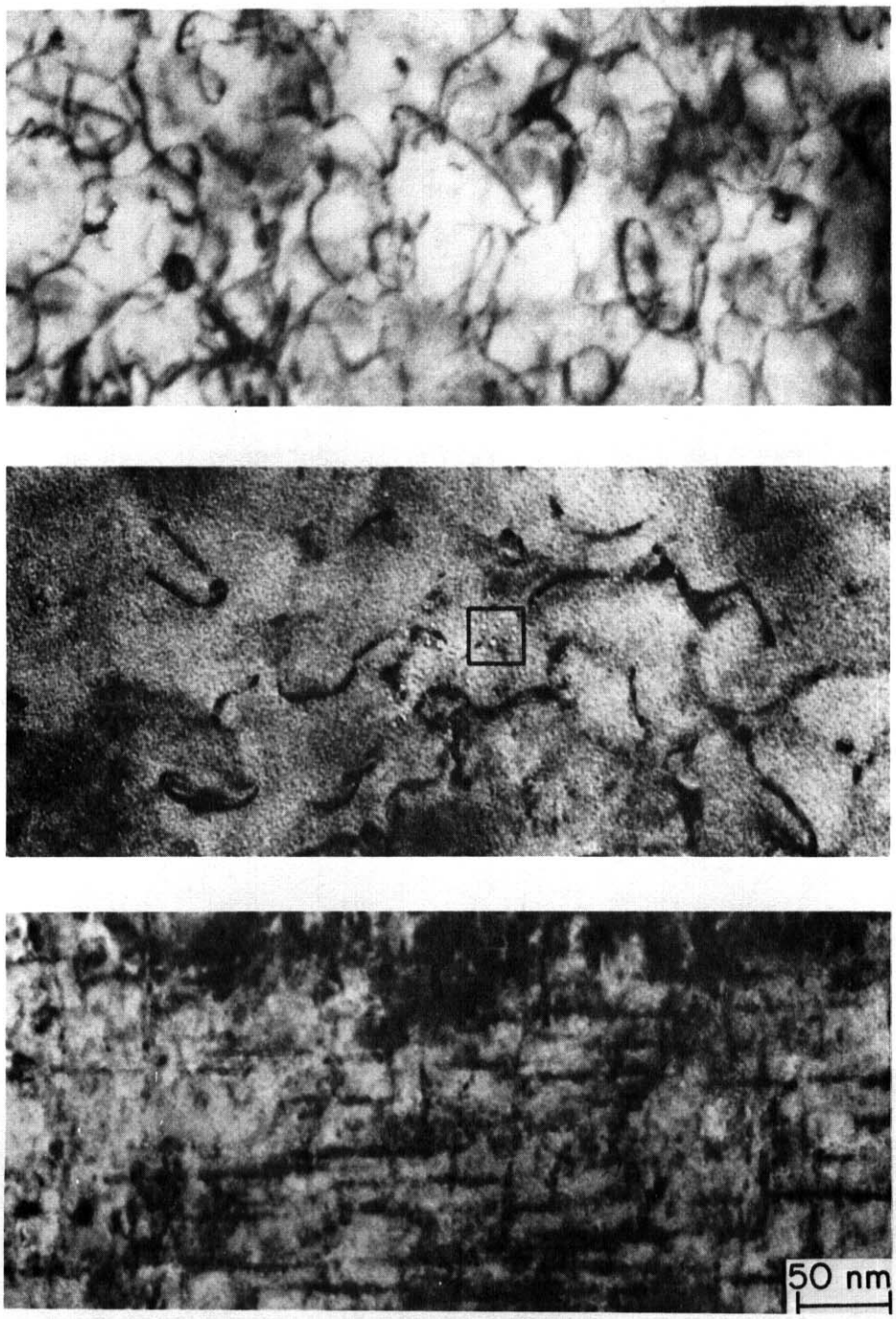

FIGURE 2. Microstructures of Ion-Irradiated V-15 Cr-5 Ti Alloy: (a) $^{51}V^{+}$ Irradiation at 675°C to 30 dpa, (b) $^{51}V^{+}$ + $^{3}He^{+}$ Irradiation at 675°C to 15 dpa (10 appm He/dpa), (c) $^{51}V^{+}$ + $^{3}He^{+}$ Irradiation at 640°C (60 dpa + 3 appm He/dpa).

The cavity-volume fractions in these specimens were estimated to be on the order of 10^{-5}. Thus, the dimensional change ($\Delta V/V$) of the V-15 Cr-5 Ti alloy that was due to cavities produced by simultaneous V^+- and He+-ion irradiation was negligible for irradiation temperatures of < 675°C and damage levels of < 15 dpa (Figure 1).

Microstructures of the alloy specimens following dual-ion irradiation at 675°C (15 dpa + 10 appm He/dpa) and 640°C (60 dpa + 3 appm He/dpa) are shown in Figures 2b and 2c, respectively. The inhomogeneous distribution of small-diameter (< 3.5 nm) cavities that were previously mentioned are shown in Figure 2b (cavities in the insert). In addition, precipitates are visible on the dislocation network. The irradiation at 640°C (Figure 2c) resulted in the formation of aligned precipitates with the {012} habit; cavities were not visible in the microstructure.

5.4 Conclusions and Discussion

The experimental results obtained in this study allow the following conclusions:

1. The swelling of the V-15 Cr-5 Ti alloy, that was due to production of voids on self-ion irradiation, was negligible for irradiation temperatures of <725°C and damage levels of < 30 dpa.

2. The swelling of the alloy, that was due to the production of cavities on simultaneous irradiation with 3.0-MeV $^{51}V^+$ and degraded 0.83-MeV $^3He^+$ ions was negligible for irradiation temperatures of < 675°C and damage levels of < 15 dpa if the He-injection rate was 10 appm He/dpa.

3. The swelling of the alloy on dual-ion irradiation was negligible for damage levels of < 60 dpa if the irradiation temperature was less than 650°C and the He-injeciton rate was 3 appm He/dpa.

4. The experimental data obtained on single-ion irradiation corroborated the low swelling of the V-15 Cr-5 Ti alloy obtained on fast neutron irradiation.

Since the irradiation temperature in this study did not encompass the full range of temperatures (625-900°C) for void swelling in V (Figure 1), it cannot be concluded that the V-15 Cr-5 Ti alloy does not swell for some combination of higher irradiation temperature (> 675°C), damage level and He-injection rate.

The void swelling of V [9-11] and the V-15 Cr [14], V-1 Ti [9] and V-15 Cr-5 Ti alloys at ~700°C on $^{58}Ni^{+}$- or self-ion irradiation that has been determined by researchers at Argonne National Laboratory is shown in Figure 3. The addition of 15 w/o Cr to V causes a substantial increase of the V swelling, whereas the addition of 1 w/o Ti to V or 5 w/o Ti to a V-15 w/o Cr alloy effectively suppresses void formation and growth. The mechanism(s) for suppression of swelling in V and its alloys by Ti additions and the enhancement of V swelling by Cr additions is not fully understood. Several researchers [9-11,14] have pointed out that the presence of a high density of precipitates in irradiated V alloyed with Ti and the absence of precipitates in irradiated V alloyed with Cr can be correlated, respectively, with the suppression or enhancement of V swelling. The results of the prsent study show that this correlation, i.e., the presence of a high-density of irradiation-produced precipitates and negligible swelling, applies to the single- and dual-ion irradiated V-15 Cr-5 Ti alloy at temperatures below 675°C. These correlations might be taken as evidence per se for enhanced defect recombination at the coherent precipitates resulting in low swelling. However, we suggest that enhanced defect recombination at the precipiates may not be the correct interpretation for the low swelling of the V-Ti alloys. Similar precipitate microstructures are observed in irradiated V [10] and irradiated O- and C-doped V [10] without substantial reduction of void formation and growth. Furthermore, in the present study, precipitates were not observed in the V-15 Cr-5 Ti alloy for irradiation temperatures within the range for peak swelling of V (> 675°C) but the swelling of the alloy was negligible. Loomis and Gerber [15] have observed a similar reduction in void swelling of Nb by a Ti (2.3%) addition. Their experimental results suggested that the strong binding of Ti solute to vacancy-oxygen complex effectively reduced the flux of the complex to void sinks and thereby reduced the void

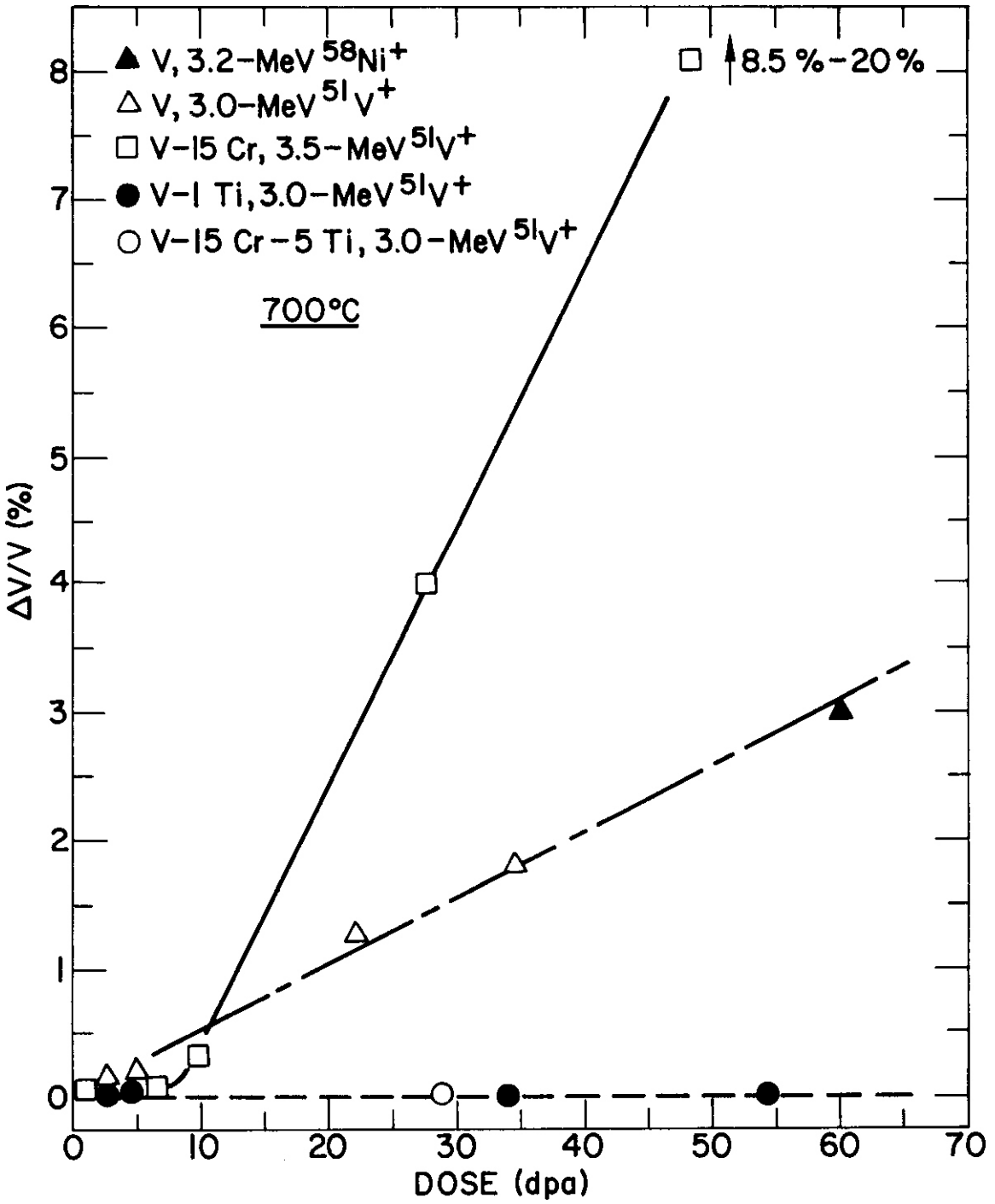

FIGURE 3. Swelling of V and V Alloys on $^{58}Ni^{+}$- or $^{51}V^{+}$-Ion Irradiation.

swelling. Using the basic premise of Loomis and Gerber, i.e., the transport of vacancy defects to sinks via complex, the low swelling of V on Ti additions might be similarly explained. Moreover, the enhanced swelling of V by Cr additions may be attributed to the low affinity of Cr atoms relative to V atoms for O (and/or C) atoms in the complex that are diffusing to vacancy sinks. An additional factor that was considered by Loomis and Gerber [15] to explain the observed effects of substitutional-atom solutes on void swelling in Nb was the relative diffusivity of the solute atoms in the host lattice. On application of this schema to the V-15 Cr alloy, the higher diffusivity of Cr atoms relative to V atoms [16] may have resulted in enhanced transport of vacancy-oxygen complex to defect sinks. If this is the case, then the concentration of Cr in the surface layers of void sinks should be reduced relative to the Cr concentration in the matrix. This expectation seems to be contradicted by experimental results which show an enrichment of Cr at the surface of irradiated V-15 Cr specimens [14].

In conclusion, we call the reader's attention to the remarkable similarities (that may be fortuities) in the dependence of void swelling on damage dose for the V-Cr and V-Cr-Ti alloys (Figure 3) and for 316 stainless steel and Ti-modified 316 stainless steel [17]. These similarities are (1) a transient stage of low swelling, (2) a stage of high swelling rate, (3) a prolonged transient stage of low swelling on addition of Ti and (4) irradiation-induced segregation of Cr.

6.0 References

1. R. E. Gold. E. E. Bloom. F. W. Clinard, Jr., D. L. Smith, R. O. Stevenson and W. G. Wolfer, Nuclear Technology/Fusion 1 (April, 1981) 169.

2. K. C. Liu, J. Nucl. Mater. 104 and 104 (1981) 913.

3. D. L. Smith and R. E. Gold, In: Proc. Second International Conference on Liquid Metal Technology in Energy Production, CONF-800401-P1 (1980) p. 10-21.

4. D. L. Smith, J. Nucl. Mater. 103 and 104 (1981) 19.

5. G. L. Kulcinski, In: Proc. International Conference on Radiation Effects and Tritium Technology for Fusion Reactors, CONF-750989 (1975) p. 1-17.

6. R. Carlander, S. D. Harkness and A. T. Santhanam, In: Effects of Radiation on Substructure and Mechanical Properties of Metals and Alloys, ASTM STP 529, American Society for Testing and Materials (1973) p. 399.

7. A. F. Bartlett, J. H. Evans, B. L. Eyre, E. A. Terry and T. M. Williams, In: Proceedings of the International Conference on Radiation Effects and Tritium Technology for Fusion Reactors, J. S. Watson and F. W. Wiffen, Eds., Vol. I (1976) p. 122.

8. FED-INTOR/TEST/82.4 Document, Chapter XII, Engineering Testing, INTOR Participant: M. A. Abdou.

9. A. T. Santhanam, A. Taylor, B. J. Kestel and C. Steves, J. Vac. Sci. Technol., 12 (1975) 528.

10. S. C. Agarwal, D. I. Potter and A. Taylor, In: Irradiation Effects on the Microstructure and Properties of Metals, ASTM STP 611, American Society for Testing and Materials (1976) p. 298.

11. A. T. Santhanam, A. Taylor and S. D. Harkness, In: Proceedings of the 1973 International Conference on Defects and Defect Clusters in B.C.C. Metals and Their Alloys, R. J. Arsenault, Ed., Vol. 18 (1973) p. 302.

12. J. O. Stiegler, In: Radiation-Induced Voids in Metals, AEC Symposium Series 26, CONF-710601, J. W. Corbett and L. C. Ianniello, Eds. (1972) p. 292.

13. F. W. Wiffen, In: Radiation-Induced Voids in Metals, AEC Symposium Series 26, CONF-710601, J. W. Corbett and L. C. Ianniello, Eds. (1972) p. 386.

14. S. C. Agarwal, L. E. Rehn and F. V. Nolfi, Jr., J. Nuc. Mater. 78 (1978) p. 336.

15. B. Loomis and S. Gerber, To be published as part of the 1982 Fall Meeting of the TMS-AIME proceedings in the Journal of Nuclear Materials.

16. D. Ablitzer and A. Vignes, In: Proceedings of the International Conference on the Properties of Atomic Defects in Metals, eds. N. L. Peterson and R. W. Siegel, Argonne National Laboratory, Oct. 1976, p. 97-108.

17. P. J. Maziaz and D. N. Braski, ADIP Semiannual Progress Report for Period Ending March 31, DOE/ER-0045/8, 1982, p. 98.

7.0 Future Work

1) The swelling of the reference V-15 Cr-5 Ti alloy should be determined at temperatures in the range of 625-800°C on dual-ion irradiation to damage levels up to 200 dpa and He-injection rates of ~5 appm/dpa.
2) The effects of a systematic reduction of the Cr concentration in the reference alloy should be determined with the intent of optimization of the combined mechancial properties and swelling.

8.0 Publications

1. G. Ayrault, Cavity Formation During Single- and Dual-Ion Irradiation in a 9 Cr-1 Mo Ferritic Alloy, J. Nucl. Mater. 113 (1982).
2. Z. Wang, G. Ayrault and H. Wiedersich, Segregation in Irradiated Titanium Alloys, J. Nucl. Mater. 108 and 109 (1982) 331.

HELIUM BUBBLE FORMATION IN Cu, Ni AND CU-Ni ALLOYS

S. J. Zinkle, R. A. Dodd, G. L. Kulcinski (University of Wisconsin-Madison), and K. Farrell (Oak Ridge National Laboratory)

1.0 Objective

The purpose of this study is to investigate cavity formation in the Cu-Ni alloy system after helium ion irradiation using transmission electron microscopy.

2.0 Summary

Copper, nickel, and Cu-Ni alloys have been irradiated with 200-400 keV ^3He ions at a constant homologous temperature of T/T_m = 0.65. The samples have been analyzed by TEM to compare helium bubble size and density. Visible bubbles were observed in all samples. The pure copper and the Cu-Ni alloys were found to contain similar bubble densities and sizes after irradiation. The pure nickel samples contained helium bubbles of smaller size and higher density as compared to the alloys.

3.0 Program

Title: Radiation Effects to Reactor Materials
Principal Investigators: G. L. Kulcinski and R. A. Dodd
Affiliation: University of Wisconsin

4.0 Relevant DAFS Program Task/Subtask

Subtask II.C.2.1 Effect of Helium on Microstructural Evolution

5.0 Accomplishments and Status

5.1 Introduction

The Cu-Ni system has been the subject of many experimental investigations over the past decade.[1-6] It is one of the few alloy systems which forms a complete solid solution over the entire composition range, although there is some evidence for a miscibility gap under certain conditions.[1-3] Its radiation damage properties are of considerable interest in that Cu-Ni alloys have been shown to be very resistant to void formation over a wide range of damage levels and temperatures.[4-6] Recently, some Cu alloys have been considered for use as high field magnet inserts in both tandem mirror[7,8] and Tokamak[9]) fusion reactors. The irradiation conditions under which this alloy system has been investigated in the past are shown in Fig. 1. Voids have been easily produced in pure Cu and pure Ni but there has been no published evidence of void formation in Cu-Ni alloys during neutron, ion, or electron bombardment. The cause of the suppressed void formation in the Cu-Ni alloys has remained uncertain.

In order to investigate some of the properties of the Cu-Ni system, we have undertaken a study of helium bubble formation. The purpose of this investigation was twofold. The first objective was to determine if helium bubble formation is possible in the Cu-Ni alloys which are resistant to void formation. A significant difference in the bubble parameters of the alloys as compared to the pure copper and nickel would indicate that there is some fundamental difference in the way that cavities are formed in the Cu-Ni alloys. Secondly, we wished to determine if there was something unusual about the formation or migration energies of vacancies in the alloys compared to the pure metals.

5.2 Experimental Procedure

Copper, nickel and Cu-Ni alloys (Cu-20 Ni, Cu-50 Ni, Cu-80 Ni) were obtained from J. L. Brimhall of Pacific Northwest Laboratory in the form of 3 mm disks.

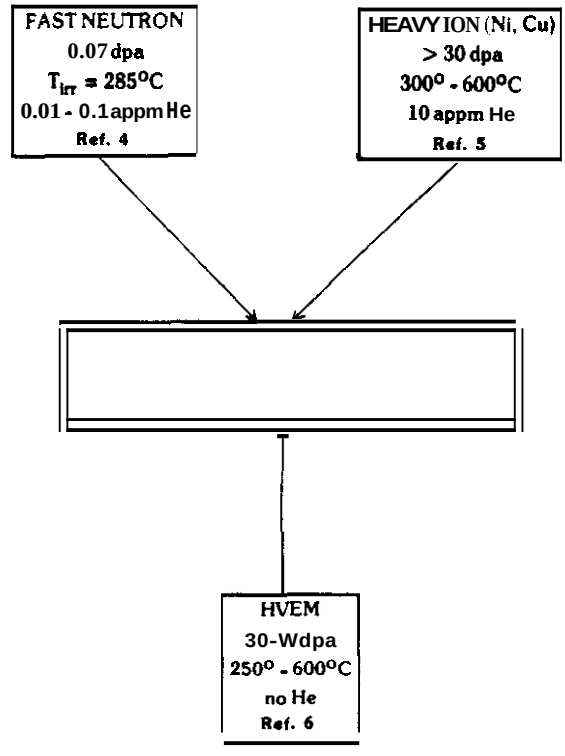

FIGURE 1. Summary of Previous Studies of Void Formation in Cu-Ni Alloys.

These samples were polished and then annealed at a homologous temperature of 0.75 T_m prior to implantation with helium. The TEM discs were irradiated with 200-400 keV ^3He ions at the Oak Ridge National Laboratory Van de Graaf facility to obtain a helium concentration of 200 appm at a depth of approximately 0.7 μm. Figure 2 shows the implanted helium profile for nickel, which was calculated using the program E-DEP-1. The incident He flux was on the order of 5 x 10^{11} He/cm^2-s and the total damage level created during the implantation was less than 10^{-3} dpa. The samples were implanted at a constant homologous temperature T/T_m = 0.65 to ensure equivalent thermal vacancy concentrations in each alloy. The temperatures ranged from 608°C for pure copper to 849°C for the pure nickel specimens. The premise of constant thermal vacancy concentration at a given homologous temperature assumes that E_f^v varies monotonically with alloy concentration, and experimental evidence indicates that this is a valid assumption. (10)

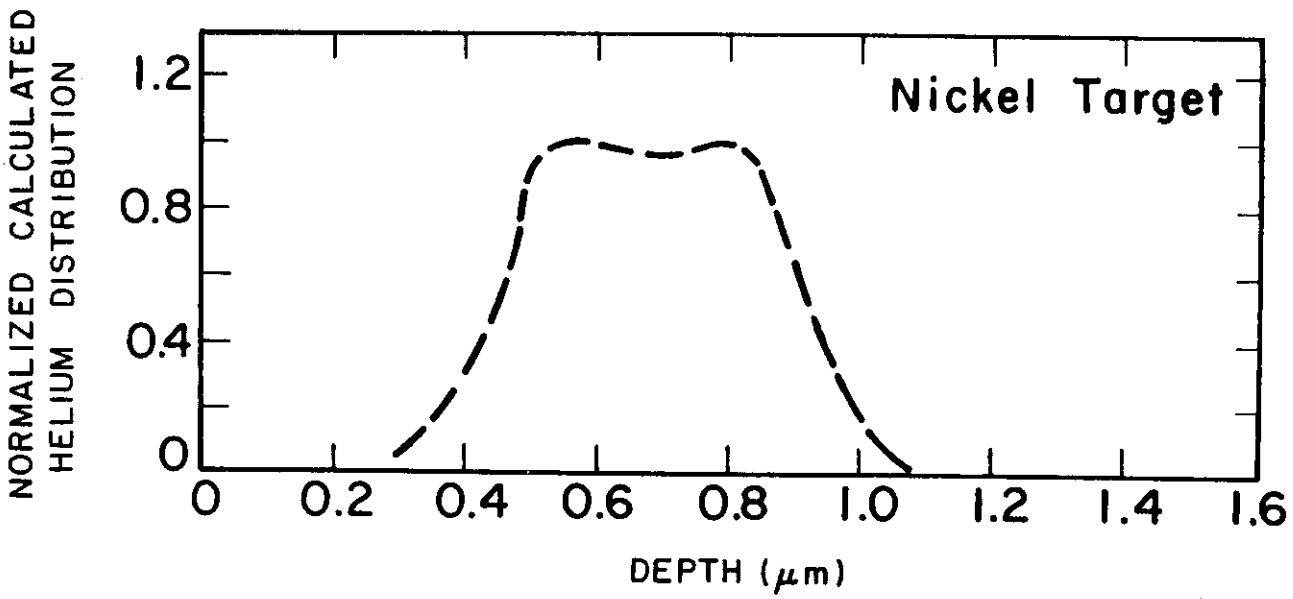

FIGURE 2. Calculated Impanted Helium Profile for the Cu-Ni Alloys Used in This Study.

All samples were held at the implantation temperature for one hour following the irradiation. The relatively high homologous temperature of $T/T_m = 0.65$ was used to ensure that there was no survival of displacement damage structure from the ^3He irradiation.

A thickness of 0.7 μm was removed from the front surface of the TEM samples using an electrolyte of 67% CH_3OH/33% HNO_3 at -20°C and a voltage of 3-4 volts. The depth removed was checked by measuring the amount of fringe shift at the step height between the polished and unpolished region of the foil with an interference microscope. The foils were then back-thinned by jet polishing with the same electrolyte at a temperature of -45°C and a voltage of 9-12 V. The samples were examined in a JEOL 200 CX electron microscope.

5.3 Results

A low density of He bubbles was observed in the pure Cu and pure Ni, and in all three of the alloys. Typical micrographs of the helium bubbles are shown in Figs. 3 and 4 for the pure elements and the alloys, respectively. The

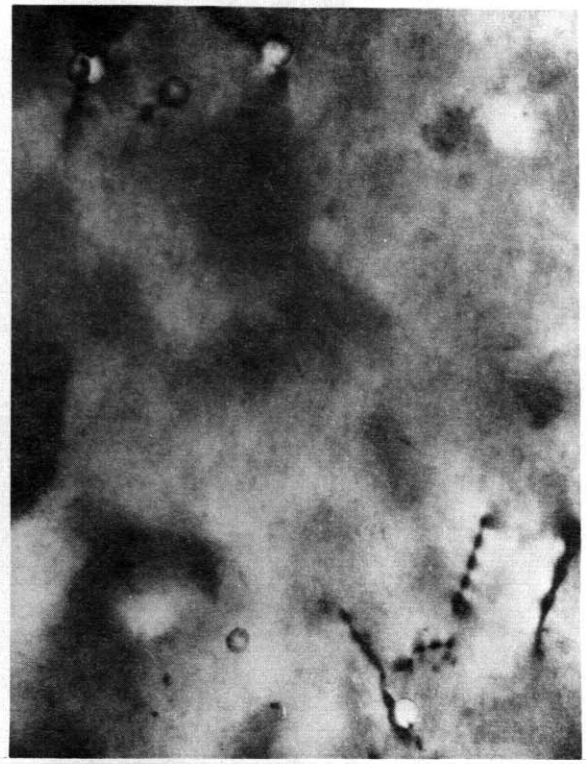

COPPER

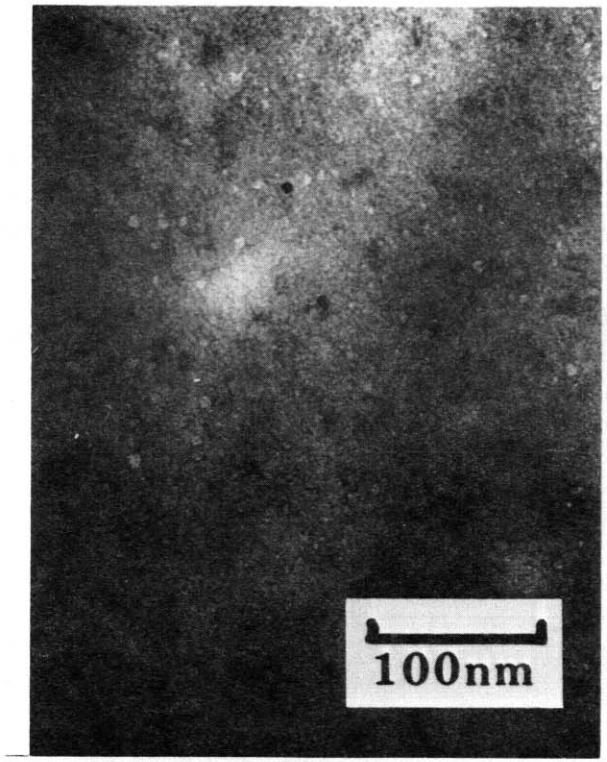

NICKEL

FIGURE 3. Helium Bubbles Observed in Pure Copper and Nickel Implanted with 200 appm He at the Homologous Temperature $T/T_m = 0.65$.

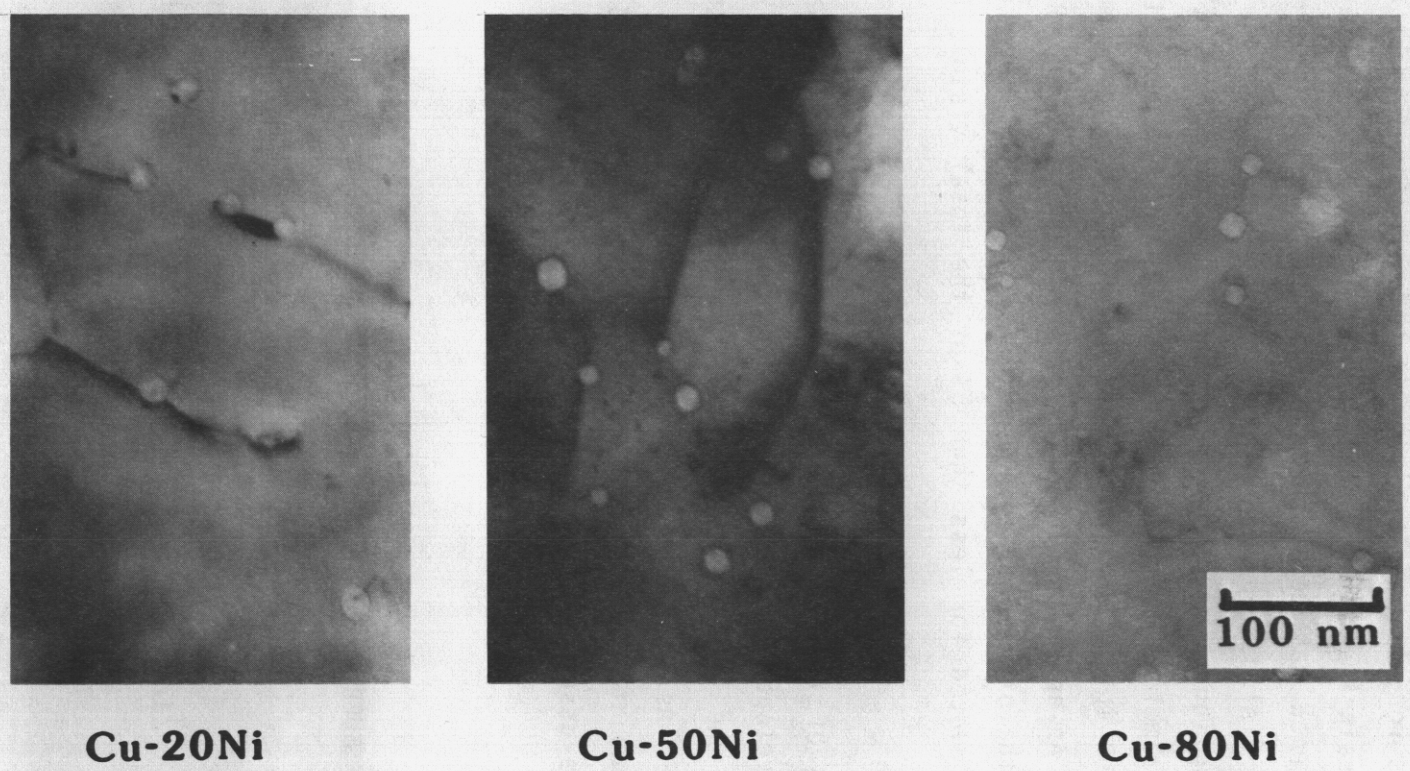

FIGURE 4. Helium Bubbles Observed in Cu-Ni Alloys Implanted with 200 appm He at the Homologous Temperature $T/T_m = 0.65$.

bubble parameters for the Cu, Ni and Cu-Ni alloys are summarized in Table 1. The helium bubbles for all samples investigated were found to be at, or in the vicinity of, a strain field such as a dislocation or grain boundary. No large systematic difference was determined between the bubble parameters at grain boundaries versus dislocations. Figure 5 shows the variation of bubble density and size as a function of alloy composition. There is essentially no dependence of these parameters on alloy composition, with the exception that the bubble distribution in the pure nickel sample is substantially more dense and of smaller size. An appreciable density of these small ($d \lesssim 5$ nm) bubbles was also observed in the other samples. For the alloy and pure copper samples the small bubbles accounted for less than 5% of the total visible helium bubble volume.

The concentration of implanted helium in the visible bubbles was calculated using a newly developed high-density equation of state for He.[11] The gas concentration in the visible bubbles as a function of alloy composition is shown in Fig. 6. As can be seen, a substantial fraction of the implanted helium can be accounted for by TEM. For this calculation, the solid-vapor surface energy was assumed to vary linearly among the alloys from 1.8 J/m^2 for

TABLE 1

BUBBLE PARAMETERS FOR Cu, Ni AND Cu-Ni ALLOYS

Material	T_{irr} (°K)	Bubble Density x 10^{20} (m^{-3})	Average Visible Bubble Size (nm)
cu	881	1.0	18
Cu-20 Ni	912	2.5	18
Cu-50 Ni	983	1.2	17
Cu-BO Ni	1071	0.83	25
Ni	1122	$\gtrsim$ 11	7

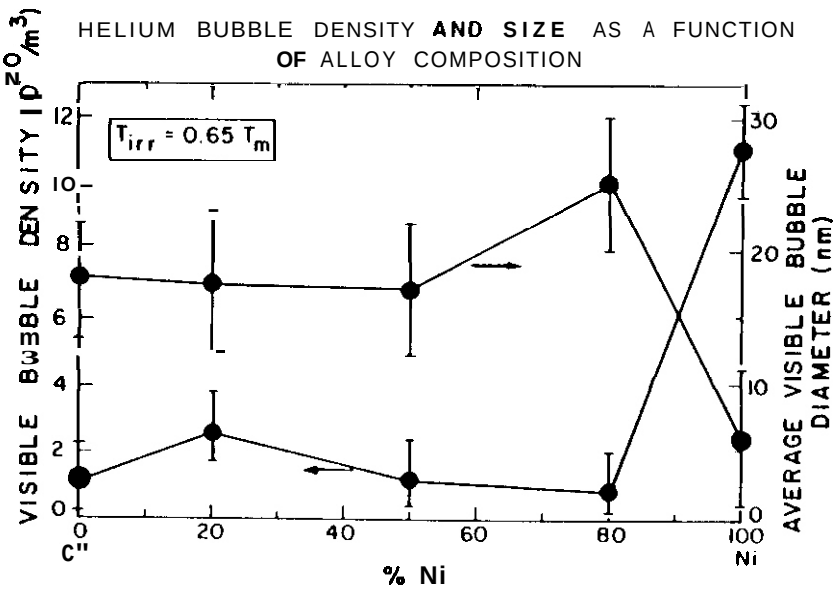

FIGURE 5. Variation in the Visible Bubble Density and Average Bubble Size with Alloy Composition.

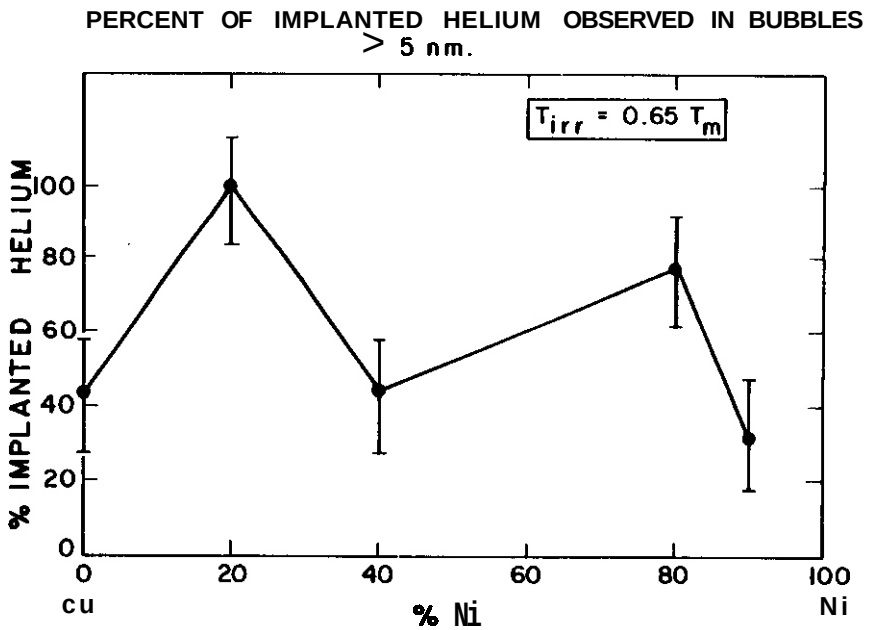

FIGURE 6. Percent of Helium Observed in Bubbles for the Cu-Ni Alloys. A recent developed high-density equation of state is used for helium. Reference 11.

copper to 2.3 J/cm^2 for nickel.[12] The helium atom per vacancy ratio for the visible bubbles was calculated to be on the order of 1/2 by utilizing the previously mentioned equation of state for helium, and assuming equilibrium bubbles.

5.4 Discussion

Helium bubbles have been found to form readily in Cu-Ni alloys at the homologous temperature of $T/T_m = 0.65$. The observed bubble parameters of the alloys are similar to those in pure Cu -- no significant differences have been found. This behavior is not unexpected as there are theoretical and experimental indications that helium tends to undergo spontaneous precipitation when implanted in metals, even when implanted at below damage threshold energies.[13,14] The fact that nothing unusual was observed in the bubble parameters for the Cu-Ni alloys indicates that there is apparently nothing anomalous about the vacancy formation energy for these alloys; otherwise, one would expect a significant difference in the bubble parameters of the alloys compared to those bubbles formed in pure metal (e.g., bubble size and/or bubble density). This conclusion is in agreement with published experimental results.[10]

The bubble parameters for the pure Ni samples were found to be substantially different from those of the pure Cu and alloy samples. The addition of Cu to Ni causes a decrease in the bubble number density and an increase in the bubble size. The cause of this effect was not determined in this study.

In summary, we have found nothing concerning helium bubble growth in the Cu-Ni system at a homologous temperature of $T/T_m = 0.65$ which would explain the suppression of void swelling in the alloys. It would be worthwhile to study helium bubble growth in this alloy system at a lower homologous temperature and at lower helium concentrations. Also, the use of subthreshold energy implantation methods would be relevant as this would eliminate the contribution of implantation-produced vacancies.

6.0 References

1. P. Barlow et al., Phil. Mag. 36 (1975) 565.
2. W. Wagner et al., J. Physics F 12 (1982) 405.
3. W. Schule et al., Z. Metallkunde 66 (1975) 50.
4. J. L. Brimhall and H. E. Kissinger, Radiation Effects 15 (1972) 259.
5. D. J. Mazey and F. Menzinger, J. Nucl. Mat. 48 (1973) 15.
6. P. Barlow, Radiation Damage in Pure F.C.C. Metals and Alloys in the HVEM, Ph.D. Thesis, University of Sussex, April 1977.
7. B. Badger et al., "TASKA - A Tandem Mirror Test Facility," UWFDM-450/KfK-3311, 1982.
8. "MARS - A Mirror Advanced Reactor Study," to be published by LLNL, 1982.
9. J. Schmidt, Private Communication, PPPL.
10. F. Lihl and H. Wildhack, Z. Metallkunde 62 (1971) 143.
11. B. Glasgow and W. G. Wolfer, to be published.
12. L. E. Murr, Interfacial Phenomena in Metals and Alloys, Addison-Wesley, Reading, MA, p. 124 (1975).
13. W. D. Wilson et al., Phys. Rev. B 24 (1981) 5616.
14. G. J. Thomas and R. Bastasz, J. Appl. Phys. 10 (1981) 6426.

7.0 Future Work

The behavior of the helium-implanted Cu-Ni alloys after HVEM irradiation is currently being investigated.

8.0 Publications

This paper will be published in the Proceedings of the Symposium on Radiation Damage Analysis for Fusion Reactors, October 24-28, 1982, St. Louis, MO.

SUPPRESSION OF VOID NUCLEATION BY INJECTED INTERSTITIALS

D. L. Plumton and W. G. Wolfer (University of Wisconsin)

1.0 Objective

The depth-distribution of voids in ion-bombardment contains valuable information on the dose-rate dependence of void nucleation and growth. The purpose of this study is to assess the effect of the injected interstitials on void nucleation. 'The ultimate goal bf this investigation is to obtain a better correlation between neutron displacement damage and ion-induced damage.

2.0 Summary

The injected ions come to rest at the end of range as interstitials without a vacancy partner. These extra interstitials perturb the delicate balance of vacancy and interstitial flux to voids. It is shown that the void nucleation rate is drastically reduced by the injected interstitials whenever recombination is an important process. As a result, void nucleation is suppressed in ion-bombardment experiments below a characteristic threshold temperature in the region of the ion deposition. This leads to a void free zone at intermediate depth in low temperature ion-bombardment experiments. The results obtained are in qualitative agreement with earlier experimental observations.

3.0 Programs

Title: Effect of Radiation and High Heat Flux on the Performance of First Wall Components
Principle Investigator: W. G. Wolfer
Affiliation: University of Wisconsin-Madison

Title: Radiation Damage Studies
Principle Investigators: G. L. Kulcinski and R. A. Dodd
Affiliation: University of Wisconsin-Madison

4.0 Relevant DAFS Program Task/Subtask

DAFS Subtask II.B.2.3
Subtask C. Correlation Methodology

5.0 Accomplishment and Status

5.1 Introduction

Ion bombardment has been in use for over a decade now as a tool to study radiation damage and void swelling in metals. As an irradiation technique, it has the advantage of obtaining data on void swelling with considerable savings in time and money compared to neutron irradiation experiments. However, the non-uniform damage distribution has been considered as a disadvantage. The development of the cross section procedure[1,2] for the post-irradiation examination has turned this disadvantage into a considerable asset of the technique; it is now possible to obtain void swelling data for different displacement rates from one sample. This increase in experimental sophistication has also enabled researchers to examine more closely the variation of void formation and growth as a function of the ion range.

The comparison of ion bombardment results with those obtained from neutron irradiations has revealed significant differences which cannot easily be explained based only on different displacement rates and different temperatures. First, swelling as a result of ion bombardment is often found to saturate at levels ranging from a few percent to several tens of a percent; in contrast, no saturation is found for comparable neutron irradiations. Second, the steady state swelling rate per dpa appears to be significantly lower than the one for neutron irradiated materials. Furthermore, this rate seems to depend on the depth.[3] There are additional differences, e.g. a denuded zone near the front surface, and the presence of an inevitable compressive stress in the bombarded layer.

Rate theory has been used to demonstrate that an increase in displacement rate leads to a shift of the temperature range over which swelling occurs.[4] However, no difference in the steady state swelling per dpa would be expected.

At low temperatures, where recombination is dominant, the injected interstitials can reduce the void growth rate as shown by Brailsford and Mansur.[5] This reduction is significant only when the bias is small, i.e. when the current of vacancies is almost equal to the current of interstitials into the void. Obviously, this will be the case for voids of the critical size. Therefore, we expect that the injected interstitials will affect void nucleation to a greater extent than void growth. The results presented in this paper confirm this expectation.

The organization of the paper is as follows: we review first in Section 2 the void nucleation theory as originally developed by Katz and Wiedersich,[6] and Russell,[7] and as further refined by Si-Ahmed and Wolfer;[8] into which we incorporate the effect of injected interstitials. Numerical results are presented in Section 3 for the void nucleation rate as a function of temperature, displacement rate, and rate of injected interstitials. Since the latter two variables are dependent on the depth, detailed results will be given for the void nucleation as a function of depth. The results are then discussed and compared with experimental observations in Section 4.

5.2 Void Nucleation With Injected Interstitials

The steady state void nucleation rate in the presence of supersaturations for both vacancies and interstitials is governed by the quantity

$$\Delta G(x) = -kT \sum \ln \left[(\alpha(j) + \gamma(j))/\beta(j - 1) \right] \tag{1}$$

which represents the nonequilibrium counterpart of the Gibbs free energy for a vacancy cluster containing x vacancies. In contrast to its conventional definition for thermodynamic equilibrium, this energy is determined by the re-

action rates $\alpha(j)$, $\beta(j)$, and $\gamma(j)$ for interstitial absorption, vacancy absorption, and vacancy re-emission, respectively, at a cluster containing j vacancies. These reaction rates depend in turn on the average point defect concentration as given by

$$\alpha(x) = 4\pi r(x)\, Z_i^o(x)\, D_i C_i \tag{2}$$

$$\beta(x) = 4\pi r(x)\, Z_v^o(x)\, D_v C_v \tag{3}$$

$$\gamma(x) = 4\pi r(x)\, Z_v^o(x)\, D_v C_v^o(x) \tag{4}$$

where $r(x)$ is the void radius, $Z_i^o(x)$ and $Z_v^o(x)$ are the void bias factors for interstitial and vacancy capture, and D_i and D_v are the diffusion coefficients for interstitial and vacancy migration. If $W(x) = 4\pi r^2(x)\gamma_0$ represents the surface energy of a void, where γ_0 is the specific surface energy, and p the gas pressure inside the void, then

$$C_v^o(x) = C_v^{eq} \frac{Z_v^o(x-1)}{Z_v^o(x)} \frac{r(x-1)}{r(x)} \exp[(W(x) - W(x-1) - p\Omega)/kT] \tag{5}$$

where Ω is the volume per atom.

The concentration of interstitials and vacancies, C_i and C_v, are given by the solution to the usual rate equations. However, in the present paper, the rate of interstitial production, P_i, as a result of both displacement damage and injection, is different from the rate of vacancy production, P_v, so that

$$D_i C_i = D_v \bar{Z}_v F \tag{6}$$

and

$$D_v C_v = D_v(\bar{Z}_i F + \bar{C}_v) - (P_i - P_v)/\bar{Z}_v S \ . \tag{7}$$

Here, S is the total sink strength, $\bar{Z}_i$ and $\bar{Z}_v$ are the sink averaged interstitial and vacancy bias factors, and $\bar{C}_v$ is the average vacancy concentration in thermodynamic equilibrium with the sinks. Note, that the vacancy concen-

tration, (such as $C_v^o(x)$) in local thermodynamic equilibrium with a particular sink type (such as a void of size x) differs both from $\bar{C}_v$ and from C_v^{eq}; the latter is the equilibrium concentration in an ideal crystal.

Equations (6) and (7) contain the quantity

$$F = \frac{S}{2\kappa n_V} \{\sqrt{(1 + M)^2 + L} - (1 + M)\} \tag{8}$$

where

$$M = \kappa D_V \bar{C}_V/(\bar{Z}_i S) - \kappa(P_i - P_v)/(\bar{Z}_i \bar{Z}_v S2) \tag{9}$$

$$L = 4\kappa P_i/(\bar{Z}_i \bar{Z}_v S^2) \tag{10}$$

and

$$\kappa = 8\pi a_0/D_V \tag{11}$$

with a_0 being the lattice parameter.

When the injected interstitials are absent as in neutron or electron irradiations, then $P_i - P_v = 0$, and the above equations reproduce those given earlier.(8)

The determination of $\Delta G(x)/kT$ allows the steady state nucleation rate to be computed by the equation

$$I_s = \{\sum_{x=1}^{N-1} \beta^{-1}(x) \exp[-\Delta G(x)/kT]\}^{-1} \tag{12}$$

where N is a cluster size large compared to the critical void size; the latter is defined as the maximum of $\Delta G(x)$.

As shown previously,(8) the void nucleation rate is critically dependent upon the void bias factors $Z_i^o(x)$ and $Z_v^o(x)$ which are given by

$$Z^o(x) = Z^b(x)/[1 + \frac{h}{r + h} (e^{\Delta u^*/kT} - 1)] . \tag{13}$$

This equation is an entirely adequate approximation to the more elaborate formulae given earlier.[8,9] Here, $h(x)$ is the effective thickness of the segregation region around a void of radius $r(x)$, $Z^b(x)$ is the bias factor of a bare void,[9] and

$$\Delta u^* \cong \frac{2(1+\nu)\mu\Omega}{(1-2\nu)}\left[\frac{1}{9}\left(\frac{v}{\Omega}\right)^2\frac{\Delta\mu}{\mu} + \left(\frac{v}{\Omega}\right)\frac{\Delta a_0}{a_0}\right] - \frac{(1+\nu)\Omega}{3(1-\nu)}\left(\frac{2\gamma_0}{r} - p\right)\left(\frac{v}{\Omega}\right)\frac{\Delta\mu}{\mu} \quad (14)$$

is the effective barrier energy of the segregation region. Here, ν is the Poisson's ratio, μ the shear modulus of the matrix, and v is the relaxation volume of the point defect. In the segregation region, the shear modulus differs by $\Delta\mu$, and the lattice parameter by Δa_0 from the corresponding average values in the matrix.

5.3 Results

The effect of injected interstitials on void nucleation will be expressed in terms of the parameter ε_i which is equal to the ratio of the injected interstitials to the interstitials produced by displacements. The total interstitial production rate is then given by

$$P_i = Pv(1 + \varepsilon_i) \quad (15)$$

where P_v is equal to the displacement rate times the survival fraction, η, for in cascade recombination.

The physical parameters listed in Table 1 were used for the numerical evaluation of the void nucleation rate, and they represent appropriate values for nickel and austenitic stainless steels.

The parameters for the void segregation shell were chosen so that the void nucleation rate in the absence of injected interstitials, at T = 500°C and for a dose rate of 10^{-3} dpa/sec, was equal to about 10^{14} voids/cm^3-sec, a value comparable to the observed one in the nickel ion-bombardment experiments on

TABLE 1

MATERIALS PARAMETERS

Parameter	Value	Dimension
Lattice parameter, a_o	0.352	nm
Surface energy, γ_o	1.0	J/m^2
Shear modulus, μ	10^5	MPa
Poisson's ratio, ν	0.3	---
Pre-exponential factor, D_{vo}	1.53×10^{-6}	m^2/s
Vacancy formation energy, E_v^f	1.67	eV
Vacancy migration energy, E_v^m	1.1	eV
Vacancy formation entropy[a], S_v^f	1.5 k	---
Interstitial relaxation volume[b], v_I	1.4 Ω	---
Vacancy relaxation volume, v_v	-0.2 Ω	---
Interstitial polarizability, α_I^G	150	eV
Vacancy polarizability, α_v^G	15	eV
Modulus variation, $\Delta\mu/\mu$	5×10^{-4}	---
Lattice parameter variation, $\Delta a_o/a_o$	5×10^{-4}	---
Cascade survival fraction, η	0.25	---
Sink strength, S	10^{14}	m^{-2}
Bias factor ratio, Z_I/Z_V	1.2	---
Thickness of segregation shell, h/r	0.1	---

[a] In units of the Boltzmann constant k.
[b] In units of the atomic volume $\Omega = a_o^3/4$.

nickel.(3) As will be seen below, the injected interstitials have a minor effect on void nucleation for the above irradiation conditions.

Including the effect of various amounts of injected interstitials, in the range ε_i = 0 to 10^{-3}, gives the void nucleation rates shown in Figs. 1 and 2 as a function of temperature. It is clearly seen that when the injected interstitials exceed 0.01% of those produced by displacements, void nucleation is severely suppressed at low temperatures. In fact, there exists a temperature threshold, below which void nucleation does not occur at all. This threshold depends on the dose rate, the injected interstitial fraction ε_i, and to a lesser extent on the sink strength, and on the vacancy migration energy.

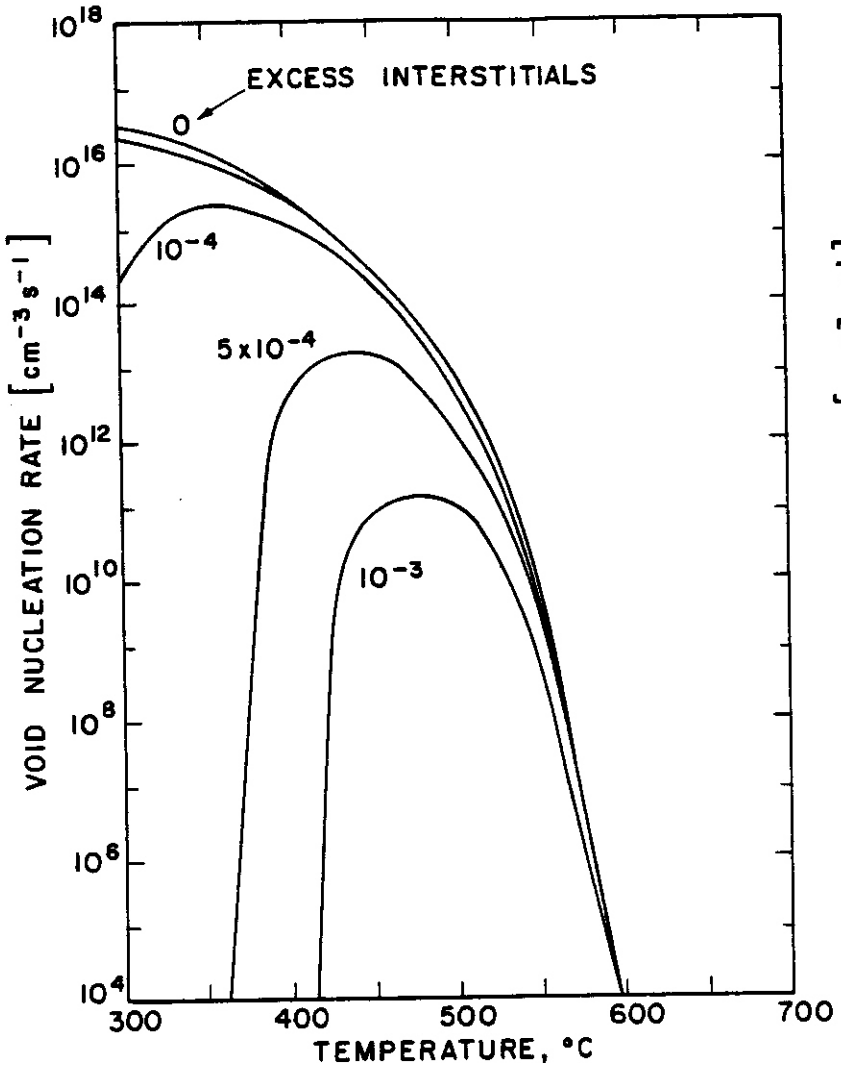

FIGURE 1. Void Nucleation Rate for a Displacement Rate of 10^{-3} dpa/s, Vacancy Migration Energy of 1.2 eV, Sink Strength of 5 x 10^{13} m^{-2}.

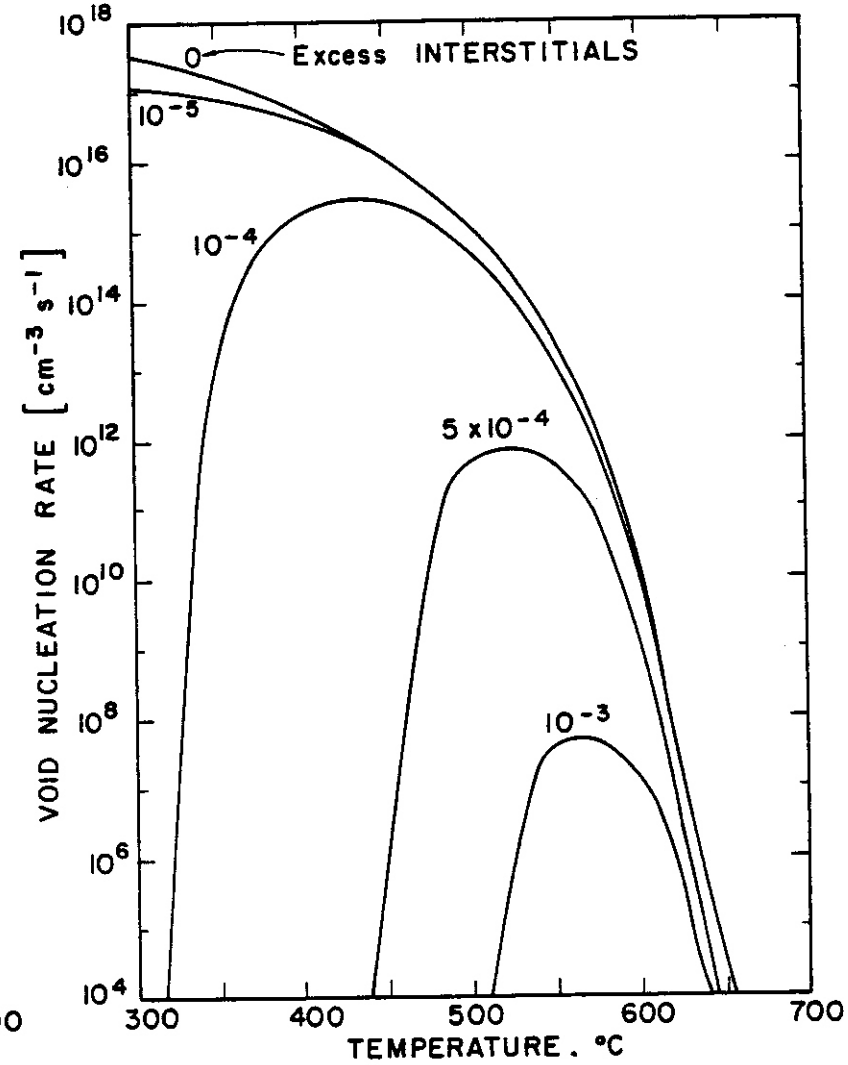

FIGURE 2 Void Nucleation Rate for a Displacement Rate of 10^{-2} dpa/s, All Other Materials Parameters as in Figure 1.

If the vacancy migration energy is assumed to be 1.4 eV (and if the vacancy formation energy is reduced so as to keep the activation energy for self-diffusion constant) the results shown in Fig. 3 are obtained. It is seen that the void nucleation rates are reduced compared to the results shown in Fig. 1, while the threshold temperatures are increased. An increase in the vacancy migration energy shifts the curves simply to higher temperatures and lower nucleation rates. The results in Figs. 1 and 2 further indicate that the most severe suppression of void nucleation is expected in regions of maximum damage production where most of the injected interstitials come to rest.

Accordingly, the suppression of void nucleation needs to be evaluated for a particular ion-bombardment of interest and as a function of depth. The case examined here is 14 MeV Ni-ion bombardment of nickel. Displacement rates and the fraction ε_i of injected interstitials were computed with the Brice code,[10] and the results are shown in Fig. 4. Note that only the depth region around the end of the range is shown in this and the following figures as this is the region of interest for the present investigation.

Using the displacement rates of Fig. 4, the void nucleation rates shown in Fig. 5 are obtained without the inclusion of the injected interstitials. As a function of depth, the void nucleation rates follow the profile of the displacement rate. However, since a variation in the displacement rate with depth is equivalent to a "temperature shift", the void nucleation rates particularly for the lower temperature range do not decrease as drastically on either side of the peak damage region as one would expect.

If the injected interstitials are now included in the void nucleation calculations, the results shown in Fig. 6 are obtained. At the temperatures of 300 and even 400°C a depression of the void nucleation becomes noticeable where the fraction ε_i of injected interstitials is greatest. Since void nucleation is sensitive to the sink strength, cascade survival fraction, vacancy migration energy, etc., the depression should also be strongly dependent on these parameters.

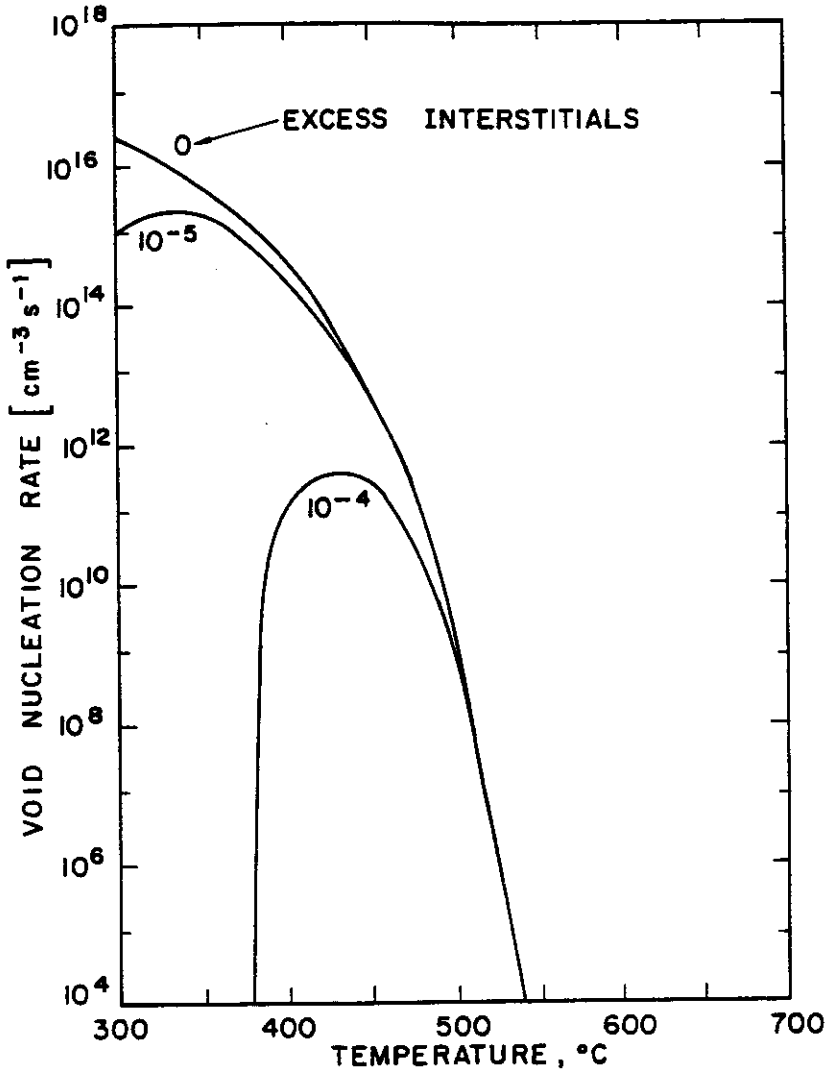

FIGURE 3. Void Nucleation Rate for a Displacement Rate of 10^{-3} dpa/s, Vacancy Migration Energy of 1.4 eV, Sink Strength of 5 x 10^{13} cm^{-2}.

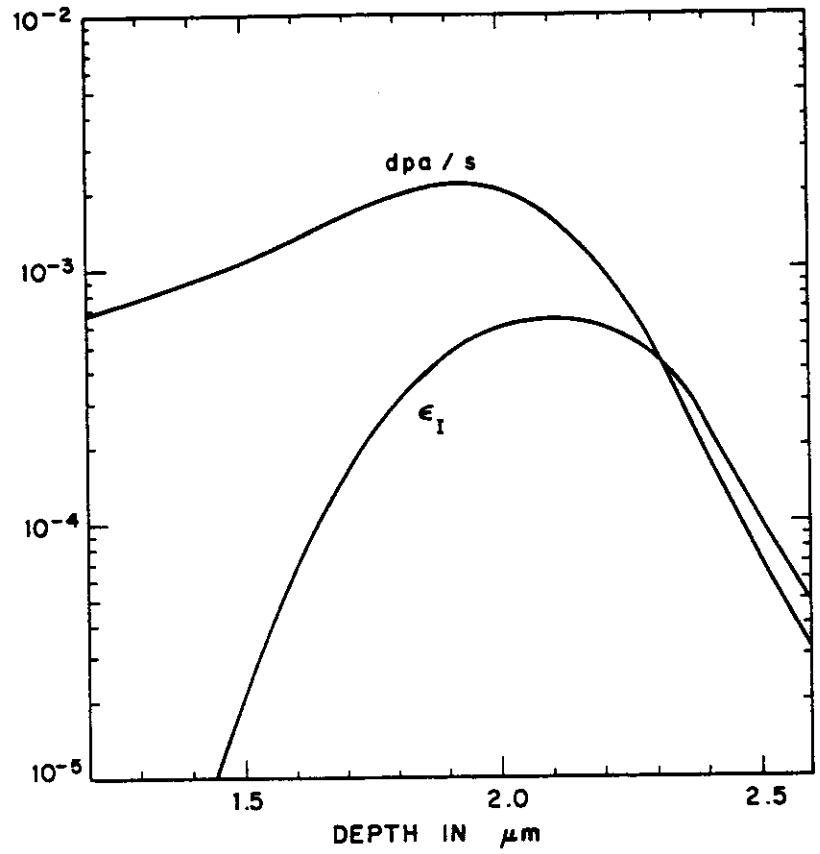

FIGURE 4. Depth Distribution of the Displacement Rate and Injected Interstitial Fraction for 14-MeV Ni Ions on Ni According to the BRICE Code.

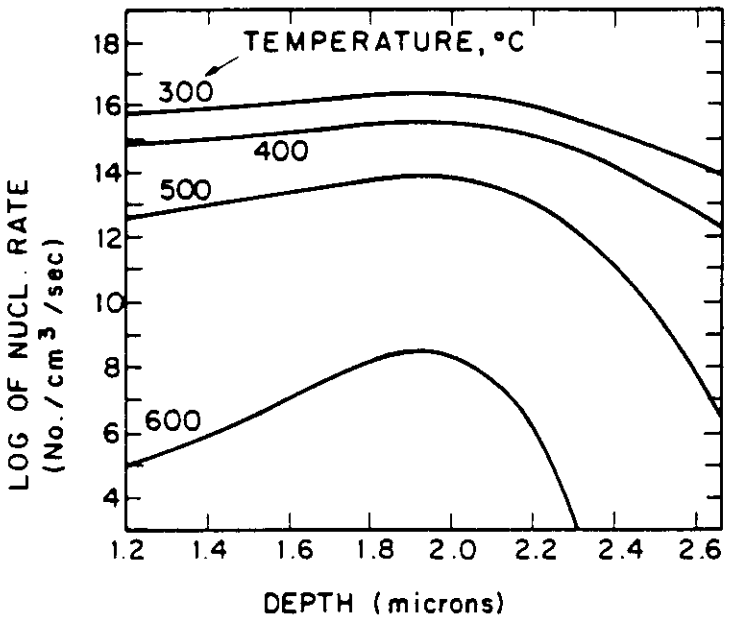

FIGURE 5. Void Nucleation Rate Without Injected Interstitials vs Depth for 14-MeV Ni Ions, Sink Strength of 10^{14} m^{-2}, Vacancy Migration Energy of 1.1 eV.

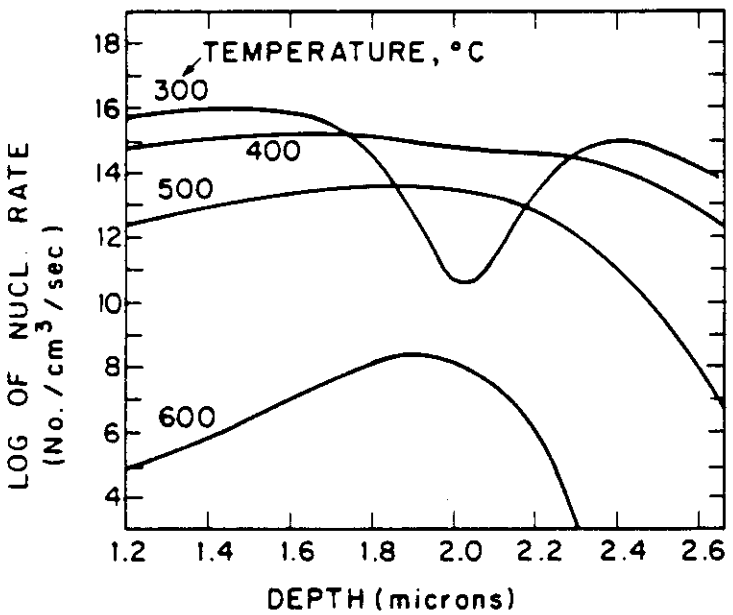

FIGURE 6. Void Nucleation Rate with Injected Interstitials and Parameters as in Figure 5.

For example, recent measurements of the vacancy formation energy by the position annihilation technique have yielded a value of 1.8 ± 0.1 eV,[11] which is significantly larger than the previously established value. Since the value of self-diffusion energy remains unaltered it implies a vacancy migration energy for nickel of 1.1 ± 0.1 eV. This value agrees then closely with the recently measured value of 1.04 ± 0.04 eV for the Stage III activation energy.[12] Suppose now that the vacancy migration energy is 1.2 eV instead of 1.1 eV used for the results in Figs. 5 and 6. As Fig. 7 shows, the suppression of void nucleation becomes more pronounced. Furthermore, if we reduce the sink strength from 10^{14} m^{-2} to 5 x 10^{13} m^{-2}, the gap in void nucleation increases even further as shown in Fig. 8.

5.4 Discussion

The suppression of void nucleation by the injected interstitials is most effective when their number becomes a significant fraction of the number of interstitials which have escaped recombination both in the cascade and in the bulk. Accordingly, the suppression is found where the ions are deposited and where recombination is the predominant fate of point defects. These conditions are identical to those valid for void growth suppression.[4] The difference lies merely in the magnitude of the suppression; it is much more dramatic for void nucleation than for void growth.

If void swelling after ion bombardment is measured either from step heights or by microscopic examinations in the peak damage region the effect of the injected interstitials is present. The swelling-temperature relationship obtained by these two techniques exhibits a sharply peaked behavior with a precipitous decline in swelling towards lower temperatures around 400°C to 500°C, depending on the displacement rate.[13] Our present results suggest that the suppression of swelling for these lower temperatures is due, in part, to the effect of injected interstitials on void nucleation.

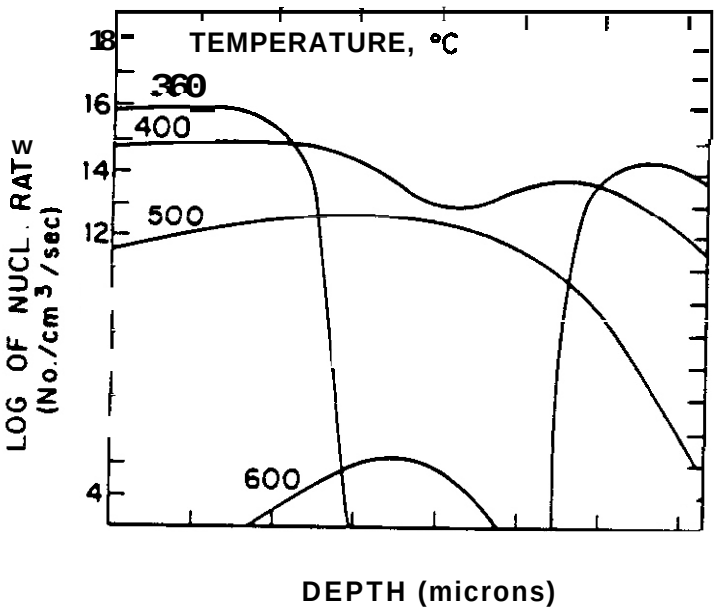

FIGURE 7. Void Nucleation Rate vs Depth, Vacancy Migration Energy *of* 1.2 eV, All Other Parameters as in Figure 6.

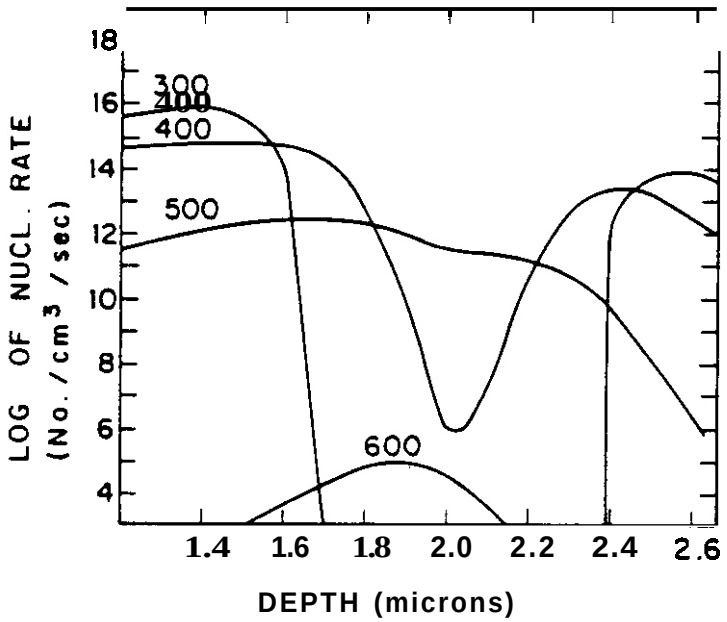

FIGURE 8. Void Nucleation Rate vs Depth, Vacancy Migration Energy of 1.2 eV, Sink Strength *of* 5 x 10^{13} m^{-2}.

The existence of a void free gap in the depth distribution has been discovered experimentally by Whitley.[3] Figure 9 shows the depth distribution of the void density in nickel irradiated with 14 MeV Cu ions at a temperature of 400°C. While the present theoretical predictions on the depth distribution of void nucleation agrees in principle with this observation of a void free gap, there are quantitative differences. First, the extent of the observed gap is larger than the predicted ones. Second, the deepest void region in this experiment is in fact beyond the end of range as computed with the Brice Code. Apart from the latter discrepancy, a direct quantitative comparison between the above experimental observation and the theoretical results cannot strictly be made for the following reasons.

The observed void distribution reflects both the processes of nucleation and growth to a visible size. In contrast, the computed nucleation rates must be interpreted in terms of a depth distribution for voids larger than the critical size, regardless of how small. The critical size is generally below the limit of visibility for transmission electron microscopy. Another difference

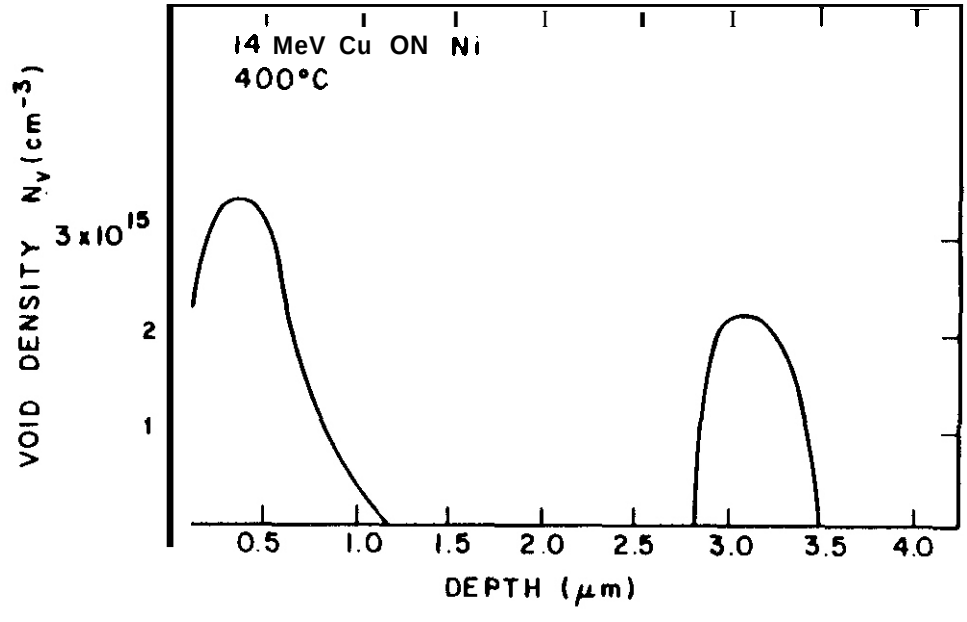

FIGURE 9. Void Density vs Depth for Nickel Irradiated at 400°C with 14-MeV Cu Ions to a Fluence *of* About 5 x 10^{16} Ions/cm^2.

arises from our assumption of a spatially uniform sink strength. Even though this is justified with regard to the initial distribution of grown-in dislocations, irradiation quickly produces a spatially nonuniform distribution of dislocation loops prior to void nucleation. Consequently, the void nucleation calculations should be carried out with this nonuniform distribution of the total dislocation density as obtained at low doses. Unfortunately, this information is not presently available.

Garner has recently shown that the injected interstitial has a pronounced effect on self-ion-induced swelling, leading both to an extension of the transient re ime of swelling and to a suppression of the steady-state swelling rate. (" He also demonstrated that the strongly peaked swelling distributions characteristic of ion irradiations were not typical of neutron irradiations and attributed the divergence to the injected interstitial. He noted, however, that within the confines of available theory, the injected interstitial was insufficient in itself to affect the steady-state swelling rate.

Whereas a reduction in the magnitude of the vacancy migration energy from 1.4 to 1.1 eV strongly reduces the predicted influence of injected interstitials on the swelling rate,[15] we have shown that it enhances the suppression of void nucleation by injected interstitials. Therefore, the work presented in this report provides a qualitative explanation for the observed difference in the low temperature dependence of neutron and ion-induced swelling. The suppression of the steady-state sweling rate at higher temperatures by the injected interstitial has not yet been explained and work is in progress to provide a theoretical explanation.

6.0 REFERENCES

1. R. A. Spurling, C. Rhodes, J. Nucl. Mat. 44 (1972) 341.
2. J. B. Whitley, G. L. Kulcinski, P. Wilkes, and H. V. Smith, Jr., J. Nucl. Mat. 7 (1979) 159.

3. J. B. Whitley, Ph.D. Thesis, University of Wisconsin, 1978.

4. A. D. Brailsford, R. Bullough, J. Nucl. Mat. 44 (1972) 121.

5. A. O. Brailsford, L. K. Mansur, J. Nucl. Mat. 71 (1977) 110.

6. J. L. Katz, H. Wiedersich, J. Chem. Phys. 55 (1971) 1414.

7. K. C. Russell, Acta Met. 19 (1971) 753.

8. A. Si-Ahmed and W. G. Wolfer, ASTM STP 783 (1982) 1008.

9. W. G. Wolfer and L. K. Mansur, J. Nucl. Mat. 91 (1980) 265.

10. D. K. Brice, Report SAND 7500622, Sandia National Laboratories, July 1977.

11. L. C. Smedskjaer, M. J. Fluss, O. G. Legnini, M. K. Chason, and R. W. Siegel, J. Phys. F: Metal Phys. 11 (1981) 2227.

12. S. K. Khana and K. Sonnenberg, Rad. Effects 59 (1981) 91.

13. W. G. Johnston, J. H. Rosolowski, A. M. Turkalo, and T. Lauritzen, J. Nucl. Mat. 47 (1973) 155.

14. F. A. Garner, "Impact of the Injected Interstitial on the Correlation of Charged Particle and Neutron-Induced Radiation Damage," Proceedings of AIME Symposium on Radiation Damage Analysis for Fusion Reactors, October 24-28, 1982, St. Louis, MO, (to be published in J. Nucl. Mat.); also in OAFS quarterly report DOE/ER-0046/11.

15. L. K. Mansur and M. H. Yoo, J. Nucl. Mat. 85 and 86 (1979), 523-532.

7.0 FUTURE WORK

It is planned to examine the effect of injected interstitials in 5 MeV Ni-ion bombardment of Ni and to use a more accurate ion implant distribution profile.

8.0 PUBLICATIONS

None.

CHAPTER 6

INSULATORS

COMPARISON OF LOW DOSE NEUTRON AND GAMMA IRRADIATION DAMAGE IN G-10CR

G. F. Hurley, J. D. Fowler, Jr., and D. L. Rohr
(Los Alamos National Laboratory)

1.0 Objective

This study is being carried out to determine the effects of neutron-irradiation at 4.2 K on epoxy and polyimide insulators, and to compare these effects with those from gamma-irradiations at the same temperature, and in the same materials.

2.0 Summary

Insulators in superconducting magnets for fusion reactors will be exposed to radiation doses of 10 to 100 MGy, with more than half the dose coming from neutrons. Samples of the epoxy-matrix laminate G-10CR were irradiated with high energy neutrons in liquid helium to a dose of 2.5 MGy, to simulate the operating environment. Mechanical and electrical properties were subsequently measured at room and liquid nitrogen temperatures. Results are compared to other studies of changes due to gammas. Dose effects due to the heterogeneous nature of this composite material and the nature of the radiation sources are discussed.

3.0 Program

Title: Radiation Damage Analysis and Computer Simulation (Radiation Effects in Organic Insulators)
Principal Investigator: G. F. Hurley
Affiliation: Los Alamos National Laboratory

4.0 Relevant DAFS Program Plan Task/Subtask

Task II.B.4: Damage Production in Insulators

Subtask II.B.4.3: Experimental Validation/Calibration of Theory

5.0 Accomplishments and Status

5.1 Introduction

In previous reports in this study,[1,2] we reviewed the requirements for organic insulation in magnetic confinement fusion reactors, and described an irradiation experiment including a preliminary characterization of the irradiation-induced degradation of electrical and mechanical properties for a series of candidate electrical insulation materials. At the dose level attained to date, only one of the materials has shown clear-cut property changes: G-10CR. The present report describes the measured changes in the electrical and mechanical properties of this material, and compares these changes to those observed by other investigators in the same material after irradiation in the Bulk Shielding Reactor (BSR).

5.2 Experimental Details

G-10CR was obtained from the Spaulding Fibre Co., in plate and sheet forms from which the various sample configurations were machined. Compression and flexure samples had their axes in the plane of the fabric and parallel to the warp direction. Electrical test samples were punched from sheet materials preserving as-fabricated upper and lower surfaces. Details of sample configuration and pre- and post-irradiation treatments have been described previously.[1,2]

Irradiation was carried out in IPNS in liquid helium to a neutron fluence of 1.52×10^{21} n/m^2, $E_n > 0.1$ MeV. Neglecting the in-reactor gamma dose which accompanies the neutron dose (<15% of the total dose), further calculations[3] have revealed the ionizing dose contributions for G-10CR as given in Table 1. It is assumed that for low doses, the dose to the glass is not important. At much higher doses, say > 10^8 Gy, damage to the glass might become non-negligible. Silica glass has been observed to become metamict with a few percent

TABLE 1

DOSIMETRY FOR G-10CR

Component	Neutron dose, >.1 MeV[+] Units of 10^{21} n/m^2	Absorbed dose[*] Units of 10^6 Gy
Epoxy Matrix	1.52 ± .03	2.48 ± .05
E-Glass Fibers	1.52 ± .03	0.801 ± .015
Laminate	1.52 ± .03	1.30 ± .03

+ Total n/m^2 = 1.44 × number given; thermal n/m^2 = .008 × number given. Range represents variation among 5 dosimetry wires analyzed.

* Absorbed dose neglects contribution from gamma rays, which is estimated to be less than 15% of the dose as stated.

volume compaction within this dose range.[4] This might greatly affect the composite behavior, even conceivably leading to rupture of the fibers.

5.3 Results

5.3.1 Electrical Tests

Measurements of D.C. conductivity and A.C. dielectric properties for G-10CR after irradiation were described previously.[2] Results showed increased D.C. conductivity measured at room temperature, an increase in dielectric constant over the frequency range 10 to 10^5 Hz, at both 80 K and room temperature, and no significant change in loss tangent measured over the same frequency range and temperatures. The increase in dielectric constant was about 6 percent, which implies a radiation-induced decrease in A.C. resistivity of 5 to 6%. Large sample-to-sample variations in loss tangent were observed at the higher frequencies.

Dielectric breakdown strength tests were conducted at room temperature in a chamber pressurized to 1.3 MPa of nitrogen gas to prevent surface flashover. Bulk breakdown was observed in all samples. Electrodes consisted of a flat,

circular, polished steel rod 6.4 mm diameter on one side of the sample, with a flat, polished steel plate 10 mm diameter on the other. The D.C. voltage was ramped from zero to the breakdown voltage at a rate of 200 V/s. Results (Table 2) indicate no significant radiation-induced changes in breakdown strength.

TABLE 2

DIELECTRIC BREAKDOWN STRENGTH OF 3 IRRADIATED AND 5 CONTROL SAMPLES AT 295 K. VARIATION IS ONE STANDARD DEVIATION.

	OBS (kV/mm)
Control	78.4 ± 7.3
Irradiated	80.2 ± 9.2

Microscopic examination of the breakdown path indicates that the normal entrance point was over a junction of two orthogonal glass reinforcement strands. The current would follow one of the strands horizontally to the next junction and exit on the other side of the sample. There were no apparent path differences between control and irradiated samples.

5.3.2 Mechanical Tests

Flexural and longitudinal compression tests were carried out at room and liquid nitrogen temperatures. Test procedures and results of the tests at 75 K have been reported.[2] The effect of irradiation was to reduce flexural strength and strain to failure by 15 and 12 percent, respectively. Longitudinal compression strength and failure strain were also reduced, though less distinctly. Results of flexure and compression testing at room temperature are presented in Figure 1. Flexure strength and modulus were reduced just over 10 percent, with no significant change in flexure strain. Change in room temperature compression strength was negligible; if any it may have increased slightly. Modulus and failure strain scattered too badly to assess changes. The level of unirradiated ultimate compressive strength is in the range

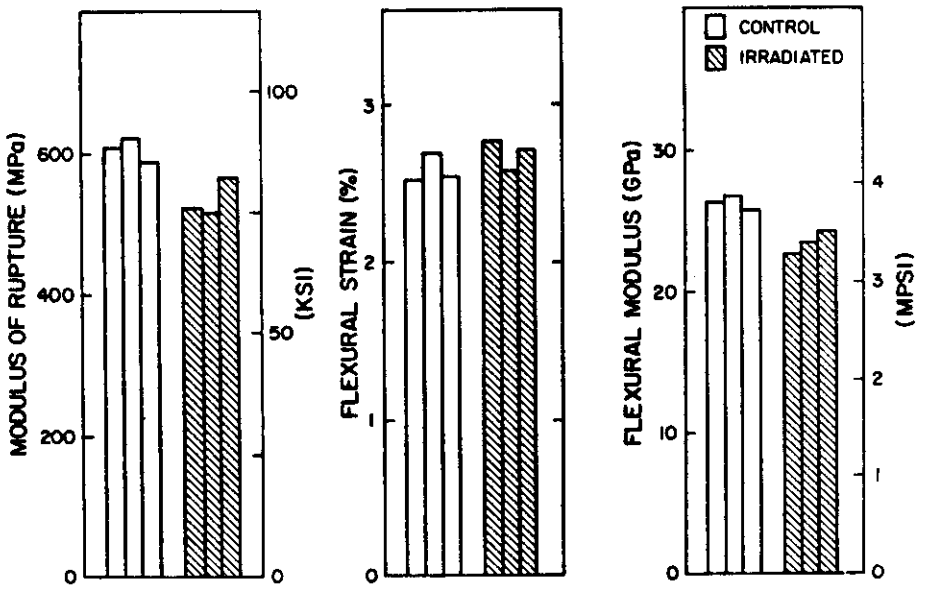

(A) G-10CR; FLEXURE; 295K

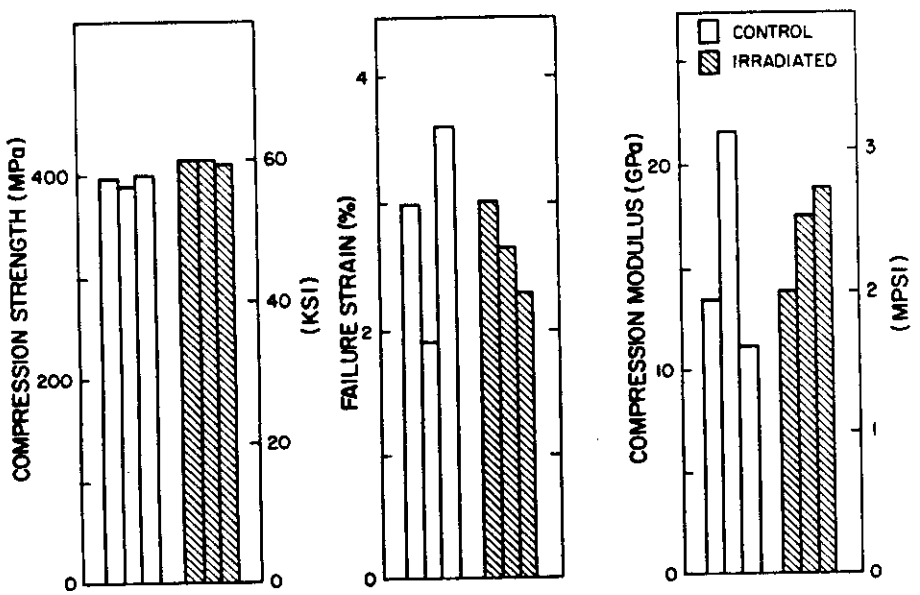

(B) G-10CR; COMPRESSION; 295K

FIGURE 1. Results of Neutron Irradiation on Flexural and Longitudinal Compression Strength of G-10CR, Measured at Room Temperature.

reported by other investigators.[5-7]

Figure 2 shows the appearance of typical fractures for each of the four compression cases. At room temperature, failure generally occurred by shear, with either a single oblique shear fracture or a wedging-type combination of two shear planes. Characteristics of fracture have been described in a comprehensive study of compression fracture in these materials.[8]

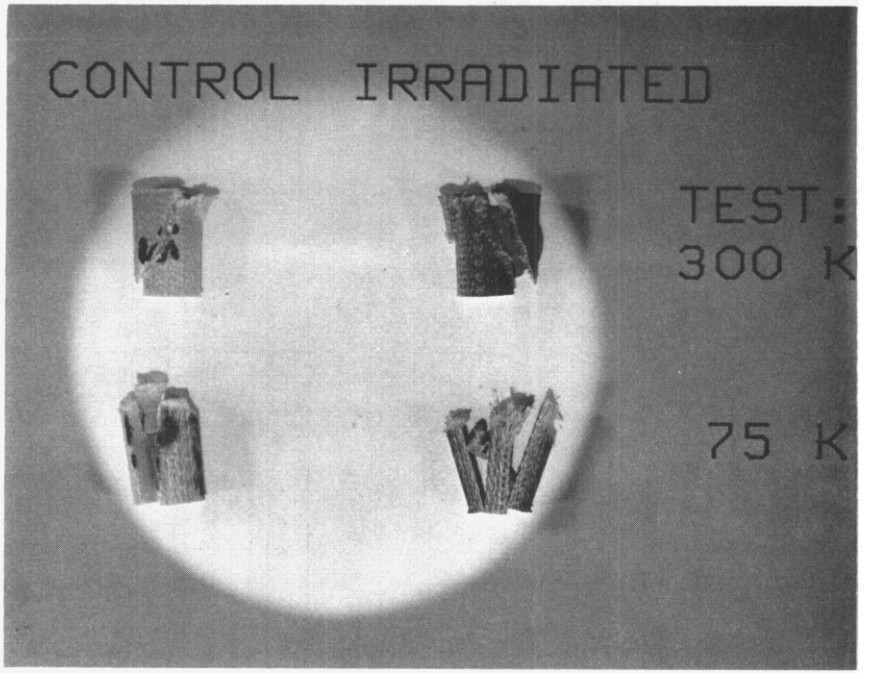

FIGURE 2. Characteristic Appearance of Longitudinal G-10CR Fractures, Before and After Neutron Irradiation, at Two Test Temperatures.

Although many of the general features observed were the same as our observations, some differences, especially in temperature dependence, were found. These may have resulted from differences in specimen configuration and test method. We see no change in fracture mode with irradiation, after room temperature testing.

Fracture at 75 K was dramatically different than at room temperature (Figure 2), with longitudinal cleavage strongly predominating. Further, a small effect of irradiation was evident in that the irradiated samples tended to separate along multiple planes with the result that the long longitudinal fractures could be comprised of parallel, interlaminar cracks linked by the fabric between the layers. Macroscopic examination of flexure samples revealed only minor changes due to irradiation after testing at 75 K,[2] and the same observation was true after room temperature testing.

Fracture surfaces of both flexure and compression samples were examined by SEM and by optical microscopy. Characteristic differences were found in the way that fibers separated from the matrix when control and irradiated samples fractured at 75 K. Representative views are shown in Figure 3, for flexure failures. In the control sample (Figure 3a), fracture occurred partly in the resin and partly along the fibers. Where the latter occurred, separation was quite clean, although generally adhesion between fibers and matrix appeared fairly good.

Irradiated samples appeared quite different, as shown in Figure 3b. Here clean separation from the matrix was rare and the fracture path tended to occur in the matrix near, but not at, the interface. This was manifested by a rough film-like material remaining on separated fibers.

5.4 Discussion

The present results may be compared with those of an ongoing study of G-10CR and other materials by Coltman and coworkers at the Oak Ridge National Laboratory (cf. Ref. 5). In that work, samples were irradiated inside a cadmium shield in the Bulk Shielding Reactor (BSR), resulting in an external dose estimated to be primarily (>96%) from interaction with gamma radiation. A complication in the work is the large thermal neutron flux in BSR, not entirely eliminated by the cadmium shield, which interacts with boron in the E-Glass reinforcement in G-10CR. Thus, extra energy is deposited from ^{10}B

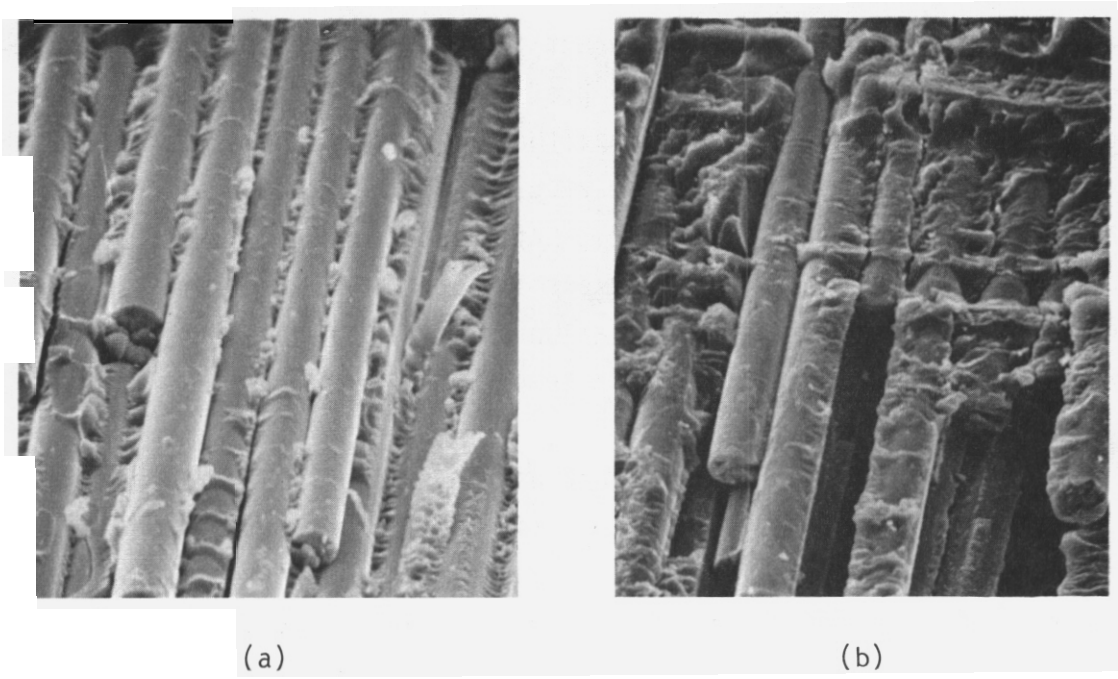

FIGURE 3. Fracture Surfaces on (a) Control Sample and (b) Neutron-Irradiated Sample. Both samples were tested at 75 K. Fiber diameter is ∿10 μm.

fissions which yield ^{7}Li and ^{4}He recoil fragments. To eliminate this extra dose, a variant of G-10CR containing boron-free S-Glass, denoted G-10CR BF, was also tested. These materials were irradiated to minimum imposed gamma ray doses of 3×10^{6} Gy.

Table 3 compares the strength retained by G-10CR in the present work (2.5×10^{6} Gy) with that reported for G-10CR and its S-Glass variant (the latter limited to flexural strength) in the previous work.[5] The gamma-irradiation data are given at 3×10^{6} Gy, and values extrapolated to 2.5×10^{6} Gy are also presented. This comparison shows that:

> Reduction of flexural strength is greater than for longitudinal compression strength, for both neutron and gamma radiation, measured at liquid nitrogen temperatures.

TABLE 3

COMPARISON OF RETAINED FLEXURE AND LONGITUDINAL COMPRESSION STRENGTH FOR G-10CR AFTER NEUTRON OR GAMMA IRRADIATION AT LIQUID HELIUM TEMPERATURE

	2.5×10^6 Gy {Neutrons}	3×10^6 Gy (Gamma}	2.5×10^6 Gy*,+ {Gamma}
Flexure Strength	85%	60% {75%}	70% {82%}
Longitudinal Compression Strength	94%	75%	88%

* Extrapolated
\+ Bracketed Values are for G-10CR BF

The degradation of flexural and longitudinal compressive strength measured after gamma irradiation of G-10CR in the BSR, extrapolated to 2.5×10^6 Gy, is substantially greater than that after fast neutron irradiation.

The flexural strength degradation at the same extrapolated dose of G-10CR BF is similar to that for G-10CR after neutron irradiation.

No data for the effects of gamma irradiation on the electrical properties are available below a dose of 2×10^7 Gy. Data at 2×10^7 Gy indicate no significant change in post-irradiation resistivity, loss tangent at 1 kHz, or breakdown strength, measured at room temperature.[9] Breakdown in that work occurred by surface flashover at comparatively low voltage stress; hence only resistivity and loss tangent can be concluded not to have changed.

Those results contrast with the small but significant decrease in post-irradiation room-temperature restivity at an equivalent neutron-induced dose an order of magnitude smaller. If the preference of breakdown paths for the fiber bundles or adjacent material is indicative of D.C. conduction paths, then radiation-induced changes in this area are the likely cause for the

resistivity decrease. This decrease, along with the observed increase in dielectric constant at both temperatures, could be a result of different damage-producing mechanisms of neutrons, as compared to gammas. In any case, these changes are much smaller than previously observed in-situ changes in radiation-induced conductivity,[9] and would in no way limit the use of the material at this dose in a superconducting magnet.

Damage to G-10CR and similar materials is complicated by the nature of the component materials and by the spatial relationship of their interactions with the irradiation source. The microstructure of G-10CR contains 10 μm glass fibers, arrayed in bundles (yarns), with small (10 μm) spacing, while the yarns themselves are much more widely separated. Prior to impregnation of the resin matrix, the glass cloth is treated with a coupling agent, in this case aminosilane,[10, *] which acts to retain adhesion between matrix and fibers. Silane typically is present in substantial quantity[11, 12] and hence may be expected to change the composition of the matrix in the vicinity of the fibers. In particular, aminosilane contains more hydrogen than the resin matrix. As the result of efficient energy transfer between fast neutrons and hydrogen, the interface region can therefore be expected to be a preferred site for initial energy deposition. Resulting damage would of course extend over the range of displaced hydrogen atoms (10's of μm) but local chemical changes could also be expected to occur as the result of bonding unsaturation.

Thus, in the two cases we are comparing--neutron-irradiation in IPNS and gamma-irradiation in BSR--the doses to the components of G-10CR vary, and in different ways. The single case of G-10CR BF, irradiated in BSR, is an exception, with the dose quite uniform throughout. G-10CR irradiated in BSR has an essentially uniform gamma ray dose enhanced by ^{10}B fission damage in a region primarily restricted to the yarns. Neutron irradiation in IPNS results in the major dose to the matrix, especially in the silane-rich areas (the yarns), and a lower dose to the fibers. Modeling of the dose distribution for these cases would seem to be a fruitful area for additional work.

---

* γ-aminopropyltriethoxysilane

5.5 Conclusions

Neutron-irradiation of G-10CR at liquid helium temperature to 2.5 MGy results in small but significant changes in mechanical and electrical properties. Flexural strength was reduced at both room temperature and 75 K, while longitudinal compression strength was reduced only in 75 K measurements. D.C. resistivity decreased in room temperature measurements, while loss tangent was not found to change at either room temperature or 80 K. The latter measurements revealed a small increase in dielectric constant at both temperatures, implying a small decrease in A.C. resistivity. Dielectric breakdown strength was determined at room temperature and did not change significantly with irradiation.

Fracture mode and fracture surfaces were examined in samples tested at both temperatures in irradiated and control forms. Macroscopic fracture mode was primarily a function of test temperature but qualitatively showed an increase in delamination in irradiated longitudinal compression samples tested at 75 K. Both flexure and compression fracture surfaces, after the 75 K test, showed a marked change in appearance with preferential failure near the fibers occurring through the resin in irradiated samples, and more cleanly at the fiber surface in control samples. This change may be associated with greater energy deposition by neutrons within the aminosilane coupling layer.

As a result of the heterogeneous nature of the composite structure of G-10CR, and the interaction with the spectral components of various irradiation sources, damage production is microscopically inhomogeneous and probably affects the detailed nature of degradation. For this reason, conclusive comparison of this data with that for the same and similar materials irradiated in BSR, will require higher fluence neutron damage data, as well as a detailed model for how and where the damage occurs and its effect on properties. The present results compare most favorably with the results for essentially pure gamma damage in boron-free G-10CR BF.

5.6 Acknowledgments

The authors wish to thank Dr. Larry Greenwood, ANL who provided the dosimetry analysis. We are also indebted to Drs. Don Parkin and Frank Clinard for their helpful comments.

6. References

1. G. F. Hurley, J. D. Fowler, Jr., and D. M. Parkin, "Neutron-Irradiation Plan for Calibration of Gamma and Neutron Damage Effects in Organic Insulators" in Damage Analysis and Fundamental Studies Quarterly Progress Report for October-December, 1981, DOE/ER-0046/8, Vol. 1, 57.

2. G. F. Hurley, J. D. Fowler, Jr., R. Liepins, B. Jorgensen, and J. Hammond, "Comparison of Neutron and Gamma Irradiation Damage in Organic Insulators," in Damage Analysis and Fundamental Studies Quarterly Progress Report for April-June, 1982, DOE/ER-0046/10, 53.

3. L. R. Greenwood, Argonne National Laboratory, Argonne, IL, Private Communication.

4. Eberhard Lell, Norbert J. Kreidl, and J. Raymond Hensler, "Radiation Effects in Quartz, Silica, and Glasses," in Progress in Ceramic Sci., J. E. Burke, ed., 4 (1966) 1.

5. R. R. Coltman, Jr., and C. E. Klabunde, "The Strength of G-10CR and G-11CR Epoxies after Irradiation at 5 K by Gamma Rays," J. Nuclear Materials, in press (1982).

6. James R. Benzinger, "The Manufacture and Properties of Radiation Resistant Laminates," Advances in Cryogenic Engineering *Materials*, 28, R. P. Reed and A. F. Clark, eds., Plenum, NY (1982) 231.

7. R. E. Schramm and M. B. Kasen, "Effect of Cryogenic Temperatures on the Mechanical Performance of Glass-Fabric-Reinforced Laminates," in Materials Studies for Magnetic Fusion Energy Applications at Low Temperatures-V R. P. Reed and N. J. Simon, eds., NBSIR-82-1667, (May, 1982) 391.

8. Betty A. Beck, "Fracture Analysis of Compression Damage in Glass Fabric/Epoxy, G-10CR, 295 K to 4 K," Ibid., Vol. IV, NBSIR-81-1645 (Apr. 1981), 507.

9. R. H. Kernohan, C. J. Long, and R. R. Coltman, Jr., "Cryogenic Radiation Effects on Electric Insulators," J. Nuclear Materials 85 & 86, (1979) 379.

10. J. R. Benzinger, Spaulding Fibre Co., Inc., Tonawanda, NY, Private Communication.

11. D. J. Tutas, R. R. Stromberg, and E. Passaglia, "Studies of the Thicknesses of Absorbed Glass Finishes by Ellipsometry," Proc. 19th Conf., SPI, Reinforced Plastics Div., (1964) Section 21C.

12. Porter Erickson and Edwin P. Plueddemann, "Historical Background of the Interface," in Composite Materials 6, Edwin P. Plueddemann, ed., (1974) 2.

7. Future Work

Additional irradiations are underway or completed in IPNS to extend the total dose out to 1×10^{22} n/m^2. Two compounds to model the epoxy matrices have been prepared and are being irradiated.

DISTRIBUTION

UC-20 (108)

UC-20c (76)

DOE-HQ/Office of Breeder Technology Projects
NE-53
Washington, DC 20545

PB Hemmig, Asst Director, Reactor Physics Tech

DOE-HQ/Office of Fusion Energy (2)
Washington, DC 20545

JF Clark, ER-70
JF Decker, ER-54, G-256

DOE-RL/Office of Asst Manaaer for Projects & Facilities Management (2)
FMIT Project Office

GM Chenevert, Project Manager

DOE-RL/Office of Asst Manaaer for Advanced Reactor Programs
Breeder Technology Division

KR Absher, Chief, Technology Development Branch

Argonne National Laboratory (5)
9700 South Cass Avenue
Argonne, IL 60439

LR Greenwood
BA Loomis
A. Taylor
H. Wiedersich
RE Nygren

Battelle Memorial Institute (3)
Pacific Northwest Laboratorv
P.O. Box 999
Richland, WA 99352

JL Brimhall
DA Dingee
TD Chikalla

Brookhaven National Laboratory
Associated Universities
Upton, Long Island, NY 11973

Chairman, Nuclear Energy Dept

Columbia University
Plasma Physics Laboratory
New York, NY 10027

RA Gross

General Atomic Company (2)
P.O. Box 81608
San Diego, CA 92138

GR Hopkins
JR Gilleland

INESCO
11011 Torreyana Rd
San Diego, CA 92121

RD Stevenson

Lawrence Livermore Laboratory (3)
P.O. Box 808
Livermore, CA 94550

WL Barmore
MW Guinan, L-396
CM Logan

Los Alamos National Laboratory (4)
P.O. Box 1663
Los Alamos, NM 87544

DJ Dudziak
J. Fowler, E-546
CR Emigh
G. Hurley, E-546

Massachusetts Institute of Technology (5)
7 Massachusetts Avenue
Cambridge, MA 02139

L. Lidsky
I- W Chen, 13-5118
NJ Grant, 8-305
DB Montgomery, NW21
JB Vander Sande, 13-5025

DISTRIBUTION (Cont'd)

Massachusetts Institute of Technology
Nuclear Reactor Laboratory
138 Albany St
Cambridge, MA 02139

OK Harling, NW12-204

McDonnell-Douglas Astronautics Co.
P.O. Box 516
St. Louis, MO 63166

D. Kummer

Mound Laboratory
P.O. Box 32
Miamisburg, OH 45342

Manager, Tech Appl & Dev

National Bureau of Standards
Gaithersburg, MD 20760

JA Grundl

Naval Research Laboratory (3)
Washington, DC 20375

I. Manning, Code 6672
JA Sprague, Code 6395
LE Steele, Code 6390

North Carolina State University
Department of Nuclear Engineering
Raleigh, NC 26707

JR Beeler, Jr.

Oak Ridge National Laboratory (12)
P.O. Box X
Oak Ridge, TN 37830

K. Farrell
ML Grossbeck
PJ Maziasz
LK Mansur
NH Packan
M. Roberts, Director,
FG Perey
J. Sheffield
JO Stiegler
C. Weisbin
FW Wiffen
Bldg 9204-1
Bldg 9201-2

Princeton University (2)
Plasma Physics Laboratory
Forrestal Campus
P.O. Box 451
Princeton, NJ 08544

K. Wakefield
H. Furth

Rockwell International
8900 DeSoto Ave
Canoga Park, CA 91304

D. Kramer

Sandia Laboratories (2)
P.O. Box 5800
Albuquerque, NM 87185

FL Vook, Org 5100

Sandia Laboratories
Livermore, CA 94550

WD Wilson

Science Applications, Inc.
1200 Prospect
LaJolla, CA 92037

Dr. H. Gurol

University of California (2)
Los Angeles, CA 90024

RW Conn
NM Ghoniem

University of Michigan
Nuclear Engineering
Ann Arbor, MI 48109

T. Kammash

University of Missouri
Mechanical & Aerospace Engineering
1006 Engineering Bldg
Columbia, MO 65211

M. Jolles

DISTRIBUTION (Cont'd)

University of Missouri
Dept of Nuclear Engineering
Rolla, MO 65401

A. Kumar

University of Virginia
Dept of Materials Science
Charlottesville, VA 22901

WA Jesser

University of Wisconsin
1500 W. Johnson Drive
Madison, WI 53706

WG Wolfer

Westinghouse
Advanced Energy Systems
Fuels Materials Technology
P.O. Box 158
Madison, PA 15663

A. Boltax, Manager

Westinghouse
Research and Development Center (2)
310 Beulah Road
Pittsburgh, PA 15235

S. Wood
JA Spitznagel

Commission for the European Communities
200, rue de la Loi
B-1049 Brussels, Belgium

J. Darvas

Energieonderzoek Centrum Nederland
Westerdionweg 3
NL-1755 ZG Petten, The Netherlands

B. Van Der Schaaf

EURATOM
Joint Research Center Ispra
Materials Science Division
I-21020 Ispra, Varese, Italy

P. Schiller

Hahn-Meitner Institute für Kernforschung
Glienickerstrasse 100
D-1000 Berlin,
Federal Republic of Germany

H. Wollenberger

Hokkaido University (2)
Metals Research Institute
Kita hu, Sapporo, Japan, 060

Mihio Kiritani, Precision Eng
Taro Takeyama

Japan Atomic Energy Research Institute (2)
Physical Metallurgy Laboratory
Tokai Research Establishment
Tokai-mura, Naka-gun, Ibaraki-ken, Japan

Shuichi Iwata, Physics
Kensuke Shiraishi, Nuclear Fuel Research

Kernforschungsanlage Julich GmbH
Postfach 1913
D-517 Julich,
Federal Republic of Germany

H. Ullmaier

Kernforschungsanlage Karlsruhe
Institüt fur Reaktorbauelemente
Postfach 3640
D-7500 Karlsruhe 1,
Federal Republic of Germany

K. Ehrlich

DISTRIBUTION (Cont'd)

Kyushu University
Research Institute for Applied Mechanics
6-10-1 Hakozaki, Higashi-ku,
Fukuoka, Japan 812

Kazunori Kitajima

National Research Council
Montreal Road
Ottawa, Canada

EV Kornelson

National Research Institute for Metals
Nuclear Materials Division
1-2-1 Sengen, Sakura-mura,
Niihari-gun, Ibaraki 305, Japan

Naoki Kishimoto

Netherlands Energy Research Foundation
Materials Department
P.O. Box 1
NL-1755 ZG Petten, The Netherlands

W. Van Witzenburg

Osaka University
Dept of Nuclear Engineering
2-1, Yamada-oka, Suita,
Osaka, Japan 565

Kenji Sumita

Science University of Tokyo
Engineering Dept
Kagurazaka, Shinjuku-ku,
Tokyo, Japan 162

RR Hasiguti

Studiecentrum voor Kernenergie
Centre d'Etude de l'Energie Nucleaire
Boeretana 200
B-2400 Mol, Belgium

J. Nihoul

Swiss Federal Institute
for Reactor Research
CH-5303 Wuerenlingen, Switzerland

WV Green

Tokyo Institute of Technology
12-1, 2-Chome, O-Okayama
Meguro-ku, Tokyo, Japan

Kensutaka Kawamura

United Kingdom Atomic Energy Authority
Atomic Energy Research Establishment
Metallurgy Division
Building 388
Oxfordshire, OX11 ORA, UK

DR Harries

University of Tokyo (3)
7-3-1 Hongo
Bunkyo-ku, Tokyo, Japan 113

Naohira Igata, Met & Mater Science
Shiori Ishino, Nuclear Eng
Taijiro Uchida

DISTRIBUTION (Cont'd)

HEDL (37)

SD Adkin	W/A-58	WN McElroy	W/C-39
TK Bierlein	W/A-1	EK Opperman	W/A-58
HR Brager	W/A-64	NF Panayotou	W/A-65
LL Carter	W/B-47	RW Powell	W/A-64
DG Doran (5)	W/A-57	RJ Puigh	W/A-58
EA Evans	W/C-23	FH Ruddy	W/C-39
FA Garner	W/A-57	FA Schmittroth	W/A-4
DS Gelles	W/A-64	WF Sheely	W/C-62
R. Gold	W/C-39	RL Simons	W/A-57
JV Hagan	W/B-41	JL Straalsund	W/A-61
HL Heinisch	W/A-57	HH Yoshikawa	W/C-44
DL Johnson	W/A-4	Central Files (3)	W/C-110
GD Johnson	W/A-65	Publ Services (2)	W/C-115
NE Kenny	W/C-115	Doc Services	W/C-123
FM Mann	W/A-4	Microfilm Services	W/C-123